Discharge variability and river incision along a climate gradient in central Chile

Dissertation

zur Erlangung des Grades eines

Doktors der Naturwissenschaften (doctor rerum naturalium)

am Fachbereich Geowissenschaften

der Freien Universität Berlin

vorgelegt von

Renee van Dongen

Berlin 2021

Erstgutachter:	Prof. Dr. Dirk Scherler
	Freie Universität Berlin
Zweitgutachter:	Prof. Dr. Taylor Schildgen
	Universität Potsdam
Tag der Disputation:	21 September 2021

Eidesstattliche Erklärung

Hiermit erkläre ich, dass ich die vorliegende Dissertation selbstständig und ohne unzulässige Hilfe verfasst habe. Bei der Verfassung dieser Dissertation wurden keine anderen als die im Text und Literaturverzeichnis aufgeführten, Hilfsmittel und Quellen verwendet. Beiträge von Koautoren zu publizierten oder zur Publikation vorbereiteten Manuskripten sind im Vorwort ("Preface") dieser Arbeit dargelegt. Ich versichere, dass die vorgelegte elektronische mit der schriftlichen Version der Dissertation übereinstimmt. Ein Promotionsverfahren zu einem früheren Zeitpunkt an einer anderen Hochschule oder einem anderen Fachbereich wurde nicht beantragt.

Koblenz, 02. Juli 2021

_____

Renee van Dongen

Los Rios Acuden

Amada de los ríos, combatida
por agua azul y gotas transparentes,
como un árbol de venas es tu espectro
de diosa oscura que muerde manzanas:
al despertar desnuda entonces,
eras tatuada por los ríos,
y en la altura mojada tu cabeza
llenaba el mundo con nuevos rocíos.

Te trepidaba el agua en la cintura.
Eras de manantiales construida
y te brillaban lagos en la frente.
De tu espesura madre recogías
el agua como lágrimas vitales,
y arrastrabas los cauces a la arena
a través de la noche planetaria,
cruzando ásperas piedras dilatadas,
rompiendo en el camino
toda la sal de la geología,
cortando bosques de compactos muros,
apartando los músculos del cuarzo.

Pablo Neruda (1904-1973)

Acknowledgements

First of all, I would like to express my gratitude to my supervisor Dirk Scherler. Thank you for giving me this opportunity, for your effort, the many scientific discussions, and your constructive feedback. The past years have been a steep learning-curve and I would have not achieved all of this without your support.

Secondly, I would like to thank Friedhelm von Blanckenburg, Todd Ehlers, Kirstin Übernickel and Leandro Paulino for initiating and coordinating the DFG-funded priority program "EarthShape", which my PhD project was part of. I am grateful to be part of this large interdisciplinary German-Chilean research network and I gained a lot from the contact with German and Chilean scientists from various disciplines.

My PhD project strongly depended on fieldwork in Chile. I would like to say muchas Gracias to Ricardo Carrillo and hartelijk bedankt to Melle Koelewijn, for your help during fieldwork. Additionally, I would like to thank Luca Mao and his team, for providing support and equipment for the fieldwork campaigns and the installation and maintenance of the river discharge stations in the EarthShape catchments.

Furthermore, I would like to thank Friedhelm von Blanckenburg and all current and former colleagues of the Earth Surface Geochemistry section at the GFZ in Potsdam. I am thankful to have been part of this section where high-level science and a great atmosphere are the standard. I am grateful for the many opportunities to discuss science, the feedback and input I received from all colleagues, and, above all, the friendships that found in this group of colleagues. Also, it was privilege to have the opportunity to work in the HELGES laboratory for my research. In specific, I would like to thank Hella Wittmann and Cathrin Schulz for the training, supervision, and support in the Cosmogenic Nuclides Laboratory. I am grateful for the help of HiWi's Kristina Martin and David Matzdorff during mineral seperation.

There are a few section 3.3 colleagues who I would like to specifically name. Many thanks to Conni Dettlaff for always helping out with administrative issues. I would like to thank René Kapannusch for being the second René in "the René(e)'s team. It has been great to get through this PhD-process together and I am very grateful for teaching me all the mineral separation labwork. Many thanks to Emma Lodes, for the good time in the field, the many scientific discussions, and thanks for proof-reading some of the chapters of this PhD thesis. Moreover, I would like to express my gratitude to Daniel Frick and Michael Henehan, for motivating and supporting me in the final phase of my PhD project.

Over the course of my PhD, I have had the privilege to work together with several external (outside of Section 3.3) scientists, who I would like to thank for the great collaborations. Many thanks to: Dadiyorto Wendi, Claudio Meier, Eric Deal and Igor Lisac.

I am thankful for the patience, understanding and support of my current colleagues at the International Centre of Water Resource and Global Change, the German Federal Institute of Hydrology, and in specific the URSACHEN team members. It was challenging to focus on two scientific projects at the same time and I am happy to fully focus on our work together.

Last but not least, I would like to express my greatest gratitude to Moritz, my family and friends. Especially the workload in the final phase of my PhD was though. Nevertheless, the endless support and the understanding of Moritz, my family and friends have kept me on my feet and encouraged me to achieve my goal.

Summary

River incision into bedrock is an important process in the context of landscape evolution. Climate can affect the river incision process in several ways. Firstly, precipitation is the main source of river discharge that is required to initiate the motion of river sediment and expose the riverbed to erosion. However, the relationship between river incision and river discharge is often non-linear, in that river discharge has to exceed a certain erosional threshold to mobilize bedload sediment and expose the riverbed to erosion. Whether this erosion threshold plays a significant role, or not, depends on the flux and grain size distribution of river sediment. Besides its effect on discharge, the climate's influence on bedrock weathering also affects river incision, by changing bedrock erodibility as well as the grain size distribution of river sediment. Finally, climate sets discharge variability, which determines how often and by how much river discharge exceeds the erosion threshold. Discharge variability is typically high in arid regions, whereas river discharge is less variable in humid regions. Although it is evident that climate has an effect on river incision, studies that have investigated the effect of climate on ^{10}Be-derived erosion rates – which in a steady state landscape equal river incision rates – have often found ambiguous relationships. This is most likely because other non-climatic factors (e.g., tectonic uplift rates, lithology, biota) interplay to obscure potential climatic trends.

In this PhD thesis, I investigate the role of climate on various aspects of the river incision process in the Coastal Cordillera of central Chile. I focus on regions that are underlain by similar granodioritic lithology, but are exposed to contrasting climate regimes (arid, semi-arid, mediterranean, and humid-temperate). Using this approach, I aimed to reduce the variations in non-climatic factors that may obscure the climatic effect on erosion and river incision processes. I used *in situ* cosmogenic-^{10}Be in river sediment to quantify erosion and river incision rates. *In situ* cosmogenic ^{10}Be is produced in quartz grains in the upper few meters of the earth's surface by high energy cosmic rays. The ^{10}Be concentration reflects the time that grains are exposed to cosmic rays, which is proportional to the residence time of grains in the surface layer (i.e., inversely to the erosion rate). As a result of this, cosmogenic-^{10}Be is frequently measured in river sediment to constrain catchment average erosion rates, which in steady state landscapes should equal river incision rates.

In the first study (Chapter 3), I investigate grain size-dependent ^{10}Be concentrations in river sediment. In most studies, the sand fraction of river sediment is used to measure ^{10}Be-derived erosion rates, however, in catchments where ^{10}Be concentrations vary between different grain size classes, this may result in biased erosion rate estimates. I investigate the controls of precipitation, hillslope angle, lithology and abrasion on grain

size-dependent ^{10}Be concentrations in Chile and in other landscapes around the world. I sampled 7 different grain size classes in 4 catchments located in the above-described climate regions in the Chilean Coastal Cordillera. The results reveal that regional precipitation regime affects grain size-dependent ^{10}Be concentrations through its effect on 1) the depth of erosion processes, and 2) the depth of biotic soil mixing, which produces a constant ^{10}Be concentration over depth. To put this in a broader perspective, I compiled ^{10}Be concentrations across different grain sizes sampled at the same sample location for 73 catchments around the world. Based on this global compilation, I conclude that grain size-dependent changes in ^{10}Be concentrations have a high likelihood of occurring in catchments with thin soil layers, where deep-seated erosion processes (e.g., landslides) excavate coarse grains from greater depth, where ^{10}Be concentrations are lower. Typically, such catchment characteristics are found in landscapes that feature steep topography (>25°) and high mean annual precipitation rates (>2000 mm yr^{-1}). I additionally find that the modification of the grain size distribution by fluvial abrasion can result in grain size-dependent ^{10}Be concentrations. This mainly occurs in catchments with easily erodible lithologies and long sediment travel distances (>2300–7000 m, depending on lithology). I conclude that roughly 50% of the previously published ^{10}Be-derived catchment average erosion rates potentially contain a grain size bias, because the catchments feature one or more of the catchment characteristics that can lead to grain size-dependent ^{10}Be concentrations.

In the second study (Chapter 4), I investigated how climatic forcing can affect discharge variability, by studying El Niño Southern Oscillation (ENSO)-induced hydrological extremes along a climate gradient in central Chile (~28-42°S). This study focusses on discharge time series of 183 river catchments, that are located in the high elevation Andes and the low elevation coastal region, and feature different hydrological regimes: snowmelt-dominated (nival) versus rainfall-dominated (pluvial). The river discharge data shows that the hydrological response to ENSO differs strongly along the climate gradient and shows clear contrasts between basins with the nival and pluvial discharge regimes. The semi-arid region experiences the strongest river discharge anomalies during both El Niño (increasing discharge) and La Niña events (decreasing discharge), whereas the hydrological anomalies are the smallest in the humid-temperate region. Furthermore, the magnitude and frequency of extreme discharge events increases in the semi-arid and mediterranean regions during the warm and wet El Niño phase, whereas discharges in the humid-temperate region are most sensitive to rainfall deficits during La Niña events revealed by a higher frequency of low flow conditions. Snow dynamics introduce large contrasts in the hydrological response between basins with the nival and pluvial discharge regimes. First of all, snowmelt dynamics induce a delayed discharge peak. Snowmelt-dominated basins, experience the largest El Niño-induced discharge peak during the snowmelt season in summer, whereas the ENSO-induced climatic anomalies are most extreme during winter and autumn. Moreover, the discharge variability is lower for snowmelt-dominated basins because snowmelt produces non-flashy river discharge over a longer hydrological response time. Finally, basins with the nival-type of discharge regime are not as strongly affected by droughts

than pluvial type of basins during La Niña, because snowmelt-generated runoff provides a minimum river discharge level. The results of this study reveal that ENSO-induced climatic and hydrological anomalies contribute strongly to the high discharge variability that has been observed in the semi-arid region. Which implies that ENSO has an important effect on river incision processes in the semi-arid region. Finally, I discuss the implications of the results of this study for water resource management in Chile.

In the next study (Chapter 5), I investigated long-term catchment average erosion rates in catchments along a climate gradient in Chile. I sampled ~10 catchments in three of the four climate regions (semi-arid, mediterranean, and humid-temperate). I specifically selected catchments that feature differences in normalized channel steepness (k_{sn}) between the catchments, which is a topographic metric that reflects tectonic uplift rates in a steady state landscape. The ^{10}Be-derived catchment average erosion rates revealed an increasing trend with k_{sn}. Besides this, however, a secondary influence of climate was evident: the slope of k_{sn}-erosion rate relationships was markedly steeper for the humid-temperate region compared to the semi-arid region. In other words, for a given normalized channel steepness index, the highest erosion rates were observed for the humid-temperate region and the lowest for the semi-arid region. I compiled and recalculated previously published ^{10}Be-derived erosion rates of ~150 catchments in Chile to compare my results to the large-scale erosional dynamics in Chile. While my new results agreed well with published erosion rates from other catchments in the Coastal Cordillera, erosion rates in the Andes are higher, which I posit is due to higher precipitation rates and steeper topography. Where previous studies had difficulties with depicting a consistent climatic signal along the latitudinal gradient, new data analysis suggests, that the erosion rates in Chile reflect a combined tectonic and climatic signal, which agrees with my own data from the Coastal Cordillera. The large degree of scatter in the compiled dataset is likely induced by non-climatic factors (e.g., lithology or biota). I conclude that, in Chile, the erosional efficiency increases with increasing precipitation, which provides empirical evidence for the understanding that arid landscapes have to become steeper than humid landscapes to reach erosion rates that equal tectonic uplift rates in a steady state landscape.

In the final study (Chapter 6), I tested whether erosion thresholds, which are set by the amount and grain size of river sediment, play a significant role in the river incision processes in catchments in the Chilean Coastal Cordillera. I applied the stochastic-threshold stream power model, calibrated with field data, and compared the best fit model results to the ^{10}Be-derived erosion rates and median grain sizes that I measured for each river catchment. The results reveal that erosion thresholds do play a role in the relatively gently sloping catchments of the Chilean Coastal Cordillera. A sensitivity test revealed that the modelled erosion rates of the semi-arid region rapidly decrease under erosion thresholds that are set by a grain size of > 1 cm. River incision still seems to occur in the humid-temperate region for erosion thresholds that are set by considerable grain sizes, but rapidly decrease for grain sizes of >10 cm. I conclude that in gently sloping basins the sensitivity of river incision rates to erosion thresholds strongly

depends on river discharge, because the channel steepness is too low to facilitate the mobilization of river sediment. The results suggest that river incision occurs rather infrequently in the semi-arid region, whereas it occurs more continuously in the humid-temperate region. I have planned to further test the sensitivity of the model to input parameters and investigate the magnitude and reoccurrence time of river incision processes in the different climate regions of the Chilean Coastal Cordillera to validate these findings, and to better understand river incision processes in gently sloping landscapes. This is the first study that tests the threshold-behaviour of the process of river incision in gently sloping basins in regions that are exposed to different climates.

To conclude, in this PhD thesis I investigated the effect of climate on several aspects that are relevant in the process of river incision. This study contributes to the general understanding of the effect of climate on landscape evolution in gently sloping mountain ranges that cover roughly ~15% of the Earth's surface.

Zusammenfassung

Die Einschneidung von Flüssen ins Festgestein ist ein wichtiger Prozess im Kontext der Landschaftsentwicklung. Die Rate mit der sich ein Fluss einschneidet, kann dabei auf unterschiedliche Weise durch das Klima beeinflusst werden. Erstens ist der Niederschlag die Hauptquelle für den Abfluss, der erforderlich ist um die Bewegung des Flusssediments zu initiieren und die Erosion des Flussbetts ermöglicht. Die Beziehung zwischen Flusseinschneidung und Abfluss ist jedoch nicht immer linear, da der Abfluss eine bestimmte Erosionsschwelle überschreiten muss, um Geschiebesediment zu mobilisieren und das Flussbett der Erosion auszusetzen. Ob diese Erosionsschwelle eine signifikante Rolle spielt, hängt von der Menge und Korngrößenverteilung des Flusssediments ab. Neben den Auswirkungen auf den Abfluss hat das Klima auch Einfluss auf die Verwitterung des Grundgesteins und somit die Korngrößenverteilung des Flusssediments. Schließlich bestimmt das Klima die Abflussvariabilität, die definiert, wie oft und in welchem Ausmaß der Abfluss die Erosionsschwelle überschreitet. Die Abflussvariabilität ist hierbei typischerweise hoch in ariden und geringer in humiden Regionen. Obwohl es offensichtlich ist, dass das Klima einen Einfluss auf Flusseinschneidung hat, haben Studien, die den Einfluss des Klimas auf die aus ^{10}Be-abgeleiteten Erosionsraten untersucht haben, oft unklare Beziehungen gefunden. Dies ist höchstwahrscheinlich darauf zurückzuführen, dass hier andere nicht-klimatische Faktoren (z.B. tektonische Hebungsraten, Lithologie, Biota) interagieren, und potenzielle klimatische Einflüsse verdecken.

In dieser Dissertation habe ich die Rolle des Klimas auf verschiedene Aspekte des Flusseinschneidungsprozesses in der zentralchilenischen Küstenkordillere untersucht. Ich konzentriere mich auf Regionen, die von einer ähnlichen granodioritischen Lithologie unterlagert sind, aber unterschiedlichen Klimaregimen ausgesetzt sind (arid, semi-arid, mediterran und feucht-gemäßigt). Mit diesem Ansatz habe ich die Variationen nicht-klimatischer Faktoren reduziert, die den klimatischen Einfluss auf Erosions- und Flusseinschneidungsprozesse verdecken können. Ich habe *in situ* kosmogenes ^{10}Be in Flusssedimenten verwendet, um die Erosions- und Flusseinschneidungssraten zu quantifizieren. *In situ* kosmogenes ^{10}Be wird in Quarzkörnern in der oberen Schicht der Erdoberfläche durch hochenergetische kosmische Strahlung produziert. Die ^{10}Be-Konzentration spiegelt die Zeit wider, in der die Körner der kosmischen Strahlung ausgesetzt sind, was proportional zur Verweilzeit der Körner in der Oberflächenschicht ist (d.h. umgekehrt proportional zur Erosionsrate). In Landschaften im stationären Zustand, entsprechen die mit ^{10}Be im Flusssediment gemessenen Erosionsraten des Einzugsgebiets den Flusseinschneidungsraten.

In der ersten Studie (Kapitel 3) habe ich korngrößenabhängige ^{10}Be-Konzentrationen in Flusssedimenten untersucht. In den meisten Studien wird die Sandfraktion von Flusssedimenten verwendet, um die aus ^{10}Be Konzentrationen abgeleiteten

Erosionsraten zu messen. In Einzugsgebieten, in denen die ^{10}Be-Konzentrationen zwischen verschiedenen Korngrößenklassen variieren, kann dies jedoch zu fehlerhaften Schätzungen der Erosionsrate führen. Ich habe die Einflüsse von Niederschlag, Hangneigung, Lithologie und Abrasion auf korngrößenabhängige ^{10}Be-Konzentrationen in Chile und in anderen Landschaften der Welt untersucht. Dazu habe ich sieben verschiedene Korngrößenklassen in vier Einzugsgebieten beprobt, die in den oben beschriebenen Klimaregionen in der chilenischen Küstenkordillere liegen. Die Ergebnisse zeigen, dass das regionale Niederschlagsregime die korngrößenabhängigen ^{10}Be-Konzentrationen, durch seinen Einfluss auf 1) die Tiefe der Erosionsprozesse und 2) die Tiefe der biotischen Bodendurchmischung, die eine konstante ^{10}Be-Konzentration über die Tiefe erzeugt, beeinflusst. Um dies in einen breiteren Kontext zu stellen, habe ich die ^{10}Be-Konzentrationen in verschiedene Korngrößen zusammengestellt, die jeweils am gleichen Probennahmeort im Gerinne in 73 Einzugsgebiete aus der ganzen Welt beprobt wurden. Basierend auf dieser globalen Zusammenstellung kann geschlossen werden, dass korngrößenabhängige Änderungen der ^{10}Be-Konzentrationen mit hoher Wahrscheinlichkeit in Einzugsgebieten mit dünnen Bodenschichten auftreten, in denen tiefgreifende Erosionsprozesse (z.B. Erdrutsche) grobe Körner aus größerer Tiefe transportieren, wo die ^{10}Be-Konzentrationen niedriger sind. Typischerweise findet man solche Einzugsgebietscharakteristika in Landschaften, die eine steile Topographie (>25°) und hohe Jahresniederschlagsraten (>2000 mm yr^{-1}) aufweisen. Zusätzlich konnte gezeigt werden, dass die Modifikation der Korngrößenverteilung durch fluviale Abrasion zu korngrößenabhängigen ^{10}Be-Konzentrationen führen kann. Dies geschieht hauptsächlich in Einzugsgebieten mit leicht erodierbarer Lithologie und langen Sedimenttransportstrecken (>2300-7000 m, je nach Lithologie). Laut meinen Ergebnissen weisen in bereits veröffentlichten Daten von ^{10}Be abgeleiteten durchschnittlichen Erosionsraten, ~50% der untersuchten Einzugsgebiete Eigenschaften auf, die zu einer Korngrößenverzerrung und somit korngrößenabhängigen ^{10}Be-Konzentrationen führen könnten.

In der zweiten Studie (Kapitel 4) habe ich untersucht, wie klimatische Einflüsse die Abflussvariabilität beeinflussen können. Hierzu wurden die durch El Niño Southern Oscillation (ENSO) verursachten hydrologischen Extreme entlang eines Klimagradienten in Zentralchile (~28-42°S) betrachtet. Diese Studie konzentriert sich auf die Abflusszeitreihen von 183 Einzugsgebieten, die sich in den hochgelegenen Anden und der niedriger gelegenen Küstenregion befinden und unterschiedliche hydrologische Regime aufweisen: Schneeschmelze-dominiert (nival) versus Regenfall-dominiert (pluvial). Die Abflussdaten zeigen, dass sich die hydrologische Reaktion auf Schwankungen in der ENSO entlang des Klimagradienten stark unterscheidet und deutliche Unterschiede zwischen den Einzugsgebieten mit dem nivalen und dem pluvialen Abflussregime aufweist. Die semi-aride Region erfährt die stärksten Abflussanomalien sowohl während El Niño (zunehmender Abfluss) als auch während La Niña (abnehmender Abfluss), während die hydrologischen Anomalien in der feucht-gemäßigten Region am geringsten sind. Darüber hinaus nimmt das Ausmaß und die

Häufigkeit von extremen Abflussereignissen in der semi-ariden und mediterranen Region während der warmen und feuchten El Niño-Phase zu. Dem gegenüber reagieren die Abflüsse in der feucht-gemäßigten Region am sensitivsten auf Niederschlagsdefizite während La Niña-Ereignissen, was sich in einer höheren Häufigkeit von Niedrigwasserbedingungen zeigt. Die Schneedynamik führt zu großen Kontrasten in der hydrologischen Reaktion zwischen Einzugsgebieten mit nivalen und pluvialen Abflussregimen. Erstens induziert die Schneeschmelzdynamik eine verzögerte Abflussspitze. Daher erfahren Schneeschmelze-dominierte Einzugsgebiete die größte El-Niño-induzierte Abflussspitze während der Schneeschmelzzeit im Sommer, obwohl die ENSO-induzierten Klimaanomalien im Winter und Herbst am ausgeprägtsten sind. Darüber hinaus ist die Abflussvariabilität in Einzugsgebieten, die von der Schneeschmelze dominiert werden, geringer, da die Schneeschmelze über eine längere hydrologische Reaktionszeit einen eher konstanten Abfluss erzeugt. Schließlich sind Einzugsgebiete mit einem nivalen Abflussregime während La Niña nicht so stark von Niedrigwasserbedingungen betroffen wie pluviale Einzugsgebiete, da der durch die Schneeschmelze erzeugte Abfluss jederzeit einen geringen Basisabfluss garantiert. Die Ergebnisse dieser Studie zeigen, dass ENSO-induzierte klimatische und hydrologische Anomalien stark zu der hohen Abflussvariabilität beitragen, die in der semi-ariden Region beobachtet wurde. Dies impliziert, dass ENSO einen wichtigen Einfluss auf die Flusseinschneidungsprozesse in der semi-ariden Region hat. Abschließend diskutiere ich die Implikationen der Ergebnisse dieser Studie für das Wasserressourcenmanagement in Chile.

In der nächsten Studie (Kapitel 5) habe ich die langfristigen Einzugsgebietserosionsraten entlang des Klimagradienten in Chile betrachtet. Dazu habe ich ~10 Einzugsgebiete in drei der vier Klimaregionen (semi-arid, mediterran und feucht-gemäßigt) beprobt. Ich habe gezielt Einzugsgebiete ausgewählt, die Unterschiede im normalized channel steepness index (k_{sn}) (Deutsch: normalisierte Flussbettgefälle) zwischen den Einzugsgebieten aufweisen, was ein morphometrischer Parameter ist, der die tektonischen Hebungsraten in einer Landschaft im stationären Zustand widerspiegelt. Die aus ^{10}Be abgeleiteten durchschnittlichen Erosionsraten der Einzugsgebiete zeigen eine Zunahme mit steigendem k_{sn}. Daneben war jedoch auch ein sekundärer Einfluss des Klimas erkennbar: Die Steigung der k_{sn}-Erosionsraten-Beziehung war hierbei für die feucht-gemäßigte Region deutlich steiler als für die semi-aride Region. Mit anderen Worten, für einen gegebenen k_{sn} Wert wurden die höchsten Erosionsraten in der feucht-gemäßigten Region und die niedrigsten in der semi-ariden Region gemessen. Ich habe bereits veröffentlichte ^{10}Be-abgeleitete Erosionsraten von ~150 Einzugsgebieten in Chile zusammengestellt und neu berechnet, um die Ergebnisse mit der großräumigen Erosionsdynamik in Chile ins Verhältnis zu setzen. Während die neuen Ergebnisse gut mit veröffentlichten Erosionsraten aus anderen Einzugsgebieten in der Küstenkordillere übereinstimmen, sind die Erosionsraten in den Anden höher, was auf höhere Niederschlagsraten und eine steilere Topographie zurückzuführen ist. Wo frühere Studien Schwierigkeiten hatten, ein konsistentes klimatisches Signal entlang des Breitengradienten darzustellen, legen neue

Datenanalysen nahe, dass die Erosionsraten in Chile ein kombiniertes tektonisches und klimatisches Signal widerspiegeln, was mit den in dieser Arbeit erhobenen Daten aus der Küstenkordillere übereinstimmt. Der große Grad an Streuung in dem zusammengestellten Datensatz ist wahrscheinlich durch Unterschiede in nicht-Klimatischen Faktoren (z.B. Lithologie, Biota) bedingt. Dies deutet darauf hin, dass in Chile die Erosionseffizienz mit zunehmendem Niederschlag zunimmt, was bedeutet, dass aride Landschaften steiler werden müssen als feuchte Landschaften, um Erosionsraten zu erreichen, die den tektonischen Hebungsraten in einer Landschaft im stationären Zustand entsprechen.

In der abschließenden Studie (Kapitel 6) habe ich getestet, ob Erosionsschwellen, die durch die Menge und Korngröße des Flusssediments festgelegt werden, eine bedeutende Rolle bei den Flusseinschneindungsprozessen in Einzugsgebieten in der chilenischen Küstenkordillere spielen. Dazu wurde das „stochastic-threshold stream power model" (Deutsch: Warhscheinlichkeitsbasiertes Schwellenwertmodell der Flusseinschneidung) angewendet, welches mit Felddaten kalibriert wurde. Die Ergebnisse des am besten passenden Modells wurden mit den für jedes Flusseinzugsgebiet gemessenen ^{10}Be-abgeleiteten Erosionsraten und medianen Korngrößen verglichen. Die Ergebnisse zeigen, dass Erosionsschwellen in Einzugsgebieten mit geringem Gefälle der chilenischen Küstenkordillere durchaus eine Rolle spielen. Ein Sensitivitätstest ergab, dass die modellierten Flusseinschneidungsraten der semi-ariden Region unter Erosionsschwellen, die durch eine Korngröße von > 1 cm gesetzt werden, schnell abnehmen. Flusseinschneidung scheint in der feucht-gemäßigten Region für Erosionsschwellen, die durch große Korngrößen gesetzt werden, noch aufzutreten, nimmt aber für Korngrößen von >10 cm schnell ab. Daraus kann geschlossen werden, dass in leicht geneigten Einzugsgebieten die Empfindlichkeit der Flusseinschneidungsraten gegenüber Erosionsschwellen stark vom Abfluss abhängt, weil der normalized channel steepness index zu gering ist, um die Mobilisierung von Flusssediment zu erleichtern. Die Ergebnisse deuten darauf hin, dass Flusseinschneidung in der semi-ariden Region eher selten auftritt, während sie in der feucht-gemäßigten Region häufiger stattfindet. Es ist geplant, die Sensitivität des Modells gegenüber den Eingangsparametern zu testen und das Ausmaß und die Wiederholungszeit von Flusseinschneidungsprozessen in den verschiedenen Klimaregionen der chilenischen Küstenkordillere zu untersuchen, um diese Ergebnisse zu validieren und Flusseinschneidungsprozesse in Einzugsgebieten mit geringem Gefälle besser zu verstehen. Soweit mir bekannt ist, ist dies ist die erste Studie, die das Schwellenverhalten des Prozesses der Flusseinschneidung in Einzugsgebieten mit geringem Gefälle und Regionen unterschiedlicher Klimazonen untersucht.

Zusammenfassend lässt sich sagen, dass in dieser Dissertation der Einfluss des Klimas auf verschiedene Aspekte, die für den Prozess der Flusseinschneidung relevant sind, untersucht wurde. Diese Studie trägt damit zum allgemeinen Verständnis der Auswirkungen des Klimas auf die Landschaftsentwicklung in Gebirgsregionen mit leichterem Gefälle bei, die etwa ~15 % der Erdoberfläche bedecken.

Preface

This PhD thesis includes 7 different chapters and is a cumulative collection of an introductory chapter, a study area description, four scientific studies and a discussion chapter. All chapters are written as manuscripts that have been, or will be, submitted to a scientific journal. Therefore, each chapter can be read and understood individually.

Below, I provide more information about the content of each chapter, the co-authors that were involved and the submission or publication status of the study.

Chapter 1 is the general introduction of this PhD thesis. This chapter introduces the scientific topic, the research gaps and the objectives of this PhD thesis.

Chapter 2 provides a detailed study area description. This chapter includes all relevant information about the geological, climatic and hydrological setting of Chile and introduces the study areas of the DFG-funded Priority Program "EarthShape".

Chapter 3 presents the first scientific study with the title: "*Cosmogenic ^{10}Be in river sediment: where grain size matters and why*". This study was published in Earth Surface Dynamics in 2019 (vol. 7, pages 393-410). Co-authors that were involved in this study are: Dirk Scherler, Hella Wittmann and Friedhelm von Blanckenburg. This study focusses on the causes and implications of grain size-dependent ^{10}Be concentrations in river sediment. Renee van Dongen and Dirk Scherler developed the scientific idea for this study. Renee van Dongen conducted field work, laboratory work and data analysis. Hella Wittmann provided cosmogenic laboratory training and supervision. Renee van Dongen prepared the manuscript with help of all co-authors.

Chapter 4 presents the second scientific study with the title: "*El Niño Southern Oscillation (ENSO)-induced hydrological anomalies in central Chile*". This study is prepared for submission to the journal: Hydrology and Earth System Sciences. Co-authors that were involved in this study are: Dirk Scherler, Dadiyorto Wendi, Claudio Meier, Eric Deal, Luca Mao and Norbert Marwan. This study focusses on ENSO-induced climatic anomalies and how these translate into hydrological anomalies along a climatic gradient in central Chile. The scientific focus of this study was developed by Renee van Dongen, Dirk Scherler and Dadiyorto Wendi. Dadiyorto Wendi applied a data gap interpolation method to improve the discharge records in this study. Data interpretation in the context with Chilean climate and hydrology was done with support of Claudio Meier and Eric Deal supported with the interpretation

of discharge variability results. Renee van Dongen prepared the manuscript with contributions from all co-authors.

Chapter 5 is a short study with the title "*Catchment average erosion rates along a climate gradient in Chile*". This study has been prepared as a manuscript for future submission, either combined with the study in Chapter 6, or as an individual study. This study focusses on the control of climate on long-term erosion rates, by sampling catchments in regions different climate but similar lithology and comparing these results to previously published erosion rates for Chile. Renee van Dongen and Dirk Scherler developed the scientific idea of this study. Fieldwork, laboratory work and data analysis has been performed by Renee van Dongen. Dirk Scherler supported with data interpretation and manuscript writing.

Chapter 6 builds on the results of Chapter 5 and has the title "*Testing the role of erosion thresholds on river incision along a climate gradient in central Chile*". This study focusses on the effect of climate on the threshold-behaviour of river incision in the gently sloping catchments of the Chilean Coastal Cordillera. This study is still in progress and is planned to be submitted to a scientific journal in the future. The scientific focus of this study was developed by Renee van Dongen and Dirk Scherler. Dirk Scherler provided the model code that was used in the study of Scherler et al. (2017). Renee van Dongen conducted the data analysis and manuscript writing, with support of Dirk Scherler.

Chapter 7 presents a final synthesis of all chapters in this PhD thesis and discusses the implications for the EarthShape project.

Table of Contents

List of Tables

List of Supplementary tables

List of Figures

List of supplementary figures

Chapter 1

Introduction

The morphology of the Earth's surface as it is today, is the cumulative result of geomorphic processes, integrated over millions of years. Mountain belts are formed by tectonic processes that exhume fresh bedrock to the surface and the processes of weathering and erosion wear them down (Willett, 1999). Factors such as tectonic uplift, climate, lithology and biota affect weathering and erosion processes and thereby control landscape evolution and the topography of the Earth's surface (e.g., Tucker and Bras, 2000; Whipple and Tucker, 1999).

The influence of climate on landscape evolution gains much attention in geomorphic research (Deal et al., 2018; Ferrier et al., 2013; Perron, 2017). Climate can affect geomorphic processes in various ways. For instance, climate can affect chemical weathering processes that transform bedrock into sediment (Brady and Carroll, 1994; Lasaga et al., 1994; Maher, 2010; White and Blum, 1995) and climate-dependent physical weathering occurs in the form of bedrock fracturing by thermal stresses, freeze-thaw cycles, segregation ice wedging and frost cracking (Anderson, 2019; Draebing and Krautblatter, 2019; Eppes et al., 2016, 2020; Eppes and Keanini, 2017; Hales and Roering, 2007; Matsuoka, 2008; McFadden et al., 2005; Walder and Hallet, 1985). Furthermore, precipitation enhances hillslope erosion by processes such as rain splash erosion (Dunne et al., 2010; Gabet and Dunne, 2003), detachment by hillslope runoff (Huang et al., 2002; Julien and Simons, 1985) and the triggering of landslides by elevated pore pressure (Chen and Lee, 2003; Tsou et al., 2011). Finally, the process of river incision is seen as one of the most important links between climate and landscape evolution, as precipitation is the primary water source for river discharge, which plays a crucial role in fluvial erosion processes (e.g., Crave and Davy, 2001; Tucker and Bras, 2000; Whipple and Tucker, 1999).

Despite the evident link between precipitation rates and geomorphic processes, field studies have often found ambiguous relationships between mean annual precipitation and erosion rates (von Blanckenburg, 2005; Burbank et al., 2003; Godard et al., 2014; Perron, 2017; Riebe et al., 2001). Possibly, because variations in non-climatic factors,

which also affect erosion rates, might overshadow trends induced by precipitation (Deal et al., 2018; Perron, 2017). Figure 1.1 presents a global compilation of published catchment average erosion rates and their relationship to mean annual precipitation (Perron, 2017; Portenga and Bierman, 2011). For a given precipitation rate, we can observe a large range of erosion rates, which has been attributed to variations in factors such as tectonic uplift rates, lithology and biological processes (Perron, 2017). Furthermore, this figure reveals a strong correlation between mean annual precipitation and vegetation cover (Figure 1.1). Since vegetation can have both an enhancing and reducing effect on erosion, this can result into an elusive combined effect on erosion rates (Dietrich and Perron, 2006; Istanbulluoglu, 2009; Istanbulluoglu and Bras, 2005).To add even more complexity, climatic conditions can change over the time scales that are relevant in the context of landscape evolution (thousands to millions of years) (Deal et al., 2018; Perron, 2017).

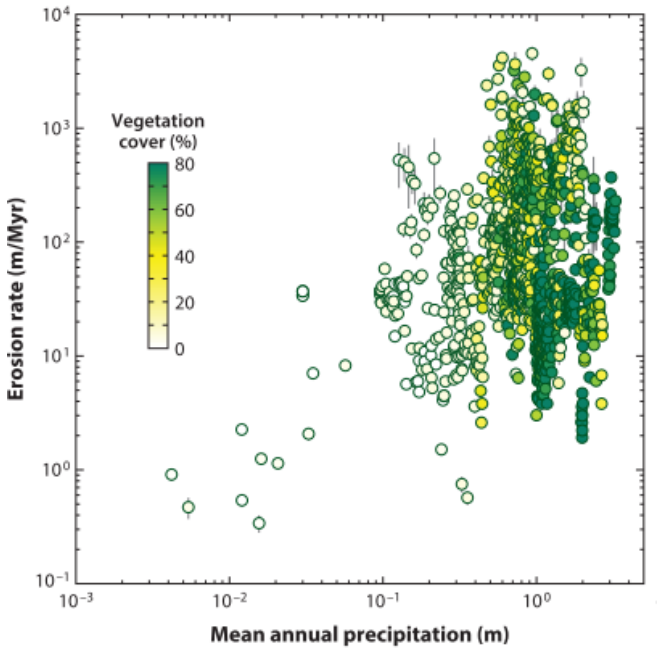

Figure 1.1: Compilation of catchment average erosion rates (n=1599) compared to mean annual precipitation rates (Perron, 2017).[1] This figure is based on a data compilation from Portenga and Bierman (2011).

As mentioned above, the process of bedrock river incision is considered as an important link between climate and landscape evolution, because precipitation is the main source of river discharge, which is an important driver of fluvial erosion (e.g., Crave and Davy, 2001; DiBiase and Whipple, 2011; Tucker and Bras, 2000; Whipple and

[1] Republished with permission of "*Annual review of earth and planetary sciences*", from "*Climate and the Pace of Erosional Landscape Evolution*", J. Taylor Perron, 45, 2017; permission conveyed through Copyright Clearance Center, Inc.

Tucker, 1999). Rivers play such a crucial role in the context of landscape evolution because the channel network defines the structure of mountain ranges, river channels set the boundary conditions for the rate and mode of hillslope erosion, and climatic and tectonic changes are propagated throughout the channel network before hillslopes respond (Perron, 2017; Whipple, 2004; Whipple and Tucker, 1999).

1.1 Process of river incision

Bedrock river incision can be described as the vertical erosion of river channels in the underlying bedrock (Tucker and Bras, 2000). River incision can be considered as a stochastic process, because river discharge must exceed a certain erosion threshold to mobilize the armouring sediment layer and expose the riverbed to erosion (Sklar and Dietrich, 2001; Turowski, 2009; Turowski et al., 2007). The erosion threshold for river incision is primarily set by the amount and the grain size of river sediment (Attal and Lavé, 2006; Sklar et al., 2006; Sklar and Dietrich, 1998, 2001; Turowski et al., 2007). Coarser grains require higher shear-stresses (i.e., river discharge) to be mobilized, compared to finer grains. When the erosion threshold is considerably high, the smaller river discharge events are non-erosive, whereas the large discharge events account for the majority of the erosive work (Figure 1.2) (e.g., Snyder et al., 2003; Tucker, 2004). The discharge variability of a river is, therefore, another important factor, because it defines how often and by how much discharge deviates from the mean (Deal et al., 2018), which is related to the exceedance probability of the erosion threshold (DiBiase and Whipple, 2011; Lague et al., 2005; Snyder et al., 2003).

Under the assumption that catchment average erosion rates reflect river incision rates in steady state landscapes, scientists have used ^{10}Be-derived erosion rates to investigate the relationship between normalized channel steepness and river incision rates for various regions around the world (Cyr et al., 2010; Dibiase et al., 2010; Harkins et al., 2007; Miller et al., 2016; Ouimet et al., 2009; Safran et al., 2005; Scherler et al., 2014). These studies found contrasting relationships (Figure 1.3), which reveals that some landscapes on the world reach steeper topography to experience erosion rates that equal tectonic uplift rates than others. These contrasts are likely related to differences in e.g., climate, lithology and vegetation cover, which all have an effect on the process of bedrock river incision. The process of bedrock river incision and the importance of erosion thresholds has been investigated for several landscapes on earth (e.g., DiBiase and Whipple, 2011; Scherler et al., 2017). However, to date, studies that specifically test the role of climate on river incision are limited (Ferrier et al., 2013).

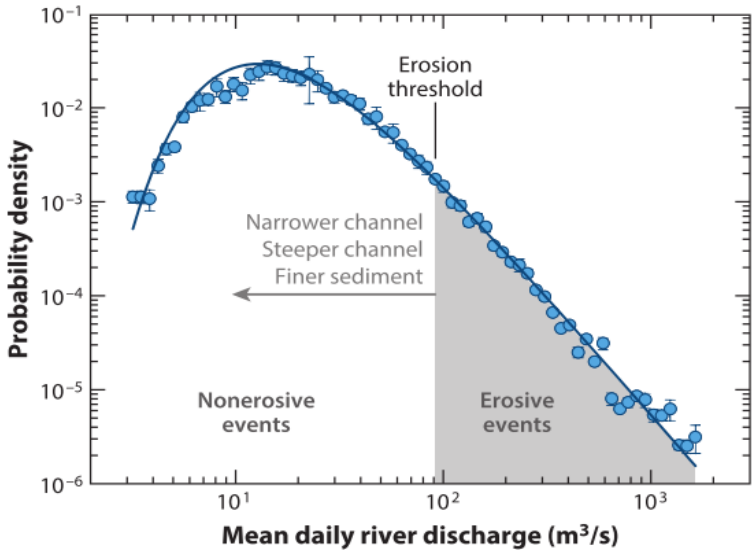

Figure 1.2: The probability density function of mean daily river discharge ($m^3\ s^{-1}$).[2] The grey area shows the discharge events that exceed the erosion threshold and are, therefore, erosive (Perron, 2017).

1.2 Effect of climate on river incision

Previous studies that tested river incision rates and the role of erosion thresholds applied the stochastic-thresholds stream power model that was calibrated with field and river discharge data (DiBiase and Whipple, 2011; Scherler et al., 2017). The river incision rates are modelled based on the normalized channel steepness, the erosion efficiency, an erosion threshold and the magnitude-frequency distribution of daily river discharge (DiBiase and Whipple, 2011; Lague et al., 2005; Molnar, 2001; Snyder et al., 2003; Tucker, 2004; Tucker and Bras, 2000; Whipple and Tucker, 1999).

Climate can affect the process of river incision in various ways. The first control is the control of climate on the erosion efficiency parameter (Whipple, 2004). The erosion efficiency parameter is a lumped factor that includes information about the bedrock quality, flow resistance and catchment-integrated mean annual runoff (e.g., Tucker, 2004; Tucker and Bras, 2000; Whipple and Tucker, 1999). As precipitation contributes to a large degree to the mean annual runoff, climate has a direct control on the erosion efficiency.

[2] Republished with permission of "*Annual review of earth and planetary sciences*", from "*Climate and the Pace of Erosional Landscape Evolution*", J. Taylor Perron, 45, 2017; permission conveyed through Copyright Clearance Center, Inc.

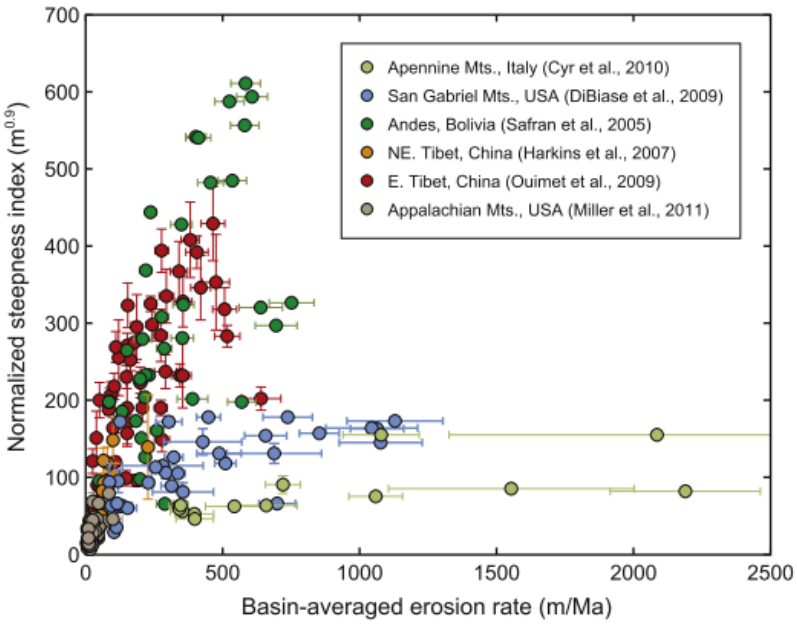

Figure 1.3: The relationship between basin average erosion rates and normalized channel steepness index for different landscapes around the world. Compilation by Kirby and Whipple (2012)[3]. Original studies include: Cyr et al. (2010); Dibiase et al. (2010); Harkins et al. (2007); Miller et al. (2011); Ouimet et al. (2009); Safran et al. (2005).

Climate can, furthermore, affect the erosion threshold. As described above, the erosion threshold is set by the amount and grain size of river sediment. Despite the fact that the grain size is primarily controlled by the bedrock lithology and bedrock fractures, chemical weathering rates, which depend on climate, can additionally contribute to grain size fining (Lebedeva and Brantley, 2017; Sklar et al., 2017).

Finally, the variability of river discharge is strongly controlled by the climatic forcing. Discharge variability is considered to be high in arid regions and low in humid regions (e.g., Lague, 2013; Scherler et al., 2017), because precipitation in arid regions occurs as infrequent but intense rainstorms, whereas humid regions are dominated by frequently occurring rainstorms induced by, for instance, cold fronts (Fuenzalida, 1982; Garreaud et al., 2009; Montecinos and Aceituno, 2003). In some places on earth, the discharge variability is primarily driven by extreme rainstorms during the monsoon and typhoon seasons (Lague et al., 2005; Scherler et al., 2017). However, large-scale atmospheric systems such as El-Niño Southern Oscillation (ENSO) and the Pacific Decadal Oscillation (PDO) additionally introduce climatic anomalies which may lead to hydrological extremes (Kiladis and Diaz, 1989).

[3] Reprinted from "*Journal of Structural Geology*", 44, Eric Kirby & Kelin X. Whipple, "*Expression of active tectonics in erosional landscapes*", Pages No. 54-75, Copyright (2012), with permission from Elsevier.

Moreover, climate exerts an additional indirect control on discharge variability through its effect on chemical weathering rates and vegetation cover regime (Dixon et al., 2016; Riebe et al., 2004). Arid landscapes, which experience low chemical weathering rates, typically have a thin regolith cover and sparse to no vegetation cover. Such landscapes are characterized by flashy and direct discharge response after a precipitation event because there are no hydrological processes that can modulate the signal (Figure 1.4a). In contrast, the presence of a soil-mantle and dense vegetation in humid landscapes introduce processes such as evapotranspiration, infiltration, and ground water recharge. These processes modulate the climatic signal, resulting in a reduced, delayed, and smoothened river discharge response (Figure 1.4b).

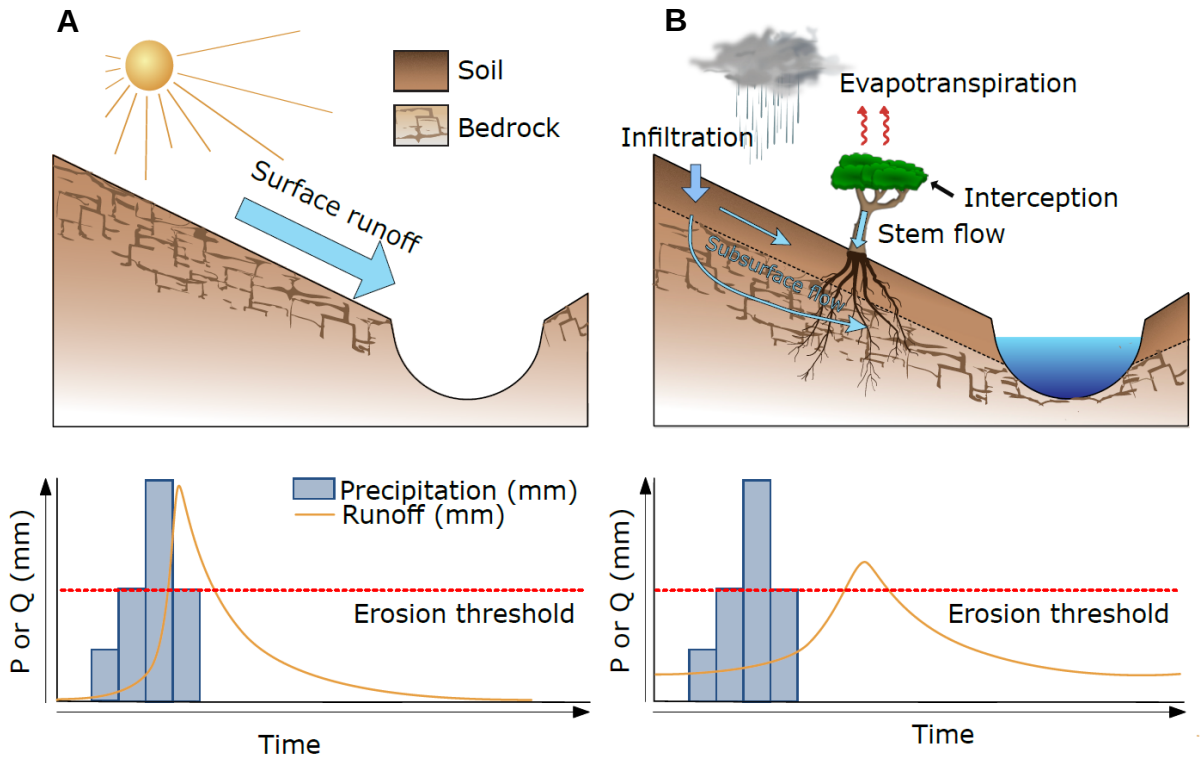

Figure 1.4: Typical response of arid (A) and humid (B) landscapes after a precipitation event. A) In arid landscapes a soil-mantle and vegetation cover are typically absent. This results in a direct and flashy response of river discharge after a precipitation event. B) The presence of a soil-mantle and vegetation cover in humid landscapes result in processes such as evapotranspiration, infiltration, subsurface flow. These processes result in a delayed, smoothened, and reduced river discharge response after a precipitation event.

1.3 Research gaps and scope of this project

The overall aim of this PhD thesis is to investigate how climate influences river incision through its effect on discharge variability and the threshold-behaviour in a well-constrained empirical setting. This PhD thesis concentrates on several aspects of this topic, which range from investigating potential biases in the method of estimating ^{10}Be-derived erosion rates, the influence of ENSO-induced climatic anomalies on discharge variability and testing the climatic controls on the fluvial erosion efficiency along a climatic gradient.

The first study (Chapter 3) of this PhD thesis focusses on the causes of potential biases in ^{10}Be-derived catchment average erosion rates. Most studies that measure ^{10}Be-derived catchment average erosion rate use the sand fraction of river sediment (Codilean et al., 2018), whereas the grain size distribution of river sediment is typically much coarser (e.g., Allen et al., 2015; DiBiase and Whipple, 2011; Roda-Boluda et al., 2018; Scherler et al., 2016). Previous studies found that ^{10}Be concentrations vary in different grain size classes of the same river sediment sample, which is commonly attributed to deep-seated erosion processes that transport coarse grains from greater depth, where ^{10}Be concentrations are lower (e.g., Aguilar et al., 2014; Belmont et al., 2007; Binnie et al., 2007; Brown et al., 1995; Puchol et al., 2014; Sosa Gonzalez et al., 2016a, 2016b; Tofelde et al., 2018; West et al., 2014). However, other studies suggested that grain size dependent ^{10}Be concentrations may also arise from fluvial processes, such as abrasion or spatial variations in sediment provenance (Carretier et al., 2009; Carretier and Regard, 2011; Lukens et al., 2016). To date a comprehensive understanding of which type of catchments are sensitive to biased erosion rates remains elusive (Carretier et al., 2015a), or has only been investigated in modelling studies (Lukens et al., 2016). This study investigates the causes of grain size-dependent ^{10}Be concentration and discusses the consequences for biased catchment average erosion rates.

The second study of this PhD-thesis (Chapter 4) focusses on climatically driven discharge variability. El Niño Southern Oscillation (ENSO) is one of the main drivers of interannual climatic variability in regions surrounding the Pacific Ocean (e.g., McPhaden et al., 2006). However, how these climatic anomalies translate into hydrological anomalies is complex because precipitation and river discharge show a non-linear relationship (Stephens et al., 2015). This non-linear relationship is affected by catchment characteristics such as: catchment area, catchment elevation, lithology, regolith thickness and vegetation cover (e.g., Post and Jakeman, 1996; Rust et al., 2020). A better understanding of how climatic anomalies translate into hydrological anomalies can improve water resources and risk management, which is of high importance as a higher frequency of climatic and hydrological extremes is predicted under global warming (Hirabayashi et al., 2013; Schlaepfer et al., 2017). This study focusses on the hydrological response to ENSO-induced climatic anomalies in river catchments along a climatic gradient in central Chile. The spatial and seasonal

differences in mean discharge and discharge variability are investigated, and the driving hydrological processes are discussed. This study ends with a discussion of the implications for water resources and flood and drought risk management.

As described above, to date many studies have found ambiguous relationships between climate and catchment average erosion rates (von Blanckenburg, 2005; Burbank et al., 2003; Godard et al., 2014; Perron, 2017; Riebe et al., 2001), which is commonly attributed to the effect of non-climatic factors have obscured the climatic trend. Therefore, a well-constrained study is required that specifically focusses on disentangling the climatic effect from other controlling factors. The third study (Chapter 5) focusses on the climatic control on catchment average erosion rates in the Coastal Cordillera of central Chile, by applying a sampling approach that reduces the effect of non-climatic effects on erosion rates.

To date, one study has systematically investigated the effect of mean annual precipitation on bedrock river incision in a well-constrained setting, on the Hawaiian island of Kaua'i (Ferrier et al., 2013). In this study, the river incision rates show a linear relationship with upstream-averaged mean annual precipitation rates. However, this study did not test for the potential control of erosion thresholds, which are found to play a role in other landscapes on earth (DiBiase and Whipple, 2011; Lague et al., 2005; Molnar, 2001; Snyder et al., 2003; Tucker, 2004; Tucker and Bras, 2000). The importance of erosion thresholds and discharge variability on river incision has been tested in landscapes in the San Gabriel Mountains in the USA (DiBiase and Whipple, 2011) and the Himalayas and Eastern-Tibet (Scherler et al., 2017). Both studies found that erosion thresholds do not have a significant effect on river incision rates in basins with a high channel steepness, however, thresholds are found to be important in gently sloping basins. A study that specifically focusses on the role of erosion thresholds in gently sloping basins is still lacking. Hence, the fourth study (Chapter 6), which is still ongoing, concentrates on the importance of erosion thresholds in the river incision process in gently sloping basins and focusses specifically on the differences between different climate regions.

All studies in this PhD thesis focus on central Chile (~26°S-42°S). Central Chile is a favourable region to study the effect of climate on earth surface processes because this region features a relatively constant geological setting (Hervé et al., 1988, 2007; Parada et al., 1988; Vázquez et al., 2016), but a large north-to-south contrast in precipitation (Pizarro et al., 2012). The geological, climatic and hydrological settings of central Chile are further introduced in Chapter 2.

Chapter 2

Study area

To study the effect of climate on discharge variability and the fluvial erosion efficiency, this PhD thesis focusses on central Chile between ~26°S and ~42°S. Central Chile provides a unique opportunity to study these processes. This region contains a well-constrained geological setting, with relatively constant tectonic uplift rates and similar lithologies along a large north-to-south stretch. Furthermore, central Chile features a strong meridional precipitation gradient, with arid conditions in the north and humid conditions in the south (Pizarro et al., 2012).

To study the effect of precipitation on grain size-dependent ^{10}Be concentrations in Chapter 3, fieldwork was conducted in four study sites in the Coastal Cordillera which were selected by the DFG priority program "EarthShape" (white circles in Figure 2.1a). These study sites are further introduced in Section 2.4. River discharge data from 183 discharge stations in central Chile (~28-42°S) were obtained for the study that focusses on ENSO-induced hydrological anomalies (Chapter 4). These stations were either located in the Coastal region (yellow circles) or the Andes (green triangles) (Figure 2.1a). Finally, to investigate the fluvial erosion efficiency along a climatic gradient in the Coastal region (Chapter 5 & 6), fieldwork was conducted in multiple catchments in three climatic zones; semi-arid (~28°-29°S), mediterranean (~32°-33°S) and humid-temperate (~37-38°S) (red squares in Figure 2.1a).

The following chapters introduce the geological (Chapter 2.1), climatic (Chapter 2.2) and hydrological (Chapter 2.3) settings in central Chile, as well as the study areas that have been selected by the DFG Priority program "EarthShape" (Chapter 2.4).

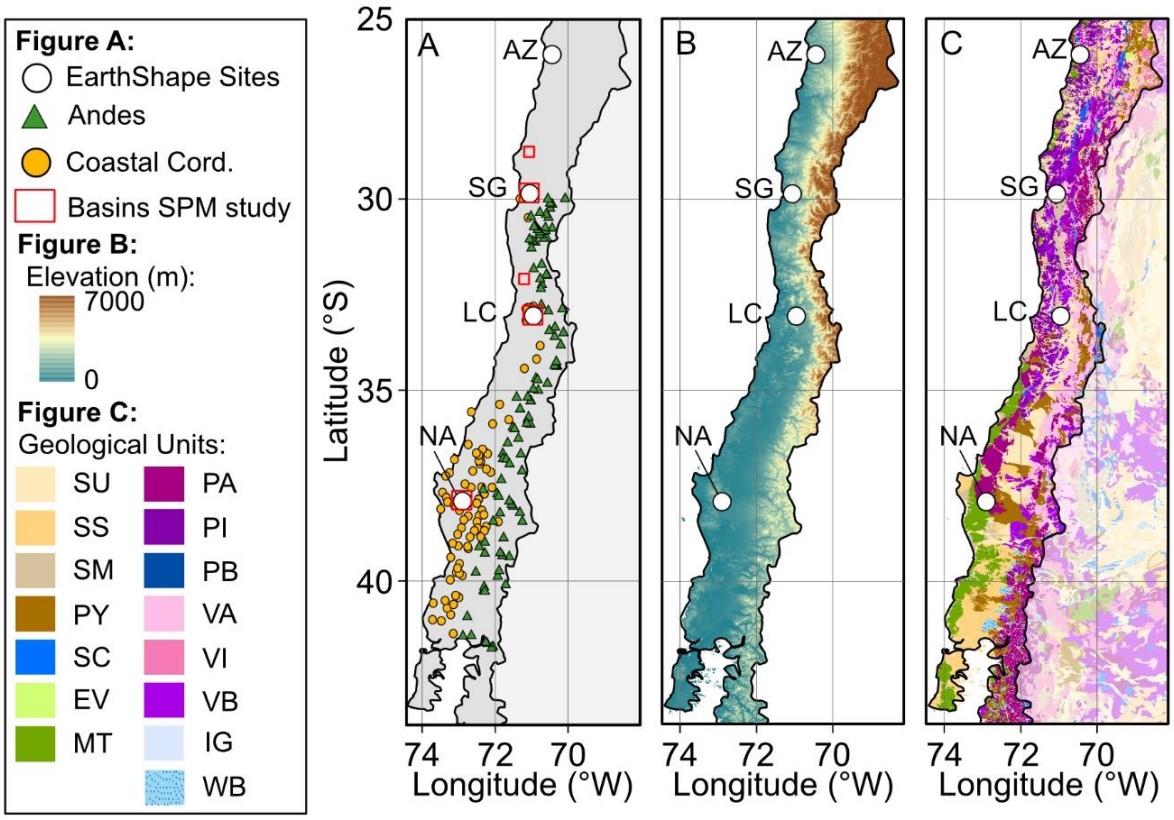

Figure 2.1: Study area locations, elevation, and geological units in central Chile. Locations of the study areas of the different studies; locations of the EarthShape sites (white circles) which are the focus of Chapter 3, locations of the hydrological stations which are used in Chapter 4, these stations are located in the Andes (green triangles) and the Coastal region (orange circles), and finally, the climatic zones where fieldwork has been conducted (red squares) in Chapter 5 and 6. B) Digital elevation Model (DEM) of central Chile. C) The geological classes based on the Global Lithological Map (GLiM; Hartmann and Moosdorf, 2012), with the geological units: unconsolidated sediments (SU), siliciclastic sedimentary rocks (SS), mixed sedimentary rocks (SM), pyroclastics (PY), carbonate sedimentary rocks (SC), evaporites (EV), metamorphic rocks (MT), acid plutonic rocks (PA), intermediate plutonic rocks (PI), basic plutonic rocks (PB), acid volcanic rocks (VA), intermediate volcanic rocks (VI), basic volcanic rocks (VB), ice and glaciers (IG) and water bodies (WB).

2.1 Geological setting

South America is positioned on the east-side of a convergent plate boundary, where the Nazca plate is subducting under the South American plate (Jordan et al., 1983). The subduction zone of the Nazca plate (formerly Farallon plate) spans from ~5°N to ~45°S and has been active since at least the Jurassic, which makes the western South America plate boundary a spatially and temporally constant tectonic setting over a large latitudinal distance. One heterogeneity in tectonic setting is the shallow subduction angle (flat slab subduction) between 31°-33°S (Barazangi and Isacks, 1977; Horton, 2018).

Central Chile is composed of several geological structures which are roughly arranged trench-parallel, as result of a west-to-east segmentation of neighbouring magmatic arcs (Kukowski and Oncken, 2006). The main geological structures are: the Coastal Cordillera, the Central Depression, and the Principal Cordillera (Melnick and Echtler, 2006; Vázquez et al., 2016). The Central Depression is absent between 27°-33°S, as a result of flat slab subduction (Charrier et al., 2007).

The Coastal Cordillera is the oldest geological unit, which developed during the Jurassic (Rutland, 1971; Scheuber et al., 1994). The western part of the Coastal Cordillera is composed of metamorphic and intrusive basement of Paleozoic-Jurassic origin, which is at some places covered by marine deposits of Late Miocene to Holocene age (Figure 2.1c). The eastern part of the Coastal Cordillera consists of Jurassic-Cretaceous granites and volcanoclastic rocks (Hervé et al., 1988, 2007; Parada et al., 1988; Vázquez et al., 2016). The uplift of the Coastal Cordillera as a separate unit from the Central Depression started in the Oligocene and is still ongoing today (Hartley et al., 2000). The Central Depression is a continental wedge-shaped forearc basin which formed during the Late Eocene-Late Pliocene (Hartley and Evenstar, 2010). The Central Depression is filled with sedimentary infill from alluvial fan and fluvial sediment deposits and ignimbrite flows from the Miocene volcanic arc (Figure 2.1c; Hartley et al., 2000; Hartley and Evenstar, 2010; Juez-Larré et al., 2010).

Since the late Cretaceous (60-80 Ma) the magmatic arc front has migrated eastward towards the Principal Cordillera which led to the onset of Andean Mountain Building (Armijo et al., 2015; Barnes and Ehlers, 2009; Juez-Larré et al., 2010). The Andes Mountain range is mainly composed of volcanic rocks and volcanic epiclastic material of Cretaceous to Quaternary age. Some older (Carboniferous to Triassic) intrusive units can also be found (SERNAGEOMIN, 2003). The Andes reaches its highest elevations in the northern part of central Chile and decreases in elevation towards the south (Figure 2.1b).

2.2 Climatic setting

Central Chile (26°S-42°S) is located between two regions of climatic extremes. It borders the Atacama desert, one of the most arid regions of the world, to the north, and Patagonia, the wettest region of the Southern Hemisphere, to the south (Miller, 1976; Montecinos and Aceituno, 2003). The Köppen climate classifications in the Coastal Cordillera are the following (from north to south): cold desert climate (BWk) in the northernmost region (26°-31°S), followed by cold semi-arid (BSk) climate (31°-33°S), hot- and cold-summer mediterranean climate (Csa and Csb) (33°-38°S) and temperate rain-oceanic (Cfb) climate in the southernmost position (38°S-42°S) (Alvarez-Garreton et al., 2018; Köppen, 1900; Kottek et al., 2006) (Figure 2.2a). The Köppen climate classifications in the Andes are elevation-driven, with tundra climate (ET) in the highest elevation part of the Andes in the north (26°-35°S) and mediterranean-influenced

subarctic climate (Dsc) in the south (35°-42°S), where the Andes Mountain range is lower in elevation.

The study area features a precipitation gradient with low mean annual precipitation rates (~7 mm) in the north (~26°S) and high mean annual precipitation (~2500 mm) in the south (~42°S) (Figure 2.2b; Fick and Hijmans, 2017). The mean annual temperature (MAT) also shows a latitudinal trend, with higher MAT in the north (~16.5°C) and lower MAT in the south (~10.5°C) (Figure 2.2c). Furthermore, an east-west gradient in climate can be observed, which is induced by the contrast in elevation between the low elevation Coastal region in the west and the high elevation Andes Mountain range in the east. Besides elevation-driven differences in temperature, which for some regions results in a ~20°C MAT difference between the Coastal Cordillera and the Andes (Figure 2.2c; Alvarez-Garreton et al., 2018), the orographic advance of the Andes also induces two to three times higher precipitation rates as compared to the Coastal region (Figure 2.2b; Barrett and Hameed, 2017; Garreaud et al., 2009; Viale and Garreaud, 2014). The meridional precipitation gradient and the differences in elevation between the Coastal Cordillera and the Andes strongly correlate with the vegetation cover, as shown by the Enhanced Vegetation Index (Figure 2.2d). Vegetation cover is close to 0% in the arid region in the north and in the alpine region of the Andes. In the humid-temperate region in the south the vegetation cover is about 70-80%.

The arid conditions of northern Chile are primarily induced by the subsidence of dry air in the large-scale mid-tropospheric Hadley Cell (Garreaud et al., 2009; Hartley et al., 2005; Rutllant et al., 2003). This is reinforced by the cold ocean surface water that is transported by the Humboldt Current and the upwelling of cold ocean water from greater depth (Hartley et al., 2005). The cold sea surface temperature cools down the air, which, in turn, leads to a lower water holding capacity of the air (Diaz and Kiladis, 1995). The climate in the arid region experiences quasi-barotropic conditions, the climate is rather constant and unaffected by cold fronts. In contrast, the climate in southern Chile is affected by the midlatitude Westerlies, that bring cold and humid frontal storms from Antarctica to the west coast of Chile (Fuenzalida, 1982; Garreaud et al., 2009; Montecinos and Aceituno, 2003). The climatic conditions in the south can be characterized as baroclinic conditions. The position of the Southern Pacific High (SPH) determines the boundary between the region under quasi-barotropic conditions (north) and the region under baroclinic conditions (south). Therefore, the seasonal migration of the SPH is the main driver of seasonal variations in climatic conditions in Chile (e.g., Barrett and Hameed, 2017; Fuenzalida, 1982; Montecinos and Aceituno, 2003).

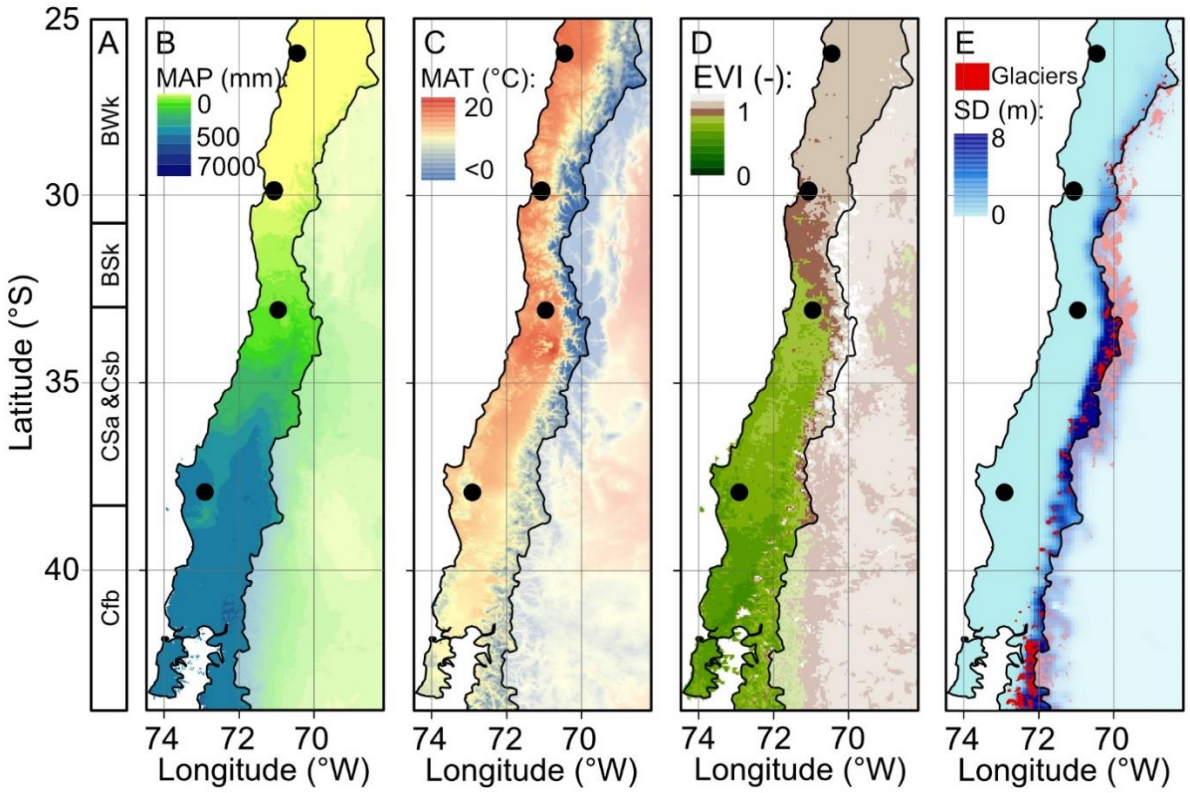

Figure 2.2: Climatic variables in central Chile.Climate zones in the Coastal Cordillera according to the Köppen climate classification: Bwk: cold desert climate, BSk; cold semi-arid, Csa; Hot-summer mediterranean climate, Csb; Cold-summer mediterranean climate, Cfb; temperate rain-oceanic climate. B) Mean Annual Precipitation (MAP) (WorldClim v2 (Fick and Hijmans (2017)) C) Mean Annual Temperature (MAT) (WorldClim v2 (Fick and Hijmans (2017)), C) Enhanced Vegetation Index (EVI (Didan (2015)).., D) Snow depth (SD) (ERA5-L dataset (Muñoz Sabater (2019)) and glaciers (Global Land Ice measurements from Space (GLIMS; Raup et al. (2007)).

The El Niño Southern Oscillation (ENSO) and Pacific Decadal Oscillation (PDO) are large oceanic-atmospheric systems that induce interannual climatic anomalies in Chile (e.g., Garreaud et al., 2009; Montecinos and Aceituno, 2003). During El Niño, warm Pacific ocean surface water is pushed towards the west coast of South America (Jaksic, 1998; Ropelewski and Halpert, 1987). El Niño is called the warm and wet phase, because the anomalously warm sea surface temperatures (SST) heat the air and increase the water holding capacity of air, which results in wet conditions (e.g., Garreaud et al., 2009; Montecinos and Aceituno, 2003). Often after the El Niño phase, the system swaps back to a reinforced state of the normal conditions - La Niña, the cold and dry phase (Diaz and Kiladis, 1995). Studies found that the position and the intensity of the Southern Pacific High are important drivers of the anomalous sea surface temperatures and climatic conditions during El Niño and La Niña (Barrett and Hameed, 2017; Montecinos et al., 2000). Chapter 4 focusses on the effect of ENSO on hydrological anomalies in central Chile.

A modelling study (Werner et al., 2018) and empirical evidence (Hartley et al., 2005) revealed that the arid conditions have been persistent since at least the Last Glacial Maximum (~21000 BP). The mediterranean and humid-temperate regions of central Chile have experienced wetter conditions during the Last Glacial Maximum and mid Holocene (~6000 BP) and in all of central Chile, the air temperatures were slightly colder during the Last Glacial Maximum and Mid-Holocene (Werner et al., 2018). This affected the type of plant communities that were present, but the different climatic conditions did not significantly affected the vegetation cover during the LGM and the mid-Holocene (Werner et al., 2018). ENSO has induced interannual climatic variations in Chile since at least the past 5000 years (Jaksic, 1998; Rollins et al., 1986).

Chile is currently undergoing a multiyear (2010-ongoing) megadrought which accounts for precipitation reductions of 25-45% (Alvarez-Garreton et al., 2021; Boisier et al., 2016; Garreaud et al., 2017, 2020). A study suggests that the Pacific Decadal Oscillation explains about half of this precipitation reduction, but also concludes that regional anthropogenic climate change partly explains the rainfall reductions (Boisier et al., 2016).

2.3 Hydrological setting

All major rivers in central Chile flow in east-west direction from the drainage divide in the Andes mountains in the east, towards the Pacific Ocean in the west. In the northern section of central Chile (25°-34°S) the Andean snow cover is permanent, whereas south of 34°S the snow cover shows a seasonal pattern (Alvarez-Garreton et al., 2018; Cordero et al., 2019). The snow and glacier covered area is highest at around 32.5-35.5°S (Figure 2.2e, Raup et al., 2007), which is driven by a combination of maximum elevation, precipitation, and orographic advance (Cortés and Margulis, 2017).

The hydrological regime of Coastal region catchments is rainfall-dominated, which means that the main discharge peak occurs during the rainy season in winter (pluvial-type). Andean-draining catchments north of 34°S can be characterized by the nival-type discharge regime; in these catchments the main discharge peak occurs during the snowmelt season in summer. Andean catchments south of 34° have a mixed discharge regime (pluvio-nival) (Alvarez-Garreton et al., 2018; Oertel et al., 2020). Due to the low precipitation rates in the northern region, most rivers appear as intermittent rivers, whereas rivers in the south are typically perennial rivers.

2.4 EarthShape study sites

The EarthShape project has selected four study sites in the Coastal Cordillera, to study the effect of biota on Earth surface processes. These sites have been selected based on similar lithology but contrasting climate and vegetation cover. The study sites include National Park Pan de Azúcar (~26.1°S), National Reserve Santa Gracia (~29.8°S), National Park La Campana (~33.0°S) and National Park Nahuelbuta (~37.8°S). The study sites characteristics are listed in Table 2.1.

Table 2.1: EarthShape study site characteristics. Mean annual precipitation (MAP) and Mean annual temperature (MAT) estimates from WorldClim2 (Fick and Hijmans, 2017)

Catchment	Latitude	Longitude	MAP	MAT
	(°N)	*(°E)*	*(mm yr^{-1})*	*(°C)*
Pan de Azúcar (AZ)	-26.112	-70.551	12	16.8
Santa Gracia (SG)	-29.76	-71.168	66	13.7
La Campana (LC)	-32.954	-71.069	367	14.1
Nahuelbuta (NA)	-37.808	-73.014	1469	6.6

The four study sites feature granodioritic lithology, however, some differences in mineralogy exist between the sites (Oeser et al., 2018). The tectonic uplift rates are rather similar between the sites. Pan de Azúcar, Santa Gracia and La Campana experience modern uplift rates of <0.2 mm yr^{-1} (Melnick, 2016). The Nahuelbuta catchment is located in the Nahuelbuta Range, which experienced an increase in uplift rates from 0.03-0.04 mm yr^{-1} to >0.2 mm yr^{-1} at 4 ± 1.2 Ma (Glodny et al., 2008; Melnick et al., 2009). However, the Nahuelbuta study site is located upstream of a major knickzone in the river channel, thus, this study site is currently unaffected by the increased uplift rate (Crosby and Whipple, 2006). None of the EarthShape study sites were glaciated during the Last Glacial Maximum (Hulton et al., 2002). The climate in these catchments varies from an arid climate in the north (Pan de Azúcar), via a semi-arid climate (Santa Gracia), and a mediterranean climate (La Campana) to a humid-temperate climate in the south (Nahuelbuta) (Köppen, 1900; Kottek et al., 2006). Due to the minor differences in lithology and a relatively similar geological history, these sites provide a unique opportunity to study the effect of climate and biota on Earth surface processes.

Chapter 3

Cosmogenic ^{10}Be in river sediment: where grain size matters and why

Renee van Dongen[1], Dirk Scherler[1,2], Hella Wittmann[1], Friedhelm von Blanckenburg[1,2]

[1] GFZ German Research Centre for Geosciences, Earth Surface Geochemistry, Potsdam, Germany.
[2] Freie Universität Berlin, Institute of Geological Sciences, Berlin, Germany.

This chapter is published in:
Earth Surface Dynamics Vol. 7, pages 393-410, 2019
Renee van Dongen, Dirk Scherler, Hella Wittmann, and Friedhelm von Blanckenburg
https://doi.org/10.5194/esurf-7-393-2019

Abstract

Concentrations of *in situ*-produced cosmogenic ^{10}Be in river sediment are widely used to estimate catchment-average denudation rates. Typically, the ^{10}Be concentrations are measured in the sand fraction of river sediment. However, the grain size of bedload sediment in most bedrock rivers cover a much wider range. Where ^{10}Be concentrations depend on grain size, denudation rate estimates based on the sand fraction alone could potentially be biased. To date, knowledge about catchment attributes that may induce grain size-dependent ^{10}Be concentrations is incomplete or has only been investigated in modelling studies. Here we present an empirical study on the occurrence of grain size-dependent ^{10}Be concentrations and the potential controls of hillslope angle, precipitation, lithology and abrasion. We first conducted a study focusing on the sole effect of precipitation in four granitic catchments located on a climate-gradient in the Chilean Coastal Cordillera. We found that observed grain size dependencies of ^{10}Be concentrations in the most-arid and most-humid catchments could be explained by the effect of precipitation on both the scouring depth of erosion processes and the depth of the mixed soil layer. Analysis of a global dataset of published ^{10}Be concentrations in different grain sizes (n=73 catchments), comprising catchments with contrasting hillslope angles, climate, lithology and catchment size revealed a similar pattern. Lower ^{10}Be concentrations in coarse grains (defined as "negative grain size dependency") emerge frequently in catchments which likely have thin soil and where deep-seated erosion processes (e.g., landslides) excavate grains over a larger depth-interval. These catchments include steep (>25°) and humid catchments (>2000 mm yr^{-1}). Furthermore, we found that an additional cause of negative grain size dependencies may emerge in large catchments with weak lithologies and long sediment travel distances (>2300-7000 m, depending on lithology) where abrasion may lead to a grain size distribution that is not representative for the entire catchment. The results of this study can be used to evaluate whether catchment-average denudation rates are likely to be biased in particular catchments.

3.1 Introduction

Catchment-average denudation rates are commonly estimated with *in situ*-produced cosmogenic ^{10}Be concentrations in river sediment (Bierman and Steig, 1996; Brown et al., 1995; Granger et al., 1996). ^{10}Be is a rare isotope that is produced within quartz minerals by high-energy cosmic rays in the upper few meters of the Earth's surface (Gosse and Phillips, 2001). Its concentration records the time minerals were exposed to cosmic radiation, which is inversely proportional to denudation rates over time scales of 10^2-10^5 years (Bierman and Steig, 1996; Brown et al., 1995; Granger et al., 1996; Lal, 1991). Most studies use a sand fraction (0.1-2 mm) of river bedload sediment to estimate catchment-average denudation rates. However, bedload grain sizes found in bedrock rivers, where this method is frequently applied, are often much coarser (Figure 3.1). The sand fraction provides a representative catchment-average denudation rate only if it is spatially and temporally representative for all erosion sources within the catchment (Bierman and Steig, 1996; von Blanckenburg, 2005; Brown et al., 1995; Gonzalez et al., 2017; Granger et al., 1996; Neilson et al., 2017; Willenbring et al., 2013). Evaluating this condition is challenging and requires a detailed understanding of the catchment and its erosion processes.

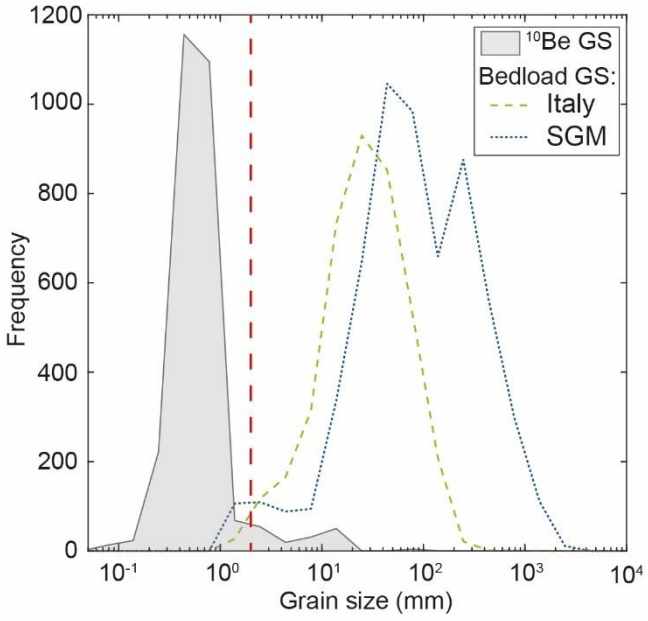

Figure 3.1: Grain size distributions of bedload sediment in rivers and grain sizes used for ^{10}Be-derived catchment-average denudation rates (^{10}Be GS, n=2735) (Codilean et al., 2018). Bedload grain size distributions were measured by pebble counts in bedrock rivers in Southern Italy and Sicily (Italy, n=3900) (Allen et al., 2015; Roda-Boluda et al., 2018) and the San Gabriel Mountains (SGM, n=5930) (DiBiase and Whipple, 2011; Scherler et al., 2016). Wolman pebble count fractions classified as <2 mm are shown as 1 mm in the figure. Dashed line indicates 2 mm.

Where ^{10}Be concentrations differ amongst grain size fractions, using a non-representative grain size fraction could bias catchment-average denudation rates by a factor of 3 or more (Lukens et al., 2016). To date, there is no general consensus of what causes grain size-dependent ^{10}Be concentrations in a catchment. Some studies inferred that lower ^{10}Be concentrations in coarse grains are caused by deep-seated erosion processes, such as landslides, which excavate material from greater depth where ^{10}Be concentrations are lower (e.g., Aguilar et al., 2014; Belmont et al., 2007; Binnie et al., 2007; Brown et al., 1995; Puchol et al., 2014; Sosa Gonzalez et al., 2016a, 2016b; Tofelde et al., 2018; West et al., 2014). In a recent study Tofelde et al. (2018) combined a detailed inventory of hillslope processes in a large, semi-arid Andean catchment, with ^{10}Be concentrations measured in the sand and gravel fraction of river sediment. They explained lower ^{10}Be concentrations in the gravel compared to the sand by the scouring depth of erosion processes. However, other studies found that grain size reduction by abrasion during fluvial transport, or spatial variations in the provenance of different grains sizes can additionally account for grain size-dependent ^{10}Be concentrations (Carretier et al., 2009; Carretier and Regard, 2011; Lukens et al., 2016; Lupker et al., 2017; Matmon et al., 2003). This is particularly true for large and high-relief catchments that cover large elevation ranges, because ^{10}Be production rates depend on atmospheric depth. Carretier et al. (2015) conducted a comprehensive study on ^{10}Be concentrations in different grain sizes on a precipitation gradient, sampling large Andean catchments. Despite significant contrasts in precipitation and, presumably, weathering and erosion processes, no systematic grain size dependency of ^{10}Be concentrations as result of precipitation emerged. A reason may be that as catchment size increases, more complexity in controlling factors is added that may blur potential trends in the data (Carretier et al., 2015a; Portenga and Bierman, 2011). Hence, it remains elusive which type of catchments are sensitive to grain size-dependent ^{10}Be concentrations and biased catchment-average denudation rates (e.g., Carretier et al., 2015), or it has only been addressed in modelling studies (e.g., Lukens et al., 2016).

This paper presents the results of an empirical study in which we investigated the occurrence and cause of grain size-dependent ^{10}Be concentrations in river sediment. Our study consists of two parts: in the first part, we investigated the sole effect of precipitation, in small, granitic catchments in the Chilean Coastal Cordillera that differ mainly by mean annual precipitation. In the second part, we compiled and investigated a global dataset with previously published grain size-dependent ^{10}Be concentrations to include more catchment attributes in our analysis. In the following, we first provide a review of processes that control the grain size distribution and ^{10}Be concentrations of river sediment, to determine relevant catchment attributes for our analysis.

3.2 Why ^{10}Be concentrations in river sediment can depend on grain size

3.2.1 Processes that control grain size

The grain size distribution of river sediment is a function of 1) weathering and 2) erosion processes at the hillslope and 3) fluvial processes that change the grain size distribution. Chemical weathering at the hillslope converts bedrock into sediment of different grain sizes at a rate that is controlled by the properties of the parent rock, the climatic regime, and denudation rates at the surface (Sklar et al., 2017). The parent rock mineralogy sets rock dissolution rates and constrains the minimum size of individual minerals. Bedrock fractures provide water pathways and expose fresh bedrock to weathering (Lebedeva and Brantley, 2017; Oberlander, 1972; Ruxton and Berry, 1957). As chemical weathering rates are set primarily by the flux of water flowing through the regolith and, to some degree, also by temperature (Lasaga et al., 1994; Maher, 2010; White et al., 1999), there is a strong dependency of weathering and sediment production on the climatic regime (Dixon et al., 2016; Riebe et al., 2004). The presence of biota in humid climates can enhance the breakdown of rock fragments because microbes play an important role in chemical weathering processes, and growing roots can fracture bedrock (Drever, 1994; Ehrlich, 1998; Gabet and Mudd, 2010; Roering et al., 2010). The size reduction of bedrock fragments in the regolith depends, besides the chemical weathering rate, also on the time they spend in the regolith layer. This regolith residence time is controlled by the thickness of the regolith layer and the denudation rate, i.e., the rate of sediment removal from the surface (Anderson et al., 2007; Attal et al., 2015; Sklar et al., 2017).

Hillslope sediment is transported towards the river channel by a variety of erosion processes. Diffusive processes are considered to operate in slowly eroding, soil mantled landscapes and move relatively fine grains at or near the surface (Roering et al., 1999). In contrast, deep-seated erosion processes (e.g., landslides) are frequent in steep and rapidly eroding bedrock landscapes (e.g., Burbank et al., 1996; Hovius et al., 1997; Montgomery and Brandon, 2002). Especially when a critical threshold hillslope angle of ~25-30° is exceeded, denudation rates are dominated by the frequency of landslides (Larsen and Montgomery, 2012; Montgomery and Brandon, 2002; Ouimet et al., 2009). Deep-seated erosion processes excavate sediment and bedrock fragments of any size from a greater depth interval (Casagli et al., 2003).

The type of erosion process is indirectly controlled by tectonic uplift rates, precipitation and lithology. In a steady state landscape, denudation rates are set by tectonic uplift, which controls river incision and hillslope steepening (DiBiase et al., 2010; Scherler et al., 2014; Whipple and Tucker, 1999). Extreme precipitation events may oversaturate hillslopes and increase the susceptibility to hillslope failure (Chen and Lee, 2003; Gabet and Dunne, 2002). Some authors argue that deep-seated erosion processes are also important in arid landscapes (Aguilar et al., 2014). Finally, the bedrock strength and

fracture abundance affects the susceptibility to hillslope failure (e.g., Clarke and Burbank, 2011; Perras and Diederichs, 2014) and constrains how much energy is needed for the detachment and transport of individual particles. Once the sediment has reached the channel, processes like downstream abrasion, selective transport and mixing of sediment sources control the grain size distribution at the sample location.

If mixing within the channel is incomplete, single tributaries or local inputs of sediment (e.g., landslides) may dominate the grain size distribution (Binnie et al., 2006; Neilson et al., 2017; Niemi et al., 2005; Yanites et al., 2009). Downstream abrasion and selective transport result in a progressively smaller grain size distribution. Abrasion wears off the outer layers of clasts (Kodoma, 1994; Sklar et al., 2006) and depends on the travel distance and velocity as well as the lithology of the clasts (Attal and Lavé, 2009). Selective transport preferentially deposits coarse grains when the transport capacity of water is low (Ferguson et al., 1996; Hoey and Ferguson, 1994) and thus further changes the grain size distribution.

3.2.2 Processes that control variations in ^{10}Be concentrations

^{10}Be concentrations in quartz grains depend on the ^{10}Be production rate and a grains' exposure time to cosmic rays (Gosse and Phillips, 2001). Processes that preferentially transport sediment from locations with contrasting ^{10}Be production rates (i.e., different soil depths or elevations within the catchment) or exposure times (i.e., locations with different denudation rates), result in a larger variation of ^{10}Be concentrations in the sediment. A certain sample location provides a spatially and temporally representative sediment sample when the sediment from different sources is sufficiently mixed (Binnie et al., 2006; Neilson et al., 2017; Niemi et al., 2005; Yanites et al., 2009). Because ^{10}Be production rates decrease exponentially with depth (Gosse and Phillips, 2001), hillslope sediment that is excavated over a larger depth interval by landslides will obtain a larger variation in ^{10}Be concentrations than sediment transported by diffusive processes near the surface (Aguilar et al., 2014; Belmont et al., 2007; Binnie et al., 2007; Brown et al., 1995; Puchol et al., 2014; Sosa Gonzalez et al., 2016a, 2016b; Tofelde et al., 2018; West et al., 2014).

In soil-mantled landscapes, bioturbation by burrowing animals and tree throw (Gabet et al., 2003) result in well-mixed surface layers with uniform ^{10}Be concentrations (Brown et al., 1995; Granger et al., 1996; Schaller et al., 2018) (Figure 3.2). These mixed soil layers are most likely to develop in humid and slowly eroding catchments, where biota is abundant. Eroded sediment from these layers is expected to have uniform ^{10}Be concentrations. In rapidly eroding and arid landscapes, however, soils are typically very thin or absent, and the eroded sediment likely yield larger variations in ^{10}Be concentrations (Figure 3.2). Furthermore, fluvial processes can affect the grain size distribution at the sample location in a way that not all parts of a catchment are equally represented in different grain size fractions. For example, sediment provenance of

grains from different elevations could play a role in catchments with heterogeneous rock types that produce different clast sizes or contain different quartz abundances (Bierman and Steig, 1996; Carretier et al., 2015a). An unequal representation of elevations in different grain size fractions may also result from hydrodynamic sorting, downstream abrasion and insufficient mixing of tributaries that drain different elevations (Carretier et al., 2009; Carretier and Regard, 2011; Lukens et al., 2016; Neilson et al., 2017). Combined with elevation-dependent ^{10}Be production rates (and provided that denudation rates are constant), this could also result in grain size-dependent ^{10}Be concentrations (Carretier et al., 2015a; Lukens et al., 2016; Matmon et al., 2003).

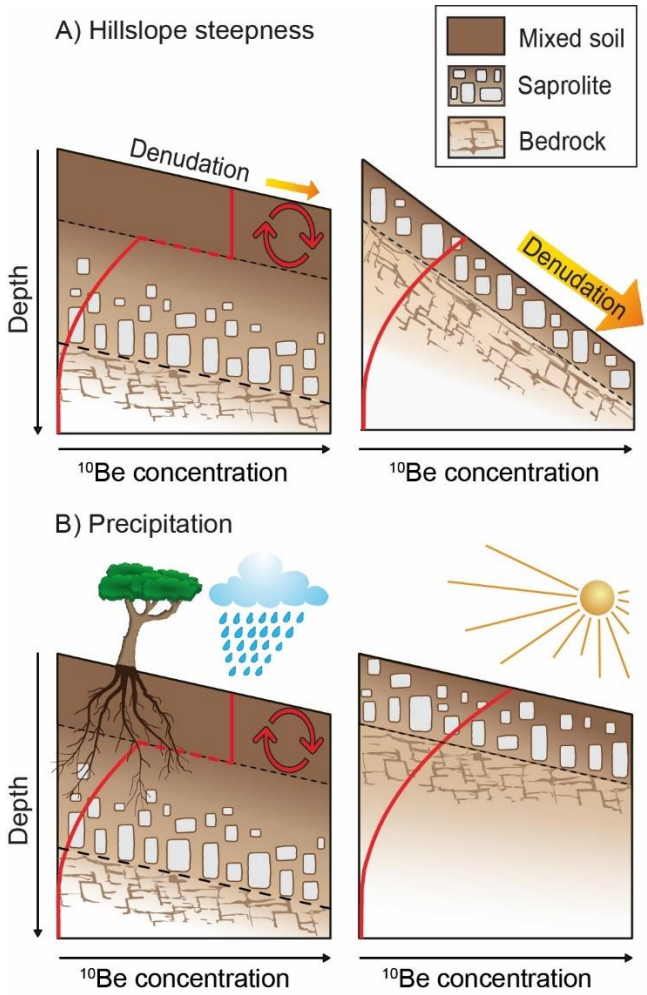

Figure 3.2: The effect of hillslope steepness and precipitation on the depth of the mixed soil layer and ^{10}Be concentrations as a function of depth. (A) Hillslope steepness and denudation rates control the thickness of the soil-mantle by the removal of material from the top. A thick soil-mantle likely develops in gently sloping and slowly eroding landscapes, whereas high denudation rates in steep landscapes prohibit the development of a thick soil-mantle. (B) Precipitation provides water for chemical weathering. Humid landscapes likely develop a thick soil-mantle, which may be absent in arid landscapes. Bioturbation in landscapes with thick soil-mantles results in a well-mixed soil layer with a uniform ^{10}Be concentration, which, in isotopic steady state, is equal to the surface concentration. In landscapes where a mixed soil layer is absent, ^{10}Be concentrations decrease exponentially with depth.

3.2.3 Catchment attributes that potentially control grain size-dependent ^{10}Be concentrations

Based on the above review of processes that may influence grain size-dependent ^{10}Be concentrations, we identified the catchment attributes mean basin slope, mean travel distance, mean annual precipitation (MAP), and lithology that we will focus on in our study. Here, we consider mean basin slope as a topographic catchment attribute that controls denudation rates and the scouring depth of diffusive or deep-seated erosion processes. We selected MAP because of its effect on both weathering rates and the scouring depth of erosion processes and lithology because it affects chemical weathering rates, the grain size of individual minerals and the susceptibility to hillslope failure. Finally, we selected mean travel distance of sediment as a metric for fluvial processes that are transport-dependent (e.g., abrasion and hydrodynamic sorting).

3.3 Study area

For our case study, we selected 4 small catchments (<10 km^2) located in the Coastal Cordillera of central Chile (Table 3.1, Figure 3.3). The Coastal Cordillera features a pronounced latitudinal climate and vegetation gradient, whereas the tectonic setting is rather uniform. The selected catchments are located in the National Park Pan de Azúcar (AZ) (~26° S), the National Reserve Santa Gracia (SG) (~30° S), the National Park La Campana (LC) (~33° S) and the National Park Nahuelbuta (NA) (~38° S).

Table 3.1: Characteristics of the sampled catchments in the Chilean Coastal Cordillera.

Catchment	Latitude	Longitude	MAP[a]	Area	Mean elevation	Mean slope[b]	Mean channel steepness[c]	D_{50}[d]	D_{84}[d]	Bedrock exposed in channel[d]
	(°N)	*(°E)*	*(mm)*	*(km^2)*	*(m)*	*(°)*	*$m^{0.9}$*	*(cm)*	*(cm)*	*(%)*
Pan de Azúcar (AZ)	-26.112	-70.551	13	0.04	339.6	8.2	7.1	0.5	1.47	39
Santa Gracia (SG)	-29.76	-71.168	88	0.88	773.2	17.2	32.2	4	19	0
La Campana (LC)	-32.954	-71.069	358	7.41	1323.8	23.1	88.8	0.35	28.3	3.9
Nahuelbuta (NA)	-37.808	-73.014	1213	5.79	1308.4	8.9	20.5	10	22	2.9

[a] Mean annual precipitation (MAP) is derived from the GPCC dataset (Meyer-Christoffer et al., 2015).

[b] Total mean basin slope calculated with a 30m DEM.

[c] Normalized channel steepness index.

[d] Results derived from Wolman pebble count.

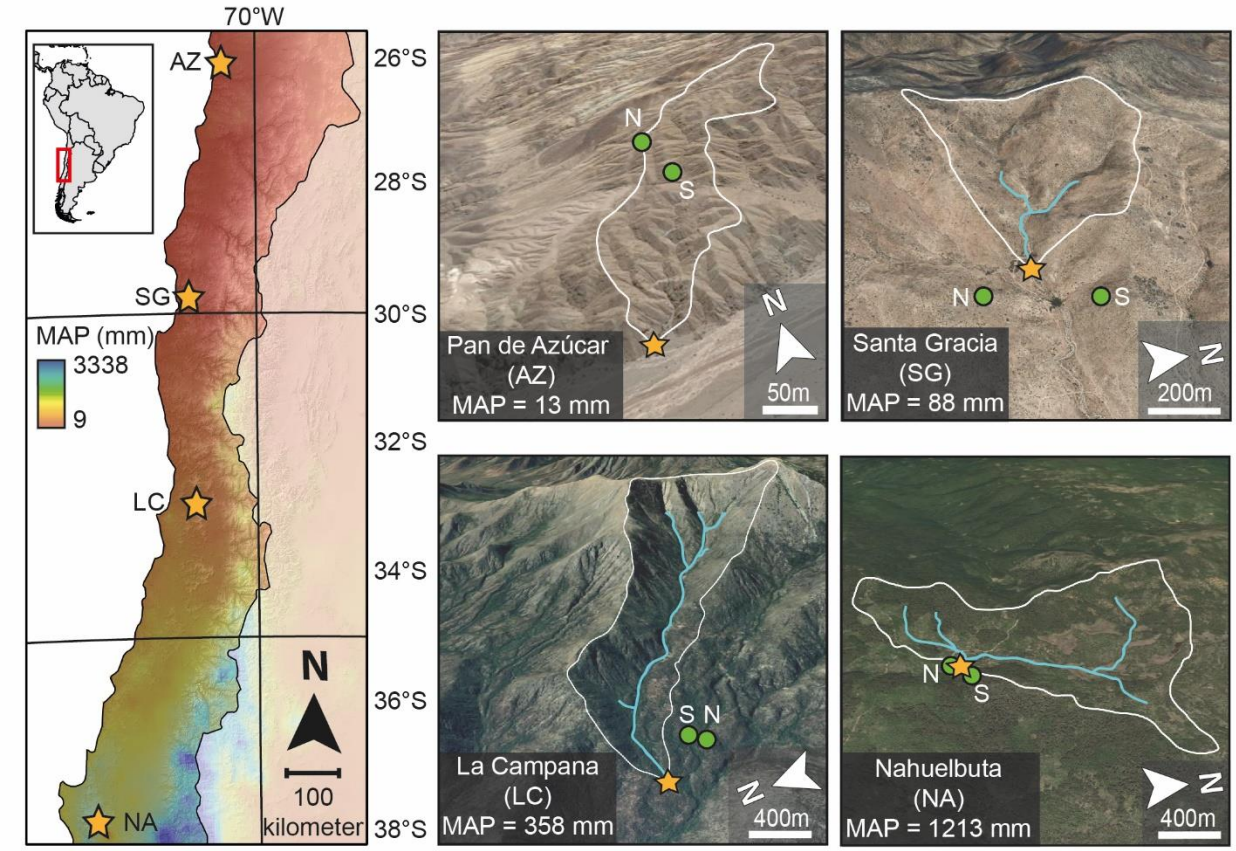

Figure 3.3: Research areas located on a precipitation gradient in the Chilean Coastal Cordillera. On the left, the catchment locations (stars) on a Mean Annual Precipitation (MAP) map from Climate Hazards Group InfraRed Precipitation (CHIRPS), underlain by a SRTM DEM-derived hillshade map. On the right, Google Earth images showing the sample locations (stars), catchment outlines (white), channels with an upstream area of 0.2km^2 (blue lines) and the locations of two ^{10}Be-depth profiles measured by Schaller et al., 2018 in soil pits on a north-facing (N) and south-facing (S) slope (green dots).

The catchments share a granodioritic lithology, though some minor variations in mineralogy exist between the sites (Oeser et al., 2018). The three northern catchments experience modern uplift rates of <0.2 mm yr^{-1} (Melnick, 2016). The southern-most catchment is located in the Nahuelbuta Range, where uplift rates increased from 0.03-0.04 mm yr^{-1} to >0.2 mm yr^{-1} at 4 ± 1.2 Ma (Glodny et al., 2008; Melnick et al., 2009). Because the sampled catchment is located upstream of a river channel knickpoint, it may not yet be influenced by the increased uplift rates (Crosby and Whipple, 2006). The climatic regime and mean annual precipitation (MAP) range from arid (MAP ~13 mm yr^{-1}) in Pan de Azúcar in the north, to semi-arid in Santa Gracia (MAP ~88 mm yr^{-1}), editerranean in La Campana (MAP ~358 mm yr^{-1}), and temperate in Nahuelbuta (MAP ~1213 mm yr^{-1}) in the south (Meyer-Christoffer et al., 2015). This latitudinal increase in MAP results in an increase in vegetation density. The Normalized Difference Vegetation Index (NDVI) (Didan, 2015) varies from 0.1 in the northern-most catchment to 0.8 in the southern-most catchment (Figure S 3.1). The increase in MAP is accompanied by an increase of chemical weathering rates measured in soil profiles located within or in

proximity of the catchments (Oeser et al., 2018). The chemical depletion fraction (CDF), a measure to quantify chemical weathering (Riebe et al., 2003), increases from ~0.1 in Pan de Azúcar (AZ), to ~0.4-0.5 in Santa Gracia (SG), and ~0.3-0.6 in La Campana (LC). Due to heterogeneities in bedrock samples collected in Nahuelbuta (NA), no reliable CDF could be assigned. ^{10}Be depth profiles measured in two midslope soil profiles, revealed an increasing thickness of the mixed soil layer, presumably due to bioturbation (Schaller et al., 2018). The depth of the mixed soil layer increases from ~0-17.5 cm in Pan de Azúcar (AZ), to ~25-45 cm in Santa Gracia (SG), ~47.5-85 cm in La Campana and ~70 cm in Nahuelbuta (NA) (Schaller et al., 2018). By selecting small and low relief catchments with similar lithology and a relatively uniform tectonic setting, we aim to explore the relationship between grain size and ^{10}Be concentrations as controlled by precipitation.

3.4 Methods

3.4.1 Sampling and analytical methods

In each of the four Chilean catchments, we collected approximately 6 kg sand and pebbles from the active channel (Figure 3.3) and conducted a Wolman pebble count (Wolman, 1954) with 1 m intervals to measure the grain size distribution at the sample locations (Figure S 3.2). We dried and sieved the samples in the laboratory to separate the grain size fractions 0.5-1 mm, 1-2 mm, 2-4 mm, 4-8 mm, 8-16 mm, 16-32 mm and 32-64 mm. Before further processing, we crushed pebbles larger than 1 mm. To isolate pure quartz, we separated and purified the river sediment using standard physical and chemical separation methods (Kohl and Nishiizumi, 1992). We spiked between 10 to 20 g of pure quartz with 0.15 mg ^{9}Be carrier, dissolved the quartz and extracted beryllium following established protocols (e.g., von Blanckenburg et al., 2004). Accelerator mass spectrometry measurements were carried out at the University of Cologne, Germany. Reported ^{10}Be/^{9}Be ratios have been normalized to the KN01-6-2 and KN01-5-3 standards, with nominal ^{10}Be/^{9}Be ratios of 5.35×10^{-13} and 6.32×10^{-12}, respectively. We calculated ^{10}Be concentrations from ^{10}Be/^{9}Be ratios and a blank correction was performed. We used MATLAB® and the CRONUS functions (Balco et al., 2008) with the time-independent (St) scaling scheme (Lal, 1991; Stone, 2000) and the SLHL production rate of 4.01 at g^{-1} yr^{-1} (Borchers et al., 2016; Phillips et al., 2016) to calculate catchment-average denudation rate estimates from the ^{10}Be concentrations.

3.4.2 Global compilation

We compiled data from previously published studies that measured ^{10}Be concentrations in different grain size fractions sampled at the same location. Because we are interested in small to medium-sized bedrock catchments, and to reduce the

effect of long-term floodplain sediment storage in large basins, we discarded basins with an area of >5000 km^2. We also removed studies that only measured sand fractions (<2 mm) as weathering and erosion processes affecting these sand-sized grain size fractions may be similar. Hence, we only selected studies measuring at least one sand fraction (mean grain size <2 mm) and at least one coarser grain size fractions (mean grain size >2 mm) (Aguilar et al., 2014; Belmont et al., 2007; Brown et al., 1995; Carretier et al., 2015a; Clapp et al., 2002; Derrieux et al., 2014; Heimsath et al., 2009; Matmon et al., 2003; Palumbo et al., 2009; Puchol et al., 2014; Reinhardt et al., 2007; Stock et al., 2009; Sullivan, 2007; Tofelde et al., 2018). From each selected catchment we compiled the reported grain size classes, the corresponding ^{10}Be concentrations (± analytical errors), and the sample location coordinates (Table S 3.1). For studies that reported a grain size fraction as 'larger than', we assumed that the upper grain size limit corresponds to twice the lower limit (e.g., reported: >2 mm, data compilation: 2-4 mm). We acknowledge that this range might be incorrect, but a fixed grain size range was required for proper data analysis. We transformed the measured grain sizes to phi-based grain size classes, which is the negative logarithmic to the base 2 of the grain size diameter (Krumbein, 1934, 1938). The range of grain sizes we investigated (0.063 to 200 mm) corresponds to phi values of -4 to 7.64. To compare data from different study areas with different ^{10}Be production rates, we normalized the ^{10}Be concentrations (± analytical uncertainties) by the arithmetic mean concentration of all samples from the same catchment.

To assess the influence of the identified catchment attributes mean basin slope, mean travel distance, mean annual precipitation, and lithology (Section 2.3) on grain-size trends in the global compilation, we used a 90-m resolution SRTM DEM (Jarvis et al., 2008). We obtained upstream areas based on the published sample coordinates and using the flow routing tools of the TopoToolbox v2 (Schwanghart and Scherler, 2014). We calculated the topographic parameters: catchment area, mean basin slope, total relief (maximum elevation - minimum elevation) and the mean travel distance of sediment to the sample location, which is calculated as the arithmetic mean travel distance of all pixels in the catchment to the sample location). The agreement between the published and recalculated topographic parameters is good, and minor deviations likely result from differences in DEM resolution (Figure S 3.3). We obtained an estimate of mean annual precipitation (MAP) in each catchment using the 0.25°-resolution gridded precipitation data set from the Global Precipitation Climatology Centre (Meyer-Christoffer et al., 2015). To classify catchment lithology we used the Global Lithological Map (GLiM; Hartmann & Moosdorf, 2012) together with the lithology reported in the original publications. We defined four different lithological classes: sedimentary, magmatic, metamorphic and mixed (>3 different rock types in a catchment).

Next, we used Sternberg's Law to estimate the extent of abrasion of bedload sediment during fluvial transport, to define a travel distance threshold after which abrasion becomes significant:

$$D(L) = D_0\, e^{-\alpha L} \qquad (1)$$

Using equation 1, we calculated the grain size *D* at the sample location, which is derived from an initial grain size D_0 at the source, that travelled distance *L* and decreased in size at a rate given by the reduction coefficient *α* (Kodama, 1994; Kodoma, 1994; Lewin and Brewer, 2002; Sklar et al., 2006; Sklar and Dietrich, 2008). The reduction coefficient depends on both grain velocity and lithology. Rocks with low tensile strength reduce faster in size during transport than rocks with high tensile strength (Attal and Lavé, 2009). We chose the reduction coefficients based on literature values for field settings (sedimentary rocks: α = 0.0003 m^{-1}, magmatic rocks: α = 0.0002 m^{-1}, metamorphic rocks: α = 0.0001 m^{-1}), which are typically higher than experimental studies due to different particle collision dynamics and the lack of weathering in experimental studies (Sklar et al., 2006). We considered the effect of abrasion to be negligible when a grain size at the sample location (D) falls in the same phi-grain size class as at its erosion source (D_0). E.g., for abrasion to be significant, a grain size of 2 mm at the erosion source, must be smaller than 1 mm at the sample location to fall in a lower phi-grain size class. This results in abrasion thresholds for sedimentary, magmatic, and metamorphic rocks of 2300 m, 3500 m, and 7000 m, respectively. For catchments underlain by mixed lithologies, the abrasion threshold lies between 2300 m and 7000 m (Attal and Lavé, 2009).

We quantified the relationship between grain size and ^{10}Be concentrations by calculating a 'grain size dependency' for each sample set (Figure 3.4). This is the slope of a linear fit through the ^{10}Be concentrations of different grain size classes. To account for uncertainties in ^{10}Be concentrations and for grain size ranges, we used a Monte Carlo approach (n=10,000) to randomly select a point between the mean ± analytical error ^{10}Be concentrations and the analyzed grain size range. We thus obtained a mean ± standard deviation grain size dependency for each catchment. A positive grain size dependency indicates higher ^{10}Be concentrations in coarser grains, and vice versa.

Next, we used the Kolmogorov-Smirnov Test (KS-test, 5% significance interval) to test whether particular mean basin slope, MAP or sediment travel distance classes showed a significantly different distribution of grain size dependencies (Kolmogorov, 1933; Smirnov, 1939). Finally, we calculated linear regression statistics between the grain size dependency values and the catchment attributes mean basin slope, MAP and mean travel distance and applied a multivariate linear regression model including the effect of all 3 catchment attributes. We did this for the entire dataset and for each individual lithology. As part of the multivariate statistics, we calculated the relative importance

(RI) of all catchment attributes, using the LMG approach (Lindeman et al., 1980), of the 'Relaimpo' R studio-package (Grömping, 2006). This provides the percentage of contribution of each catchment attribute to the multivariate regression model R^2.

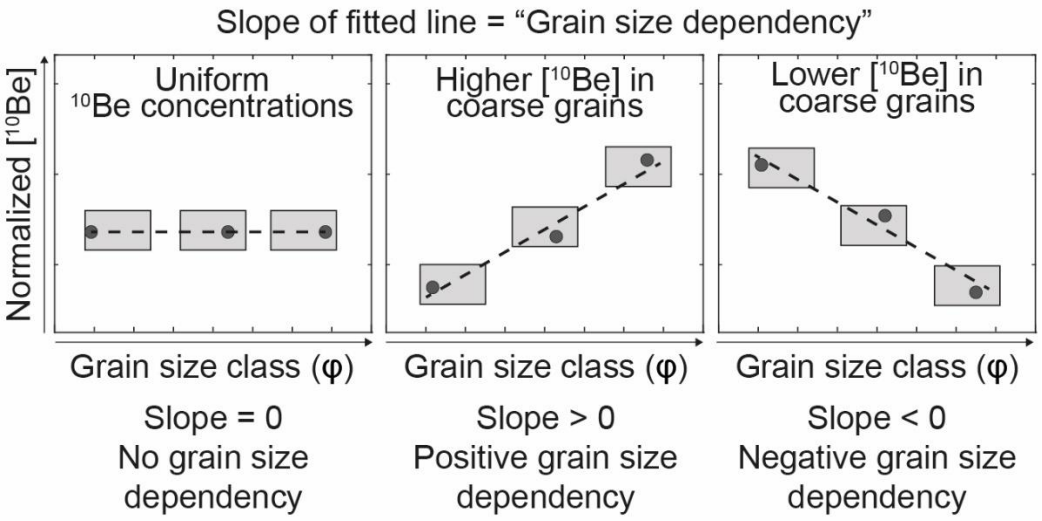

Figure 3.4: Schematic showing the concept of measuring grain size dependency. A random point was selected from within each grain size range and from the corresponding ^{10}Be concentrations ± analytical error (boxes). The slope of a line fitted to the randomly selected points represents the grain size dependency. We used a Monte Carlo simulation of 1000 runs to account for the width of the grain size range and the analytical errors on ^{10}Be concentrations. This yields a mean grain size dependency with error bars.

3.5 Results

3.5.1 Chilean Coastal Cordillera

The measured ^{10}Be concentrations in the most arid catchment (AZ) range from 2.8 to 4.6 ×10^5 atoms (g quartz)$^{-1}$, resulting in catchment-average denudation rates of 5.8 ± 0.7 to 10.1 ± 1.1 mm kyr^{-1} (Table 3.2). In the semi-arid catchment (SG), the ^{10}Be concentrations range from 3.6 to 5.2 ×10^5 atoms (g quartz)$^{-1}$, which corresponds to catchment-average denudation rates of 7.5 ± 0.8 to 11.0 ± 1.4 mm kyr^{-1} (Table 3.2). The ^{10}Be concentrations in the Mediterranean catchment (LC) are a factor 10 lower compared to the other catchments and range from 0.2 to 0.6 ×10^5 atoms (g quartz)$^{-1}$, which results in catchment-average denudation rates of 103.7 ± 12.4 to 384.1 ± 54.5 mm kyr^{-1} (Table 3.2).

The temperate catchment (NA) yielded ^{10}Be concentrations ranging from 1.8 to 2.9 ×10^5 atoms (g quartz)$^{-1}$, resulting in catchment-average denudation rates of 24.0 ± 2.6 to 40.2 ± 4.5 mm kyr^{-1} (Table 3.2). Only the arid (AZ) and Mediterranean (LC) catchments

show a consistent, but noisy trend between ^{10}Be concentrations and grain sizes. In the arid catchment (AZ), ^{10}Be concentrations are decreasing with increasing grain size. The 2σ-variability of ^{10}Be concentrations measured in all grain size fractions deviates ±18% from the mean (Figure 3.5). In the Mediterranean catchment (LC), the ^{10}Be concentrations of all grain size fractions vary up to ±40% from the mean and display a noisy but positive grain size dependency, i.e., increasing ^{10}Be concentrations with increasing grain size (Figure 3.5). In both the semi-arid (SG) and temperate catchments (NA), the 2σ-variability in ^{10}Be concentrations is low (±12% and ±14%, respectively) and rather unsystematic (Figure 3.5). The smallest grain size fractions (0.5-4 mm) in the semi-arid catchment (SG) show a decreasing trend, but this trend increases again for coarser grain size fractions (4-32 mm). In the temperate catchment (NA), ^{10}Be concentrations are uniform in the five smallest grain size fractions (0.5-16 mm), but this trend breaks down at the two largest grain size fractions (16-64 mm), which have lower ^{10}Be concentrations.

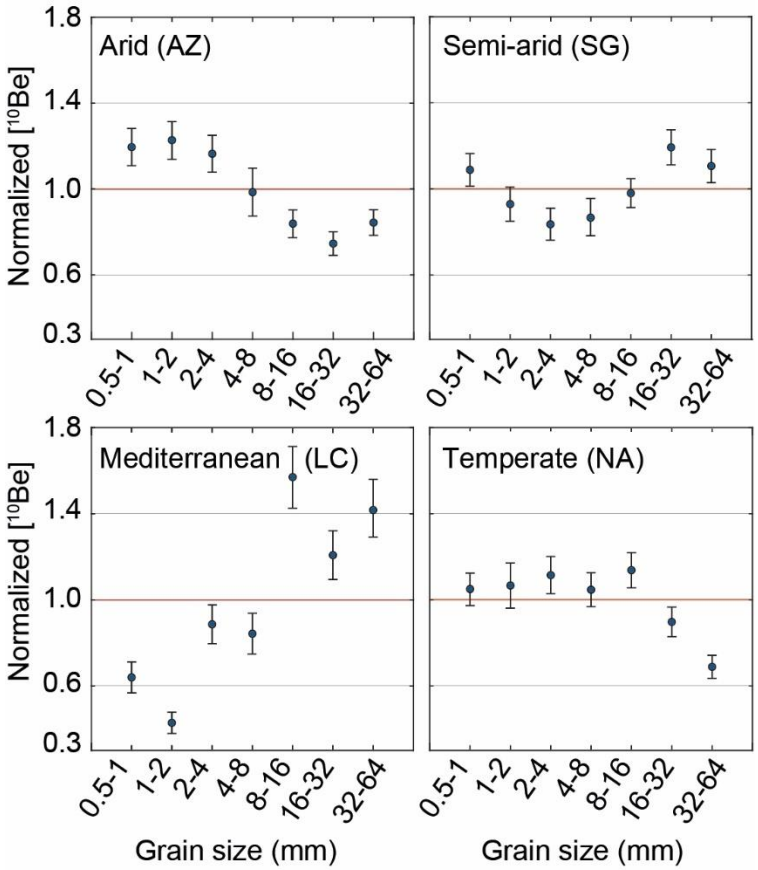

Figure 3.5: Normalized ^{10}Be concentrations (±2σ analytical error) measured in 7 different grain size classes. The ^{10}Be concentrations are normalized to the arithmetic mean of all grain size fractions within a catchment. The red line indicates the normalized catchment-average ^{10}Be concentration.

Table 3.2: Cosmogenic nuclide samples from the Chilean Coastal Cordillera. IGSN number, analyzed quartz mass, ^{9}Be carries mass, $^{10}Be/^{9}Be$ ratio (±1σ), ^{10}Be concentrations (±2σ analytical error), spallation (P_{sp}) and muogenic (P_{mu}) production rates and calculated denudation rates (±2σ).

Catchment	Grain size	IGSN	Quartz mass	^{9}Be Carrier mass	$^{10}Be/^{9}Be$ ratio ± 1σ	$[^{10}Be]$ ± 2σ	P_{sp}	P_{mu}	Denudation rate ± 2σ
	(mm)		*(g)*	*(mg)*	*x 10^{-14}*	*(x 10^{5} atoms g^{-1})*	*(atoms g_{qtz}^{-1} yr^{-1})*	*(atoms g_{qtz}^{-1} yr^{-1})*	*(mm kyr^{-1})*
Pan de Azúcar (AZ)	0.5-1	GFRD10010	9.9	0.153	43.0 ± 1.5	4.48 ± 0.33	4.13	0.085	6.04 ± 0.69
	1-2	GFRD10011	17.9	0.153	79.9 ± 2.8	4.60 ± 0.34			5.86 ± 0.67
	2-4	GFRD10012	18.7	0.154	78.6 ± 5.8	4.36 ± 0.32			6.21 ± 0.72
	4-8	GFRD10013	18.2	0.153	65.3 ± 3.6	3.69 ± 0.42			7.5 ± 1.1
	8-16	GFRD10014	18.1	0.154	55.2 ± 2.1	3.14 ± 0.24			8.9 ± 1.0
	16-32	GFRD10015	15.0	0.153	40.8 ± 1.5	2.80 ± 0.21			10.2 ± 1.1
	32-64	GFRD10016	18.7	0.153	57.6 ± 2.0	3.16 ± 0.22			8.9 ± 1.0
	Mean	-	-		-	3.75 ± 0.24			7.66 ± 0.69
Santa Gracia (SG)	0.5-1	GFRD1000Q	18.7	0.154	85.4 ± 2.9	4.71 ± 0.33	6.02	0.097	8.26 ± 0.91
	1-2	GFRD1000R	14.1	0.153	55.1 ± 2.3	4.02 ± 0.34			9.8 ± 1.2
	2-4	GFRD1000S	13.8	0.153	49.0 ± 2.1	3.62 ± 0.32			11.0 ± 1.4
	4-8	GFRD1000T	13.8	0.153	50.3 ± 2.4	3.76 ± 0.37			10.5 ± 1.4
	8-16	GFRD1000U	20.0	0.154	82.5 ± 2.7	4.25 ± 0.29			9.3 ± 1.0
	16-32	GFRD1000V	19.3	0.154	97.0 ± 3.2	5.17 ± 0.35			7.48 ± 0.82
	32-64	GFRD1000W	19.5	0.154	90.9 ± 3.0	4.79 ± 0.33			8.12 ± 0.89
	Mean	-	-		-	4.33 ± 0.26			9.21 ± 0.84
La Campana (LC)	0.5-1	GFRD1000C	19.4	0.154	4.98 ± 0.28	0.264 ± 0.030	9.94	0.11	257 ± 35
	1-2	GFRD1000D	20.0	0.154	3.44 ± 0.20	0.177 ± 0.021			384 ± 55
	2-4	GFRD1000E	17.0	0.154	6.05 ± 0.30	0.366 ± 0.037			185 ± 24
	4-8	GFRD1000F	16.9	0.154	5.70 ± 0.32	0.348 ± 0.039			194 ± 27
	8-16	GFRD1000G	19.5	0.154	12.29 ± 0.54	0.648 ± 0.059			104 ± 12
	16-32	GFRD1000H	20.0	0.154	9.69 ± 0.44	0.498 ± 0.047			135 ± 17
	32-64	GFRD1000J	16.5	0.154	9.43 ± 0.43	0.588 ± 0.055			144 ± 14
	Mean	-	-		-	0.413 ± 0.033			200 ± 22
Nahuelbuta (NA)	0.5-1	GFRD10002	19.8	0.154	51.4 ± 1.8	2.67 ± 0.19	10.72	0.11	26.0 ± 2.8
	1-2	GFRD10003	18.7	0.153	49.5 ± 2.4	2.72 ± 0.27			25.6 ± 3.3
	2-4	GFRD10004	18.7	0.153	51.8 ± 1.9	2.84 ± 0.22			24.5 ± 2.8
	4-8	GFRD10005	19.2	0.154	49.7 ± 1.8	2.67 ± 0.20			26.1 ± 2.9
	8-16	GFRD10006	20.0	0.153	56.6 ± 1.9	2.90 ± 0.21			23.9 ± 2.6
	16-32	GFRD10007	19.6	0.154	43.5 ± 1.6	2.29 ± 0.18			30.6 ± 3.4
	32-64	GFRD10008	19.6	0.153	33.5 ± 1.3	1.76 ± 0.14			40.2 ± 4.5
	Mean	-	-		-	2.55 ± 0.16			27.4 ± 2.4

3.5.2 Global compilation

The global compilation includes 73 catchments covering a wide range of different hillslope angles, sediment travel distances, MAP and lithologies (Figure 3.6).

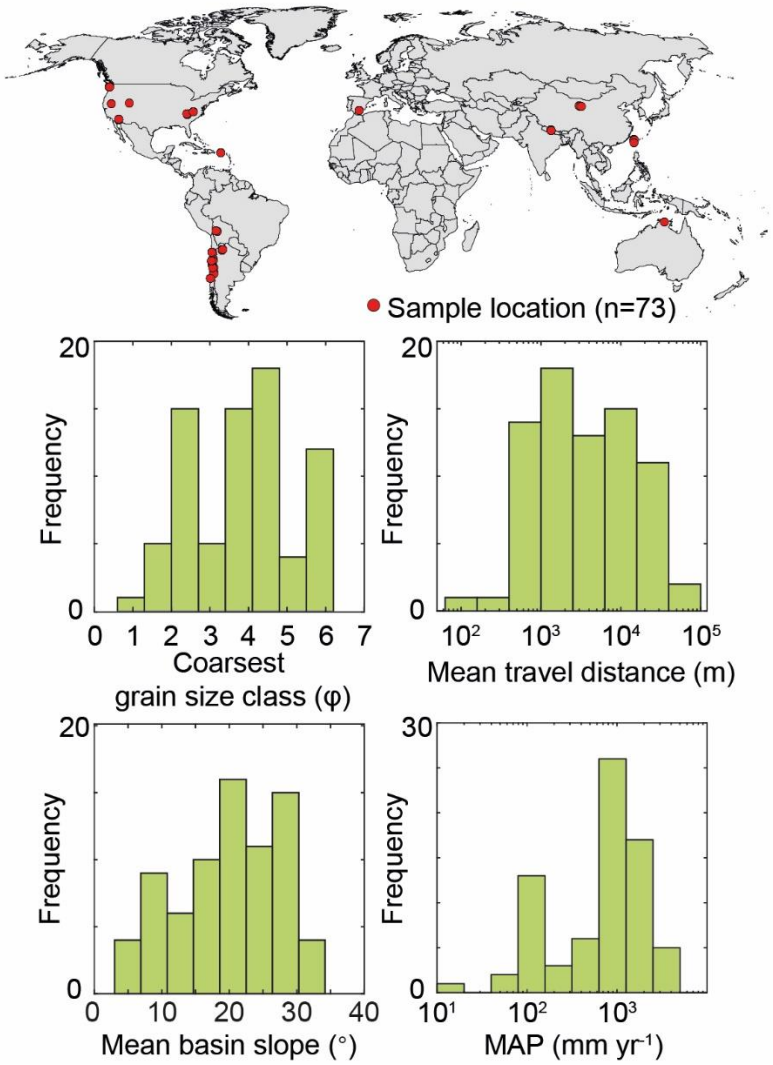

Figure 3.6: Sample locations and catchment attributes of all catchments in the global compilation (n=73). (A) Coarsest phi-grain size classes measured in each study (the smallest grain size was always a sand fraction (<2 mm)). (B) Mean travel distance of sediment, calculated as the arithmetic mean of each grid cell's travel distance towards the catchment outlet. (C) Mean basin slope of each catchment, calculated as the arithmetic mean of the hillslope angles at each grid cell. (D) Mean annual precipitation (MAP) in each catchment, derived from the Global Precipitation Climatology Centre (GPCC) dataset (Meyer-Christoffer et al., 2015).

Figure 3.7 shows the data of all catchments, classified in 4 slope classes and colour-coded by lithology. Each box represents the normalized ^{10}Be concentrations ± analytical uncertainties and the grain size range of a single sample. Uncertainties in ^{10}Be

concentrations tend to be larger for samples from steeper catchments (>10°), which may be related to higher denudation rates and therefore lower ^{10}Be concentrations. Generally, uncertainties are larger for low ^{10}Be/^{9}Be ratios. In catchments with mean basin hillslope angles <10°, ^{10}Be concentrations are relatively similar across all grain size classes. In steeper hillslope classes, coarse grains reveal lower ^{10}Be concentrations compared to fine grains, with the largest deviations in catchments with hillslope angles >25° (Figure 3.7). We discern no pattern related to lithology from this figure but we emphasize that magmatic catchments are more abundant in shallow sloping catchments, whereas metamorphic catchments are more abundant in steep catchments.

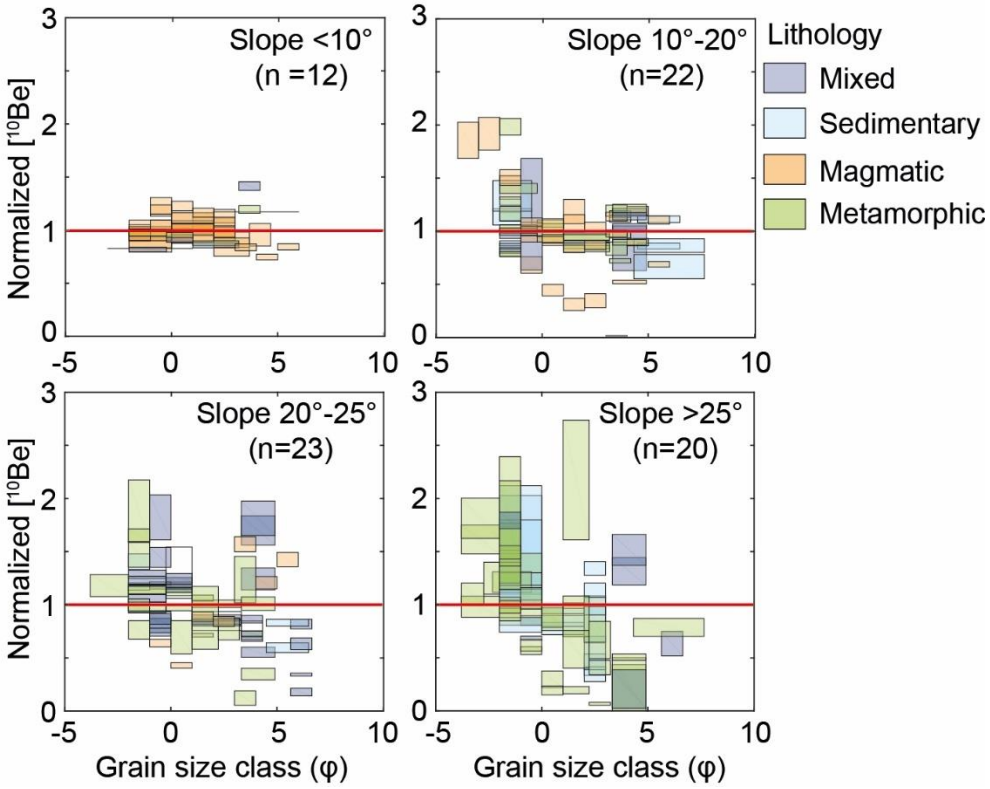

Figure 3.7: All global compilation samples divided into mean basin slope classes and colour-coded by lithology. The boxes indicate normalized mean ^{10}Be concentrations ± analytical errors and the phi-grain size range. The ^{10}Be concentrations are normalized by the arithmetic mean ^{10}Be concentration of all samples from the same catchment.

Figure 3.8 (and Figure S 3.4, for plots separated by lithology) shows the grain size dependencies of individual catchments, resulting from the slope of a linear fit to the ^{10}Be concentrations of all grain size classes (see methods section and Figure 3.4). Overall, we observe more sample sets that display significantly (i.e., error bar does not overlap with 0) negative (56.2%) trends in grain size-dependent ^{10}Be concentrations, than positive (32.8%; Figure 3.8). 11.0% of the sample sets have grain size dependencies that are not significantly different from zero, and thus reveal no grain size dependency. Furthermore, negative grain size dependencies are typically stronger (i.e., higher absolute differences between grain sizes) than positive grain size dependencies.

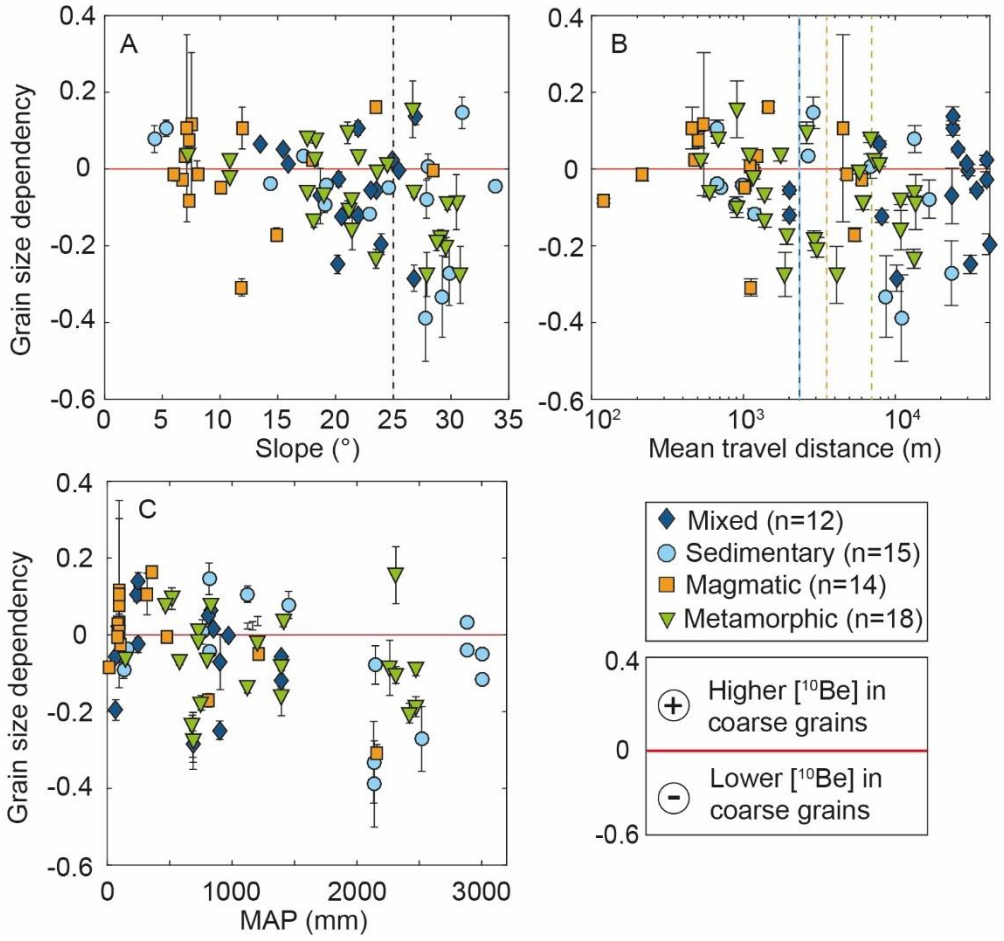

Figure 3.8: Grain size dependencies of all catchments in the global compilation (n=73), as a function of (A) mean basin slope, (B) mean travel distance and (C) mean annual precipitation (MAP). Coloured symbols depict lithological classes. Grain size dependencies are derived from the slope of a linear fit to the normalized ^{10}Be concentrations and grain sizes from a sample set, as described in Figure 3.4. Dashed lines indicate the threshold hillslope (Figure A) and abrasion thresholds (Figure B) mentioned in the text. Global compilation statistics are provided in in Table S4 and Figure S4 of the data supplement.

The calculated grain size dependencies reveal a significant breakpoint at a mean hillslope angle of ~15° (KS-test, Figure 3.8a). Catchments with mean hillslope angles <15° reveal a distribution with predominantly weak grain size dependencies. Steep catchments with hillslope angles >15° show a wider distribution with predominantly negative grain size dependencies (62.3% significantly negative). 70.0% of the catchments that exceed the threshold hillslope (>25°) have significantly negative grain size dependencies. Our analysis of sediment travel distance shows that the amount and magnitude of negative grain size dependencies slightly increase at longer sediment travel distances (Figure 3.8b). However, catchments that exceeded the abrasion threshold (sedimentary: 2300 m, magmatic: 3500 m, metamorphic: 7000 m, mixed: 2300-7000 m) show no significantly different grain size dependency distribution based on the KS-test. Finally, the data suggests a slightly increasing amount and magnitude of negative grain size dependencies with increasing MAP. Humid catchments (MAP >2000 mm yr^{-1}) reveal a distribution of predominantly (90%) significantly negative grain size dependencies, which is significantly different (KS-test) from catchments with MAP <2000 mm yr^{-1} (Figure 3.8c). However only a low number of catchments with MAP >2000 mm yr^{-1} compose the distribution. Catchments underlain by sedimentary and metamorphic rocks show the most significant negative grain size dependencies (66.7% and 65.4%, respectively), followed by catchments underlain by mixed lithologies (50.0%). The number of significantly negative grain size dependencies is lowest for catchments underlain by magmatic lithologies (37.5%). None of the lithologies revealed a significantly different grain size dependency distribution based on the KS-test.

Linear regressions of grain size dependencies as a function of mean basin slope revealed significantly negative trends for all lithologies combined ($p = 0.002$) and for metamorphic catchments ($p= 0.017$) but not for the other lithologies alone (Table S 3.2, Figure S 3.4). MAP showed a significantly negative relationship with grain size dependencies for all lithologies combined ($p= 0.007$), and for catchments underlain by magmatic ($p= 0.006$) lithology. However, the trend for magmatic catchments mainly results from one negative data point at higher MAP. No significant linear trends emerged between mean travel distance and grain size dependencies for any of the lithologies.

When considering the combined influence of mean basin slope, MAP and mean travel distance with a multivariate linear model, we found that the variance of all lithologies combined is significantly described ($p= 0.004$) by two out of all 3 factors, but that the explained variance is low ($R^2= 0.190$, Table S 3.3). Most of the variance is related to mean basin slope (relative importance, RI = 9.1%), followed by MAP (RI = 7.6%), whereas mean travel distance revealed no significant contribution (Table S 3.3, Figure 3.9). Furthermore, multivariate models yielded significant results when considering only magmatic ($p= 0.031$, $R^2= 0.552$) and metamorphic catchments ($p= 0.077$, $R^2= 0.276$). In magmatic catchments, a large proportion of the variability is ascribed to MAP (RI =

51.4%), which results from the above-mentioned negative data point at higher MAP. Finally, most of the variability in magmatic catchments was significantly described by mean basin slope (RI = 22.0%). Multivariate statistics yielded insignificant results for mixed and sedimentary lithologies, possibly due to too few catchments to disclose unambiguous trends.

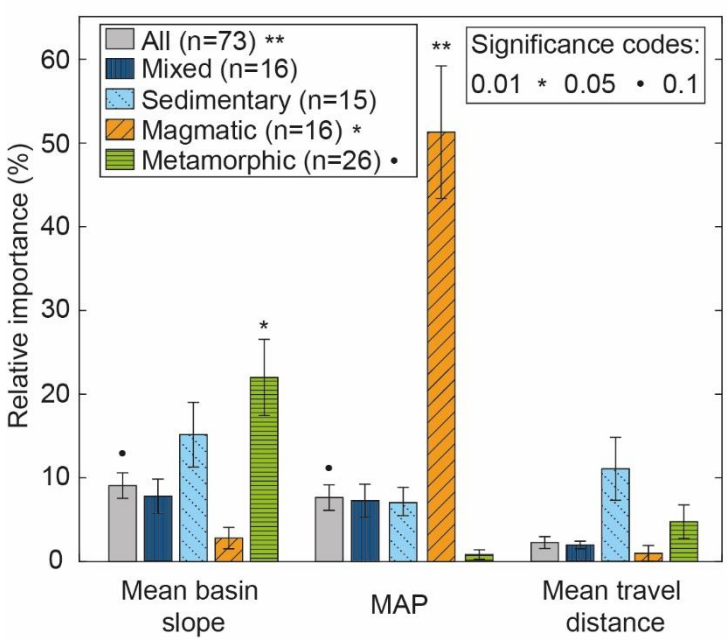

Figure 3.9: Relative importance of mean basin slope, MAP and mean travel distance to the multivariate linear regression R^2-value. Results are given for all lithologies combined (grey) and differentiated by lithology (colors). Multivariate linear regression results are provided in Table S 3.3.

3.6 Discussion

3.6.1 Grain size-dependent ^{10}Be concentrations in the Chilean Coastal Cordillera

The sampled catchments on the climatic gradient in the Chilean Coastal Cordillera only show a systematic trend of ^{10}Be concentrations with grain size in the arid (AZ) and Mediterranean catchments (LC). In both catchments, the ^{10}Be concentrations of river sediment correspond to concentrations measured in the subsurface of the soil profiles (Figure 3.10; Schaller et al., 2018). Because the difference between ^{10}Be production rates of the catchment on average and at the soil profiles is small (<10%), we can compare measured ^{10}Be concentrations directly. In the arid catchment (AZ), both the negative grain size dependencies and the fact that ^{10}Be concentrations correspond to concentrations at ~1 m depth in the soil profiles suggest that erosion processes (e.g.,

rock falls, landslides, gully head retreat), which excavate sediment from intermediate to greater depth during rare precipitation events or earthquakes (e.g., Mather et al., 2014; Pinto et al., 2008), may occur in this catchment. All of the measured ^{10}Be concentrations in river sediment in the Mediterranean catchment (LC) are considerably lower than the concentrations measured at the surface of soil profiles in close proximity of catchment (Figure 3.10; Schaller et al., 2018). This suggests that the catchment experiences faster erosion processes compared to the location of the soil pit, which is confirmed by debris flow scars observed at high elevation in the catchment (Figure S 3.5). Deep-seated erosion processes and insufficient mixing in a small-sized catchment may make a sample non-representative for the entire catchment (Niemi et al., 2005; Yanites et al., 2009). However, the noisy, but overall positive, grain size dependency in the Mediterranean catchment (LC) contradicts with this hypothesis, as debris flows would presumably excavate coarse grains from greater depth. Higher ^{10}Be production rates at the elevation where debris flows originate, and the condition that coarse grains only origin from that area cannot account for the positive grain size dependency alone. Without being able to clarify this issue, the lower ^{10}Be concentrations of river sediment, combined with the observed greater scatter in the positive grain size dependency may hint at selective transport and longer residence times of coarse grains at higher elevations.

The ^{10}Be concentrations in river sediment from the semi-arid (SG) and temperate (NA) catchments show little variations and are similar to concentrations measured near the surface in soil pits (Figure 3.10; Schaller et al., 2018). Within the temperate catchment (NA), the uniform ^{10}Be concentrations in grains <16 mm, suggests that these originate from the ~70 cm thick mixed soil layer, whereas the lower ^{10}Be concentrations in grains >16 mm suggests these may be derived from below the mixed layer (Figure 3.10; Schaller et al., 2018). In the semi-arid (SG) catchment, the measured samples from the channel show similar ^{10}Be concentrations compared to those measured in the mixed soil layer of the north-facing hillslope and higher ^{10}Be concentrations compared to the mixed layer of the south-facing hillslope (Figure 3.10; Schaller et al., 2018). This suggests that grains are unlikely to be derived from greater depth, where ^{10}Be concentrations are lower.

We propose that the existing or missing trends in the arid (AZ), semi-arid (SG) and temperate (NA) catchments are mainly related to differences in precipitation and the excavation depth of the erosion processes. These catchments show minor variations in mean basin slope, hence we do not expect big differences in erosion processes due to changes in slope alone. Furthermore, the limited relief of these catchments excludes differences in ^{10}Be production rates and local sediment sources to influence observed differences in ^{10}Be concentrations. However, steeper hillslope angles and higher total relief may have overruled the effect of precipitation in the La Campana catchment. We do not expect a control related to the different catchment sizes in any of the

catchments, because granitic rock have a low abrasion breakdown rate (Attal and Lavé, 2009) and the mean travel distances were small (<1 km).

In summary, we think our new samples from the Chilean Coastal Cordillera suggest an influence of MAP on grain size-dependent ^{10}Be concentrations only in the most-arid and most-humid catchments by its effect on the thickness of the mixed soil layer and the scouring depth of erosion processes that transport larger grains from below the mixed soil layer.

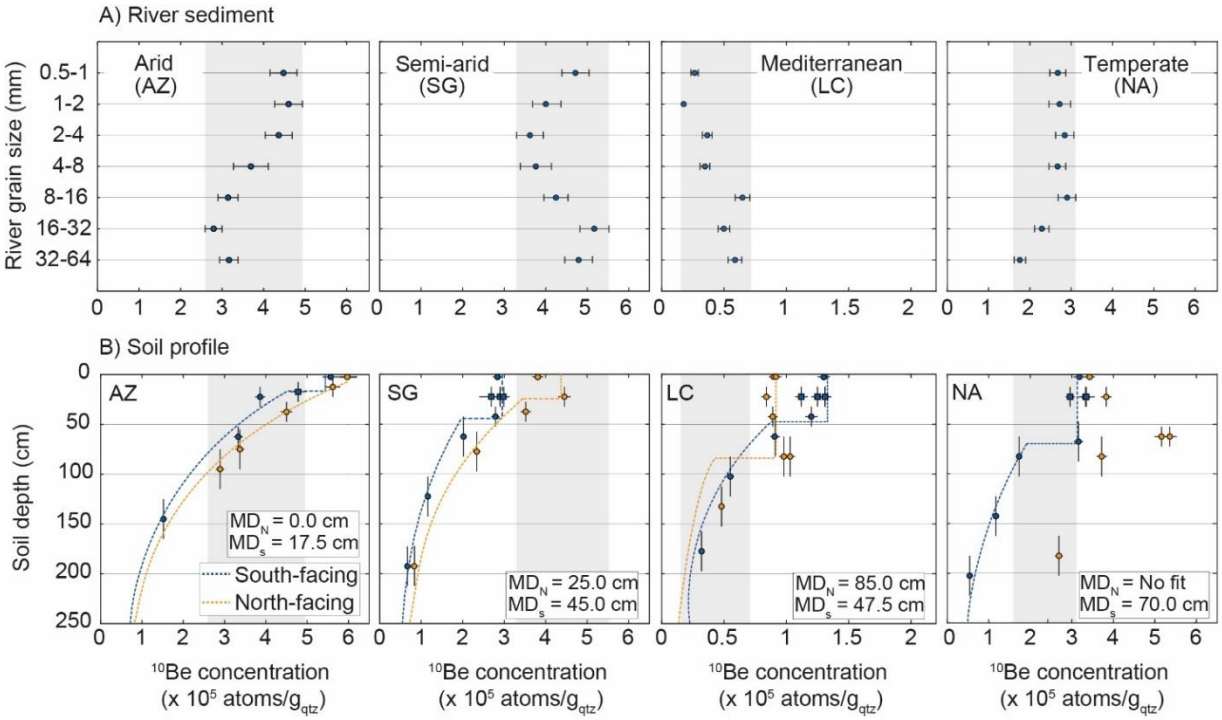

Figure 3.10: Comparison of ^{10}Be concentrations measured in (A) river sediment, and (B) North and South-facing soil profiles (Schaller et al., 2018) , from the same catchments in the Chilean Coastal Cordillera. MD_N and MD_S are the soil mixing depths of the North and South-facing hillslopes, respectively. Note the reduced x-axis range of the Mediterranean catchment (LC). Shaded areas show range of ^{10}Be concentrations in river sediment for comparison with soil profiles.

3.6.2 Grain size-dependent ^{10}Be concentrations in the global compilation

3.6.2.1 Mean basin slope

The effect of mean basin slope on grain size-dependent ^{10}Be concentrations is apparent as weak grain size dependencies in gently sloping catchments, and predominantly negative grain size trends in steep catchments (Figure 3.7, Figure 3.8a). Mean basin slope may control grain size-dependent ^{10}Be concentrations through its effect on the thickness of soils and the scouring depth of erosion processes. In gently-

sloping catchments, denudation rates are typically low (e.g., Portenga and Bierman, 2011) and well-mixed soil layers with uniform ^{10}Be concentrations can develop. Diffusive erosion processes transport sediment from near the surface, which results in uniform ^{10}Be concentrations. In contrast, in steep landscapes, denudation rates are usually high and soils are thin or absent if denudation rates exceed the soil production limit (~170 mm kyr^{-1}; Dixon and von Blanckenburg, 2012). Such catchments are typically dominated by deep-seated hillslope processes (Hovius et al., 1997). Negative grain size dependencies thus occur because coarse grains are excavated from greater depth, where ^{10}Be concentrations are lower. The highest percentage of negative grain size dependencies are found in catchments steeper than 25°. In these catchments, many hillslopes have likely reached the threshold hillslope angle of ~25-30°, at which denudation rates are dominated by the frequency of landslides (Larsen and Montgomery, 2012; Montgomery and Brandon, 2002; Ouimet et al., 2009). Linear regression models revealed a stronger control of mean basin slope on grain size-dependent ^{10}Be concentrations than MAP and mean travel distance, however the R^2-values of the regression models were low (Table S 3.3 and Figure 3.9). This conforms with previous studies that also found negative grain size dependencies which emerged from a transition of transport-limited to detachment-limited erosion processes and, therefore, deep-seated erosion processes (Binnie et al., 2007; Brown et al., 1995; Lukens et al., 2016; Reinhardt et al., 2007; Sosa Gonzalez et al., 2016a, 2016b; Tofelde et al., 2018). It is notable that the most-negative grain size dependencies occur in catchments underlain by sedimentary rocks (Table S 3.2 and Figure S 3.4). This may be due to lower rock mass strength of sedimentary rocks, which partly stems from the presence of bedding planes, making them more susceptible to hillslope failure (e.g., Clarke and Burbank, 2011; Perras and Diederichs, 2014).

3.6.2.2 Sediment travel distance

Our results revealed a weak negative control of sediment travel distance on grain size dependencies, however no significant relationships were found. The negative control is strongest for sedimentary catchments in which negative grain size dependencies appear to be more frequent in catchments with long sediment travel distances (Figure 3.8b). For sedimentary catchments the most negative grain size dependencies appear when travel distances exceeded the abrasion threshold. Possibly the lower rock strength of sedimentary rocks promotes the breakdown into smaller particles and increases the grain's sensitivity to abrasion (Attal and Lavé, 2009; Sklar and Dietrich, 2001). Due to abrasion, distant erosion sources may be overrepresented in finer grain size fractions, and underrepresented in coarser ones (Lukens et al., 2016). As travel distance scales with elevation (Figure S 3.6) and, therefore, ^{10}Be production rates, sediment from high elevations may have inherently higher nuclide concentrations (Lal, 1991). In contrast, coarse grains, which experienced less abrasion may origin from lower elevations, with lower ^{10}Be production rates. This elevation-dependence of

certain grain size fractions may induce a negative grain size-dependency. Secondly, if abrasion were to reduce river sediment of decimetre- or meter-scale to sand size, the centre of such clasts would have lower concentrations (Carretier and Regard, 2011; Lupker et al., 2017). However, the associated travel distance has to be considerably longer, and the initial clast must be large. For example, abrasion of an initial 25-cm sized granitic cobble over a distance of ~8 km would result in a size reduction of 10 cm and expose a centre with a ^{10}Be concentration that is only 8.5% lower compared to the outer layers (Balco et al., 2008; Sklar et al., 2006). The by-product of abrasion, which typically is of silt or clay size (Sklar et al., 2006), unlikely affects the measured ^{10}Be concentrations, as it is finer than the grain size classes typically analyzed (Lukens et al., 2016). We did not observe a control of sediment travel distance in catchments with mixed lithologies. The provenance of distinct grain sizes from different lithologies has not resulted in a dominantly positive or negative grain size dependency. Possibly, because the spatial arrangement of different lithologies in a landscape is not necessarily elevation-dependent, or because these lithologies yield minor differences in grain sizes.

3.6.2.3 Mean Annual Precipitation

The global compilation suggested an additional control of MAP on grain size-dependent ^{10}Be concentrations. The amount and magnitude of negative grain size trends seems to increase with increasing MAP. The highest percentage of negative grain size dependencies is found in humid catchments (>2000 mm yr^{-1}). However, this trend is related to a low total number of catchments. Negative grain size dependencies at higher MAP values could be related to higher denudation rates and increasing depth of erosion processes (e.g., precipitation-induced landslides; Chang et al., 2007; Chen et al., 2006; Lin et al., 2008). This differs from our interpretation of the results from the Chilean Coastal Cordillera, in which we emphasize the control of MAP on the thickness of the mixed soil layer. The discrepancy with the global compilation may result from the additional effect of hillslope angle, which also influences the thickness of the soil mantle and the depth of erosion processes (Heimsath et al., 2009).

3.7 Implications

Our results and the above discussion suggest that grain size trends in ^{10}Be concentrations are best explained by the effects of hillslope angle and MAP on the presence and thickness of mixed soil layers and the scouring depth of erosion processes. In large catchments, an additional effect may emerge by abrasion during transport, which could induce a non-representative grain size distribution. At present, however, it is difficult to quantify the relative roles of hillslope angle, precipitation, travel distance, and lithology, because these parameters tend to be partly correlated. For example, high and steep topography is often associated with high amounts of

orographic precipitation, and long travel distances are associated with high total relief (Figure S 3.6).

In any case, the presumed role that soils and different hillslope erosion processes play for grain size-dependent ^{10}Be concentrations is likely not linearly related to variables like mean hillslope angle or mean annual precipitation. Instead, our results are consistent with the presence of thresholds. Landslides likely become important when hillslope angles exceed a critical threshold (Burbank et al., 1996) and once precipitation is high enough to sustain vegetation and soils, diffusive processes may dominate gently-sloping and soil-mantled landscapes. Such a threshold control on the occurrence of grain size-dependent ^{10}Be concentrations may be the reason why our linear regression statistics, yielded mostly insignificant results or low R^2-values (Figure 3.9 and Table S 3.3). More data may allow better constraining the controls and relative importance of these factors in the future. It additionally highlights the importance of systematic studies on single factors, like our study on the sole effect of MAP in the Chilean Coastal Cordillera.

We evaluated the likelihood of grain size-dependent ^{10}Be concentrations and a potential bias in previously published ^{10}Be-derived catchment-average denudation rates, by comparing our findings with a recently published global compilation (Codilean et al., 2018). Out of 2537 different catchments with an area <5000 km², 55.7% have hillslope angles >15°, where our data first shows significant grain size effects, and 23.3% have hillslope angles >25°. When considering sediment travel distances, using the relationship between catchment area and sediment travel distance that emerged from our global compilation (R^2= 0.99; Figure S 3.6) about 61.9%, 49.8% and 29.2% of the catchments have exceeded the sediment travel distances of 2300 m, 3500 m and 7000 m, respectively. Finally, 11.5% of the catchments have MAP >2000 mm yr^{-1}, based on GPCC-derived MAP at the sample location. Therefore, previously published catchment-average denudation rates may more frequently be biased as a result of steep hillslopes and long sediment travel distance and less frequently by the influence of MAP. When considering a combined effect of all controlling factors in each catchment (slope >25°, sediment travel distance >7000 m and MAP >2000 mm yr^{-1}), 49.1% of the catchments are predicted to be devoid of grain size dependencies of ^{10}Be concentrations and biased catchment-average denudation rates, whereas 50.9% might contain a bias because one or more of the controlling factors has exceeded the threshold values that emerged from our study.

3.8 Conclusion

In this paper, we used a field study in Chile and a global compilation of previously published data to assess in what type of catchments grain size-dependent ^{10}Be concentrations may lead to biased estimates in catchment-average denudation rates. Our results suggest that mean basin slope and MAP control grain size-dependent ^{10}Be concentration through their effect on the presence and thickness of a mixed soil layer and the depth of erosion processes. Hillslope steepness appears to exert the most important influence on grain size-dependent ^{10}Be concentrations. Our global compilation results show that the influence of MAP is limited to humid catchments (>2000 mm yr^{-1}), whereas our case study in Chile suggests an additional control in arid catchments (<100 mm yr^{-1}). Furthermore, grain size-dependent ^{10}Be concentrations may occur in large catchments with long sediment travel distances (>2300 m to >7000 m, depending on lithology), where abrasion may induce non-representative grain size distributions, but this control is less apparent in the current data. We suggest that due to the presence of thresholds, catchment steepness, MAP and sediment travel distance are non-linearly related to grain size-dependent ^{10}Be concentrations, which complicates efforts to disentangle and quantify their relative roles. The results of our study can be used to evaluate whether catchment-average denudation rates may be biased in particular catchments.

3.9 Author contributions

R. van Dongen carried out fieldwork, laboratory work, and data evaluation. D. Scherler conceived the study and was the main advisor during fieldwork, data evaluation, and manuscript writing. H. Wittmann was responsible for the cosmogenic-^{10}Be laboratory training and laboratory supervision. F. von Blanckenburg and H. Wittmann were available for extensive discussion during data evaluation. R. van Dongen prepared the manuscript with contributions and edits from all co-authors.

3.10 Acknowledgements

We acknowledge support from the German Science Foundation (DFG) priority research program SPP-1803 "EarthShape: Earth Surface Shaping by Biota" (grant SCHE 1676/4-1 to D.S.). We are grateful to the Chilean National Park Service (CONAF) for providing access to the sample locations and on-site support of our research. We also thank L. Mao, R. Carrillo and M. Koelewijn for their support during fieldwork, S. Binnie and S. Heinze from Cologne University for conducting AMS measurements, and M. Henehan for his help with statistical analysis. We thank A. Schmidt, S. Tofelde and 2 anonymous reviewers for their constructive reviews.

3.11 Supplementary tables

Table S 3.1: Global compilation of ^{10}Be-concentrations in different grain size classes.

First Author	Year	Official sample name	Latitude (°N)	Longitude (°E)	[^{10}Be] (atoms g^{-1})	1σ-[^{10}Be] (atoms g^{-1})	Min Grain size (mm)	Max Grain size (mm)	Mean basin slope (°)	MAP (mm yr^{-1})	Lithology	Travel distance (m)	Catchment area (km^2)
Aguilar	2014	Transito	-28.990	-70.280	4.80E+05	1.36E+04	0.5	1	24.05	63.80	Mixed[a]	34117.33	3417.45
Aguilar	2014	Transito	-28.990	-70.280	3.32E+05	1.78E+04	50	100	24.05	63.80	Mixed[a]	34117.33	3417.45
Aguilar	2014	Carmen	-28.800	-70.460	8.33E+05	5.35E+04	0.5	1	24.77	69.14	Mixed[a]	41366.77	3290.45
Aguilar	2014	Carmen	-28.800	-70.460	3.19E+05	2.66E+04	10	30	24.77	69.14	Mixed[a]	41366.77	3290.45
Belmont	2007	Upper EFMC	47.687	-124.242	2.16E+04	7.45E+02	0.25	0.5	19.41	2882.30	Sedimentary	972.14	3.59
Belmont	2007	Upper EFMC	47.687	-124.242	1.63E+04	5.25E+02	22.6	90	19.41	2882.30	Sedimentary	972.14	3.59
Belmont	2007	Lower EFMC	47.658	-124.243	2.75E+04	7.45E+02	0.25	0.5	17.75	2882.30	Sedimentary	2650.95	14.30
Belmont	2007	Lower EFMC	47.658	-124.243	3.45E+04	9.40E+02	22.6	90	17.75	2882.30	Sedimentary	2650.95	14.30
Belmont	2007	Upper WC	47.740	-124.046	2.98E+04	8.80E+02	0.25	0.5	25.44	3008.40	Sedimentary	712.26	2.06
Belmont	2007	Upper WC	47.740	-124.046	2.11E+04	8.15E+02	22.6	90	25.44	3008.40	Sedimentary	712.26	2.06
Belmont	2007	Lower WC	47.730	-124.038	2.23E+04	1.16E+03	0.25	0.5	24.01	3008.40	Sedimentary	1177.90	4.92
Belmont	2007	Lower WC	47.730	-124.038	9.46E+03	7.35E+02	22.6	90	24.01	3008.40	Sedimentary	1177.90	4.92
Brown	1995	ICA	18.252	-65.786	4.06E+04	7.80E+03	4	8	13.84	2159.60	Magmatic	1121.09	7.02
Brown	1995	ICA	18.252	-65.786	3.66E+04	6.80E+03	2	4	13.84	2159.60	Magmatic	1121.09	7.02
Brown	1995	ICA	18.252	-65.786	5.24E+04	6.40E+03	1	2	13.84	2159.60	Magmatic	1121.09	7.02
Brown	1995	ICA	18.252	-65.786	8.03E+04	9.10E+03	0.5	1	13.84	2159.60	Magmatic	1121.09	7.02
Brown	1995	ICA	18.252	-65.786	1.69E+05	1.64E+04	0.25	0.5	13.84	2159.60	Magmatic	1121.09	7.02
Brown	1995	ICA	18.252	-65.786	2.26E+05	1.81E+04	0.125	0.25	13.84	2159.60	Magmatic	1121.09	7.02

First Author	Year	Official sample name	Latitude (°N)	Longitude (°E)	[^{10}Be] (atoms g^{-1})	1σ-[^{10}Be] (atoms g^{-1})	Min Grain size (mm)	Max Grain size (mm)	Mean basin slope (°)	MAP (mm yr^{-1})	Lithology	Travel distance (m)	Catchment area (km^2)
Brown	1995	ICA	18.252	-65.786	2.18E+05	2.01E+04	0.063	0.125	13.84	2159.60	Magmatic	1121.09	7.02
Carretier	2015	ELK1-5	-29.848	-70.494	1.77E+05	2.30E+04	0.5	1	25.77	88.04	Mixed[a]	39751.03	3324.72
Carretier	2015	ELK1-5	-29.848	-70.494	1.87E+05	1.70E+04	0.5	1	25.77	88.04	Mixed[a]	39751.03	3324.72
Carretier	2015	ELK1-5	-29.848	-70.494	1.38E+05	1.20E+04	50	100	25.77	88.04	Mixed[a]	39751.03	3324.72
Carretier	2015	ELK1-5	-29.848	-70.494	3.71E+05	3.00E+04	10	30	25.77	88.04	Mixed[a]	39751.03	3324.72
Carretier	2015	ILL1-3	-31.600	-71.113	4.69E+05	1.30E+04	0.5	1	22.77	236.60	Mixed[a]	24053.62	1363.74
Carretier	2015	ILL1-3	-31.600	-71.113	7.68E+05	6.40E+04	10	30	22.77	236.60	Mixed[a]	24053.62	1363.74
Carretier	2015	CHO1-3	-31.692	-71.268	1.96E+05	6.70E+03	0.5	1	21.16	246.68	Mixed[a]	40290.21	4129.30
Carretier	2015	CHO1-3	-31.692	-71.268	7.95E+04	3.10E+03	50	100	21.16	246.68	Mixed[a]	40290.21	4129.30
Carretier	2015	CHO1-3	-31.692	-71.268	4.21E+05	3.80E+04	10	30	21.16	246.68	Mixed[a]	40290.21	4129.30
Carretier	2015	ACO1-3	-32.835	-70.545	1.01E+05	2.90E+03	0.5	1	27.53	248.10	Mixed[a]	23826.16	2515.76
Carretier	2015	ACO1-3	-32.835	-70.545	1.94E+05	1.90E+04	10	30	27.53	248.10	Mixed[a]	23826.16	2515.76
Carretier	2015	TIN1-3	-34.677	-70.871	9.94E+04	5.30E+03	0.5	1	26.42	967.95	Mixed[a]	30354.61	1699.45
Carretier	2015	TIN1-3	-34.677	-70.871	1.77E+05	1.70E+04	10	30	26.42	967.95	Mixed[a]	30354.61	1699.45
Carretier	2015	TIN1-3	-34.677	-70.871	7.39E+04	1.35E+04	50	100	26.42	967.95	Mixed[a]	30354.61	1699.45
Carretier	2015	LON1-2	-35.184	-71.116	6.44E+04	2.91E+04	0.5	1	19.56	905.21	Mixed[a]	23700.45	1965.70
Carretier	2015	LON1-2	-35.184	-71.116	4.66E+04	1.17E+04	10	30	19.56	905.21	Mixed[a]	23700.45	1965.70
Carretier	2015	MAU1-3	-35.727	-71.021	1.29E+05	1.50E+04	0.5	1	20.99	900.01	Mixed[a]	31146.17	2983.92
Carretier	2015	MAU1-3	-35.727	-71.021	1.26E+04	2.50E+03	50	100	20.99	900.01	Mixed[a]	31146.17	2983.92
Clapp	2002	YGP 2	33.040	-114.522	1.11E+05	9.00E+03	0.25	0.5	8.32	106.44	Magmatic	6017.34	189.61
Clapp	2002	YGP 2	33.040	-114.522	1.39E+05	1.00E+04	0.5	1	8.32	106.44	Magmatic	6017.34	189.61
Clapp	2002	YGP 2	33.040	-114.522	1.08E+05	8.00E+03	1	2	8.32	106.44	Magmatic	6017.34	189.61
Clapp	2002	YGP 2	33.040	-114.522	1.18E+05	1.00E+04	2	4	8.32	106.44	Magmatic	6017.34	189.61

First Author	Year	Official sample name	Latitude (°N)	Longitude (°E)	[^{10}Be] (atoms g^{-1})	1σ-[^{10}Be] (atoms g^{-1})	Min Grain size (mm)	Max Grain size (mm)	Mean basin slope (°)	MAP (mm yr^{-1})	Lithology	Travel distance (m)	Catchment area (km^2)
Clapp	2002	YGP 2	33.040	-114.522	9.90E+04	1.30E+04	4	12.7	8.32	106.44	Magmatic	6017.34	189.61
Clapp	2002	YGP 2	33.040	-114.522	1.09E+05	1.20E+04	12.7	25.4	8.32	106.44	Magmatic	6017.34	189.61
Clapp	2002	YGP 4	33.089	-114.531	1.15E+05	1.10E+04	0.25	1	8.66	95.16	Magmatic	4523.64	40.74
Clapp	2002	YGP 4	33.089	-114.531	1.34E+05	1.10E+04	1	4	8.66	95.16	Magmatic	4523.64	40.74
Clapp	2002	YGP 11	33.076	-114.572	1.51E+05	7.00E+03	1	4	13.17	95.16	Magmatic	547.51	1.60
Clapp	2002	YGP 11	33.076	-114.572	1.70E+05	9.00E+03	4	8	13.17	95.16	Magmatic	547.51	1.60
Clapp	2002	YGP 12	33.076	-114.572	1.39E+05	1.00E+04	0.25	1	8.87	95.16	Magmatic	215.14	0.28
Clapp	2002	YGP 12	33.076	-114.572	1.38E+05	7.00E+03	1	4	8.87	95.16	Magmatic	215.14	0.28
Clapp	2002	YGP 12	33.076	-114.572	1.32E+05	9.00E+03	4	8	8.87	95.16	Magmatic	215.14	0.28
Clapp	2002	YGP 13	33.077	-114.570	1.36E+05	1.10E+04	0.25	1	9.34	95.16	Magmatic	505.68	2.15
Clapp	2002	YGP 13	33.077	-114.570	1.58E+05	8.00E+03	1	4	9.34	95.16	Magmatic	505.68	2.15
Clapp	2002	YGP 13	33.077	-114.570	1.78E+05	1.00E+04	4	8	9.34	95.16	Magmatic	505.68	2.15
Clapp	2002	YGP 14	33.086	-114.558	1.20E+05	8.00E+03	0.25	1	9.98	95.16	Magmatic	1127.38	3.34
Clapp	2002	YGP 14	33.086	-114.558	1.30E+05	5.00E+03	1	4	9.98	95.16	Magmatic	1127.38	3.34
Clapp	2002	YGP 14	33.086	-114.558	1.22E+05	6.00E+03	4	8	9.98	95.16	Magmatic	1127.38	3.34
Clapp	2002	YGP 15	33.082	-114.535	1.20E+05	7.00E+03	0.25	1	9.08	95.16	Magmatic	1220.81	4.39
Clapp	2002	YGP 15	33.082	-114.535	1.22E+05	1.10E+04	1	4	9.08	95.16	Magmatic	1220.81	4.39
Clapp	2002	YGP 15	33.082	-114.535	1.35E+05	6.00E+03	4	8	9.08	95.16	Magmatic	1220.81	4.39
Clapp	2002	YGP 19	33.155	-114.516	1.77E+05	1.00E+04	0.25	0.5	9.04	106.44	Magmatic	4776.46	60.75
Clapp	2002	YGP 19	33.155	-114.516	1.93E+05	9.00E+03	0.5	1	9.04	106.44	Magmatic	4776.46	60.75
Clapp	2002	YGP 19	33.155	-114.516	2.06E+05	9.00E+03	1	4	9.04	106.44	Magmatic	4776.46	60.75
Clapp	2002	YGP 19	33.155	-114.516	1.63E+05	8.00E+03	4	12.7	9.04	106.44	Magmatic	4776.46	60.75
Derrieux	2014	Ta-3	24.320	121.280	1.09E+04	3.25E+03	0.25	1	30.60	2134.40	Sedimentary	8706.79	185.34

First Author	Year	Official sample name	Latitude (°N)	Longitude (°E)	[^{10}Be] (atoms g^{-1})	1σ-[^{10}Be] (atoms g^{-1})	Min Grain size (mm)	Max Grain size (mm)	Mean basin slope (°)	MAP (mm yr^{-1})	Lithology	Travel distance (m)	Catchment area (km^2)
Derrieux	2014	Ta-3	24.320	121.280	3.05E+03	7.10E+02	4	8	30.60	2134.40	Sedimentary	8706.79	185.34
Derrieux	2014	Ta-4	24.300	121.260	1.18E+04	3.33E+03	0.25	1	29.55	2139.30	Sedimentary	10980.83	299.53
Derrieux	2014	Ta-4	24.300	121.260	2.47E+03	5.00E+02	4	8	29.55	2139.30	Sedimentary	10980.83	299.53
Derrieux	2014	Cho-3	23.790	121.000	3.12E+03	7.40E+02	0.25	1	31.31	2518.90	Sedimentary	23431.84	1795.06
Derrieux	2014	Cho-3	23.790	121.000	1.17E+03	3.40E+02	4	8	31.31	2518.90	Sedimentary	23431.84	1795.06
Derrieux	2014	Mu-2	23.960	121.490	2.48E+03	7.30E+02	0.25	1	31.76	2263.00	Metamorphic	13631.11	502.64
Derrieux	2014	Mu-2	23.960	121.490	1.85E+03	4.60E+02	4	8	31.76	2263.00	Metamorphic	13631.11	502.64
Derrieux	2014	Lu0808	22.900	121.080	3.70E+03	5.50E+02	0.25	1	29.29	2147.90	Sedimentary	16699.73	549.71
Derrieux	2014	Lu0808	22.900	121.080	2.83E+03	7.10E+02	4	8	29.29	2147.90	Sedimentary	16699.73	549.71
Derrieux	2014	Lu0808	22.870	121.040	2.73E+03	5.80E+02	0.25	1	29.29	2147.90	Sedimentary	16699.73	549.71
Granger	1996	B-2	40.095	-120.065	3.00E+05	1.00E+04	0.5	1	14.27	319.76	Magmatic	460.53	0.88
Granger	1996	B-2	40.095	-120.065	3.00E+05	2.00E+04	1	2	14.27	319.76	Magmatic	460.53	0.88
Granger	1996	B-2	40.095	-120.065	3.70E+05	5.00E+04	2	4	14.27	319.76	Magmatic	460.53	0.88
Heimsath	2009	TC	-12.453	133.270	2.60E+05	4.00E-02	0.125	2	5.26	1452.70	Sedimentary	13451.52	391.31
Heimsath	2009	TC	-12.453	133.270	3.69E+05	4.70E-02	4	64	5.26	1452.70	Sedimentary	13451.52	391.31
Matmon	2003	GSCO-1	35.504	-83.301	2.64E+05	1.00E+04	0.25	0.85	21.39	1395.40	Metamorphic	10903.36	365.09
Matmon	2003	GSCO-1	35.504	-83.301	2.66E+05	7.00E+03	0.85	2	21.39	1395.40	Metamorphic	10903.36	365.09
Matmon	2003	GSCO-1	35.504	-83.301	1.65E+05	4.00E+03	2	4	21.39	1395.40	Metamorphic	10903.36	365.09
Matmon	2003	GSCO-1A	35.504	-83.301	2.95E+05	9.00E+03	0.25	0.85	21.39	1395.40	Metamorphic	10903.36	365.09
Matmon	2003	GSCO-1A	35.504	-83.301	2.92E+05	1.00E+04	0.85	2	21.39	1395.40	Metamorphic	10903.36	365.09
Matmon	2003	GSCO-1A	35.504	-83.301	2.62E+05	9.00E+03	2	10	21.39	1395.40	Metamorphic	10903.36	365.09
Matmon	2003	GSCO-1A	35.504	-83.301	1.89E+05	6.00E+03	10	20	21.39	1395.40	Metamorphic	10903.36	365.09
Matmon	2003	GSCO-7	35.600	-83.413	2.78E+05	7.00E+03	0.25	0.85	21.43	1408.90	Metamorphic	1746.52	2.75

First Author	Year	Official sample name	Latitude (°N)	Longitude (°E)	[^{10}Be] (atoms g^{-1})	1σ-[^{10}Be] (atoms g^{-1})	Min Grain size (mm)	Max Grain size (mm)	Mean basin slope (°)	MAP (mm yr^{-1})	Lithology	Travel distance (m)	Catchment area (km^2)
Matmon	2003	GSCO-7	35.600	-83.413	2.78E+05	7.00E+03	0.85	2	21.43	1408.90	Metamorphic	1746.52	2.75
Matmon	2003	GSCO-7	35.600	-83.413	3.05E+05	8.00E+03	2	4	21.43	1408.90	Metamorphic	1746.52	2.75
Matmon	2003	GSLR-2	35.598	-83.515	2.56E+05	8.00E+03	0.25	0.85	21.43	1391.00	Mixed[a]	1746.52	8.66
Matmon	2003	GSLR-2	35.598	-83.515	2.30E+05	8.00E+03	0.85	2	21.43	1391.00	Mixed[a]	1746.52	8.66
Matmon	2003	GSLR-2	35.598	-83.515	1.65E+05	6.00E+03	2	10	21.43	1391.00	Mixed[a]	1746.52	8.66
Matmon	2003	GSLR-2	35.598	-83.515	1.45E+05	5.00E+03	10	20	21.43	1391.00	Mixed[a]	1746.52	8.66
Matmon	2003	GSLR-3	35.598	-83.516	1.78E+05	6.00E+03	0.25	0.85	22.66	1391.00	Mixed[a]	1995.53	16.58
Matmon	2003	GSLR-3	35.598	-83.516	2.02E+05	9.00E+03	0.85	2	22.66	1391.00	Mixed[a]	1995.53	16.58
Matmon	2003	GSLR-3	35.598	-83.516	1.47E+05	5.00E+03	2	10	22.66	1391.00	Mixed[a]	1995.53	16.58
Matmon	2003	GSLR-3	35.598	-83.516	1.45E+05	6.00E+03	10	20	22.66	1391.00	Mixed[a]	1995.53	16.58
Matmon	2003	GSLR-7	35.663	-83.593	2.40E+05	8.00E+03	0.25	0.85	19.71	1391.00	Mixed[a]	8154.97	109.58
Matmon	2003	GSLR-7	35.663	-83.593	2.45E+05	8.00E+03	0.85	2	19.71	1391.00	Mixed[a]	8154.97	109.58
Matmon	2003	GSLR-7	35.663	-83.593	1.65E+05	5.00E+03	2	10	19.71	1391.00	Mixed[a]	8154.97	109.58
Matmon	2003	GSLR-7	35.663	-83.593	1.32E+05	4.00E+03	10	20	19.71	1391.00	Mixed[a]	8154.97	109.58
Palumbo	2010	Y2	39.210	99.614	1.02E+05	7.50E+03	20	200	17.70	153.48	Sedimentary	674.01	1.35
Palumbo	2010	Y2	39.210	99.614	1.34E+05	9.00E+03	0.2	0.71	17.70	153.48	Sedimentary	674.01	1.35
Palumbo	2010	Y10	39.046	100.021	7.00E+04	7.50E+03	0.2	0.71	20.49	131.07	Sedimentary	898.05	3.14
Palumbo	2010	Y10	39.046	100.021	3.50E+04	6.00E+03	20	200	20.49	131.07	Sedimentary	898.05	3.14
Palumbo	2010	L7	39.046	100.649	1.08E+05	8.50E+03	0.2	0.71	30.23	145.87	Metamorphic	593.71	1.24
Palumbo	2010	L7	39.046	100.649	7.00E+04	7.50E+03	20	200	30.23	145.87	Metamorphic	593.71	1.24
Puchol	2014	CA-950	28.376	84.289	2.61E+04	2.20E+03	0.072	0.25	29.78	2420.46	Metamorphic	3075.50	32.52
Puchol	2014	CA-950	28.376	84.289	2.65E+04	2.10E+03	0.25	0.5	29.78	2420.46	Metamorphic	3075.50	32.52
Puchol	2014	CA-950	28.376	84.289	9.20E+03	6.00E+02	0.5	1	29.78	2420.46	Metamorphic	3075.50	32.52

First Author	Year	Official sample name	Latitude (°N)	Longitude (°E)	[^{10}Be] (atoms g^{-1})	1σ-[^{10}Be] (atoms g^{-1})	Min Grain size (mm)	Max Grain size (mm)	Mean basin slope (°)	MAP (mm yr^{-1})	Lithology	Travel distance (m)	Catchment area (km^2)
Puchol	2014	CA-950	28.376	84.289	1.42E+04	1.50E+03	1	2	29.78	2420.46	Metamorphic	3075.50	32.52
Puchol	2014	CA-950	28.376	84.289	1.44E+04	3.10E+03	2	4.7	29.78	2420.46	Metamorphic	3075.50	32.52
Puchol	2014	CA-950	28.376	84.289	6.60E+03	1.10E+03	4.7	9.4	29.78	2420.46	Metamorphic	3075.50	32.52
Puchol	2014	CA-948	28.375	84.289	8.90E+03	9.00E+02	0.075	0.25	27.58	2312.50	Metamorphic	906.08	2.50
Puchol	2014	CA-948	28.375	84.289	8.40E+03	7.00E+02	0.25	0.5	27.58	2312.50	Metamorphic	906.08	2.50
Puchol	2014	CA-948	28.375	84.289	5.60E+03	5.00E+02	0.5	1	27.58	2312.50	Metamorphic	906.08	2.50
Puchol	2014	CA-948	28.375	84.289	2.70E+03	7.00E+02	1	2	27.58	2312.50	Metamorphic	906.08	2.50
Puchol	2014	CA-948	28.375	84.289	1.97E+04	5.10E+03	2	4.7	27.58	2312.50	Metamorphic	906.08	2.50
Puchol	2014	CA-953	28.372	84.294	1.36E+04	1.20E+03	0.075	0.25	20.75	2312.50	Metamorphic	907.21	2.70
Puchol	2014	CA-953	28.372	84.294	1.70E+04	1.40E+03	0.25	0.5	20.75	2312.50	Metamorphic	907.21	2.70
Puchol	2014	CA-953	28.372	84.294	8.00E+03	1.80E+03	1	2	20.75	2312.50	Metamorphic	907.21	2.70
Puchol	2014	CA-953	28.372	84.294	1.01E+04	3.40E+03	2	4.7	20.75	2312.50	Metamorphic	907.21	2.70
Puchol	2014	CA-953	28.372	84.294	8.90E+03	1.20E+03	4.7	9.4	20.75	2312.50	Metamorphic	907.21	2.70
Puchol	2014	CA-957	28.371	84.296	1.44E+04	1.50E+03	0.075	0.25	28.94	2473.00	Metamorphic	2919.75	38.72
Puchol	2014	CA-957	28.371	84.296	7.90E+03	6.00E+02	0.25	0.5	28.94	2473.00	Metamorphic	2919.75	38.72
Puchol	2014	CA-957	28.371	84.296	8.40E+03	8.00E+02	0.5	1	28.94	2473.00	Metamorphic	2919.75	38.72
Puchol	2014	CA-957	28.371	84.296	7.00E+03	1.00E+03	1	2	28.94	2473.00	Metamorphic	2919.75	38.72
Puchol	2014	CA-957	28.371	84.296	4.60E+03	1.40E+03	2	4.7	28.94	2473.00	Metamorphic	2919.75	38.72
Puchol	2014	CA-957	28.371	84.296	5.30E+03	1.40E+03	4.7	9.4	28.94	2473.00	Metamorphic	2919.75	38.72
Puchol	2014	CA-964	28.306	84.330	1.90E+04	1.80E+03	0.075	0.15	29.55	2473.00	Metamorphic	6100.94	138.54
Puchol	2014	CA-964	28.306	84.330	2.16E+04	2.60E+03	0.15	0.25	29.55	2473.00	Metamorphic	6100.94	138.54
Puchol	2014	CA-964	28.306	84.330	2.25E+04	1.70E+03	0.25	0.5	29.55	2473.00	Metamorphic	6100.94	138.54
Puchol	2014	CA-964	28.306	84.330	1.13E+04	2.50E+03	1	2	29.55	2473.00	Metamorphic	6100.94	138.54

First Author	Year	Official sample name	Latitude (°N)	Longitude (°E)	[^{10}Be] (atoms g^{-1})	1σ-[^{10}Be] (atoms g^{-1})	Min Grain size (mm)	Max Grain size (mm)	Mean basin slope (°)	MAP (mm yr^{-1})	Lithology	Travel distance (m)	Catchment area (km^2)
Puchol	2014	CA-964	28.306	84.330	1.97E+04	3.40E+03	2	4.7	29.55	2473.00	Metamorphic	6100.94	138.54
Puchol	2014	CA-964	28.306	84.330	9.60E+03	2.00E+03	4.7	9.4	29.55	2473.00	Metamorphic	6100.94	138.54
Reinhardt	2007	MRS3	36.998	-3.497	2.11E+05	1.05E+04	0.25	0.5	18.94	468.09	Metamorphic	678.63	1.35
Reinhardt	2007	MRS3	36.998	-3.497	3.12E+05	1.40E+04	8	16	18.94	468.09	Metamorphic	678.63	1.35
Reinhardt	2007	MRS17	36.998	-3.497	1.70E+04	1.00E+03	0.25	0.5	18.81	578.24	Metamorphic	1371.00	3.38
Reinhardt	2007	MRS17	36.998	-3.497	1.22E+04	9.00E+02	8	16	18.81	578.24	Metamorphic	1371.00	3.38
Reinhardt	2007	MRS21B	36.998	-3.497	1.05E+04	1.20E+03	0.25	0.5	21.40	516.74	Metamorphic	2603.48	18.62
Reinhardt	2007	MRS21B	36.998	-3.497	1.70E+04	3.00E+03	8	16	21.40	516.74	Metamorphic	2603.48	18.62
Safran	2005	Bol-34	-16.801	-67.213	5.71E+04	5.00E+03	0.25	1	28.12	761.46	Sedimentary	6865.98	208.11
Safran	2005	Bol-34	-16.801	-67.213	4.07E+04	3.00E+03	1	4	28.12	761.46	Sedimentary	6865.98	208.11
Safran	2005	Bol-34	-16.801	-67.213	5.96E+04	3.50E+03	4	8	28.12	761.46	Sedimentary	6865.98	208.11
Safran	2005	Bol-35b	-16.779	-67.222	1.03E+05	4.80E+03	0.25	1	35.29	819.50	Sedimentary	1017.25	4.18
Safran	2005	Bol35b	-16.779	-67.222	8.97E+04	4.00E+03	1	4	35.29	819.50	Sedimentary	1017.25	4.18
Safran	2005	Bol35b	-16.779	-67.222	8.83E+04	3.80E+03	4	8	35.29	819.50	Sedimentary	1017.25	4.18
Safran	2005	Bol46	-16.357	-67.809	6.42E+04	5.50E+03	0.25	1	30.91	815.99	Sedimentary	2886.08	28.05
Safran	2005	Bol46	-16.357	-67.809	6.70E+04	4.10E+03	1	4	30.91	815.99	Sedimentary	2886.08	28.05
Safran	2005	Bol46	-16.357	-67.809	1.06E+05	5.10E+03	4	8	30.91	815.99	Sedimentary	2886.08	28.05
Stock	2009	RM creek	40.540	-111.800	1.20E+05	3.10E+03	0.25	0.5	29.52	475.84	Magmatic	1169.72	1.78
Stock	2009	RM creek	40.540	-111.800	1.18E+05	3.10E+03	2	4	29.52	475.84	Magmatic	1169.72	1.78
Sullivan	2007	CS-01A	36.618	-80.778	6.44E+05	1.70E+04	0.25	0.85	6.26	1124.20	Sedimentary	671.44	2.03
Sullivan	2007	CS-01B	36.618	-80.778	7.16E+05	2.00E+04	0.85	2	6.26	1124.20	Sedimentary	671.44	2.03
Sullivan	2007	CS-01C	36.618	-80.778	6.75E+05	1.90E+04	2	9	6.26	1124.20	Sedimentary	671.44	2.03
Sullivan	2007	CS-01D	36.618	-80.778	1.11E+06	3.20E+04	9	18	6.26	1124.20	Sedimentary	671.44	2.03

First Author	Year	Official sample name	Latitude (°N)	Longitude (°E)	[^{10}Be] (atoms g^{-1})	1σ-[^{10}Be] (atoms g^{-1})	Min Grain size (mm)	Max Grain size (mm)	Mean basin slope (°)	MAP (mm yr^{-1})	Lithology	Travel distance (m)	Catchment area (km^2)
Sullivan	2007	CS-02A	36.446	-80.848	5.11E+05	1.60E+04	0.25	0.85	7.93	1205.70	Metamorphic	1087.43	3.18
Sullivan	2007	CS-02B	36.446	-80.848	5.00E+05	1.30E+04	0.85	2	7.93	1205.70	Metamorphic	1087.43	3.18
Sullivan	2007	CS-02C	36.446	-80.848	4.60E+05	1.20E+04	2	9	7.93	1205.70	Metamorphic	1087.43	3.18
Sullivan	2007	CS-02D	36.446	-80.848	6.26E+05	1.90E+04	9	18	7.93	1205.70	Metamorphic	1087.43	3.18
Sullivan	2007	CS-03A	36.466	-80.834	3.73E+05	1.20E+04	0.25	0.85	11.57	1164.90	Metamorphic	7293.54	93.56
Sullivan	2007	CS-03B	36.466	-80.834	3.68E+05	1.20E+04	0.85	2	11.57	1164.90	Metamorphic	7293.54	93.56
Sullivan	2007	CS-03C	36.466	-80.834	3.24E+05	1.00E+04	2	9	11.57	1164.90	Metamorphic	7293.54	93.56
Sullivan	2007	CS-03D	36.466	-80.834	4.36E+05	1.20E+04	9	18	11.57	1164.90	Metamorphic	7293.54	93.56
Sullivan	2007	CS-04A	36.472	-80.858	3.30E+05	1.10E+04	0.25	0.85	10.99	1205.70	Metamorphic	1165.05	5.19
Sullivan	2007	CS-04B	36.472	-80.858	3.44E+05	1.10E+04	0.85	2	10.99	1205.70	Metamorphic	1165.05	5.19
Sullivan	2007	CS-04C	36.472	-80.858	3.01E+05	9.00E+03	2	9	10.99	1205.70	Metamorphic	1165.05	5.19
Sullivan	2007	CS-04D	36.472	-80.858	3.10E+05	9.00E+03	9	18	10.99	1205.70	Metamorphic	1165.05	5.19
Sullivan	2007	CS-06	36.539	-80.860	2.39E+05	6.00E+03	0.25	0.85	16.85	1124.20	Metamorphic	523.81	1.12
Sullivan	2007	CS-06A	36.539	-80.860	2.20E+05	7.00E+03	0.85	2	16.85	1124.20	Metamorphic	523.81	1.12
Sullivan	2007	CS-06B	36.539	-80.860	2.25E+05	7.00E+03	2	9	16.85	1124.20	Metamorphic	523.81	1.12
Sullivan	2007	CS-06C	36.539	-80.860	2.66E+05	8.00E+03	9	18	16.85	1124.20	Metamorphic	523.81	1.12
Sullivan	2007	CS-06D	36.539	-80.860	4.81E+05	1.60E+04	0.25	0.85	17.77	1124.20	Metamorphic	1389.10	5.67
Sullivan	2007	CS-07A	36.556	-80.799	3.55E+05	1.20E+04	0.85	2	17.77	1124.20	Metamorphic	1389.10	5.67
Sullivan	2007	CS-07B	36.556	-80.799	2.87E+05	1.00E+04	2	9	17.77	1124.20	Metamorphic	1389.10	5.67
Sullivan	2007	CS-07C	36.556	-80.799	2.48E+05	7.00E+03	9	18	17.77	1124.20	Metamorphic	1389.10	5.67
Tofelde	2018	M08	-24.547	-65.870	9.39E+05	2.89E+04	10	30	14.09	854.00	Mixed[a]	29442.24	2439.39
Tofelde	2018	M08	-24.547	-65.870	8.70E+05	2.66E+04	0.25	0.5	14.09	854.00	Mixed[a]	29442.24	2439.39
Tofelde	2018	T11	-24.550	-65.861	2.47E+05	7.86E+03	10	30	12.19	834.00	Mixed[a]	7900.64	151.32

First Author	Year	Official sample name	Latitude (°N)	Longitude (°E)	[^{10}Be] (atoms g^{-1})	1σ-[^{10}Be] (atoms g^{-1})	Min Grain size (mm)	Max Grain size (mm)	Mean basin slope (°)	MAP (mm yr^{-1})	Lithology	Travel distance (m)	Catchment area (km^2)
Tofelde	2018	T11	-24.550	-65.861	1.72E+05	5.56E+03	0.25	0.5	12.19	834.00	Mixed[a]	7900.64	151.32
Tofelde	2018	M15	-24.491	-65.858	9.17E+05	2.81E+04	10	30	13.71	814.00	Mixed[a]	25904.19	1854.05
Tofelde	2018	M15	-24.491	-65.858	6.91E+05	2.13E+04	0.25	0.5	13.71	814.00	Mixed[a]	25904.19	1854.05
Tofelde	2018	T26	-24.900	-65.673	1.26E+03	1.10E+03	10	30	28.16	687.00	Metamorphic	4107.75	36.84
Tofelde	2018	T26	-24.900	-65.673	9.55E+03	3.38E+03	0.25	0.5	28.16	687.00	Metamorphic	4107.75	36.84
Tofelde	2018	T27	-24.843	-65.714	9.90E+02	1.13E+03	10	30	25.18	687.00	Metamorphic	1880.38	10.84
Tofelde	2018	T27	-24.843	-65.714	7.46E+03	1.70E+03	0.25	0.5	25.18	687.00	Metamorphic	1880.38	10.84
Tofelde	2018	T28	-24.647	-65.810	2.02E+05	7.98E+03	10	30	22.10	732.00	Metamorphic	7842.03	125.28
Tofelde	2018	T28	-24.647	-65.810	1.89E+05	6.47E+03	0.25	0.5	22.10	732.00	Metamorphic	7842.03	125.28
Tofelde	2018	T32	-24.751	-65.748	2.79E+04	1.70E+03	10	30	27.06	753.00	Metamorphic	1926.27	11.70
Tofelde	2018	T32	-24.751	-65.748	8.20E+04	3.46E+03	0.25	0.5	27.06	753.00	Metamorphic	1926.27	11.70
Tofelde	2018	T35	-24.366	-65.798	6.90E+05	2.22E+04	10	30	16.21	834.00	Metamorphic	6829.13	110.06
Tofelde	2018	T35	-24.366	-65.798	4.46E+05	1.40E+04	0.25	0.5	16.21	834.00	Metamorphic	6829.13	110.06
Tofelde	2018	T43	-24.809	-65.801	7.85E+03	1.23E+03	10	30	21.30	682.00	Metamorphic	13233.12	855.69
Tofelde	2018	T43	-24.809	-65.801	3.73E+04	1.37E+03	0.25	0.5	21.30	682.00	Metamorphic	13233.12	855.69
Tofelde	2018	T44	-24.810	-65.800	2.17E+03	1.91E+03	10	30	24.69	685.00	Mixed[a]	10225.85	194.71
Tofelde	2018	T44	-24.810	-65.800	1.89E+04	8.26E+02	0.25	0.5	24.69	685.00	Mixed[a]	10225.85	194.71
Tofelde	2018	T59	-24.405	-65.822	7.69E+05	2.43E+04	10	30	13.33	814.00	Magmatic	5432.42	110.30
Tofelde	2018	T59	-24.405	-65.822	2.17E+06	6.70E+04	0.25	0.5	13.33	814.00	Magmatic	5432.42	110.30
Tofelde	2018	T68	-24.497	-65.878	9.87E+05	3.03E+04	10	30	15.60	803.00	Metamorphic	13480.43	526.82
Tofelde	2018	T68	-24.497	-65.878	1.41E+06	4.31E+04	0.25	0.5	15.60	803.00	Metamorphic	13480.43	526.82
Tofelde	2018	T69	-24.566	-65.864	9.01E+05	2.76E+04	10	30	21.26	732.00	Metamorphic	5762.00	87.09
Tofelde	2018	T69	-24.566	-65.864	9.44E+05	3.01E+04	0.25	0.5	21.26	732.00	Metamorphic	5762.00	87.09

First Author	Year	Official sample name	Latitude (°N)	Longitude (°E)	[^{10}Be] (atoms g^{-1})	1σ-[^{10}Be] (atoms g^{-1})	Min Grain size (mm)	Max Grain size (mm)	Mean basin slope (°)	MAP (mm yr^{-1})	Lithology	Travel distance (m)	Catchment area (km^2)
van Dongen	2019	NA 0.5-1	-37.808	-73.014	2.67E+05	9.64E+03	0.5	1	8.93	1213.00	Magmatic	1026.09	5.79
van Dongen	2019	NA 1-2	-37.808	-73.014	2.72E+05	1.34E+04	1	2	8.93	1213.00	Magmatic	1026.09	5.79
van Dongen	2019	NA 2-4	-37.808	-73.014	2.84E+05	1.10E+04	2	4	8.93	1213.00	Magmatic	1026.09	5.79
van Dongen	2019	NA 4-8	-37.808	-73.014	2.67E+05	9.98E+03	4	8	8.93	1213.00	Magmatic	1026.09	5.79
van Dongen	2019	NA 8-16	-37.808	-73.014	2.90E+05	1.04E+04	8	16	8.93	1213.00	Magmatic	1026.09	5.79
van Dongen	2019	NA 16-32	-37.808	-73.014	2.29E+05	8.73E+03	16	32	8.93	1213.00	Magmatic	1026.09	5.79
van Dongen	2019	NA 32-64	-37.808	-73.014	1.76E+05	6.83E+03	32	64	8.93	1213.00	Magmatic	1026.09	5.79
van Dongen	2019	LC 0.5-1	-32.954	-71.069	2.64E+04	1.48E+03	0.5	1	23.05	358.00	Magmatic	1457.47	7.41
van Dongen	2019	LC 1-2	-32.954	-71.069	1.77E+04	1.03E+03	1	2	23.05	358.00	Magmatic	1457.47	7.41
van Dongen	2019	LC 2-4	-32.954	-71.069	3.66E+04	1.86E+03	2	4	23.05	358.00	Magmatic	1457.47	7.41
van Dongen	2019	LC 4-8	-32.954	-71.069	3.48E+04	1.96E+03	4	8	23.05	358.00	Magmatic	1457.47	7.41
van Dongen	2019	LC 8-16	-32.954	-71.069	6.48E+04	2.93E+03	8	16	23.05	358.00	Magmatic	1457.47	7.41
van Dongen	2019	LC 16-32	-32.954	-71.069	4.98E+04	2.33E+03	16	32	23.05	358.00	Magmatic	1457.47	7.41
van Dongen	2019	LC 32-64	-32.954	-71.069	5.88E+04	2.77E+03	32	64	23.05	358.00	Magmatic	1457.47	7.41

First Author	Year	Official sample name	Latitude (°N)	Longitude (°E)	[^{10}Be] (atoms g^{-1})	1σ-[^{10}Be] (atoms g^{-1})	Min Grain size (mm)	Max Grain size (mm)	Mean basin slope (°)	MAP (mm yr^{-1})	Lithology	Travel distance (m)	Catchment area (km^2)
van Dongen	2019	SG 0.5-1	-29.760	-71.168	4.71E+05	1.64E+04	0.5	1	17.23	88.00	Magmatic	480.83	0.88
van Dongen	2019	SG 1-2	-29.760	-71.168	4.02E+05	1.71E+04	1	2	17.23	88.00	Magmatic	480.83	0.88
van Dongen	2019	SG 2-4	-29.760	-71.168	3.62E+05	1.61E+04	2	4	17.23	88.00	Magmatic	480.83	0.88
van Dongen	2019	SG 4-8	-29.760	-71.168	3.76E+05	1.87E+04	4	8	17.23	88.00	Magmatic	480.83	0.88
van Dongen	2019	SG 8-16	-29.760	-71.168	4.25E+05	1.45E+04	8	16	17.23	88.00	Magmatic	480.83	0.88
van Dongen	2019	SG 16-32	-29.760	-71.168	5.16E+05	1.77E+04	16	32	17.23	88.00	Magmatic	480.83	0.88
van Dongen	2019	SG 32-64	-29.760	-71.168	4.79E+05	1.66E+04	32	64	17.23	88.00	Magmatic	480.83	0.88
van Dongen	2019	AZ 0.5-1	-26.112	-70.551	4.48E+05	1.63E+04	0.5	1	8.20	13.00	Magmatic	120.00	0.04
van Dongen	2019	AZ 1-2	-26.112	-70.551	4.60E+05	1.67E+04	1	2	8.20	13.00	Magmatic	120.00	0.04
van Dongen	2019	AZ 2-4	-26.112	-70.551	4.36E+05	1.62E+04	2	4	8.20	13.00	Magmatic	120.00	0.04
van Dongen	2019	AZ 4-8	-26.112	-70.551	3.69E+05	2.10E+04	4	8	8.20	13.00	Magmatic	120.00	0.04
van Dongen	2019	AZ 8-16	-26.112	-70.551	3.14E+05	1.22E+04	8	16	8.20	13.00	Magmatic	120.00	0.04
van Dongen	2019	AZ 16-32	-26.112	-70.551	2.80E+05	1.02E+04	16	32	8.20	13.00	Magmatic	120.00	0.04
van Dongen	2019	AZ 32-64	-26.112	-70.551	3.16E+05	1.11E+04	32	64	8.20	13.00	Magmatic	120.00	0.04

Table S 3.2: Grain size dependencies as linear function (y= ax + b) of mean basin slope, MAP and mean travel distance. Mean ± 2σ values result from 10,000 Monte Carlo runs.

Factor	Lithology	Mean[a] a	2σ[a] a	Mean[a] b	2σ[a] b	Mean[a] R^2	2σ[a] R^2	Mean[a] p	2σ[a] p	Significance code[b]
Mean basin slope	All	-6.16E-03	1.02E-03	7.21E-02	2.28E-02	0.134	0.020	0.002	0.002	**
Mean basin slope	Mixed	-6.79E-03	1.37E-03	9.66E-02	3.06E-02	0.050	0.019	0.419	0.095	
Mean basin slope	Sedimentary	-7.88E-03	1.28E-03	1.04E-01	2.14E-02	0.199	0.044	0.104	0.043	
Mean basin slope	Magmatic	9.84E-04	2.01E-03	-1.37E-02	4.23E-02	0.007	0.006	0.789	0.103	
Mean basin slope	Metamorphic	-9.18E-03	1.06E-03	1.38E-01	1.89E-02	0.238	0.051	0.017	0.016	*
Mean travel distance	All	-1.74E-02	3.40E-03	9.28E-02	2.82E-02	0.037	0.010	0.114	0.056	
Mean travel distance	Mixed	1.95E-02	4.17E-03	-2.40E-01	3.91E-02	0.026	0.011	0.564	0.085	
Mean travel distance	Sedimentary	-4.91E-02	1.16E-02	3.19E-01	8.09E-02	0.163	0.048	0.150	0.071	
Mean travel distance	Magmatic	-9.61E-03	1.91E-02	6.46E-02	1.25E-01	0.014	0.012	0.699	0.138	
Mean travel distance	Metamorphic	-2.88E-02	6.21E-03	1.64E-01	4.87E-02	0.065	0.024	0.228	0.093	
MAP	All	-4.99E-05	7.51E-06	2.18E-03	1.07E-02	0.106	0.019	0.007	0.007	**
MAP	Mixed	-6.12E-05	9.98E-06	-6.67E-03	8.57E-03	0.057	0.018	0.382	0.080	
MAP	Sedimentary	-4.88E-05	7.48E-06	1.25E-02	1.26E-02	0.102	0.021	0.252	0.052	
MAP	Magmatic	-1.49E-04	2.02E-05	5.55E-02	2.68E-02	0.498	0.074	0.006	0.026	**
MAP	Metamorphic	-1.27E-05	1.07E-05	-4.94E-02	1.24E-02	0.010	0.012	0.692	0.190	

[a] Mean ± 2σ values result from 10,000 Monte Carlo runs.

[b] Significance codes correspond to mean p-values: 0 '***' 0.001 '**' 0.01 '*' 0.05 '•' 0.1 ' ' 1

Table S 3.3: Multivariate statistics and relative importance (RI) results for the factors mean basin slope (MBS), mean annual precipitation (MAP) and mean travel distance (MTD). Mean ± 2σ values result from 10,000 Monte Carlo runs.

Lithology	Factor	Mean[a] b	2σ[a] b	Mean[a] p	2σ[a] p	Sign. code[b]	Mean[a] RI	2σ[a] RI	Mean[a] R^2	2σ[a] R^2	Mean[a] Adj.-R^2	2σ[a] Adj. -R^2	Mean[a] p-value multivariate model	2σ[a] p-value multivariate model	Sign. code[b]
All	MBS	-4.24E-03	9.39E-04	0.051	0.031	•	9.071	1.527	0.190	0.026	0.154	0.027	0.004	0.006	**
All	MAP	-3.63E-05	5.82E-06	0.054	0.036	•	7.637	1.525	0.190	0.026	0.154	0.027	0.004	0.006	**
All	MTD	-9.43E-03	3.50E-03	0.386	0.137		2.258	0.717	0.190	0.026	0.154	0.027	0.004	0.006	**
Mixed	MBS	-1.12E-02	1.20E-03	0.238	0.050		7.795	2.051	0.170	0.025	-0.037	0.031	0.510	0.071	
Mixed	MAP	-1.28E-04	1.94E-05	0.283	0.072		7.262	1.976	0.170	0.025	-0.037	0.031	0.510	0.071	
Mixed	MTD	-2.46E-02	8.71E-03	0.645	0.115		1.975	0.455	0.170	0.025	-0.037	0.031	0.510	0.071	
Sedimentary	MBS	-6.08E-03	1.08E-03	0.217	0.074		15.152	3.858	0.334	0.056	0.152	0.072	0.210	0.083	
Sedimentary	MAP	-3.40E-05	5.67E-06	0.400	0.073		7.167	1.683	0.334	0.056	0.152	0.072	0.210	0.083	
Sedimentary	MTD	-3.22E-02	1.05E-02	0.351	0.131		11.071	3.755	0.334	0.056	0.152	0.072	0.210	0.083	
Magmatic	MBS	3.78E-03	1.89E-03	0.305	0.165		2.789	1.286	0.552	0.081	0.440	0.101	0.031	0.064	*
Magmatic	MAP	-1.58E-04	1.98E-05	0.007	0.031	**	51.421	7.927	0.552	0.081	0.440	0.101	0.031	0.064	*
Magmatic	MTD	-4.67E-04	2.06E-02	0.798	0.147		0.966	0.949	0.552	0.081	0.440	0.101	0.031	0.064	*
Metamorphic	MBS	-8.97E-03	1.08E-03	0.027	0.020	*	21.990	4.554	0.276	0.048	0.177	0.055	0.077	0.049	•
Metamorphic	MAP	1.22E-05	1.11E-05	0.696	0.176		0.847	0.555	0.276	0.048	0.177	0.055	0.077	0.049	•
Metamorphic	MTD	-1.98E-02	6.23E-03	0.377	0.140		4.758	2.015	0.276	0.048	0.177	0.055	0.077	0.049	•

[a] Mean ± 2σ values result from 10,000 Monte Carlo runs.

[b] Significance codes correspond to mean p-values: 0 '***' 0.001 '**' 0.01 '*' 0.05 '•' 0.1 ' ' 1

3.12 Supplementary figures

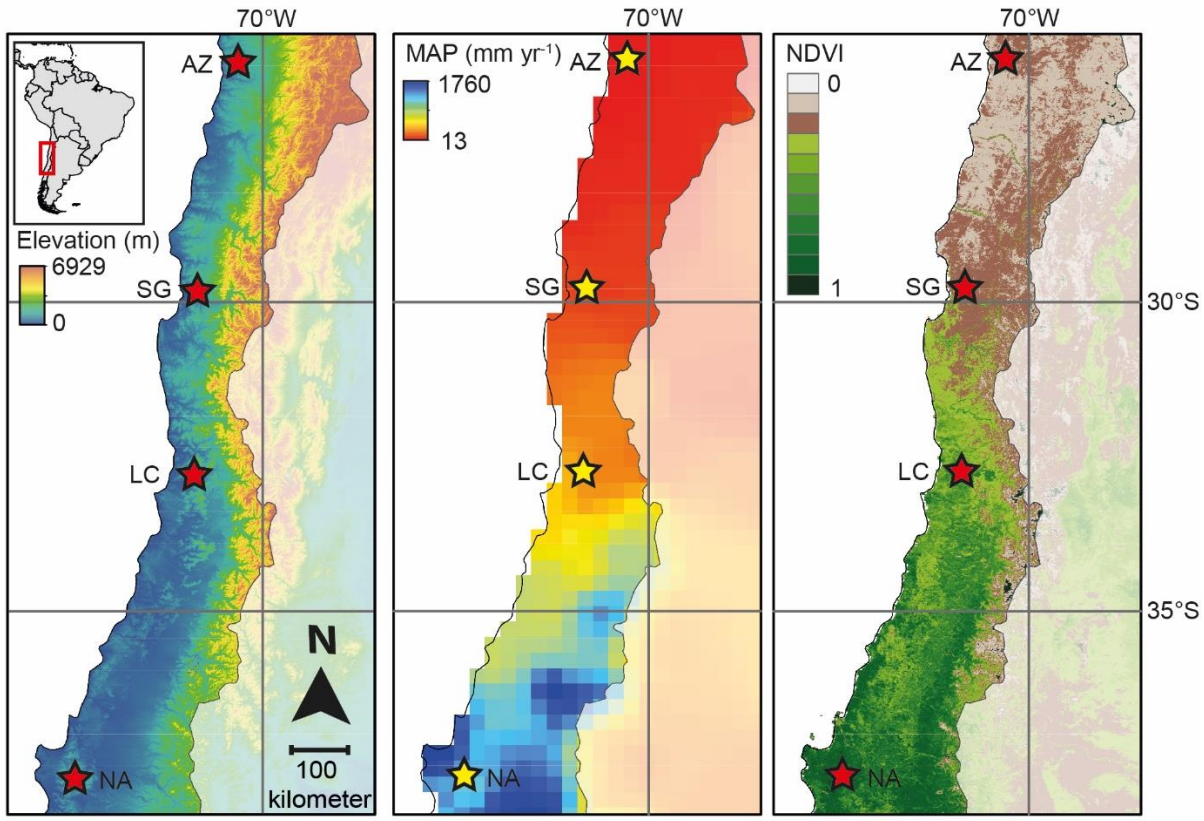

Figure S 3.1: Elevation, mean annual precipitation (MAP) and Normalized Difference Vegetation Index (NDVI) maps of Chile with locations of the study areas (stars). AZ = Pan de Azúcar, SG = Santa Gracia, LC = La Campana, NA = Nahuelbuta.

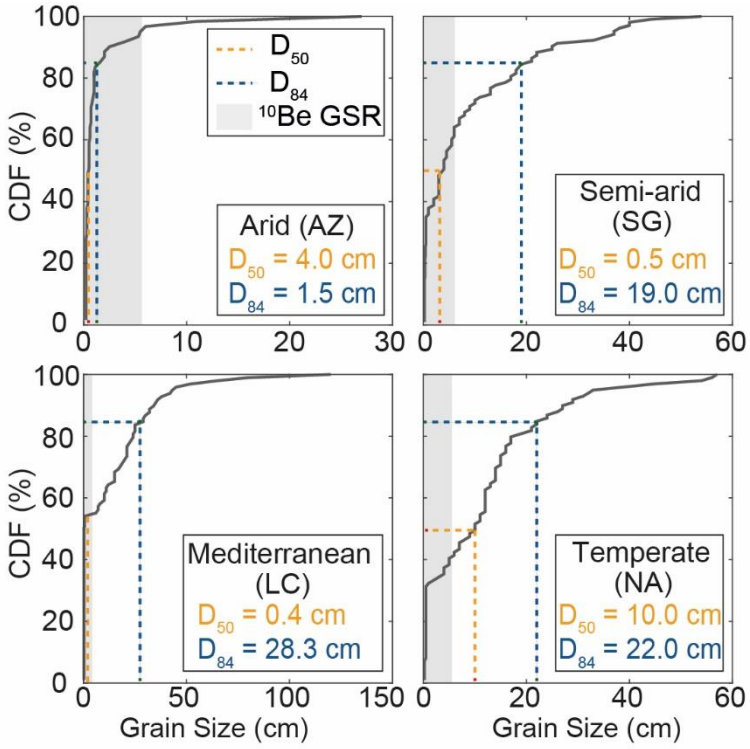

Figure S 3.2: Cumulative distribution function (CDF) of Wolman pebble count results from the studied catchments in the Chilean Coastal Cordillera. Red lines indicate calculated D_{50} grain sizes and green lines indicate D_{84} grain sizes. Grey shaded areas indicate the grain size range (0.5-64 mm) used for ^{10}Be analysis (^{10}Be GSR).

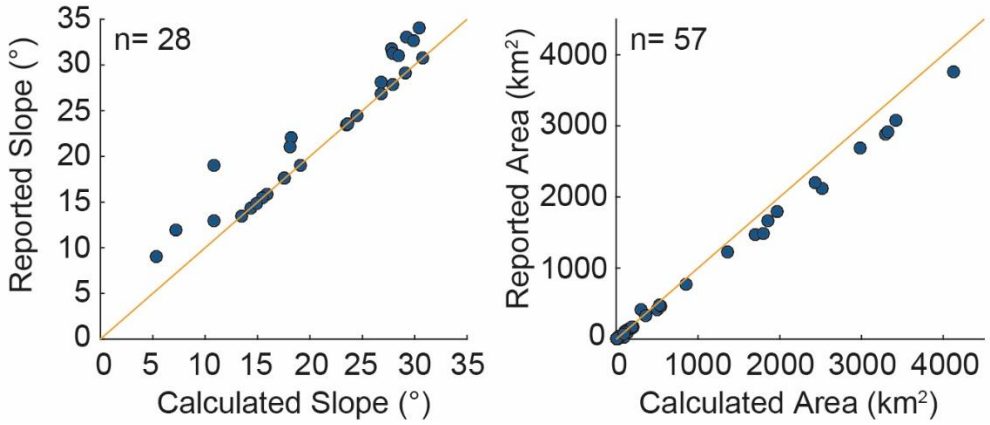

Figure S 3.3: Comparison of published and recalculated catchment parameters. The slight offset of recalculated catchment area and hillslope angle is most likely related to the use of different DEM resolutions.

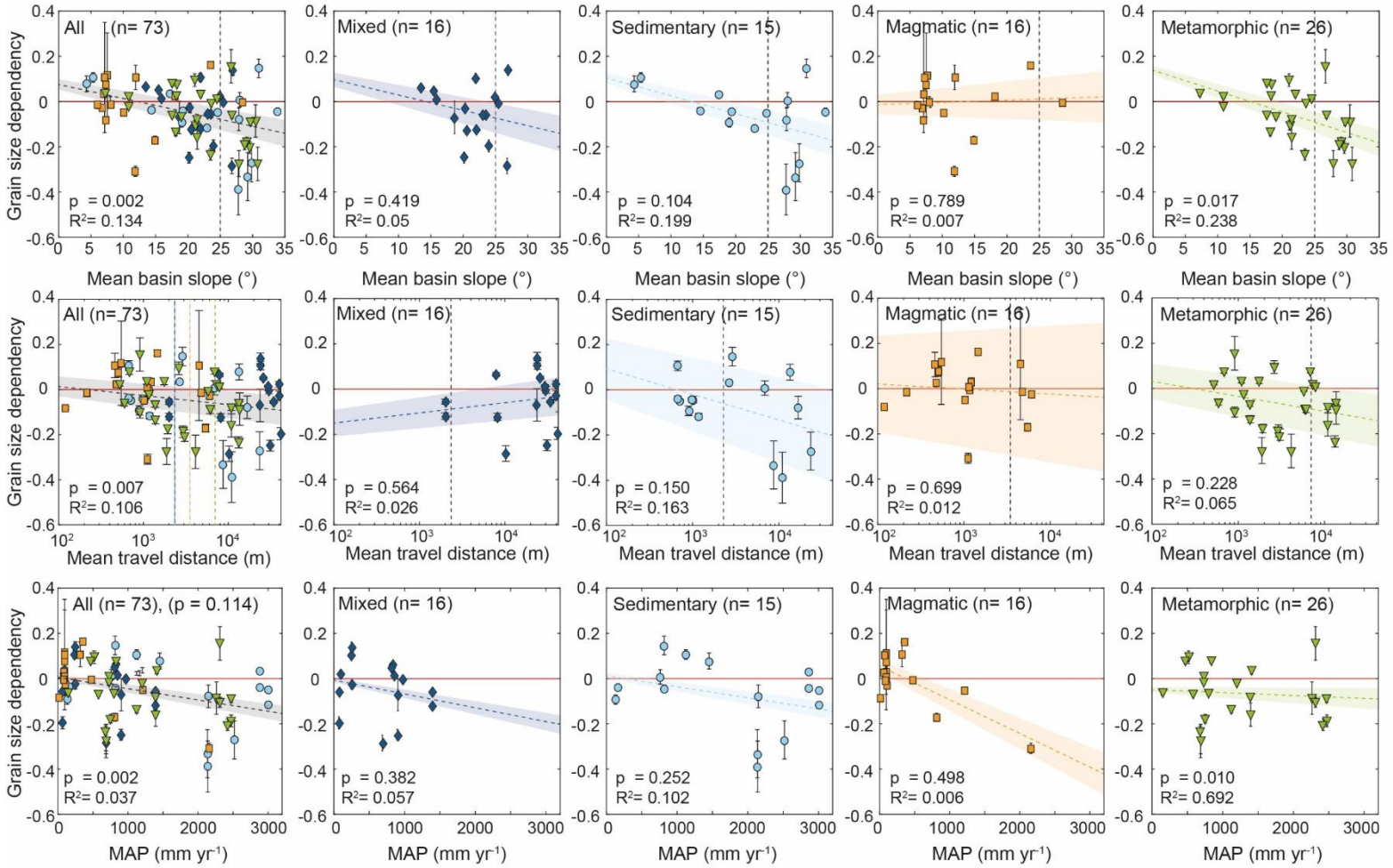

Figure S 3.4: Grain size dependencies as a linear function (y= ax + b) of mean basin slope, mean annual precipitation and mean travel distance. Plots are shown for all lithologies combined, and each individual lithology. Shaded background of each linear fit is the standard deviation of the fit resulting from 10,0000 Monte Carlo runs. Grey shaded areas represent exceeded threshold hillslopes (TH; upper row) and lithology-dependent. abrasion thresholds (AT; middle row). Linear model fit data is presented in Table S 3.2.

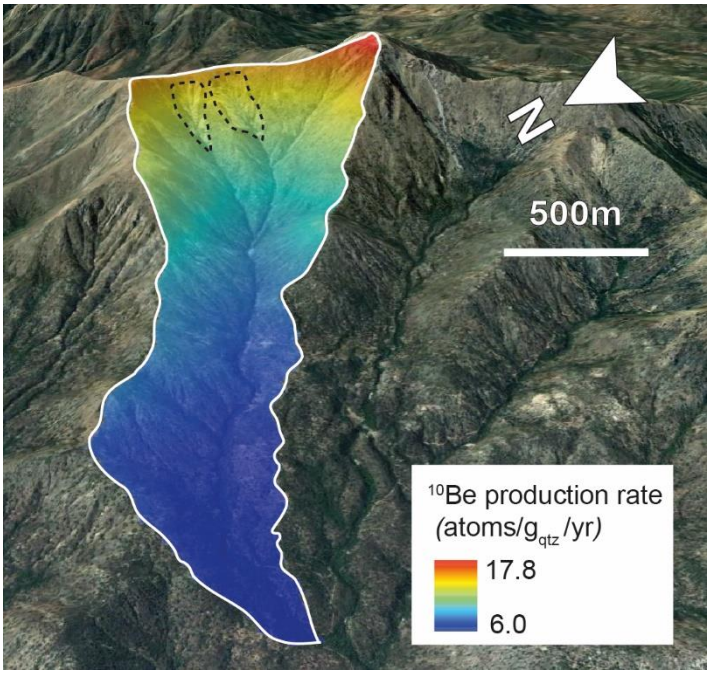

Figure S 3.5: La Campana catchment with debris flow source areas (dotted outlines) and ^{10}Be production rates. Background is a Google Earth image (Google Earth Pro, 2018).

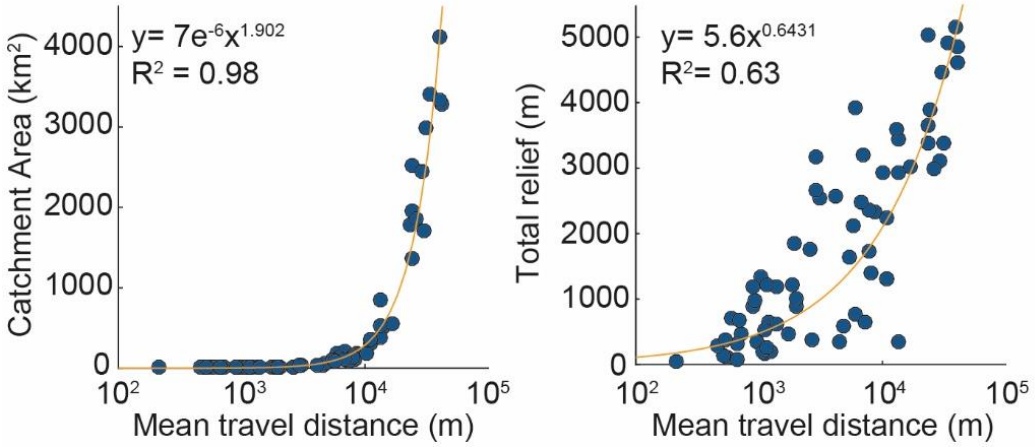

Figure S 3.6: Covariance of catchment attributes in the global compilation catchments. Upper: covariance of mean travel distance (m) and catchment area (km^2), lower: covariance of mean travel distance (m) and total relief (m). Global compilation data is presented in Table S 3.1.

Chapter 4

El Niño Southern Oscillation (ENSO)-induced hydrological anomalies in central Chile

Renee van Dongen[1,2], Dirk Scherler[1,3], Dadiyorto Wendi[4], Claudio I. Meier[5], Eric Deal[6], Luca Mao[7], Norbert Marwan[8]

[1] GFZ German Research Centre for Geosciences, Earth Surface Geochemistry, Potsdam, Germany.
[2] International Centre for Water Resources and Global Change (UNESCO), German Federal Institute of Hydrology, Koblenz, Germany.
[3] Freie Universität Berlin, Institute of Geological Sciences, Berlin, Germany.
[4] GFZ German Research Centre for Geosciences, Hydrology, Potsdam, Germany.
[5] University of Memphis, Department of Civil Engineering, Memphis (TN), United States of America.
[6] ETH Zürich, Department of Earth Sciences, Zürich, Switzerland.
[7] University of Lincoln, School of Geography, Lincoln, United Kingdom.
[8] Potsdam Institute for Climate Impact Research (PIK), Member of the Leibniz Association, Potsdam, Germany.

This chapter is prepared as a manuscript to submit to the journal "Hydrology and Earth System Sciences (HESS)"

Abstract

The El Niño Southern Oscillation (ENSO) is a major driver of climatic anomalies around the globe. How these climatic anomalies translate into hydrological anomalies is important for water resources management, but difficult to predict due to the non-linear relationship between precipitation and river discharge, and contrasts in hydrological response in regions with different hydrological regimes. In this study we investigate how ENSO-induced climatic anomalies translate into hydrological anomalies by focussing on Central Chile (29-42°S), a relatively small area affected by ENSO, that displays steep latitudinal and elevational climatic gradients. We use a large dataset (183 discharge stations) of daily discharge timeseries together with monthly temperature and precipitation data. Based on the Multivariate ENSO Index (MEI) we classified the discharge data for the time period 1950-2009 into El Niño (MEI>0.5), La Niña (MEI<-0.5) and non-ENSO periods (-0.5>MEI<0.5). For both El Niño and La Niña periods, we calculated relative differences in mean monthly temperature, precipitation, and specific discharge, as compared to non-ENSO conditions. Furthermore, we investigated the differences in mean daily discharge variability as well as the occurrence of low flows and high flows during El Niño and La Niña phases, as compared to non-ENSO phases. The results reveal that precipitation and specific discharge generally increase during El Niño events, while they decrease during La Niña events. However, there exist large spatial and seasonal variations. The mean monthly precipitation and specific discharge anomalies during both the El Niño and the La Niña phases are strongest in the semi-arid region (29-32°S), followed by the mediterranean (32°-36°S) and humid-temperate (36°-42°S) regions. During El Niño events, the semi-arid and mediterranean regions experience mean monthly specific discharge increases of up to +180% and +105%, respectively, and a considerable increase in the frequency and magnitude of high flows. In contrast, discharges in the humid-temperate region are most sensitive to rainfall deficits during La Niña events, as revealed by an increased frequency of low flows. We find that the different hydrological regimes (rainfall or snow-dominated) show large contrasts in how ENSO-induced climatic anomalies are translated into hydrological anomalies, in that snowmelt dynamics induce a delayed discharge peak during El Niño, provide a minimum streamflow during dry La Niña conditions and reduces the discharge variability in rivers. Finally, we discuss the implications for water resources management, highlighting the need for different ENSO prediction and mitigation strategies in central Chile, according to catchment hydrological regime.

4.1 Introduction

Global warming is expected to impact the course of the water cycle, exacerbating hydrological extremes. Large global models studies have predicted increasing climate change-related flood hazard risks in large parts of the world (Hirabayashi et al., 2013), whereas other regions would be affected by an increase in extent of terrestrial drylands and the intensification of droughts (Schlaepfer et al., 2017). Floods and droughts have strong socioeconomic and ecological impacts through their effects on food security (Adams et al., 1999; Iizumi et al., 2014), wild-fires (Beckage et al., 2003; Fasullo et al., 2018; Harrison, 2013), ecosystems (Poveda et al., 2011; Williams and de Vries, 2020), land degradation (Inman and Jenkins, 1999; Morera et al., 2017), and natural hazards (Ward et al., 2014, 2016). Therefore, a better understanding of how climatic anomalies translate into hydrological extremes is becoming increasingly important for future water resources and risk management strategies.

In many regions on Earth, one of the main drivers of interannual climatic anomalies, and thus, hydrological extremes, is the El Niño-Southern Oscillation (ENSO) (McPhaden et al., 2006; Salas et al., 2020). ENSO is an oceanic-atmospheric phenomenon that causes sea surface temperature and wind pattern variations over the tropical Pacific Ocean, resulting in climatic anomalies in South America, Australia, South-East Asia and Africa (Mason and Goddard, 1994; Ropelewski and Halpert, 1987). Central Chile, located on the west coast of South America, is one of such regions affected by ENSO. Previous studies of ENSO-induced climatic anomalies in Chile (e.g., Garreaud et al., 2009; Montecinos et al., 2000; Montecinos and Aceituno, 2003; Meza, 2013) identified El Niño as the warm and wet phase, while La Niña is the cold, dry phase. These climatic anomalies show strong seasonal and spatial variations that are related to the position and intensity of the South Pacific High (Figure 4.1) (Charrier et al., 2007; Garreaud et al., 2009; Montecinos et al., 2000; Montecinos and Aceituno, 2003).

How ENSO-induced climatic anomalies translate into hydrological anomalies and in particular hydrological extremes is not easily assessed, due to the non-linear relationship between precipitation and river discharge (Stephens et al., 2015), and the multiple effects of air temperature on the water holding capacity of the atmosphere, evapotranspiration, and snowmelt (Emerton et al., 2017, 2019; De Perez et al., 2017). Furthermore, a basin's sensitivity to climatic anomalies is also controlled by catchment characteristics such as catchment area, elevation, bedrock lithology, regolith thickness, and vegetation cover (e.g., Post and Jakeman, 1996; Rust et al., 2020). Asymmetric streamflow responses to ENSO-induced precipitation have been observed for river basins around the world, induced by snow dynamics, soil moisture and the integration of cumulative hydrological processes in large basis, whereas other catchments showed a symmetric response to climate anomalies (Lee et al., 2018; Mosley, 2000). A recent collaborative study on climate change effects on river floods in Europe revealed substantial regional variations in such extreme events (Blöschl et al., 2019; Kemter et al., 2020); in spite of not focussing on ENSO-induced climatic anomalies, this work

demonstrates the need for high-resolution studies to capture the spatial complexity of hydrological response to climate. Additionally, it suggests that water resources management strategies should be planned at the regional scale rather than as a general policy for a large, typically administrative region.

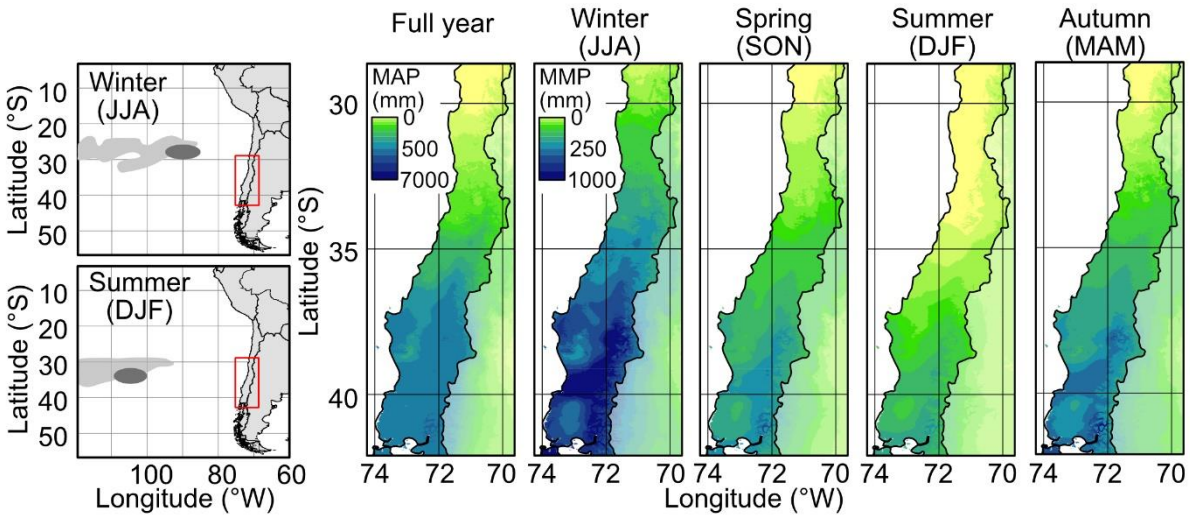

Figure 4.1: Seasonal variations of the Southern Pacific High (SPH) location and precipitation rates. A) Location of the Southern Pacific High anticyclone in the winter and summer seasons according to the studies of Barrett and Hameed (2017) (light grey area, SPH locations between 1980-2013) and Schneider et al. (2017) (dark grey spot). The red boxes indicate the extent of the research area. B) Mean annual precipitation (MAP) and seasonal variations in mean monthly precipitation (MMP) in central Chile. The colormaps have a logarithmic scale.

Central Chile (29°- 42°S) features a strong latitudinal climatic gradient, from semi-arid conditions in the north to a humid-temperate climate in the south (Pizarro et al., 2012; Valdés-Pineda et al., 2016), as well as large elevation differences between the high elevation Andes mountain range in the east and the low elevation coastal region in the west. Due to these altitudinal contrasts, the Andes and the coastal region are characterized by different hydrological regimes. High elevation Andean catchments in the northern part of central Chile experience their main discharge peak during the glacier- and snowmelt season in summer (nival-type), whereas river discharges peaks during the winter rainy season for basins in the coastal region (pluvial-type) (Alvarez-Garreton et al., 2021; Oertel et al., 2020). Given the strong latitudinal and altitudinal gradients that occur over a relatively small area, with a relatively dense hydrometeorological network, central Chile is well-suited for a detailed investigation of how ENSO-induced climatic anomalies are converted into hydrological anomalies.

ENSO-induced hydrological anomalies likely cause relevant socioeconomic impacts in Central Chile, as the strongest climatic anomalies occur in the semi-arid and mediterranean regions (~29°-36°S), where the majority (~60%) of the population resides (Valdés-Pineda et al., 2014). These regions are strongly dependent on fresh

water for crop irrigation, domestic water use, and hydropower generation (Alvarez-Garreton et al., 2018; Cordero et al., 2019; Masiokas et al., 2006; Meza, 2005). A detailed understanding of how ENSO induces hydrological anomalies is therefore crucial for water resources management in central Chile.

Previous studies have investigated the effect of ENSO on precipitation and temperature anomalies (e.g., Garreaud et al., 2009; Montecinos et al., 2000; Montecinos and Aceituno, 2003; Ropelewski and Halpert, 1987), snow dynamics (e.g., Cordero et al., 2019; Cortés and Margulis, 2017; Masiokas et al., 2006), and hydrology (e.g., Piechota et al., 1995; Rubio-Álvarez and McPhee, 2010; Waylen et al., 1993; Waylen and Caviedes, 1990) in central Chile. Generally, these studies reported enhanced precipitation and river discharge during the warm and wet El Niño phase, and reduced precipitation and river discharge during the cold and dry La Niña phase, but the reported climatic and hydrological anomalies suggest strong seasonal and spatial deviations. The studies of Waylen et al. (1993) and Oertel et al. (2020) compared streamflow and precipitation data to investigate the differences in response to ENSO. Both studies reported a time lag between the precipitation and streamflow responses and attributed this to snow dynamics. However, these studies focussed predominantly on Andean basins and included a relatively sparse coverage of river basins (15 and 20 river basins, respectively, over a latitudinal distance of ~ 1200 km). Furthermore, the observations of these studies are based on comparison of timeseries of proximate river and precipitation gauging stations and lack a direct comparison of upstream-averaged precipitation and river discharge rates.

To date, a study on the spatial and temporal differences in ENSO-induced climatic and hydrological anomalies, which concentrates on both the Andes and the coastal region is still lacking, especially if one considers the availability of a spatially dense network of stream-gauging stations. Accordingly, in this study we investigate how ENSO-induced climatic anomalies translate into hydrological anomalies across central Chile (29°-42°S), by using a large quality-controlled dataset which includes daily discharge data from 183 stations (Alvarez-Garreton et al., 2018). We focus on the ENSO-induced mean monthly temperatures and precipitation anomalies, and how these are converted into mean specific discharge anomalies as well as in differences in the low- and high-flow regimes. Finally, we discuss the implications of our results for water resources management.

4.2 Climate in central Chile

Central Chile (29°-42°S) covers a north-to-south climatic gradient ranging from cold semi-arid (BSk) and cold desert climates in the northern-central region (29°-32°S), across a subhumid mediterranean (Csb) climate in the central region (32°-36°S), to humid mediterranean and temperate rain-oceanic (Cfb) climates in the southern-central region (36°- 42°S) (Köppen, 1900; Kottek et al., 2006). For simplicity, we reduced the climate classifications to semi-arid (29°- 32°S), mediterranean (32°- 36°S), and

humid-temperate (36°- 42°S) (Figure 4.2). Besides the north-south contrast in climate, the elevation differences between the low elevation coastal region and the high elevation Andes Mountain range, approximately 100 km farther to the east, promote an additional east-west climatic contrast in temperature and precipitation. On average, the orographic lifting effected by the Andes accounts for a two to three times higher precipitation rate in the mountains as compared to the coastal region, at any given latitude (Barrett and Hameed, 2017; Garreaud et al., 2009; Viale and Garreaud, 2014).

The South Pacific High (SPH) is a semi-permanent anticyclone centred over the south-eastern Pacific Ocean, which controls most of the seasonal and interannual climatic variability in Chile (e.g., Barrett and Hameed, 2017; Montecinos and Aceituno, 2003; Schneider et al., 2017). The position of the SPH determines the boundary between the arid region in the north, which is affected by the subsidence of dry air in the Hadley cell (quasi-barotropic conditions), and the humid region in the south, under the influence of the westerlies (baroclinic conditions). Therefore, the seasonal migration of the SPH and thus, the boundary between the quasi-barotropic and baroclinic conditions, plays a crucial role in seasonal temperature and precipitation variations (e.g., Barrett and Hameed, 2017; Fuenzalida, 1982; Montecinos and Aceituno, 2003). During winter, when the SPH is positioned at its most north-eastern position (26-30°S, 85-95°W) (Ancapichún and Garcés-Vargas, 2015; Barrett and Hameed, 2017; Schneider et al., 2017) (Figure 4.1a), extratropical cyclones associated with the westerlies have their largest meridional extent (Fuenzalida, 1982; Montecinos and Aceituno, 2003), resulting in wet conditions in the humid and mediterranean regions (Figure 4.1b). In summer, though, most of central Chile experiences dry and warm conditions, when the SHP is located at its most south-western position (33-36°S, 100-108°W) (Ancapichún and Garcés-Vargas, 2015; Montecinos and Aceituno, 2003). Under such conditions, dry air from the Hadley cell subsides over a large meridional extent (Dima and Wallace, 2003), leading to low precipitation rates in the semi-arid and mediterranean regions of Chile (Figure 4.1b).

Many studies have found that the position and intensity of the Southern Pacific High play important roles in the ENSO-induced precipitation anomalies (Barrett and Hameed, 2017; Kiladis and Diaz, 1989; Montecinos et al., 2000; Montecinos and Aceituno, 2003). In South America, El Niño conditions develop from pressure differences above the Pacific Ocean that weaken or reverse the equatorial trade winds, pushing warm ocean surface waters from the western Pacific Ocean towards the west coast of South America (Jaksic, 1998; Ropelewski and Halpert, 1987). Due to the anomalously warm sea surface temperatures (SST) near the coast of South America, this is also termed the warm phase of an ENSO event. La Niña, or the cold phase, occurs when the system changes to a reinforced condition of the normal state, in which the Humboldt Current brings cold water along the west coast of South America, which then flows towards the eastern Pacific Ocean. Typically, this cold phase happens after an El Niño phase (Diaz and Kiladis, 1995).

During El Niño phases the SPH intensity weakens, which results in the blocking of the storm tracks on the Amundsen-Bellinghausen Sea and the intensification of the westerlies at mid-latitudes, resulting in wetter conditions over central Chile (Garreaud and Battisti, 1999; Montecinos and Aceituno, 2003; Rutllant and Fuenzalida, 1991). During La Niña, a strengthening of the SPH occurs, which drives a southward displacement of the midlatitude storm tracks, resulting in a larger region under the influence of the dry conditions of the Hadley Cell (Montecinos and Aceituno, 2003). As the boundary between the areas under quasi-barotropic and baroclinic conditions follows a seasonal north-south movement, controlled by the position of the SPH, the climatic anomalies are found to predominantly concentrate on the semi-arid region during winter, when this boundary is at its northern-most position, whereas they centre on the humid-temperate region during spring, when this boundary is located further south (Montecinos and Aceituno, 2003). When ENSO conditions prevail, either El Niño or La Niña, the SPH changes its intensity in the summer season. This induces different climatic anomalies during El Niño and La Niña summers, as compared to the other seasons under ENSO phases (Garreaud et al., 2009; Montecinos et al., 2000; Montecinos and Aceituno, 2003).

Several studies have highlighted reduced correlations between ENSO indices and streamflow from the 1920s to about 1950, for South America (e.g., Dettinger et al., 2000; Elliott and Angell, 1988). This has been attributed to a reduced ENSO intensity and presumably weaker oceanic-atmospheric teleconnections (Dettinger et al., 2000). Hence, we decided to exclude this time period from our study, including river discharge data only from 1950 onwards. Furthermore, since 2010, Chile has been affected by a long-lasting megadrought, with 25-45% reductions in precipitation (Alvarez-Garreton et al., 2021; Boisier et al., 2016; Garreaud et al., 2017, 2020). Recent studies suggest that this megadrought is not related to ENSO (Garreaud et al., 2020), but is instead partly induced by the Pacific Decadal Oscillation and, to a smaller extent, by anthropogenic climate change that affected the ozone layer (Boisier et al., 2016, 2018a). To exclude any influence of this megadrought on the results of this study, we did not consider any data after 2009. Therefore, this study focusses on the 60-year time period from 1950 to 2009.

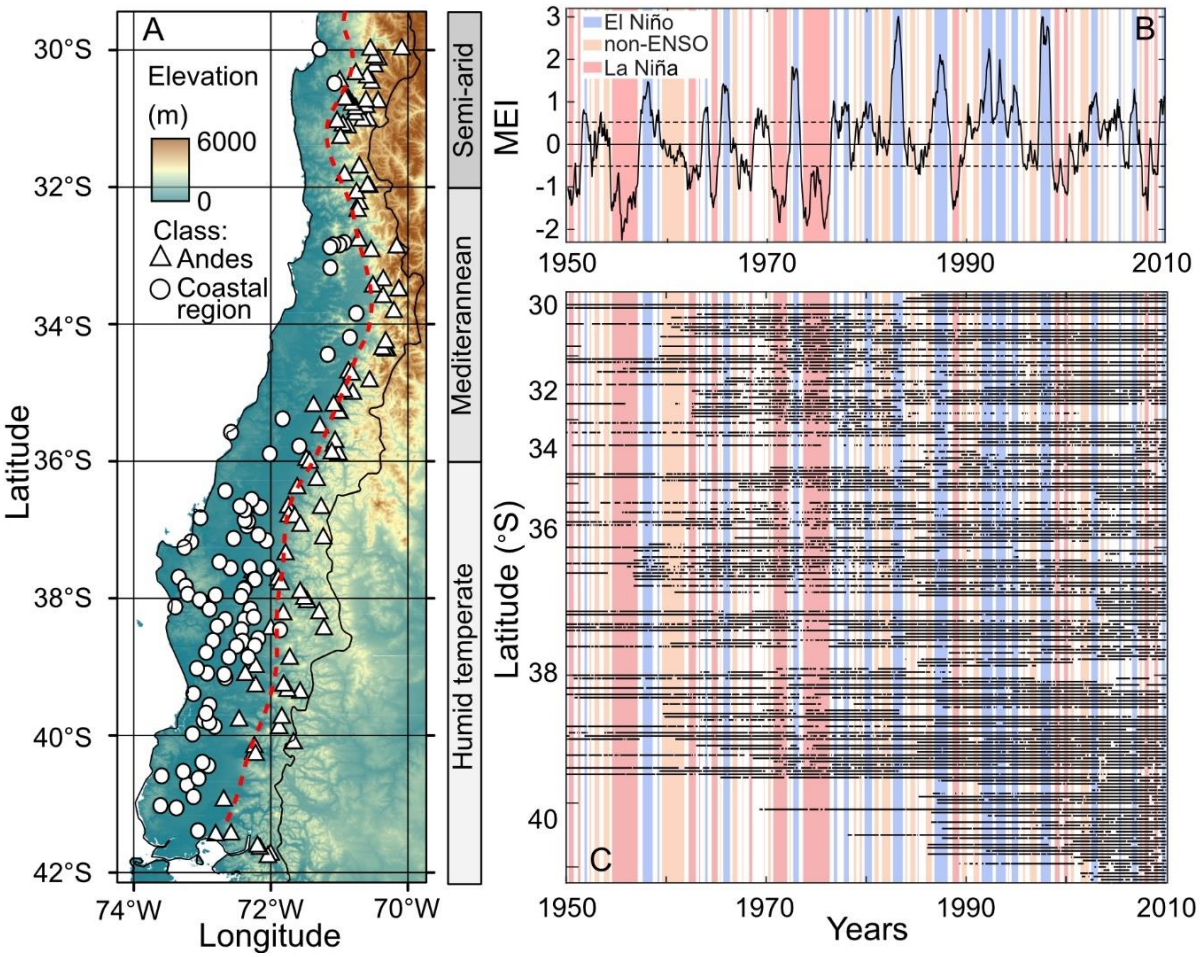

Figure 4.2: Locations of river discharge station and data coverage in comparison to Multivariate ENSO Index (MEI) values. A) 90m resolution Digital Elevation Model of central Chile (Jarvis et al., 2008), with the locations of the river discharge stations in the Andes (triangles) and coastal region (circles). On the right, the extent of the climatic zones: semi-arid (29-32°S), mediterranean (32-36°S), and humid-temperate (36-42°S). B) Multivariate ENSO index (MEI; Wolter and Timlin, 1993, 1998, 2011) with the classified El Niño (blue), La Niña (red) and non-ENSO (yellow) events. C) Data coverage of each river discharge station over the time period 1950-2009.

4.3 Methodology

4.3.1 Daily river discharge data

The study is based on the Catchment Attributes and MEtereology for Large sample Studies for Chile (CAMELS-CL) dataset, which includes 516 river discharge stations across Chile (17.8°-55.0°S). The data is monitored by the Dirección General de Aguas (DGA; part of the Public Works Ministry) and provided by the Center for Climate and Resilience Research (CR^2). CAMELS-CL is a quality-checked meteo-hydrological dataset that includes daily river discharge time series from stream gauging stations and daily meteorological timeseries (temperature, precipitation, potential evapotranspiration, and snow water equivalent) derived from gridded data products

(Alvarez-Garreton et al., 2018). Additionally, the dataset provides information on catchment attributes such as human intervention levels, land cover, and the presence of large dams.

As explained above, in this study we focus on the time period from 1950 to 2009, for which both discharge data in the CAMELS-CL dataset and Multivariate ENSO Index data (MEI; Wolter and Timlin, 1993, 1998, 2011) - on which we based the ENSO-phase classification - exist. Based on the below-explained requirements, we selected 183 catchments from the CAMELS-CL dataset for further analysis (Table S 4.1). First, we selected stations based on data availability during the chosen time period (1950-2009), requiring a record length of at least 10 years (Figure S 4.1a, b). We furthermore excluded catchments with large hydropower or irrigation dams (Figure S 4.1c), as well as basins with >10% of anthropogenic water extraction as compared to the annual discharge (Figure S 4.1d). The latter quantity is called the human intervention degree and is computed from the annual volume of granted water extraction rights (provided by the National Water Atlas; DGA, 2016), expressed as a flow rate, normalized by mean annual river discharge (Alvarez-Garreton et al., 2018). Unfortunately, information on the actual extraction volumes is currently lacking (Alvarez-Garreton et al., 2018). Based on a 30-m resolution land cover dataset provided for Chile (Zhao et al., 2016), we furthermore excluded catchments for which >5% of the surface area is covered with impermeable surfaces (e.g., cities) (Figure S 4.1e), as well as catchments where >50% of the area is used for agriculture (Figure S 4.1f). Finally, we excluded catchments which are located directly downstream of large (>10% of catchment area) lakes (Figure S 4.1g), because these regulate discharge due to their large storage capacity.

For the semi-arid and mediterranean climate zones (29°-36°S), many of the coastal region catchments had to be removed due to the presence of dams or considerable human water extraction. Increasing the threshold for the human intervention degree did not increase the number of such catchments, likely because the occurrence of water extraction correlates with the presence of dams and extensive water extraction volumes for irrigation and the mining industry are common in these regions (Aitken et al., 2016). Hence, the majority of the 183 catchments used in this study are located in the humid-temperate region (36°-44°S) (Figure S 4.1h). After all filtering, we classified the river catchments into Andean (high elevation) or coastal region (low elevation) river catchments (Figure S 4.1h). We could not classify the catchments based on an elevation-threshold, because the Andes decrease in elevation towards the south. Instead, we derived a hillslope map from a 90m digital elevation model (DEM) provided by the Shuttle Radar Topography Mission (SRTM; Jarvis et al., 2008), and created a boundary based on increasing hillslope angles at the Andean foot slopes (red line in Figure 4.2a). Some large catchments drain both the Andes and coastal region; these were classified according to the region where the majority (>50% of the catchment area) of the basin is located. After this classification, the final data set consists of 100 Andean and 83 coastal region catchments (Figure 4.2a and Table S 4.1).

At most stations, the daily discharge records contain missing values, with gap lengths that vary from a single day up to several months (Figure 4.2c). To reduce adverse effects of data gaps on our analysis, we further processed the discharge records in the following order (Figure S 4.2). First, we removed all months containing data gaps of >10 days (Figure S 4.2a). Second, we determined specific, tolerable gap lengths for each station, based on a maximum-tolerated lag length for which the Pearson autocorrelation function (ACF) coefficient r of the mean daily flows is above 0.7 (Figure S 4.2b and c). Missing discharges over gap lengths below the specific tolerable gap length threshold were linearly interpolated. This assumes that the minimum ACF value of 0.7 is a safe indicator to perform the linear interpolation. We ensured that p-values are below 0.001 to preserve the significance of the linear relationship. In the following analysis, we only used months that did not have any remaining daily data gaps, after applying the above steps (Figure S 4.2d). Finally, we computed daily mean specific discharge by normalizing the discharge by catchment area, as reported in the metadata. This facilitates direct comparison between daily runoff and daily precipitation data, as they have the same units (mm day^{-1}).

4.3.2 Precipitation and temperature data

The CAMELS-CL dataset also includes mean daily precipitation and temperature data from various data providers. However, the time period for these records (1979-2016) does not cover the entire period of the discharge data. To allow for direct comparison between ENSO-induced temperature, precipitation, and specific discharge anomalies, we require climatic data with a longer temporal overlap with the river discharge data. Because of the monthly resolution of the Multivariate ENSO index, a monthly climatic product was deemed sufficient for such purposes. We selected the 0.25° resolution mean monthly precipitation (MMP) dataset from the Global Precipitation and Climatology Centre (GPCC; Meyer-Christoffer et al., 2015) which provides MMP starting in 1891, and the 0.50° resolution mean monthly surface air temperature dataset from the Climate Prediction Centre (CPC; Fan and van den Dool, 2008), which provides MMT time series starting in 1948. We used the DEM of each catchment and calculated MMP and MMT values for each grid cell using the nearest-neighbour linear interpolation method. Next, we calculated an average value for the basin based on the arithmetic mean of all grid cells. Based on this approach, we obtained for each station both basin averaged MMP and MMT timeseries for the study period (1950-2009).

We compared both GPCC precipitation and CPC temperature data to the mean monthly precipitation and temperature data from the CR2MET dataset (Figure S 4.3 and Figure S 4.4). The CR2MET dataset is a 0.05° gridded historical climate data product for Chile, calibrated with a large network of climate stations, which is found to perform well (Alvarez-Garreton et al., 2018; Boisier et al., 2018). Recall that we cannot use this dataset for our analysis of ENSO effects, as it only covers the period 1979 to 2019. The GPCC dataset was found to underestimate precipitation (by up to ~100 mm) in steep Andean catchments in the mediterranean and humid-temperate regions (>32°S)

(Figure S 4.3). We also explored the performance of other precipitation datasets (WorldClim2 (Fick and Hijmans, 2017) and CHIRPS (Funk et al., 2014)); however, they did not perform considerably better than the GPCC dataset, and their data range does not cover the full 1950-2009 period. Comparing the CPC and CR2MET datasets revealed that the CPC dataset underestimates land-measured mean monthly temperatures during the summer (average -2.34°C) and autumn (average -2.45°C) seasons in the mediterranean and humid-temperate regions and year-round in the semi-arid region (average -5.95 °C) (Figure S 4.4).

Despite the apparent underestimation of precipitation and temperature in the GPCC and CPC datasets, respectively, as compared to the CR2MET, we decided to use these datasets in our study. Due to their complete data coverage for the 1950-2009 period, they allow for direct comparison between ENSO-induced differences in MMT, MMP and MMQsp. Moreover, the MMP and MMT biases seem rather systematic and persistent, hence, the dataset should still be able to capture the relative variability between the different ENSO phases. It is worth noting that in the following analyses, we only used MMP and MMT values for those months with discharge data, at each station.

4.3.3 ENSO-classification

The ENSO-phases classification in this study is based on the value of the original Multivariate ENSO Index (MEI; Wolter and Timlin, 1993, 1998)). We applied the original MEI value, as the recently released MEI.v2 version only provides values of the index from 1979 on. Following the method suggested by the MEI developers, we compare the two-month-averaged MEI index (month(i) and month(i-1)) to the climatic and hydrological data of month(i). This is advised because the atmospheric response to tropical SST anomalies shows a time lag (Wolter, 2018).

To preclude any potential effects of the delayed atmospheric response to ENSO, we applied a conservative classification method to classify climatic and hydrological data in different ENSO classes. This method assures we only include data from longer-lasting ENSO-phases, excluding transient periods (i.e., single months that briefly exceed the ENSO thresholds). First, we defined the thresholds for El Niño events (MEI > 0.5), La Niña events (MEI < -0.5) or else non-ENSO periods (-0.5 < MEI < 0.5). We only classified data in the different ENSO classes when a certain MEI threshold was exceeded for three or more consecutive months in a row. Months that did not meet these criteria were discarded from the analysis. This method resulted in the classification of 169 months as El Niño, 156 months as La Niña, and 175 months as non-ENSO, over the time period 1950-2009 (Figure 4.2b). A total of 220 months were not classified in any of the ENSO-classes, because MEI values were in a transition period between different ENSO phases and were not sufficiently stable for three consecutive months. The distribution of El Niño events, La Niña events, and non-ENSO periods is not evenly distributed over the seasons of the year, for the 1950-2009 time period. El Niño phases occur less often in the autumn and winter months, whereas La

Niña phases show a slightly lower occurrence during the winter season (Figure S 4.5). Non-ENSO phases are relatively equally distributed over the four seasons, with a slightly higher occurrence during spring. The distribution of non-ENSO periods over the 1950-2009 time period is relatively evenly distributed (Figure S 4.6), but El Niño events occurred more often after 1975 while La Niña events occurred more often before 1975.

4.3.4 Data analysis

We investigated ENSO-related differences in climate and river discharge for the entire year, as well as the four seasons. We classified the months into Austral seasons: summer – December, January, February; autumn – March, April, May; winter – June, July, August, and spring – September, October, November. Based on the seasonality of precipitation, snow melt, and runoff, the hydrological year is defined from autumn to summer (Alvarez-Garreton et al., 2018), which is also the order of seasons shown in the figures of this paper.

For each gauging station, we produced a mean monthly specific discharge (MMQsp) timeseries based on the daily discharge timeseries. Only for those months with available discharge data, we classified MMQsp, the CPC-derived MMT, and GPCC-derived MMP data in different ENSO-phases classes based on MEI values, as explained in Section 4.3.3. Next, we further classified the data within each ENSO-class according to the above-defined seasons. If a seasonal ENSO-class contained sufficient data (>10 months), we calculated long-term average MMT, MMP, and MMQsp values for each season. To be able to evaluate seasonal differences as well as annual differences between El Niño and La Niña events, compared to non-ENSO phases, we also calculated the mean annual temperature (MAT), mean annual precipitation (MAP), and mean annual specific discharge (MAQsp) for each station. To exclude biases towards any certain season that occurs more frequently in a particular ENSO-phase, we calculated MAT, MAP, and MAQsp based on the arithmetic mean of the long-term monthly values for each season. Next, we computed the relative differences in MMP, MMT, and MMQsp of El Niño and La Niña phases versus non-ENSO phases, which we present as percent deviations from non-ENSO conditions. We summarized the percent differences in MMT, MMP, and MMQsp for each climatic and elevation (coastal region or Andes) region in boxplots, and reported the differences based on the median values of all stations in each region and the 5^{th}- and 95^{th}-percentile values.

Furthermore, we investigated whether the frequency of high-flows and low-flows change during El Niño and La Niña phases, as compared to non-ENSO conditions, which provides important information for flood and drought risk management (Figure 4.3a). For each station, we first defined low-flow and high-flow thresholds based on the 5^{th}-percentile (Q_5) and 95^{th}-percentile (Q_{95}) values of the empirical distribution of the non-ENSO daily specific discharges. Next, for each one of the three cases (El Niño, La Niña, and non-ENSO conditions) we calculated two areas under the corresponding empirical probability density function (pdf) of daily specific discharges: the area below

the low-flow (Q_5) threshold, as well as that above the high-flow (Q_{95}) threshold. For simplicity, we termed these areas the quantile areas (QA) (Figure 4.3a). The quantile area above the high-flow threshold (QA_{95}) reflects the frequency and magnitude of the high-flow regime, whereas the quantile area below the low-flow threshold (QA_5) reflects the frequency and magnitude of the low-flow regime. Finally, we calculated the relative differences in each quantile area during El Niño and La Niña events, as the percent difference compared to non-ENSO periods (ΔQA). Changes in quantile area can occur due to changes in both the frequency and magnitude of low-flow and high-flow events. It is worth noticing here that although we use the terminology "high flow" and "low flow" for this analysis, their association to floods and droughts is not necessarily straightforward nor robust. A high-flow regime defined based on Q_{95} cannot directly considered to be a flood, although the Q_{95}-threshold has often been used in other studies to define floods. The same applies to droughts, as we only determine our low-flow regime based on Q_5, instead of using more complex notions such as the effective drought, which could be defined as water scarcity for a certain defined period of days to weeks, depending on the region and basin size. In this study we decided to adopt the terminology high-flow and low-flow regime instead.

Differences in the quantile areas (ΔQA) during El Niño and La Niña events can be the result of either 1) changes in the mean specific discharge (i.e., a shift of the entire empirical distribution of the daily specific discharges towards higher or lower discharge magnitudes) or 2) changes in the shape of the empirical daily specific discharge distribution, i.e., when the left or right tails of the distribution become lighter or heavier (Figure S 4.7). A change in the shape of the empirical distribution of the daily specific discharge would occur if ENSO differentially affects certain ranges of specific discharge more strongly than others. For both the process understanding of the hydrological response to ENSO and the context of water resources management, it is important to understand which range of specific discharge magnitudes are affected. Hence, we additionally investigated the variability of daily specific discharge (i.e., how often and by how much discharge deviates from the mean discharge), and how that differs between El Niño, La Niña, and non-ENSO phases. To study discharge variability, previous studies have parameterized the shape of the magnitude-frequency distribution of daily discharge with various distributions (e.g., Pareto (Molnar et al., 2006), inverse gamma (Lague et al., 2005), stretched exponential (Rossi et al., 2016), and Pearson (Botter et al., 2007; Deal et al., 2018)). A study in a region with distinct low- and high-flow seasons fitted the high-flow and low-flow regimes with the weighted sum of two inverse gamma distributions (Scherler et al., 2017). The inverse gamma distribution combines an exponential tail for the low-flow regime with a power law distribution for the high-flow regime, and better fits the roll-over from lower towards higher discharge magnitudes compared to, e.g., a Pareto distribution (Lague et al., 2005). Therefore, we decided to use this method to investigate the differences in the shape of daily discharge distributions when El Niño or La Niña events occur, as compared to non-ENSO periods. We tested the use of both a single and the weighted sum of two inverse gamma fits but decided for a single inverse gamma fit, due to the limited amount of daily discharge

data when the data are divided across the different ENSO phases and seasons. Inverse gamma fitting yields the shape parameter 'k', which represents the relationship between mean discharge and extreme events and can be interpreted as a measure of the discharge variability. Low k values are associated with daily discharge distributions with high variability, while high k values are associated with distributions displaying low discharge variability. In this analysis of daily discharge variability, we only included stations with reliable fits (R^2 of >0.97) (Figure 4.3b). Again, we calculated the relative differences in the k-parameter (Δk) for the two ENSO stages (El Niño, La Niña) as their percent differences compared to non-ENSO conditions (Figure 4.3c).

Anticipating possible differences when analysing on an annual versus a seasonal basis, we conducted both analyses (ΔQA and Δk) for each individual season, as well as for the annual data. All results from the two different methods, for both El Niño and La Niña phases, are presented in individual figures in the data supplement. In these, we show the ΔQA and Δk results for all stations, but we also computed the mean for all stations located within each 1° latitudinal window (solid line), as well as the 1 σ -standard deviation (shaded background) (Figure 4.3c). As the differences in quantile areas (ΔQA) are a function of changes in both the mean specific discharge and the shape of the daily specific discharge distribution (Δk), we combined the ΔQA and Δk results for each 1°-latitudinal window into a single plot (Figure 4.3d). In this figure, the marker values and error bars on the x-axis represent the mean percent difference and 1σ-standard deviation in ΔQA, respectively, for all stations within a 1°-latitudinal window, while the marker colour depicts the mean Δk value over that latitudinal window. Figure 4.3d directly shows whether any differences in either the high-flow or the low-flow regimes occur during El Niño or La Niña events, as compared to non-ENSO periods (ΔQA, x-axis), and whether these are related to a change in shape of the daily discharge distribution (Δk, color-coding).

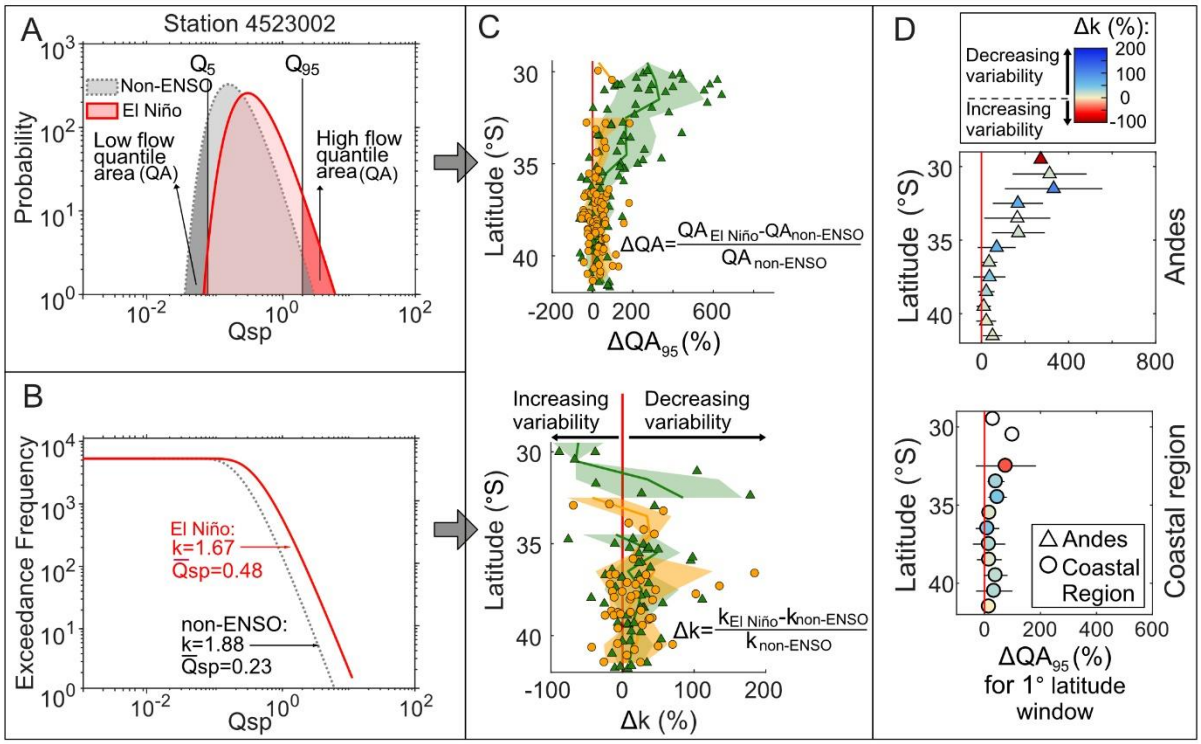

Figure 4.3: Description of the ΔQA and inverse gamma fitting methods, to investigate the differences in the high-flow and low-flow regimes and discharge variability. This example is based on a comparison between El Niño and non-ENSO and focusses on the high-flow regime in panels C and D (QA_{95}). A) Example of an empirical probability distribution for station 4523002_Río Grande en Puntilla San Juan (Table S 4.1). The figure shows the empirical daily specific discharge distributions (Qsp) for El Niño (red) and non-ENSO (grey). The areas above and below the 5th- and 95th-percentiles of non-ENSO events (Q_5 and Q_{95}) represent the low flow quantile area (QA_5) and high flow quantile area (QA_{95}), respectively. B) The exceedance frequency distribution of daily specific discharge data (Qsp) for the El Niño (red) and non-ENSO (grey) phases is parameterized using inverse gamma fitting (Lague et al., 2005). High discharge variability is characterized by a heavy tailed distribution and a low k-parameter, whereas low discharge variability is characterized by a high k-parameter. Only inverse gamma fits with sufficient data (>3 months of data) and a good fit (r2>0.97) are used for further analysis. C) For all 183 stations, the differences in low flow and high flow quantile areas (ΔQA_5 and ΔQA_{95}, upper panel) and discharge variability (Δk, lower panel) are calculated as percent difference of El Niño relative to the non-ENSO phase. The resulting ΔQA and Δk values plotted separately for Andean stations (green triangles) and coastal region stations (orange circles). Furthermore, a latitudinal average (solid line) and 1σ standard deviation (shaded background) is calculated for all stations within a 1°-latitudinal window. D) Finally, the results of both methods are combined in one figure. The markers indicate the mean ΔQA and the error bars the 1σ-standard deviation for all stations in each 1° latitude window. The symbols are color-coded by the value of Δk. Red values indicate increasing discharge variability and blue values decreasing discharge variability, based on the inverse gamma fit.

4.4 Results

In this chapter we report the differences in mean monthly temperature (MMT), mean monthly precipitation (MMP), mean monthly specific discharge (MMQsp), and the frequency of low flows and high flows during El Niño and La Niña events, as compared to non-ENSO periods. We analyse all data on both yearly and seasonal bases. Furthermore, we present the differences across the three climatic regions: semi-arid (29-32°S), mediterranean (32-36°S) and humid-temperate (36-42°S), as well as the contrasts between the Andes and the coastal regions. For all combinations of regions and seasons, including the annual case, we report median values of these differences, corresponding to the median of all station values in that region, over that season. Furthermore, we report the 5th and 95th percentile values for each region and season (T_5 and T_{95} for temperature, P_5 and P_{95} for precipitation and Q_5 and Q_{95} for discharge).

4.4.1 El Niño

4.4.1.1 Differences in MMT and MMP

Compared to non-ENSO phases, the mean monthly temperature is higher in about two third of the studied river catchments during El Niño events, but the magnitude of the MMT increase is rather small (Figure 4.4 and Table S 4.2). Most of the catchments that show lower temperatures during El Niño are located in the semi-arid region, where we also observe large variations in temperature anomalies, with temperature decreases of up to -86.6% (T_5) and increases of up to +33.9% (T_{95}) (Table S 4.3). The largest temperature increases when averaging across all regions are found in the autumn and winter seasons, with median temperature increases of +3.9% and +3.7%, respectively (Table S 4.3). During the autumn and winter, the increase in temperature is highest in the humid-temperate region, where temperatures accrue by up to +34.2% and +23.2% (T_{95}), respectively. During summer, the majority of the catchments (79.5%, Table S 4.2) show lower temperatures, albeit with only a minor median decrease of -1.6% (Table S 4.3).

Across the entire study area and throughout almost all seasons, we predominantly observe higher mean monthly precipitation during El Niño phases, as compared to non-ENSO conditions (Figure 4.4 and Table S 4.2). The exception is the summer season, in which roughly two thirds (61.2%) of the river catchments experience reduced mean monthly precipitation. The catchments displaying decreased MMP during the summer season are predominantly located in the humid-temperate and semi-arid regions and show MMP decreases of up to -67.3% (P_5, Table S 4.3). On a yearly basis, the highest increase in precipitation is found in the semi-arid region (median: +28.9%), followed by the mediterranean region (median: +23.0%) and the humid-temperate region (median: +9.9%). The highest precipitation increase in the humid-temperate region occurs during spring.

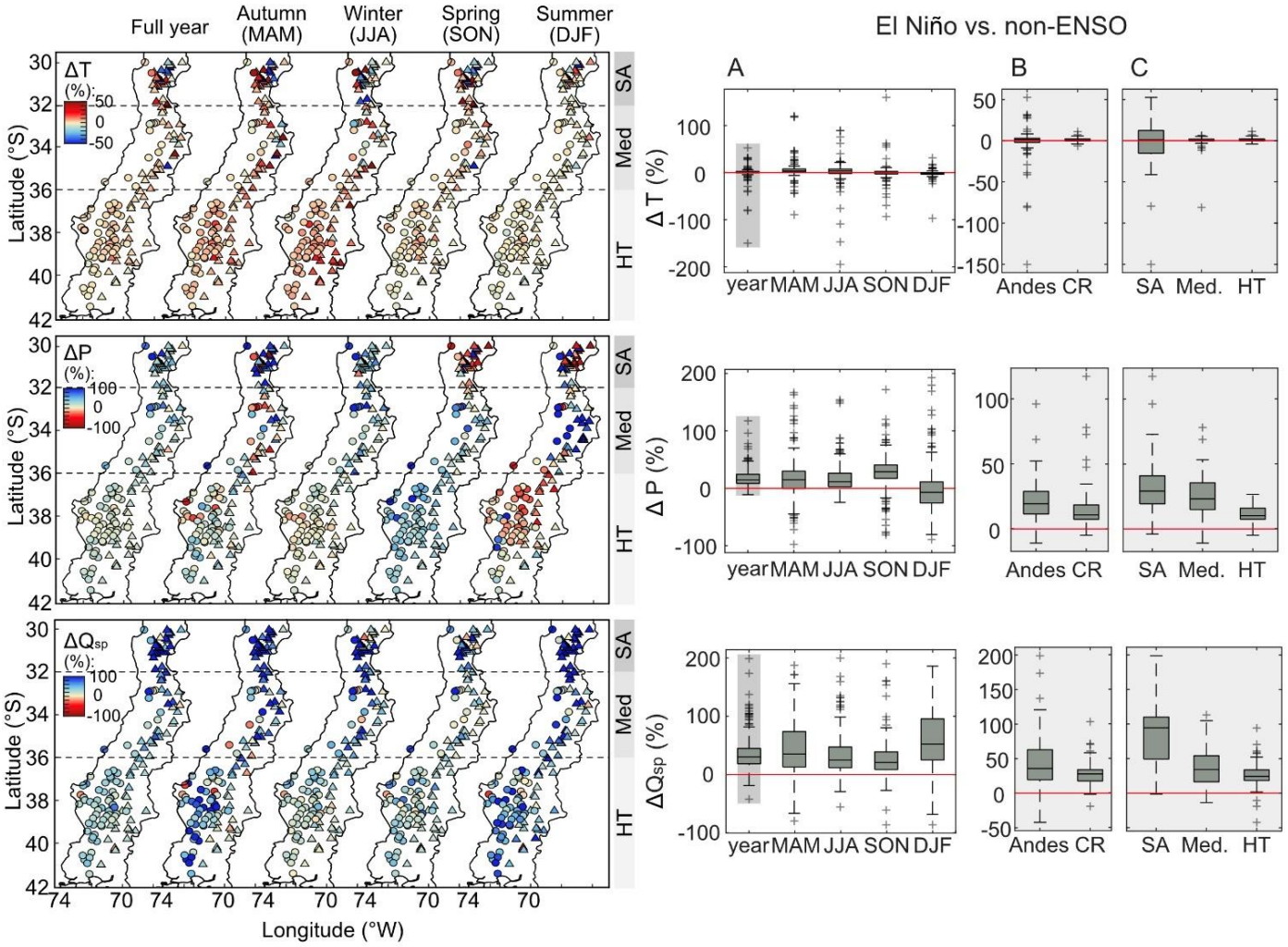

Figure 4.4: Differences (in %) in mean monthly temperature (ΔT), precipitation (ΔP), and specific discharge (ΔQ_{sp}) during El Niño events relative to non-ENSO conditions. The maps on the left show the spatial and seasonal differences for the full year and the different seasons. The dotted lines indicate the boundaries between the different climate zones, which are indicated in the subpanels on the right: semi-arid (SA), mediterranean (Med), and humid-temperate (HT). The boxplots in column A) show the variation of the data for the full year and the individual seasons. The grey shaded area represents the y-axis extent of the boxplot columns B) and C) that are based on the annual data. Boxplot column B) shows the differences between the Andes and the coastal region (CR), while boxplot column C) shows the differences between the three climate zones. The precipitation and temperature anomalies for the full 1950-2009 period are shown in the data supplement (Figure S 4.8).

Overall, it seems that the increase in mean monthly precipitation is higher in the Andes compared to the coastal region. However, this may be because Andean stations are predominantly located in the semi-arid and mediterranean regions, whereas coastal region catchments dominate in the humid-temperate region. The precipitation and temperature anomalies that occur during El Niño events, based on the full 1950-2009 dataset, are shown in the data supplement (Figure S 4.8).

4.4.1.2 Differences in MMQsp and discharge variability

During El Niño events, the mean monthly specific discharges are higher in the majority of the catchments (95.4%, Table S 4.2) as compared to non-ENSO periods (Figure 4.4). The increases in specific discharge are evident across all seasons, but the largest increase is found in summer with a median change of +52.4% (Table S 4.3). The relative increase in specific discharge is highest in the semi-arid region (median: +110.3%), followed by the mediterranean region (median: +34.5%) and the humid-temperate region (median: +24.4%). Interestingly, the magnitude of specific discharge increase is higher than the increase in mean monthly precipitation. For all stations and all seasons, the Kolmogorov-Smirnov test revealed significant differences in the daily specific discharge distributions between El Niño and non-ENSO phases.

The observed expansions in the quantile area of the high-flow regime (ΔQA_{95}) reveal significant increases in either the frequency or the magnitude of high flows -or both- during El Niño phases, when comparing to non-ENSO conditions, particularly in Andean catchments located in the semi-arid and mediterranean climate zones (Figure 4.5; see Figure S 4.9 for individual station data). This observation holds across all seasons, but the increases in the high flow quantile area are less extreme in the spring season. Catchments in the humid-temperate region display only minor differences in the quantile area of high flows on an annual basis, but ΔQA_{95} increases more noticeably during the autumn and summer seasons (Figure 4.5, see Figure S 4.9 for individual station data). Even though there is some scatter, the differences in the quantile area of low flows (ΔQA_5) show predominantly negative values, which reveals that low flows occur less often during El Niño phases, as compared to non-ENSO phases (Figure 4.5, see Figure S 4.9 for individual station data).

The results from the inverse gamma fitting reveal both increased and decreased discharge variability, as indicated by the color-coding in Figure 4.5 (see Figure S 4.10 for individual station data). On an annual basis, we find a decrease in discharge variability during El Niño events (blue markers), despite the above-described increases in the quantile area of the high-flow regime (Figure 4.5). This reveals that, on an annual basis, either the frequency or the magnitude of the high discharges -or both- increase significantly with El Niño, but the frequency of intermediate discharges increases even more, so that overall, the variability of discharge is reduced (i.e., even though they increase, extreme discharges deviate less from the mean, because the latter increases further) (Figure S 4.7c). However, on a seasonal basis we also observe increasing discharge variability (decreasing k-value, red colors). This occurs in the semi-arid

region during autumn and winter, in the mediterranean region during winter, and in some parts of the humid-temperate region during autumn, spring and summer. This reveals that in these regions and for these seasons, El Niño has affected the high-flow regime more strongly than the low and intermediate flow regimes. Because the high-flow regime deviates more strongly from the mean, the discharge variability has increased.

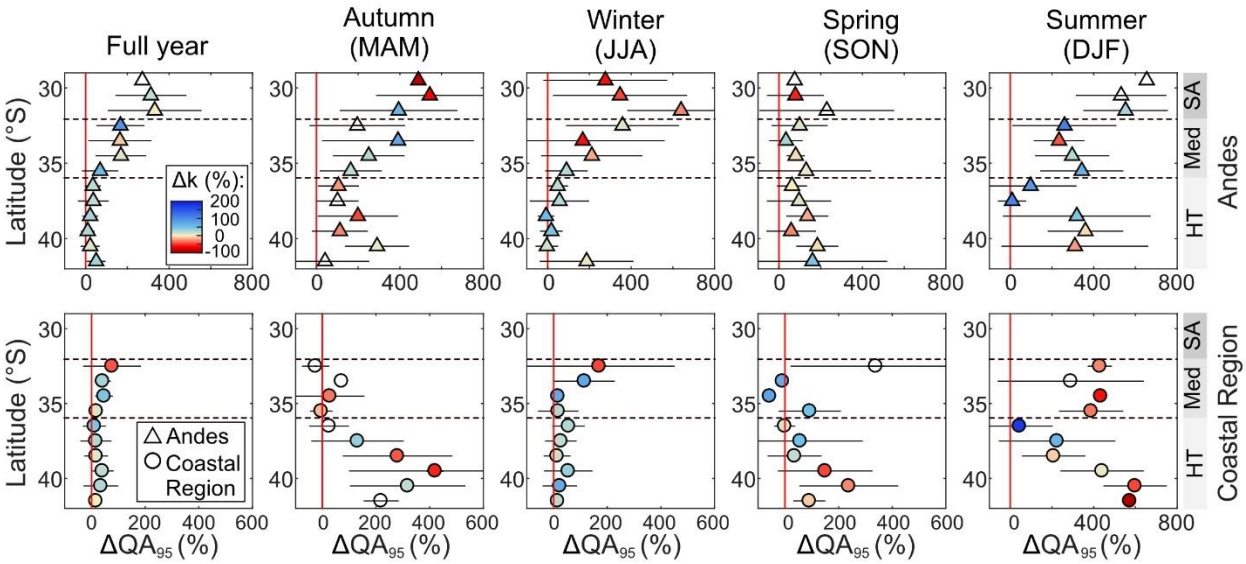

Figure 4.5: Latitudinal (1°) averages of the percent differences in the quantile area (ΔQA) and k-parameter (Δk) when comparing the high-flow regime during El Niño events to non-ENSO conditions. See Figure S 4.9 and Figure S 4.10 for individual station results for ΔQA and Δk. The method to create this figure is described in Figure 4.3. The markers present the mean value, and the error bars the 1σ-standard deviation, for all stations located in each 1°-latitudinal window. The upper row presents the changes in high-flow regime for the Andean region, while the lower row shows the changes for the coastal region. The markers are color-coded by the difference in k-parameter between El Niño and non-ENSO periods. Redder markers reveal increasing discharge variability, while bluer markers reflect decreasing discharge variability, according to the inverse gamma fitting. When the marker color is missing, no high-quality (R^2>0.97) fit exists for the latitudinal window.

4.4.2 La Niña

4.4.2.1 Differences in MMT and MMP

During La Niña events, about two third of the catchments (63.9%) experience higher mean monthly temperatures (Figure 4.6 and Table S 4.4) compared to non-ENSO phases. There is a latitudinal contrast in the regions that predominantly experience increasing versus decreasing temperatures. In the semi-arid region in the north, temperatures are lower in the majority of the catchments (70.8%); slightly more than half of the catchments show decreasing temperatures in the mediterranean region (58.1%), whereas in the humid-temperate region in the south the temperatures are higher in the majority (84%) of the catchments (Table S 4.4). The highest temperature

anomalies are found in the semi-arid region, where temperature decreases by up to -157.9% (T_5) and increases by up to +75.0% (T_{95}) (Table S 4.5). The temperature increase in the humid-temperate region is highest during the autumn and spring seasons, and lowest during the summer season (Figure 4.6 and Table S 4.5). Over the entire study area, mean monthly precipitation rates are lower in most of the catchments (97.1%) during La Niña phases compared to non-ENSO periods (Figure 4.6 and Table S 4.4). As observed with El Niño conditions, one exception in the typical pattern is the summer season, during which 44.4% of the catchments experience higher MMP (Table S 4.4). The catchments with increased MMP in summer are mainly located in the north (semi-arid and mediterranean climate zones) (Figure 4.6). The decreases in mean monthly precipitation are highest during the autumn (median: -40.5%) and spring (median: -31.9%) seasons (Figure 4.6 and Table S 4.5). The decrease in MMP shows a latitudinal pattern, being highest in the semi-arid region (median: -28.5%), followed by the mediterranean (median: -23.1%), and lowest in the humid-temperate (median: -19.4%) regions. The precipitation and temperature anomalies during La Niña events, based on the full 1950-2009 data, are shown in the data supplement (Figure S 4.11).

4.4.2.2 Differences in MMQsp and discharge variability

The mean monthly specific discharge is lower in most of the catchments (88.1%) during La Niña phases, as compared to non-ENSO conditions, a signal that is persistent throughout all seasons (Figure 4.6 and Table S 4.4). Similar to the patterns in precipitation, the largest decreases in specific discharge are found in the autumn (median: -33.1%) and winter seasons (median: -28.3%) (Table S 4.5). Likewise, the reduction in specific discharge is largest in the semi-arid region (median: -54.1%) in the north, whereas the mediterranean and humid-temperate regions show almost similar decreases in specific discharge (median: -19.3% and -17.1%, respectively) (Table S 4.5).

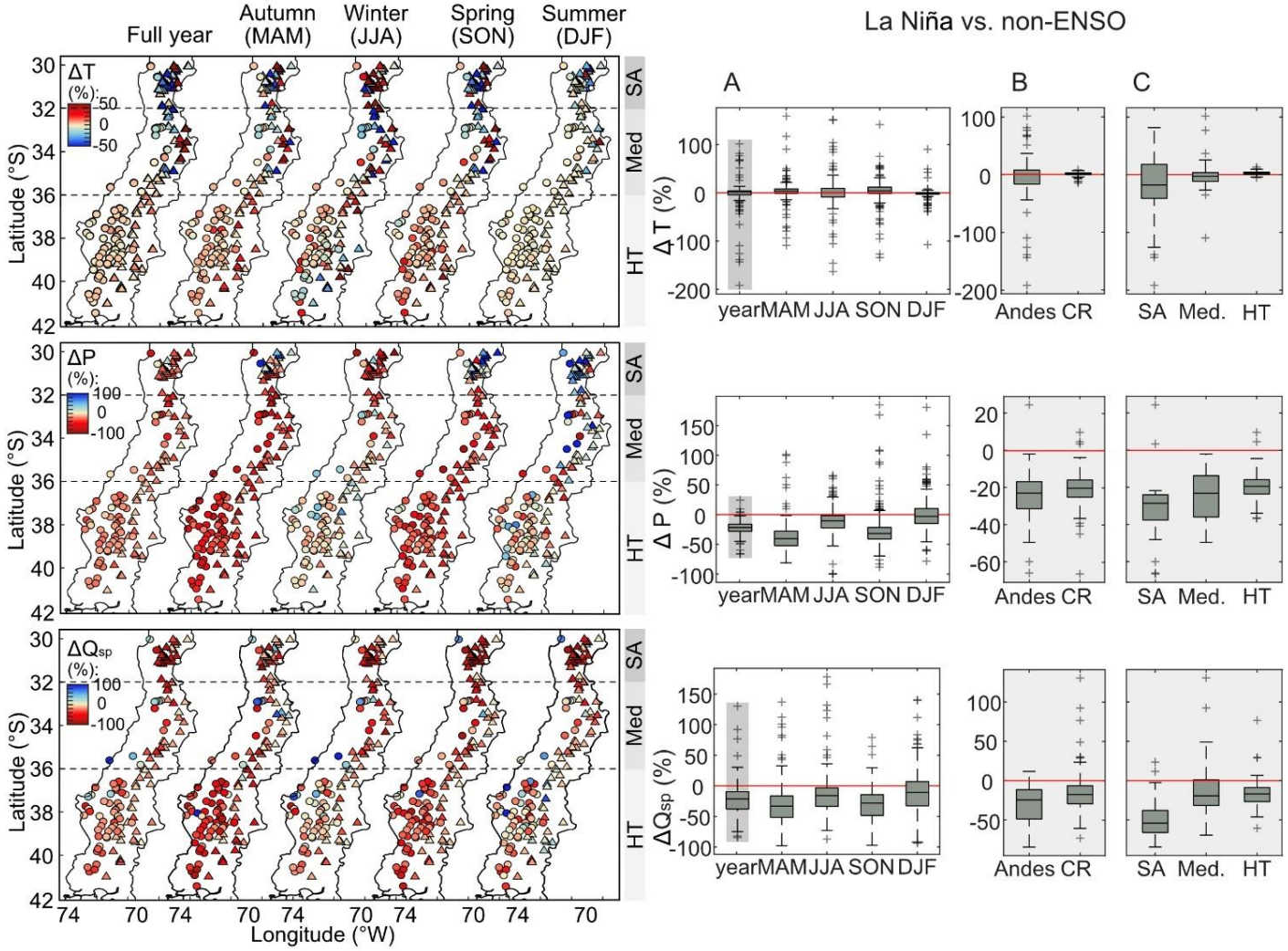

Figure 4.6: Differences (in %) in mean monthly temperature (ΔT), precipitation (ΔP), and specific discharge (ΔQ_{sp}) during El Niño events relative to non-ENSO conditions. The maps on the left show the spatial and seasonal differences for the full year and the different seasons. The dotted lines indicate the boundaries between the different climate zones, which are indicated in the subpanels on the right: semi-arid (SA), mediterranean (Med), and humid-temperate (HT). The boxplots in column A) show the variation of the data for the full year and the individual seasons. The grey shaded area represents the y-axis extent of the boxplot columns B) and C) that are based on the annual data. Boxplot column B) shows the differences between the Andes and the coastal region (CR), while boxplot column C) shows the differences between the three climate zones. The precipitation and temperature anomalies for the full 1950-2009 period are shown in the data supplement (Figure S 4.11).

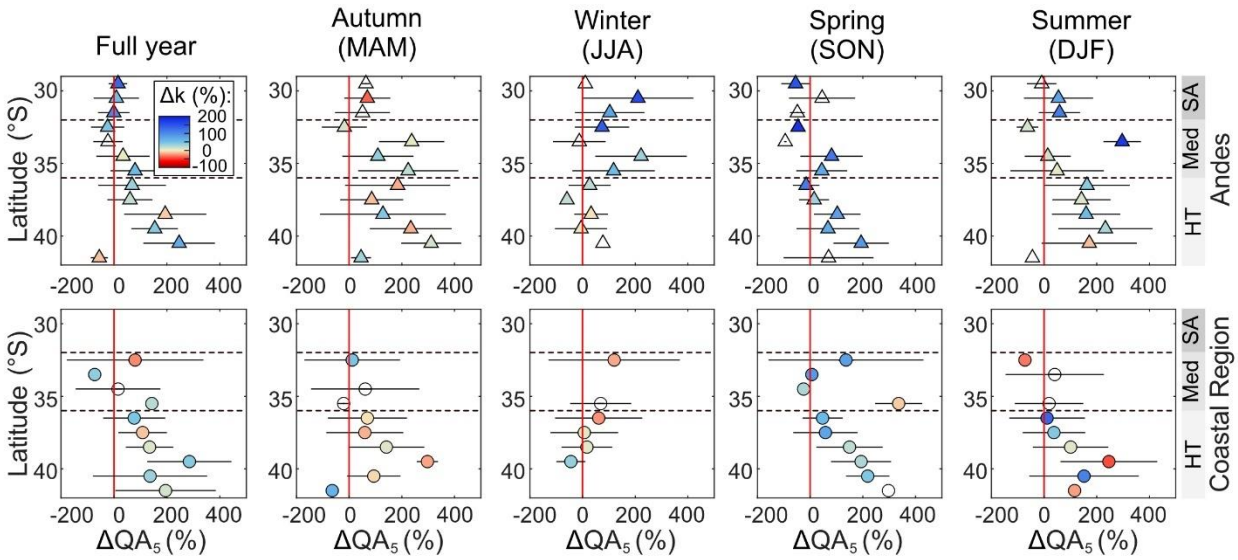

Figure 4.7: Latitudinal (1°) averages of the differences in the quantile area of the low-flow regime during La Niña events compared to non-ENSO conditions. See Figure S 4.12 and Figure S 4.13 for individual station results of ΔQA and Δk. The method to create this figure has been described in Figure 4.3. ΔQA and Δk present the percent differences of La Niña events relative to non-ENSO conditions. The markers present the mean value and the error bars the 1σ-standard deviation of all stations in each 1°-latitudinal window. The upper row presents the changes in high-flow regime for the Andean region, the lower row the changes for the coastal region. The markers are color-coded by the difference in k-parameter between La Niña and non-ENSO periods. Red markers reveal increasing discharge variability and blue markers reveal decreasing discharge variability according to the inverse gamma fitting. When the marker color is missing, no high-quality (R^2>0.97) fit exists for the latitudinal window.

Despite some scatter, the quantile areas for high flows (ΔQA_{95}) predominantly decrease during La Niña events as compared to non-ENSO phases (Figure S 4.12). This pattern is persistent over all seasons except for the summer, in which some catchments show increases in ΔQA_{95}. However, the scatter and lack of clear pattern prevent a meaningful discussion of this observation. The quantile area for low flows (ΔQA_5) is higher during La Niña events as compared to non-ENSO phases, especially in the humid-temperate region (Figure 4.7, see Figure S 4.12 for individual station data). This reveals that low-flow events either occur more frequently or show a decrease in magnitude, or both. This pattern is persistent over the autumn, spring, and summer seasons. For the winter season a roughly opposite latitudinal pattern is visible. The quantile area of low flow is higher in the northern region and lower in the humid-temperate region, relative to the other seasons. The inverse gamma fitting results reveal overall decreasing discharge variability over almost the entire latitudinal extent in the Andes, except for the autumn (Figure 4.7, see Figure S 4.13 for individual station data). Discharge variability increases in many catchments in the coastal region, except for the spring season, when it predominantly decreases (Figure 4.7, see Figure S 4.13 for individual station data).

4.5 Discussion

4.5.1 Temperature and precipitation anomalies during El Niño and La Niña

Previous studies that investigated ENSO-induced climatic anomalies in this part of the world typically present El Niño in central Chile as the warm and wet phase, while La Niña is described as the cold and dry phase (Díaz and Kiladis, 1995; Garreaud et al., 2009; Jaksic, 1998; Montecinos et al., 2000), a behaviour linked to anomalous sea surface temperatures (SST) in the Southern Pacific Ocean (Díaz and Kiladis, 1995; see Section 4.2). Overall, our study confirms the spatial and seasonal patterns in temperature and precipitation anomalies found in previous studies (Garreaud et al., 2009; Garreaud and Battisti, 1999; Meza, 2013; Montecinos et al., 2000; Montecinos and Aceituno, 2003; Oertel et al., 2020). Mean monthly temperatures are slightly higher in most of the catchments during El Niño events, except for some catchments in the semi-arid region which experience colder temperatures. The warmer air temperatures during El Niño phases have been attributed to the heating of air over the warmer ocean (Díaz and Kiladis, 1995). Garreaud et al. (2009) also reported colder temperatures in the semi-arid region, which they attributed to the higher precipitation and cloud cover, that reduce direct solar insolation and increase surface moisture. Although the nature of our data does not allow us to determine whether this is indeed the driving mechanism, we do find that the region with the strongest precipitation increases overlaps with the region with colder temperatures. During La Niña phases, temperatures decrease in the two northern regions (semi-arid and mediterranean) but increase in the humid-temperate region in the south, as compared to non-ENSO conditions. This finding of higher temperatures in the south contradicts the typically cold conditions that are associated with La Niña events in central Chile, driven by cold sea surface temperatures (Diaz and Kiladis, 1995). However, Montecinos et al. (2000) also pointed out that La Niña phases cannot be considered as exactly the opposite of the warm and wet El Niño conditions. Even though there are spatial and seasonal variations in MMT anomalies during El Niño and La Niña years, a seasonal pattern that can, like MMP, be attributed to the position or intensity of the SPH, is lacking. Potentially, the abnormal behaviour of the SPH during the summer season, as compared to the rest of the year, could be the reason why the temperature anomalies in summer deviate from the temperature anomalies in the other seasons, but this needs to be further investigated.

The largest relative changes in precipitation during both El Niño and La Niña phases are found in the semi-arid region, followed by the mediterranean region, and then the humid-temperate region. We suggest that this stems from the fact that an increase or decrease of a few millimetres of MMP in a semi-arid region results in a large relative change, as compared to a difference of a few millimetres in a more humid region (Garreaud et al., 2009). The wetter-than-normal conditions that we report during El Niño agree with previous studies and can be linked to a weakening of the intensity of the SPH, whereas the drier-than-normal conditions during La Niña can be linked to a

strengthening of the intensity of the SPH (Garreaud and Battisti, 1999; Montecinos and Aceituno, 2003; Rutllant et al., 2003). The seasonal variation in the latitudinal position of the strongest climatic anomalies has been attributed to the seasonal movement in the position of the SPH (Montecinos and Aceituno, 2003). During both El Niño and La Niña events, the precipitation anomalies during the summer season deviate from those in other seasons. This has been observed in previous studies and is related to the contrasting summer behaviour of the SPH, as compared to the other seasons (Garreaud et al., 2009; Montecinos et al., 2000; Montecinos and Aceituno, 2003). The anomalously dry conditions in the summer season during El Niño phases have been linked to the intensification of ridges in the southern tip of the SPH, which are also responsible for the arid conditions in northern Chile (Montecinos and Aceituno, 2003).

4.5.2 Specific discharge anomalies during El Niño and La Niña

Mean monthly values of specific discharge (MMQsp) follow the expectations of wet conditions during El Niño and dry conditions during La Niña, but we observe distinct spatial and seasonal patterns. Following the MMP anomalies pattern, the largest relative differences in MMQsp during El Niño and La Niña phases are found in the semi-arid region, followed by the mediterranean region, and then the humid-temperate region. As was discussed for the MMP anomalies (Section 4.5.1), this can be explained by the fact that a change of similar absolute magnitude has a larger relative effect in a semi-arid region as compared to a humid region.

The ENSO-induced hydrological anomalies during both El Niño and La Niña events are most extreme in the Andean catchments, compared to catchments from the coastal region. The Andes feature higher elevation and steeper topography compared to the coastal region and are therefore characterised by lower temperatures, sparser vegetation cover (Alvarez-Garreton et al., 2018), and likely thinner regolith thicknesses. All these factors impose reduced evapotranspiration and infiltration rates, which most likely lead to less modulated, flashier river discharge responses to precipitation events in the Andes, when compared to the coastal region. However, it is not possible to assess whether these contrasting catchment attributes affect the observed differences in hydrological anomalies between the coastal region and the Andes, because both regions are subjected to different climatic forcing in the first place.

Even though the annual patterns of MAP and MAQsp anomalies during the El Niño phase look very similar, the seasonal MMQsp patterns are quite different from the corresponding MMP patterns, suggesting a non-linear relationship between precipitation and river discharge (Figure 4.4). Direct comparison between ΔMMP and ΔMMQsp during El Niño events reveals that the seasonal deviations between precipitation and river discharge anomalies are largest in the Andes as compared to the coastal region (Figure 4.8). Furthermore, the MMP and MMQ anomalies deviate most strongly in the summer and autumn seasons, as reflected by the large scatter, but show smaller deviations during the winter season. We explain these observations by the time

lag between precipitation input and river discharge output, introduced by inter-seasonal hydrological storage within each catchment. At such timescale, water can naturally be stored in a catchment mostly in the form of snow accumulation, groundwater storage, or else storage in the unsaturated zone of regolith or fractured bedrock. We suggest that the higher precipitation input during El Niño autumn and winter in the northern Andean catchments will partly enhance streamflow (Figure 4.4) but also enhance snow accumulation, causing a delayed hydrological response during the snow melt season, as indicated by the strong increases in mean discharge and high flow during summer. This is supported by previous studies that measured enhanced snow accumulation in the Andes during El Niño events (Cordero et al., 2019; Cortés and Margulis, 2017; Masiokas et al., 2006; Oertel et al., 2020). Other studies reported a similar river discharge response in northern-Andean basins during El Niño spring and summer and also attributed this to an enhanced snow melt peak (Piechota et al., 1995; Waylen et al., 1993; Waylen and Caviedes, 1990). Finally, Masiokas et al. (2006) directly compared ENSO-induced snow accumulation to streamflow patterns and found highly significant correlations and similar interannual fluctuations between mean snow water equivalent in the Andes and river discharge of 10 Chilean and Argentinean rivers between 31-37°S. However, as briefly mentioned above, a fraction of the winter precipitation in northern-Andean basins also produces direct streamflow. This can be observed by strong increases in MMQsp (Figure 4.4), the increase in the high-flow quantile area (Figure 4.5), and the extreme outliers in the ΔMAP-ΔMAQsp comparison plot (Figure 4.8). An increase in winter streamflow in high-elevation Andean basins has also been observed in previous studies and has been attributed to El Niño-induced warm precipitation (i.e., rainfall) and rain-on-snow events, which produce high magnitude river discharge (Waylen et al., 1993; Waylen and Caviedes, 1990).

Catchments that are located in the humid-temperate region receive the highest precipitation anomalies during spring, due to the seasonal southward shift of the SPH (Montecinos and Aceituno, 2003). Because catchments have thick regolith and large soil moisture and groundwater storages these higher precipitation anomalies likely infiltrate in the regolith, result in groundwater recharge and provide baseflow in the summer and autumn seasons, observed by lower MMP anomalies but higher MMQ values.

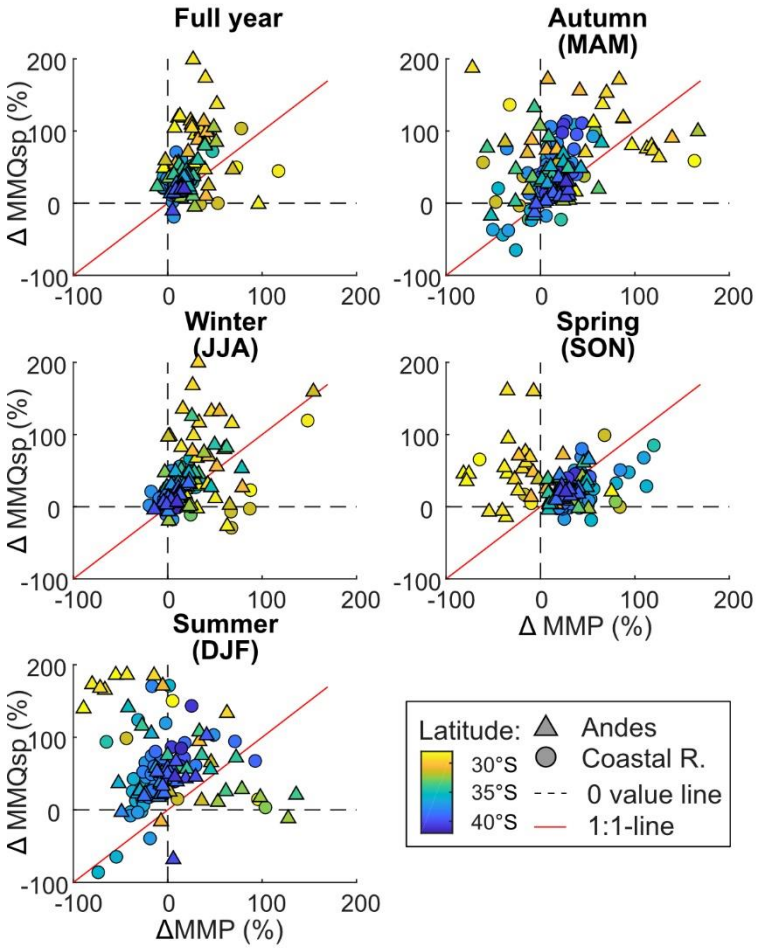

Figure 4.8: Scatterplot comparing differences in mean monthly precipitation (MMP) and mean monthly specific discharge (MMQsp) between El Niño and non-ENSO conditions. The scatter includes basins located in the Andes (triangles) and the coastal region (dots), the color-coding represents the latitude. The dotted lines indicate the boundaries between the positive and negative domain. Red line is the 1:1-line.

The observed increase in high flows (increasing ΔQA_{95}) during El Niño may be partially explained by a two times higher likelihood of intense precipitation events (Poveda et al., 2020). However, the enhanced snow accumulation and groundwater storage can additionally contribute to an increased high-flow signal during the snowmelt and baseflow season. The snow melt and groundwater contribution to baseflow provides an additional discharge contribution on top of already wet El Niño conditions (Figure 4.5).

Despite those few cases where the increase in the quantile area of high flow (ΔQA_{95}) overlapped with increasing discharge variability (e.g., winter in the semi-arid region), we observe that for Andean catchments both on an annual basis and for most seasons, an increase in ΔQA_{95} is combined with decreasing discharge variability. This reveals that during El Niño, the daily discharge distribution often shifts towards higher discharge magnitudes, but the maximum magnitude of high flows does not significantly increase (Figure S 4.7c). The decrease in discharge variability likely results from the fact that

enhanced snow melt strongly contributes the shift of the discharge distributions towards higher discharge magnitudes. Less variable discharge is typical for snow covered basins (Deal et al., 2018; Rossi et al., 2016; Waylen et al., 1993), because snow melt produces non-flashy river discharge over a longer hydrological response time, as it has an upper bound controlled by available solar radiation. The fact that the increase in the quantile area of high flow (ΔQA_{95}) for coastal region catchments often pairs with increasing discharge variability reveals in coastal region catchments the occurrence of high flow events is induced by intense El Niño precipitation storms (Poveda et al., 2020).

To conclude, during El Niño events, both the mean river discharge and high-flow regime predominantly increase in the semi-arid and the mediterranean regions. Andean snow dynamics is found to be an important hydrological process that introduces seasonal modulation of the ENSO-induced climatic anomalies. The implications of such increases for water resources management are discussed in Section 4.5.3.

During La Niña events, both the annual and seasonal MMQsp anomalies show a similar spatial pattern when compared to the MMP anomalies (Figure 4.6). The decrease in both MMP and MMQsp is highest in the semi-arid region, followed by the mediterranean and humid-temperate regions. Strikingly, at the annual scale, the shift of the discharge distribution towards low-flow magnitudes during La Niña phases predominantly occurs in the humid-temperate region (Figure 4.7), which indicates that the large reductions in mean discharge in the semi-arid and mediterranean regions are predominantly driven by decreases in the intermediate to high discharge magnitudes. This is also explained by decreasing discharge variability (Δk, blue markers) in Andean catchments (Figure 4.7). We interpret this to be caused by the presence of snow cover and glaciers in the semi-arid and mediterranean regions, which maintain the low-flow regime, even during periods of low precipitation (Masiokas et al., 2006; Milana, 1998). This may partly result in runoff directly generated from snow or glacier melt, but also by groundwater recharge or by snow melt water in snow-dominated basins, which are all mechanisms generating streamflow at a later stage (Alvarez-Garreton et al., 2021; Ayala et al., 2020). As La Niña events often follow upon El Niño events, part of the El Niño-enhanced snow accumulation has been found in some years to still remain, in the case of high-elevation catchments (Cordero et al., 2019; Cortés and Margulis, 2017; Masiokas et al., 2006). Furthermore, as water from snowmelt is the main water source for groundwater recharge and snow-dominated catchments have a longer hydrological memory, higher groundwater levels from resulting from enhanced snow accumulation during El Niño can provide higher baseflow during subsequent La Niña events (Alvarez-Garreton et al., 2021). We also suggest that this snow melt contribution to river discharge in Andean catchments is the reason why discharge variability decreases during La Niña (Deal et al., 2018; Rossi et al., 2016; Waylen et al., 1993).

The fact that persistent snow cover and glaciers are less abundant in the humid-temperate region, characterizes this region within the pluvial-type hydrological regime (Alvarez-Garreton et al., 2021; Oertel et al., 2020). Snowmelt cannot maintain a minimum baseflow in this region, which makes it more sensitive to precipitation deficits

during La Niña events. This is also reflected in the variability of discharge, which mainly increases during La Niña in this region. The implications of these observations for water resources management are further discussed in Section 4.5.3.

4.5.3 Implications for water resources management

This study reveals that ENSO-induced hydrological anomalies vary strongly in magnitude and seasonality across the various climatic zones and the Andes and coastal region. This confirms the importance of high-resolution observational studies to cover regional differences in the hydrological response to climatic anomalies, as well as the need for region-specific water resources and risk management strategies (Ayala et al., 2020; Blöschl et al., 2019; Kemter et al., 2020).

As observed for other regions on the world (Lee et al., 2018; Mosley, 2000), snow dynamics also plays a crucial role in modulating the ENSO-induced climatic anomalies in Andean catchments in central Chile. Not only do the high precipitation anomalies during El Niño winters drive a direct, rainfall-induced increase in discharges in the same winter season, but furthermore, they result in enhanced snow accumulation, and thus cause a second, snowmelt-generated increase in river discharges in the subsequent summer (Piechota et al., 1995; Waylen et al., 1993; Waylen and Caviedes, 1990). This specifically affects the semi-arid and mediterranean regions, which experience MMQsp increases of up to +180% and +105% (Q_{95}, Table S 4.3), respectively, as well as strong increases in the high-flow regime (Figure 4.4 and Figure 4.5). In fact, the semi-arid and mediterranean regions are known as flood- risk prone areas, with reports of past large floods coinciding with El Niño events (Aceituno et al., 2009; Jenny et al., 2002; Waylen and Poveda, 2002).

Despite its influence on flood risk, the augmented enhanced snow cover typically resulting from El Niño events is also crucial for water availability in the semi-arid and mediterranean regions (Cordero et al., 2019; Masiokas et al., 2006). Snowmelt-generated runoff has the potential to reduce the impact of droughts (during, e.g., subsequent La Niña events) in these regions, because waters from snow and glacier melt contribute a minimum discharge level, as discussed in Section 4.5.2 (Masiokas et al., 2006; Milana, 1998).

The effects of ENSO on snow accumulation and river discharge, therefore, present major socioeconomic challenges for the semi-arid and mediterranean regions in central Chile, where ~55% of the population of the country resides. On the one hand, enhanced flooding risks during El Niño events constitute a significant threat to the population and infrastructure (Ward et al., 2014, 2016). On the other, the predominant source for crop irrigation, domestic water use, and hydropower generation in these regions is river discharge from snow and glacier melt (Alvarez-Garreton et al., 2018; Cordero et al., 2019; Masiokas et al., 2006). Even though the precipitation deficits incurred during La Niña periods affect the hydrology of the humid-temperate region

most strongly, as shown by a higher frequency of low-flow events, these have presumably smaller socioeconomic impact, as this region generally receives higher rainfall, has larger groundwater storages, and the current water demands for crop irrigation and hydropower are much smaller, in relative terms, as compared to the mediterranean and semi-arid part of the country (Alvarez-Garreton et al., 2018; Masiokas et al., 2006).

This study highlights the need for incorporating probabilistic ENSO flood and drought risk forecasting on top of regular meteorological forcing forecast, to improve flood and drought predictions. However, the strong modulation of the ENSO-induced climatic anomalies shows that flood and drought risk assessments cannot be derived directly from ENSO-induced precipitation anomalies, but should also consider other hydrologically-relevant processes (Emerton et al., 2017, 2019; De Perez et al., 2017), such as snow dynamics, groundwater fluctuations, and antecedent hydrological conditions (e.g., Alvarez-Garreton et al., 2021; Masiokas et al., 2006). Considering the lead time of ENSO forecasts, and the subsequent time lag between snow accumulation and river discharge generation, there is potential for early flood and drought warning and mitigation in snow-covered basins.

Furthermore, water resources management strategies are required to mitigate increasing water-related challenges for central Chile under future climate change, as modelling studies predict that the climate will shift towards more arid conditions (Boisier et al., 2018a; Cai et al., 2020). Moreover, as the zero-degree isotherm is expected to rise in Andean basins (Mardones and Garreaud, 2020), as Andean glaciers are rapidly shrinking due to climate change (Barcaza et al., 2017; Braun et al., 2019; Dussaillant et al., 2019), it is likely that currently snowmelt-dominated basins will shift towards a rainfall-dominated discharge regime in the future. How the frequency and amplitude of ENSO events will respond to future climate change is debated. Stevenson (2012) compared results from different climate models and observed an increase in ENSO amplitude in only 4 out of 11 models, whereas other studies suggest a future increase in the frequency of El Niño events (Cai et al., 2014). Under an increased frequency of El Niño events, the semi-arid and mediterranean regions may experience wetter-than-normal conditions more frequently, which is advantageous under the predicted expanding arid conditions. However, due to the above-described expected transition of snowfall-dominated towards rainfall-controlled hydrology, the strong increases in winter precipitation would increase the risk of winter floods. Therefore, on top of drought-mitigation strategies for the overall more-arid future climate, flood risk management may become increasingly important in the semi-arid and mediterranean regions, to mitigate El Niño-induced winter floods.

No matter whether or not the amplitude and frequency of ENSO events increase under climate change, it is clear that ENSO-induced climatic anomalies and the resulting inter-seasonal hydrological anomalies will undoubtedly add extra complexity to climate adaptation strategies. Modelling studies on the changes in climate and ENSO

amplitude and frequency, and the specific effects they would have on central Chile are needed to anticipate future water-related challenges in central Chile.

4.6 Conclusion

In this study, we investigated the effects of the El Niño Southern Oscillation (ENSO) on climatic and hydrological anomalies for 183 river catchments located in central Chile. Generally, we observed increasing precipitation and specific discharge rates during El Niño and decreasing precipitation and discharge rates during La Niña but detected large spatial and seasonal variations. The semi-arid region experiences the strongest climatic and hydrological anomalies during both El Niño and La Niña phases, followed by the mediterranean and the humid-temperate regions. Furthermore, we conclude that rain- and snow-dominated catchments display a contrasting hydrological response to ENSO, as snow dynamics in the Andes strongly modulate the ENSO-induced climatic anomalies, whereas rainfall-dominated basins show a discharge response that is somewhat modulated by groundwater dynamics, but overall, shows larger similarities to the ENSO-induced climatic anomalies.

During El Niño, river catchments located in the semi-arid and mediterranean regions are found to experience high-flow conditions in the winter, when the climatic anomalies are highest, but also during the summer as result of a delayed discharge peak induced by enhanced snowmelt. River discharge in catchments located in the rainfall-dominated basins in the humid-temperate region are most strongly affected by precipitation deficits during La Niña, whereas snowmelt-generated runoff provides a minimum low flow in snowmelt-dominated basins.

These ENSO-induced climatic and hydrological anomalies add extra complexity on top of an already challenging climate change scenario for central Chile. This poses major socio-economic challenges, in particular for the semi-arid and mediterranean regions of Chile, where the majority of the population resides, that are strongly dependent on river water for hydropower generation, crop irrigation, and domestic use. We conclude that improved probabilistic ENSO flood and drought risk forecasts and water resources management strategies are required to mitigate floods and droughts under future climate change: These strategies should be performed differently for snow- and rainfall-dominated catchments, due to their different responses to ENSO.

4.7 Author contributions

R. van Dongen carried out the data analysis with help from all co-authors. D. Scherler acquired the project funding and was the main supervisor. D. Wendi conducted the interpolation of the data gaps in the daily discharge time series. C. Meier supported with the data interpretation in the context with Chilean climate and hydrology. R. van Dongen prepared the manuscript with contributions from all co-authors.

4.8 Competing interests

The authors declare that they have no conflict of interest.

4.9 Acknowledgements

We acknowledge support from the German Science Foundation (DFG) priority research programme SPP-1803 "EarthShape: Earth Surface Shaping by Biota" (grant SCHE 1676/4-1 to D.S.).

4.10 Supplementary tables

Table S 4.1: Station information for all discharge stations used in this study: ID, station name, coordinates, classified (class) as located in the Andes or the coastal region (Coastal), start and end date of the monitoring period, amount of daily discharge observations (n), catchment area (Area), and mean catchment elevation (Mean elevation).

ID	Station Name	Latitude	Longitude	Class	Start monitoring period	End monitoring period	n	Area	Mean elevation
		(°N)	*(°E)*					*(km^2)*	*(m)*
4302001	Río Toro antes Junta Río La Laguna	-29.971	-70.093	Andes	05/06/1985	09/03/2018	11185	467.4	467.4
4311001	Estero Derecho en Alcohuaz	-30.221	-70.493	Andes	03/11/1983	31/07/2017	12249	338.2	338.2
4313001	Río Cochiguaz en El Peñón	-30.122	-70.434	Andes	11/08/1983	08/06/2017	12252	675.3	3510.8
4314001	Río Claro en Montegrande	-30.090	-70.493	Andes	24/01/1947	31/03/1983	12673	1249.1	3328.8
4314002	Río Claro en Rivadavia	-29.978	-70.553	Andes	16/03/1914	09/03/2018	34943	1512.8	3198.9
4400001	Estero Culebrón en El Sifón	-29.979	-71.286	Coastal	01/03/1986	08/07/2017	11020	190.4	286.6
4501001	Río Hurtado en San Agustín	-30.462	-70.536	Andes	17/12/1962	18/02/2018	18321	672.4	3723.7
4501002	Río Hurtado en Las Breas	-30.383	-70.600	Andes	10/06/1928	30/11/1977	10721	840.2	3564.7
4502001	Río Hurtado en La Cortadera	-30.333	-70.767	Andes	16/02/1968	28/02/1983	4388	1258.0	3061.0
4503001	Río Hurtado en Angostura de Pangue	-30.439	-71.002	Andes	01/09/1918	09/03/2018	32616	1837.3	2554.2
4506002	Río Hurtado en Entrada Embalse Recoleta	-30.477	-71.069	Coastal	26/05/1928	31/01/1984	7585	2259.2	2265.4
4511002	Río Grande en Las Ramadas	-31.012	-70.581	Andes	18/05/1961	08/02/2018	18920	568.5	3097.6
4512001	Río Tascadero en Desembocadura	-31.012	-70.664	Andes	23/10/1962	31/07/2017	18576	241.0	2888.4
4513001	Río Grande en Cuyano	-30.924	-70.773	Andes	05/05/1959	09/03/2018	20719	1286.6	2726.1
4514001	Río Mostazal en Cuestecita	-30.813	-70.613	Andes	03/10/1969	31/07/2017	16358	393.7	3066.7
4515002	Río Mostazal en Carén	-30.842	-70.769	Andes	24/07/1972	31/07/2017	13538	640.2	2588.9
4516001	Río Grande en Coipo	-30.783	-70.822	Andes	01/12/1942	26/04/1978	9143	2134.2	2548.1

ID	Station Name	Latitude (°N)	Longitude (°E)	Class	Start monitoring period	End monitoring period	n	Area (km^2)	Mean elevation (m)
4520001	Río Los Molles en Ojos de Agua	-30.744	-70.439	Andes	22/05/1970	31/07/2017	16041	155.3	3677.9
4522001	Río Rapel en Paloma	-30.733	-70.617	Andes	02/10/1941	23/03/1983	4702	510.5	3221.4
4522002	Río Rapel en Junta	-30.708	-70.873	Andes	01/04/1959	31/07/2017	18595	820.6	2661.3
4523001	Río Grande en Agua Chica	-30.702	-70.900	Andes	15/09/1946	28/02/1983	12390	3015.8	2544.0
4523002	Río Grande en Puntilla San Juan	-30.705	-70.924	Andes	01/03/1942	09/03/2018	25038	3529.4	2483.6
4530001	Río Cogotí en Fraguita	-31.112	-70.885	Andes	14/09/1971	09/03/2018	14957	490.5	2601.4
4531001	Río Cogotí en Cogotí 18	-31.083	-70.956	Andes	01/01/1942	31/03/1983	9880	530.9	2500.9
4531002	Río Cogotí Entrada Embalse Cogotí	-31.033	-71.040	Andes	10/01/1953	25/02/2018	18232	753.1	2123.7
4533002	Río Pama en Valle Hermoso	-31.266	-70.991	Andes	27/10/1987	31/07/2017	10022	155.7	2289.8
4703001	Río Choapa sobre el Río Valle	-31.983	-70.567	Andes	07/12/1965	03/12/1982	4366	1091.6	3188.7
4703002	Río Choapa en Cuncumén	-31.967	-70.594	Andes	14/10/1965	09/03/2018	17941	1131.6	3142.3
4711001	Río Choapa en Salamanca	-31.812	-70.930	Andes	01/06/1931	09/03/2018	20875	2211.9	2634.9
4712001	Río Chalinga en La Palmilla	-31.696	-70.716	Andes	29/10/1991	24/01/2018	9330	243.9	3037.6
5100001	Río Sobrante en Piadero	-32.225	-70.712	Andes	06/08/1928	09/03/2018	19263	241.1	2609.6
5101001	Río Pedernal en Tejada	-32.071	-70.756	Andes	22/12/1962	31/07/2017	14260	56.1	1624.6
5200001	Río Alicahue en Colliguay	-32.330	-70.738	Andes	30/11/1963	09/03/2018	17991	348.0	2402.6
5401003	Río Juncal en Juncal	-32.863	-70.168	Andes	15/02/1913	09/03/2018	20985	343.1	3661.9
5411001	Estero Pocuro en El Sifón	-32.916	-70.540	Andes	19/12/1930	31/07/2017	26261	181.0	2006.1
5411002	Estero Pocuro antes Junta Río Aconcagua	-32.764	-70.725	Andes	01/11/1929	01/08/1983	7779	488.8	1393.2
5420002	Estero de los Campos antes Junta Río Aconcagua	-32.802	-70.929	Coastal	12/07/1962	08/07/1983	7348	105.7	713.8
5422001	Estero Las Vegas en Desembocadura	-32.835	-70.998	Coastal	01/07/1962	04/06/2002	12562	328.4	840.5
5423004	Estero Romeral antes Junta Río Aconcagua	-32.833	-71.083	Coastal	20/07/1962	30/06/1984	5333	37.0	804.8
5423006	Estero Rabuco en Fundo Rabuco	-32.867	-71.133	Coastal	01/01/1969	07/09/1983	5012	124.4	801.2
5702001	Río Volcón en Queltehues	-33.806	-70.209	Andes	26/10/1914	09/03/2018	29614	523.4	3366.8
5705001	Río Colorado antes Junta Río Olivares	-33.490	-70.134	Andes	30/03/1977	09/03/2018	11834	783.4	3737.2

ID	Station Name	Latitude	Longitude	Class	Start monitoring period	End monitoring period	n	Area	Mean elevation
		(°N)	*(°E)*					*(km^2)*	*(m)*
5706001	Río Olivares antes Junta Río Colorado	-33.488	-70.137	Andes	09/02/1977	09/03/2018	13787	541.6	3690.0
5707002	Río Colorado antes Junta Río Maipo	-33.588	-70.367	Andes	25/07/1940	09/03/2018	25235	1662.8	3418.7
5715001	Río Paine en Longitudinal	-33.833	-70.750	Coastal	04/12/1962	07/12/1983	6602	317.6	773.3
5721001	Estero Yerba Loca antes Junta San Francisco	-33.341	-70.364	Andes	03/11/1986	09/03/2018	11372	110.0	3424.3
5730008	Quebrada Ramón en Recinto EMOS	-33.433	-70.514	Andes	13/02/1991	31/01/2016	8456	35.6	1982.6
5741001	Estero Puangue en Boquerón	-33.167	-71.131	Coastal	26/06/1929	31/07/2017	22212	144.2	1136.5
6000003	Río Las Leas antes Junta Río Cachapoal	-34.363	-70.306	Andes	26/11/2006	09/03/2018	3699	172.8	2949.8
6002001	Río Cortaderal antes Junta Río Cachapoal	-34.367	-70.326	Andes	06/09/1985	09/03/2018	5575	425.7	2961.1
6003001	Río Cachapoal 5 Km. aguas abajo Junta Cortaderal	-34.346	-70.376	Andes	27/06/1989	09/03/2018	8421	964.7	2930.0
6006001	Río Pangal en Pangal	-34.247	-70.328	Andes	08/11/1985	09/03/2018	10515	519.9	3071.2
6011001	Estero de la Cadena antes Junta Río Cachapoal	-34.184	-70.844	Coastal	10/05/1983	09/03/2018	11355	598.9	706.0
6018001	Estero Zamorano en Puente El Niche	-34.431	-71.168	Coastal	16/10/1985	30/06/2017	9833	1022.6	672.3
6025001	Río Tinguiririca aguas abajo Junta Río Azufre	-34.816	-70.564	Andes	08/05/1970	22/04/1993	5519	970.4	2841.5
6027001	Río Claro en El Valle	-34.687	-70.874	Andes	01/05/1970	09/03/2018	16057	349.4	1604.5
6028001	Río Tinguiririca bajo Los Briones	-34.719	-70.827	Andes	01/11/1921	09/03/2018	26634	1438.3	2549.8
7103001	Río Claro en Los Queñes	-34.998	-70.809	Andes	01/05/1929	30/06/2017	31614	354.4	1856.6
7104001	Estero El Manzano antes Junta Río Teno	-34.965	-70.942	Andes	01/08/1959	30/10/1984	8408	133.7	1276.1
7112001	Río Colorado en Junta con Palos	-35.278	-71.003	Andes	11/11/1917	30/06/2017	21702	877.9	2288.2
7115001	Río Palos en Junta con Colorado	-35.274	-71.016	Andes	01/05/1947	09/03/2018	18048	490.0	1973.4
7116001	Estero Upeo en Upeo	-35.173	-71.091	Andes	15/02/1963	30/06/2017	17984	367.2	1197.1
7317003	Río Melado en Zona De Presa	-35.754	-71.086	Andes	20/12/2002	09/03/2018	5559	2269.4	1921.4
7317005	Río Melado en El Salto	-35.884	-71.019	Andes	01/01/2003	09/03/2018	5375	2127.6	1964.3
7320003	Río Claro en San Carlos	-35.699	-71.068	Andes	01/01/2000	09/03/2018	5574	401.2	1932.8
7330001	Río Perquilauquén en San Manuel	-36.376	-71.623	Andes	02/09/1930	09/03/2018	27100	502.4	1100.3

ID	Station Name	Latitude (°N)	Longitude (°E)	Class	Start monitoring period	End monitoring period	n	Area (km^2)	Mean elevation (m)
7340001	Estero Cardo Verde en Lo Ubaldo	-35.883	-72.017	Coastal	19/08/1968	31/12/1984	3776	158.6	122.8
7350003	Río Longaví en El Castillo	-36.256	-71.338	Andes	21/05/1964	15/06/2017	16410	466.9	1563.6
7354001	Río Achibueno en Los Peñascos	-35.964	-71.488	Andes	22/03/1947	30/09/1986	12580	974.2	1263.9
7354002	Río Achibueno en La Recova	-36.003	-71.442	Andes	01/11/1986	09/03/2018	11069	894.3	1328.9
7355003	Río Ancoa antes Tunel Canal Melado	-35.867	-71.117	Andes	30/11/1961	16/04/1995	6672	84.5	1682.7
7358001	Río Putagán en Yerbas Buenas	-35.772	-71.585	Coastal	14/04/1946	31/01/2016	22857	390.5	471.5
7372001	Río Claro en Camarico	-35.178	-71.385	Andes	01/03/1936	30/03/2017	23490	703.0	969.3
7374001	Río Lircay en Puente Las Rastras	-35.486	-71.293	Andes	18/12/1961	30/06/2017	17973	382.3	1052.0
7381001	Estero Los Puercos en Puente Los Puercos	-35.374	-71.829	Coastal	20/02/1986	30/06/2017	10936	558.8	205.5
7400001	Río Loanco en Desembocadura	-35.569	-72.583	Coastal	03/07/1987	30/09/2010	7535	222.7	350.9
8104001	Río Sauces antes Junta con Ñuble	-36.665	-71.274	Andes	31/10/1966	30/06/2017	16326	606.7	1682.9
8112001	Río Niblinto antes Canal Alimentador Embalse Coihueco	-36.655	-71.756	Andes	02/02/1971	30/06/2017	10374	162.0	1157.1
8117001	Río Chillán en Longitudinal	-36.633	-72.217	Coastal	14/02/1958	12/05/1983	6036	730.8	542.4
8117004	Río Chillán en Esperanza	-36.787	-71.749	Andes	03/03/1939	03/09/1994	19878	206.0	1295.3
8117005	Río Chillán en Camino a Confluencia	-36.617	-72.317	Coastal	29/09/1956	30/06/2017	15908	798.3	502.2
8117006	Río Chillán en Esperanza N 2	-36.800	-71.661	Andes	27/11/2003	09/03/2018	4702	167.4	1411.6
8117008	Río Quilmo en Camino a Yungay (Ca)	-36.667	-72.150	Coastal	19/07/1957	17/04/1995	9591	129.0	281.7
8118001	Río Changaral Camino a Portezuelo	-36.550	-72.283	Coastal	01/10/1956	31/07/2004	13309	1131.9	165.8
8123001	Río Itata en Cholguán	-37.150	-72.067	Coastal	22/01/1924	30/06/2017	30629	859.6	833.7
8124001	Río Itata en General Cruz	-36.933	-72.350	Coastal	05/01/1956	30/06/2017	18576	1661.5	612.8
8124002	Río Itata en Trilaleo	-37.067	-72.183	Coastal	11/11/1957	30/06/2017	17585	1147.7	752.0
8130002	Río Diguillín en San Lorenzo (Atacalco)	-36.924	-71.576	Andes	23/05/1946	09/03/2018	25113	204.4	1510.9
8132001	Río Diguillín en Longitudinal	-36.867	-72.333	Coastal	21/09/1956	30/06/2017	17388	1299.8	785.0
8133001	Río Itata en Cerro Negro	-36.850	-72.383	Coastal	14/09/1956	31/08/1984	9816	3187.4	649.4

ID	Station Name	Latitude	Longitude	Class	Start monitoring period	End monitoring period	n	Area	Mean elevation
		(°N)	*(°E)*					*(km^2)*	*(m)*
8134003	Río Larqui en Santa Cruz de Cuca	-36.700	-72.383	Coastal	16/01/1985	30/06/2017	10823	636.3	150.0
8135002	Río Itata en Balsa Nueva Aldea	-36.650	-72.450	Coastal	12/09/1956	09/03/2018	20611	4510.1	503.6
8144001	Río Lonquén en Trehuaco	-36.425	-72.667	Coastal	08/10/1985	12/11/2014	6105	1161.1	173.7
8220001	Río Andalién Camino a Penco	-36.817	-73.033	Coastal	01/11/1960	09/03/2018	18247	751.7	210.0
8304001	Río Lonquimay antes Junta Río Biobío	-38.433	-71.233	Andes	28/03/1985	31/05/2016	10989	466.7	1359.2
8307002	Río Biobío en Llanquén	-38.201	-71.299	Andes	01/01/2000	09/03/2018	5471	3355.6	1459.7
8312000	Río Biobío en Angostura Ralco 1	-38.037	-71.478	Andes	01/01/2000	09/03/2018	5106	5127.5	1453.3
8312001	Río Biobíoantes Junta Huiri Huiri	-37.990	-71.520	Andes	07/12/2002	30/06/2017	5045	5233.1	1451.8
8313000	Río Pangue en Captación	-37.899	-71.581	Andes	19/11/2002	09/03/2018	5254	135.6	1515.2
8317001	Río Biobío en Rucalhue	-37.711	-71.902	Andes	01/06/1937	09/03/2018	27455	7252.5	1383.1
8317002	Río Lirquén en Cerro El Padre	-37.776	-71.863	Andes	10/12/1942	30/06/2017	26750	103.4	668.1
8319001	Río Biobío en Longitudinal	-37.602	-72.278	Andes	05/04/1965	03/04/2017	4685	7860.0	1307.2
8323001	Río Duqueco en Cerrillos	-37.542	-72.312	Coastal	01/07/1962	09/03/2018	17547	1338.9	741.0
8323002	Río Duqueco en Villucura	-37.550	-72.033	Coastal	01/01/1941	30/06/2017	26218	817.0	1022.8
8330001	Río Mulchén en Mulchén	-37.717	-72.250	Coastal	23/03/1937	09/03/2018	24450	428.2	462.2
8332001	Río Bureo en Mulchén	-37.717	-72.233	Coastal	12/05/1929	31/03/2009	25167	540.8	663.2
8334001	Río Biobío en Coihue	-37.550	-72.590	Coastal	23/11/1928	09/03/2018	11910	11136.9	1078.6
8342001	Río Renaico en Longitudinal	-37.850	-72.383	Coastal	18/06/1982	30/06/2017	11795	688.1	833.3
8343001	Río Mininco en Longitudinal	-37.864	-72.394	Coastal	01/06/1963	30/06/2017	18805	440.4	449.6
8350001	Río Malleco en La Laguna	-38.214	-71.828	Andes	01/06/1960	10/03/1984	5646	46.1	1254.9
8351001	Río Malleco en Collipulli	-37.965	-72.436	Coastal	19/02/1920	09/03/2018	23205	415.1	800.9
8356001	Río Rahue en Quebrada Culén	-37.943	-72.809	Coastal	01/07/1997	30/06/2017	6938	671.6	214.1
8362001	Río Nicodahue en Pichún	-37.462	-72.753	Coastal	01/04/1988	28/05/2015	8681	741.1	584.7
8372002	Río Polcura en Cuatro Juntas	-37.107	-71.242	Andes	19/11/2002	09/03/2018	5169	235.4	1995.7
8376001	Río Rucúe en Camino a Antuco	-37.340	-71.794	Andes	18/11/1983	16/10/2016	9615	210.9	1213.8

ID	Station Name	Latitude	Longitude	Class	Start monitoring period	End monitoring period	n	Area	Mean elevation
		(°N)	*(°E)*					*(km^2)*	*(m)*
8385001	Río Claro en Camino Yumbel-Estación	-37.118	-72.545	Coastal	09/01/1985	31/08/2000	5342	531.1	137.3
8430001	Río Laraquete en El Cajón	-37.167	-73.167	Coastal	01/03/1985	31/12/1996	3972	35.4	395.5
8530001	Río Carampangue en Carampangue	-37.250	-73.267	Coastal	15/12/1970	31/12/1983	3806	912.8	394.0
8720001	Río Lebu en Las Corrientes (en Los Alamos)	-37.683	-73.350	Coastal	17/05/1963	11/05/2015	5974	667.7	372.2
8821001	Río Cayucupil en Cayucupil	-37.817	-73.250	Coastal	10/08/1950	31/12/1983	11325	170.3	779.3
8821002	Río Butamalal en Butamalal	-37.817	-73.250	Coastal	10/08/1950	10/05/2017	19164	123.4	778.9
8822002	Río Elicura en Puente Elicura	-37.933	-73.217	Coastal	01/08/1987	31/01/2003	5206	68.6	564.2
8910001	Río Lleu-Lleu en Desagüe Lago Lleu-Lleu	-38.117	-73.400	Coastal	01/04/1972	30/06/2017	15617	581.9	295.4
9101002	Río Purén en Purén	-38.013	-73.043	Coastal	01/09/1994	30/04/2009	5148	289.7	564.3
9102001	Río Lumaco en Lumaco	-38.150	-72.900	Coastal	18/10/1947	09/03/2018	24170	855.0	340.8
9104001	Río Traiguén en Victoria	-38.217	-72.317	Coastal	24/10/1950	30/06/2017	22983	93.8	513.0
9104002	Río Dumo en Santa Ana	-38.150	-72.300	Coastal	01/01/1987	28/02/2017	10741	393.3	484.8
9107001	Estero Chufquén en Chufquén	-38.300	-72.667	Coastal	25/08/1987	28/02/2017	9751	854.2	428.9
9107002	Estero Chanco Camino Curacautín	-38.267	-72.250	Coastal	01/09/1969	30/04/1983	3897	38.6	476.7
9111001	Río Quillén en Longitudinal	-38.450	-72.433	Coastal	18/08/1959	30/04/1983	8093	148.2	456.9
9113001	Río Quillén en Galvarino	-38.400	-72.783	Coastal	29/09/1959	06/09/2016	20037	710.7	284.5
9116001	Río Cholchol en Cholchol	-38.608	-72.848	Coastal	01/03/1929	09/03/2018	22722	5055.8	342.1
9122002	Río Blanco en Curacautín	-38.451	-71.866	Coastal	22/10/1986	28/10/2015	10048	170.9	1296.6
9123001	Río Cautín en Rari-Ruca	-38.430	-72.011	Andes	01/03/1929	09/03/2018	31264	1305.3	1124.6
9126001	Río Collín en Codahue	-38.578	-72.186	Coastal	27/07/1996	29/09/2015	5930	254.6	688.3
9127001	Río Muco en Puente Muco	-38.617	-72.417	Coastal	07/03/1950	30/06/2017	22372	650.4	536.7
9129002	Río Cautín en Cajón	-38.687	-72.503	Coastal	03/03/1949	09/03/2018	23763	2755.4	762.7
9131001	Río Quepe en Vilcún	-38.683	-72.233	Coastal	23/03/1946	30/04/2015	21841	378.9	931.2
9134001	Río Huichahue en Faja 24000	-38.850	-72.333	Coastal	17/01/1985	31/01/2017	11050	348.1	605.2
9135001	Río Quepe en Quepe	-38.850	-72.617	Coastal	13/12/1929	29/02/2016	19166	1666.1	506.0

ID	Station Name	Latitude	Longitude	Class	Start monitoring period	End monitoring period	n	Area	Mean elevation
		(°N)	*(°E)*					*(km^2)*	*(m)*
9140001	Río Cautín en Almagro	-38.780	-72.947	Coastal	16/05/1965	30/06/2017	17778	5549.4	552.7
9402001	Río Allipén en Melipeuco	-38.865	-71.734	Andes	17/01/1985	26/10/2016	11104	829.6	1292.6
9404001	Río Allipén en Los Laureles	-38.983	-72.233	Andes	18/03/1946	09/03/2018	24896	1674.1	1020.6
9412001	Río Trancura en Curarrehue	-39.360	-71.581	Andes	01/09/1968	09/03/2018	17286	356.9	1195.3
9414001	Río Trancura antes Río Llafenco	-39.333	-71.767	Andes	01/10/1970	30/06/2017	16287	1379.4	1146.7
9416001	Río Liucura en Liucura	-39.256	-71.824	Andes	01/10/1971	30/06/2017	14372	349.0	1038.1
9420001	Río Toltén en Villarica	-39.267	-72.233	Andes	05/03/1929	09/03/2018	30759	2931.8	964.4
9423001	Río Toltén en Coipué	-39.100	-72.383	Andes	16/12/1929	09/03/2018	11064	3488.0	879.5
9433001	Río Puyehue en Quitratué	-39.150	-72.667	Coastal	07/10/1947	10/04/2017	23672	153.7	200.3
9434001	Río Donguil en Gorbea	-39.100	-72.683	Coastal	06/10/1947	10/04/2017	18343	770.6	206.2
9436001	Río Mahuidanche en Santa Ana	-39.083	-72.933	Coastal	17/03/1987	30/06/2017	10508	384.6	189.0
9437002	Río Toltén en Teodoro Schmidt	-39.014	-73.083	Coastal	12/02/1991	09/03/2018	9735	6622.6	611.8
10100002	Río Fui en Desagüe Lago Pirihueico	-39.875	-71.890	Andes	01/03/1926	20/03/2017	11231	1498.5	1171.1
10100006	Río Huahum en la Frontera	-40.097	-71.676	Andes	16/04/2002	31/03/2017	5107	1029.1	1194.8
10102001	Río Liquiñe en Liquiñe	-39.727	-71.850	Andes	22/07/1986	24/04/2016	9780	367.9	1122.3
10111001	Río San Pedro en Desagüe Lago Riñihue	-39.767	-72.475	Andes	01/01/1929	30/06/2017	13047	4384.5	873.6
10121001	Río Collileufú en Los Lagos	-39.858	-72.825	Coastal	01/02/1987	30/04/2017	10405	627.5	196.7
10122001	Río Calle Calle en Balsa San Javier	-39.775	-72.983	Coastal	01/02/1987	30/05/2008	7663	6621.2	684.2
10122003	Río Calle Calle en Pupunahue	-39.804	-72.903	Coastal	08/03/2007	09/03/2018	4005	6497.1	693.9
10134001	Río Cruces en Rucaco	-39.550	-72.900	Coastal	01/05/1969	09/03/2018	17553	1804.8	281.9
10137001	Río Iñaque en Máfil	-39.668	-72.950	Coastal	20/02/1928	30/04/2017	12615	539.8	203.8
10140001	Río Santo Domingo en Rinconada de Piedra	-39.383	-73.133	Coastal	01/03/1992	31/10/2016	8790	107.8	335.1
10142003	Río Futa en Tres Chiflones	-39.972	-73.147	Coastal	23/05/2002	30/06/2017	5054	518.4	316.9
10304001	Río Calcurrupe en Desembocadura	-40.250	-72.267	Andes	01/07/1986	30/04/2017	10749	1725.6	935.8
10305001	Río Caunahue Camino a Llifén	-40.152	-72.251	Andes	01/01/1997	31/03/2017	6902	355.7	951.5

ID	Station Name	Latitude (°N)	Longitude (°E)	Class	Start monitoring period	End monitoring period	n	Area (km^2)	Mean elevation (m)
10306001	Río Nilahue en Mayay	-40.267	-72.233	Andes	01/08/1987	09/03/2018	11123	376.0	815.9
10327001	Río Chirre antes Junta Río Pilmaiquén	-40.433	-72.917	Coastal	30/07/2001	31/05/2017	4949	777.2	388.0
10328001	Río Pilmaiquén en San Pablo	-40.384	-73.002	Coastal	23/03/1929	30/06/2017	20410	2475.4	561.6
10343001	Río Coihueco antes Junta Pichicope	-40.933	-72.700	Andes	01/08/1987	31/03/2017	10318	313.7	607.6
10351001	Río Toro en Tegualda	-41.050	-73.383	Coastal	30/05/2000	30/04/2017	5796	340.4	162.0
10356001	Río Negro en Chahuilco	-40.714	-73.228	Coastal	01/03/1986	09/03/2018	10835	2285.7	151.9
10362001	Río Damas en Tacamo	-40.618	-73.059	Coastal	01/02/1986	31/03/2017	10916	467.6	132.1
10363002	Río Forrahue en Aromos	-40.886	-73.133	Coastal	04/12/1991	30/04/2017	8455	169.4	134.6
10364001	Río Rahue en Forrahue	-40.517	-73.283	Coastal	27/02/1986	31/07/2017	10587	5614.2	234.4
10401001	Río Tranallaguín en Carrico	-40.583	-73.600	Coastal	09/06/2000	30/04/2017	4198	413.5	279.0
10405002	Río Hueyusca en Camarones	-41.017	-73.617	Coastal	30/08/2001	30/04/2017	5468	218.5	360.9
10411002	Río Negro en Las Lomas	-41.383	-73.067	Coastal	25/04/1989	30/04/2017	8899	253.7	118.1
10431000	Río Blanco antes Junta Río Chamiza	-41.428	-72.593	Andes	17/10/2002	23/04/2015	3871	30.5	528.7
10432003	Río Chico antes Río Chamiza	-41.439	-72.818	Andes	14/03/2003	09/03/2018	4552	136.9	298.5
10503001	Río Manso antes Junta Río Puelo	-41.722	-72.014	Andes	27/05/2001	30/04/2017	5225	3589.5	1184.1
10514001	Río Puelo antes Junta con Manso	-41.757	-72.053	Andes	24/07/2001	23/08/2016	5041	4784.3	1012.7
10520001	Río Puelo en Desagüe Lago Tagua Tagua	-41.639	-72.169	Andes	30/05/2002	22/11/2016	4616	8640.9	1073.7
10523002	Río Puelo en Carrera Basilio	-41.604	-72.206	Andes	01/01/2003	09/03/2018	5361	8851.6	1071.7

Table S 4.2: The proportion of catchments (in percentage) which show increasing (+) or decreasing (-) values for mean monthly temperature (MMT), mean monthly precipitation (MMP), and mean monthly specific discharge (MMQsp) during El Niño, as compared to the non-ENSO phase. The data are presented for different seasons: autumn (MAM), winter (JJA), spring (SON), summer (DJF), for catchments located in the Andes and the coastal region (CR), and for different climate zones: semi-arid (SA), mediterranean (Med) and humid-temperate (HT).

	MMT		MMP		MMQsp	
	+ (%)	- (%)	+ (%)	- (%)	+ (%)	- (%)
Year	65.77	34.23	94.90	5.10	95.43	4.57
MAM	79.73	20.27	74.03	25.97	87.35	12.65
JJA	72.67	27.33	87.26	12.74	89.44	10.56
SON	53.02	46.98	83.77	16.23	86.67	13.33
DJF	20.53	79.47	38.78	61.22	92.36	7.64
Andes	64.94	35.06	96.20	3.80	94.51	5.49
CR	66.67	33.33	93.59	6.41	96.43	3.57
SA	46.43	53.57	96.55	3.45	96.00	4.00
Med	61.11	38.89	94.59	5.41	90.48	9.52
HT	71.76	28.24	94.51	5.49	97.22	2.78

Table S 4.3: Percent differences in mean monthly temperature (MMT), precipitation (MMP), and specific discharge (MMQsp) for El Niño events relative to non-ENSO conditions. Data are reported for each season, spatial class: Andes, coastal region (CR), and climate zone: semi-arid (SA), mediterranean (Med), and humid-temperate (HT), and are presented as percentiles (X_x) and the interquantile range (IQR) between X_{25} and X_{75}.

	MMT						MMP						MMQsp					
	T_5	T_{25}	T_{50}	T_{75}	T_{95}	IQR	P_5	P_{25}	P_{50}	P_{75}	P_{95}	IQR	Q_5	Q_{25}	Q_{50}	Q_{75}	Q_{95}	IQR
Year	-15.43	-0.61	1.20	2.43	11.55	3.04	-0.13	8.40	14.37	24.35	51.17	15.95	3.23	18.46	30.40	44.75	104.87	26.28
MAM	-18.89	1.43	3.91	7.77	34.21	6.33	-46.84	-0.57	14.65	29.85	109.51	30.42	-25.07	13.11	35.31	73.78	121.13	60.67
JJA	-23.36	-1.93	3.70	7.56	23.17	9.49	-4.73	2.62	11.46	26.18	67.80	23.56	-5.45	11.65	24.79	47.29	118.04	35.64
SON	-18.70	-3.01	0.19	2.51	10.62	5.52	-36.21	17.10	28.80	40.68	83.12	23.58	-7.79	8.70	20.69	39.03	80.05	30.34
DJF	-8.27	-3.71	-1.59	-0.25	9.10	3.46	-67.32	-25.75	-7.15	11.22	98.76	36.96	-3.30	24.95	52.43	95.55	169.52	70.60
Andes	-40.20	-2.03	1.46	2.95	29.70	4.98	2.19	11.33	19.22	28.70	51.10	17.37	-0.70	19.59	35.88	62.95	118.29	43.36
CR	-3.02	-0.36	1.00	2.23	4.48	2.59	-2.02	7.22	10.62	18.33	51.09	11.11	5.60	17.81	27.84	34.18	59.40	16.37
SA	-86.56	-15.15	1.16	12.43	33.93	27.58	6.64	19.16	28.94	40.71	97.15	21.55	7.17	49.43	94.66	110.27	179.99	60.84
Med	-10.63	-0.40	0.39	1.96	5.91	2.36	-1.20	14.69	22.96	35.34	63.30	20.65	-2.91	16.49	34.48	54.34	104.10	37.85
HT	-2.63	-0.23	1.39	2.22	4.58	2.45	-0.72	7.29	9.94	15.79	20.89	8.50	7.83	18.30	24.43	33.85	53.18	15.55

Table S 4.4: The proportion of catchments (in percentage) which show increasing (+) or decreasing (-) values for mean monthly temperature (MMT), mean monthly precipitation (MMP), and mean monthly specific discharge (MMQsp) during La Niña, as compared to the non-ENSO phase. The data are presented for different seasons: autumn (MAM), winter (JJA), spring (SON), summer (DJF), for catchments located in the Andes and the coastal region (CR) and for different climate zones: semi-arid (SA), mediterranean (Med) and humid-temperate (HT).

	MMT		MMP		MMQsp	
	+ (%)	- (%)	+ (%)	- (%)	+ (%)	- (%)
Year	63.8	36.2	2.9	97.1	11.9	88.1
MAM	69.2	30.8	5.8	94.2	12.0	88.0
JJA	52.7	47.3	21.4	78.6	20.1	79.9
SON	71.8	28.2	13.6	86.5	8.2	91.8
DJF	32.5	67.6	44.4	55.6	35.4	64.6
Andes	53.7	46.3	1.4	98.6	6.8	93.2
CR	74.6	25.4	4.4	95.6	17.4	82.6
SA	29.2	70.8	7.4	92.6	7.1	92.9
Med	41.9	58.1	0.0	100.0	26.5	73.5
HT	84.0	16.0	2.5	97.5	7.4	92.6

Table S 4.5: Percent differences in mean monthly temperature (MMT), precipitation (MMP), and specific discharge (MMQsp) for La Niña events relative to non-ENSO conditions. Data are reported for each season, spatial class: Andes, coastal region (CR), and climate zone: semi-arid (SA), mediterranean (Med), and humid-temperate (HT), and are presented as percentiles (X_x) and the interquantile range (IQR) between X_{25} and X_{75}.

	MMT						MMP						MMQsp					
	T_5	T_{25}	T_{50}	T_{75}	T_{95}	IQR	P_5	P_{25}	P_{50}	P_{75}	P_{95}	IQR	Q_5	Q_{25}	Q_{50}	Q_{75}	Q_{95}	IQR
Year	-43.58	-3.98	1.69	4.32	51.50	8.30	-44.05	-28.04	-21.69	-16.25	-4.55	11.79	-66.91	-37.91	-21.47	-9.50	25.33	28.41
MAM	-36.96	-1.29	4.10	8.00	34.96	9.29	-73.73	-52.30	-40.50	-27.76	12.69	24.55	-79.66	-51.68	-33.05	-16.39	35.86	35.29
JJA	-55.88	-8.87	0.38	9.45	60.81	18.32	-46.75	-22.62	-10.44	-1.59	35.92	21.02	-60.10	-33.48	-15.92	-3.17	52.93	30.31
SON	-54.14	-1.36	4.34	12.02	49.85	13.38	-57.56	-41.11	-31.85	-21.49	47.57	19.61	-77.58	-48.36	-28.31	-14.40	6.88	33.96
DJF	-24.99	-3.10	-0.84	0.52	4.41	3.61	-40.83	-14.91	-3.01	10.18	58.79	25.09	-76.30	-32.74	-10.90	6.96	61.42	39.70
Andes	-127.66	-16.33	0.66	8.15	69.92	24.48	-47.89	-31.44	-23.06	-16.87	-6.70	14.57	-69.38	-48.77	-24.51	-11.52	0.77	37.24
CR	-8.63	-0.01	1.96	3.24	5.83	3.25	-39.41	-25.23	-20.39	-16.00	-3.23	9.24	-44.45	-29.35	-17.56	-6.57	50.31	22.78
SA	-157.91	-40.98	-17.84	17.95	72.55	58.93	-66.11	-37.60	-28.53	-23.93	6.61	13.67	-82.27	-66.11	-54.09	-38.03	12.81	28.08
Med	-34.59	-11.68	-2.71	3.83	74.95	15.52	-44.95	-35.88	-23.12	-13.72	-4.04	22.16	-48.10	-31.72	-19.33	0.95	83.51	32.68
HT	-1.95	0.63	2.47	4.37	9.36	3.75	-31.65	-23.59	-19.42	-15.84	-6.97	7.74	-41.54	-26.85	-17.05	-8.95	4.07	17.90

4.11 Supplementary figures

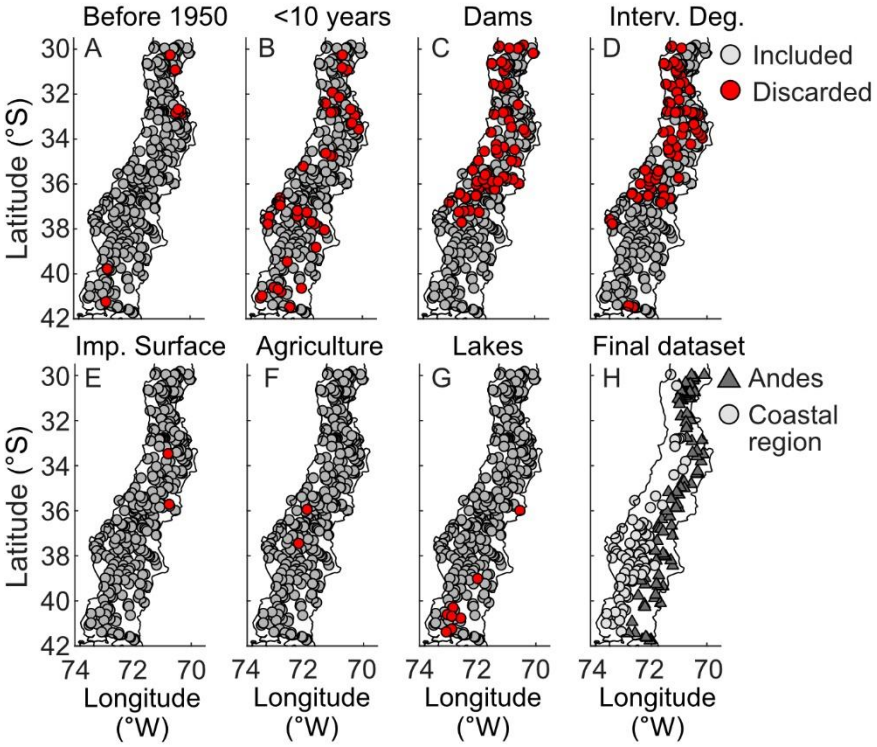

Figure S 4.1: The excluded catchments (red dots) from the original CAMELS-CL dataset based on different criteria. A) Excluded stations with data availability only before 1950, B) excluded stations with <10 years of data. C) excluded stations with large dams in their basin), D) excluded stations with a human intervention degree of >10%, E) excluded stations with >5% of the basin area covered with impermeable surfaces, F) excluded stations with >50% of the basin area with agricultural land-use, G) excluded stations located downstream of large lakes (>10% of basin area). H) The final dataset used in this study, with 183 gaging stations categorized in basins that drain the Andes and catchments that drain the coastal region.

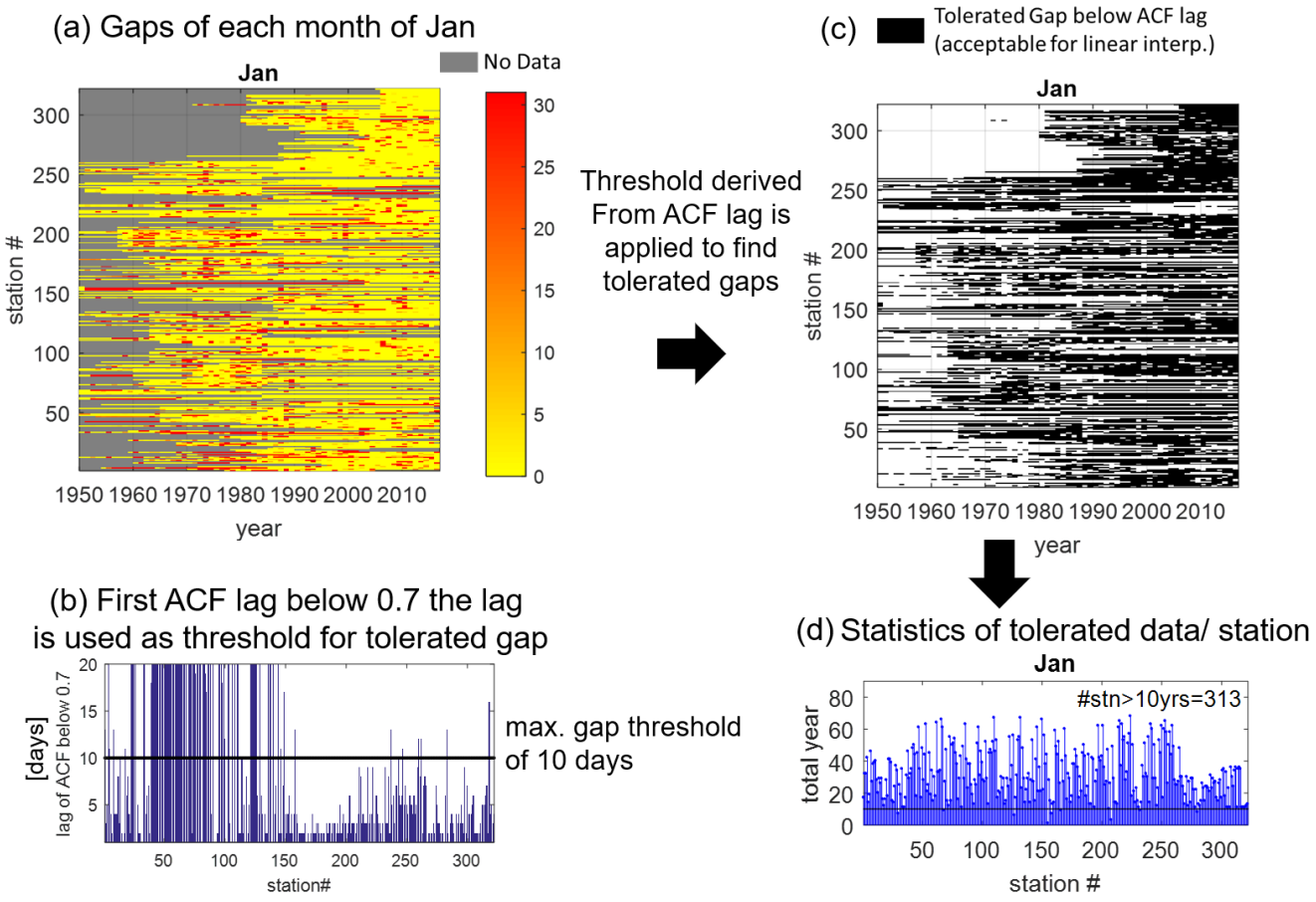

Figure S 4.2: Illustration of data gaps interpolation method, based on an example for January. (A) Gaps statistics per month and per station are calculated, and all months with gap lengths above 10 days are removed. (B) A specific tolerated gap length per station is decided upon calculating its discharge series lag autocorrelation (ACF). (C) Lags that have a ACF below 0.7 is chosen as a specific threshold of tolerated gap length for the month. This assumes that the remaining minimal gaps can now be linearly interpolated to result in full month of continuous daily data. (D) Overview of the resulting data length per station after the interpolation method.

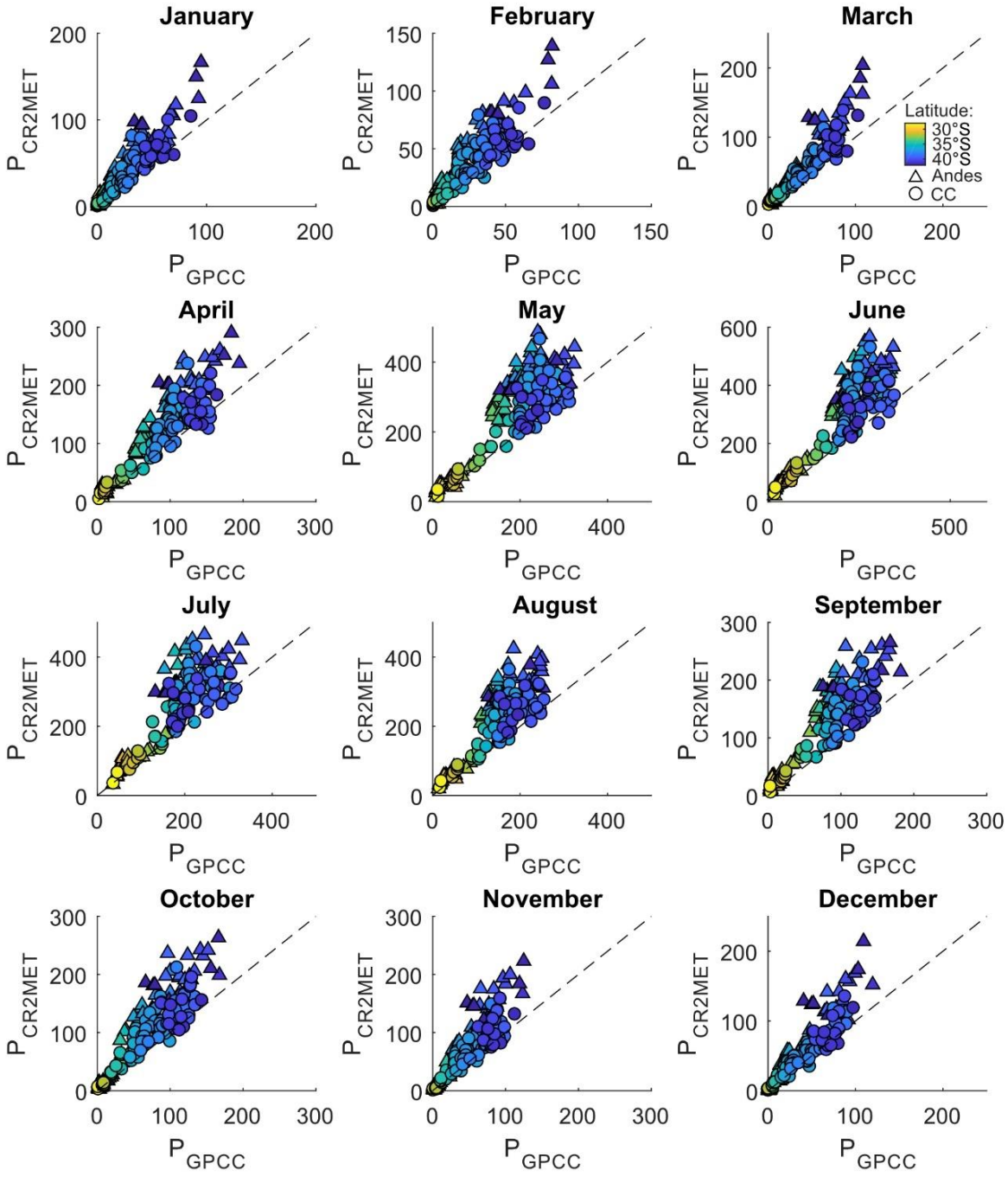

Figure S 4.3: Monthly precipitation dataset quality check. A monthly comparison between the mean monthly precipitation (MMP) values based on the precipitation dataset from the Centre for Climate and Resilience Research (CR2MET; Boisier et al. 2018) and the Global Precipitation Climatology Centre (GPCC; Meyer-Christoffer et al. 2015). Each datapoint represents a station, comparing the long-term averaged MMP values over the time period 1979-2009.

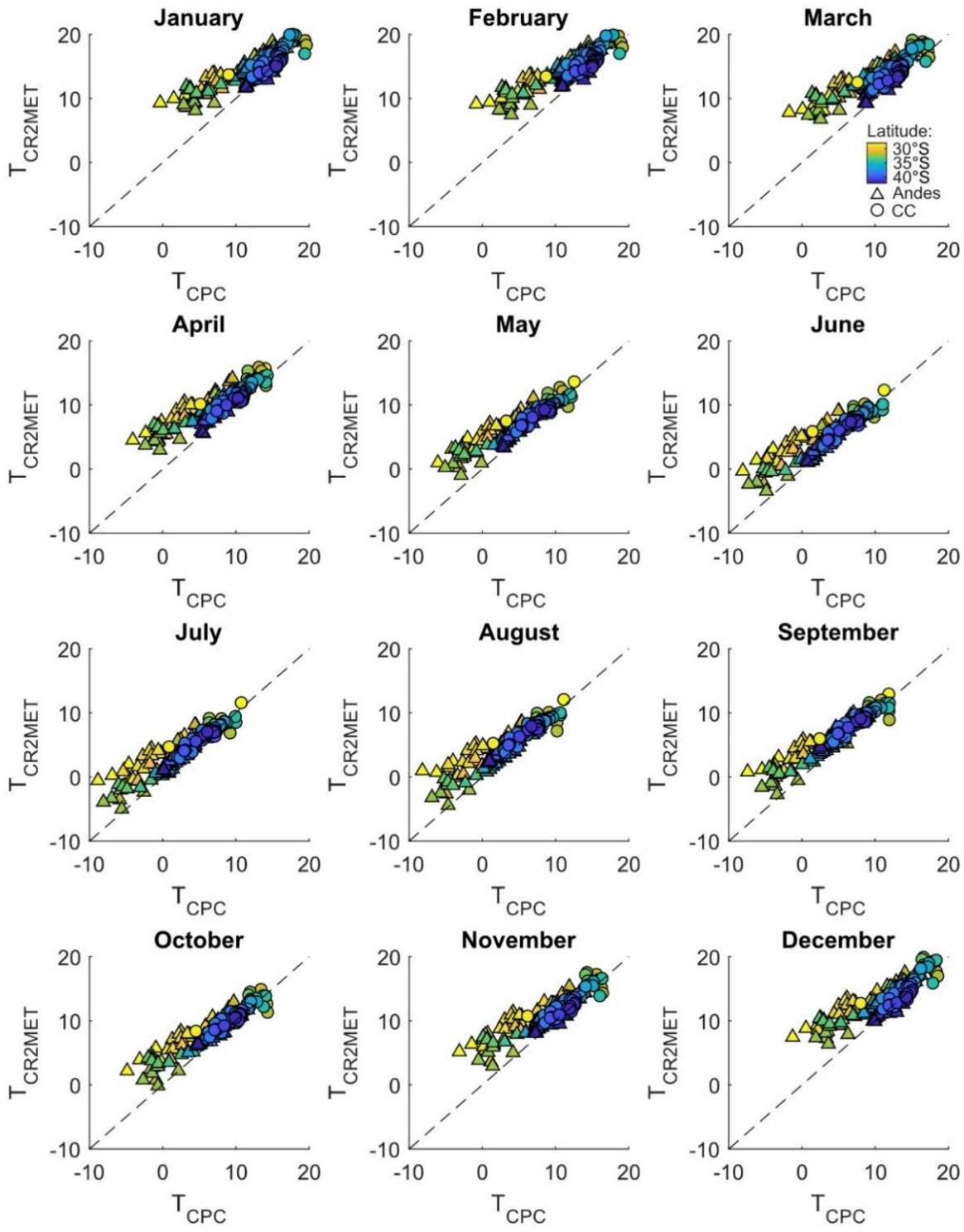

Figure S 4.4: Monthly temperature dataset quality check. A monthly comparison between the mean monthly temperature (MMT) values based on the temperature dataset from the Center for Climate and Resilience Research (CR2MET; Boisier et al. 2018) and the Climate Prediction Center (CPC; Fan and van den Dool, 2008). Each datapoint represents a station, comparing the long-term averaged MMT values over the time period 1979-2009.

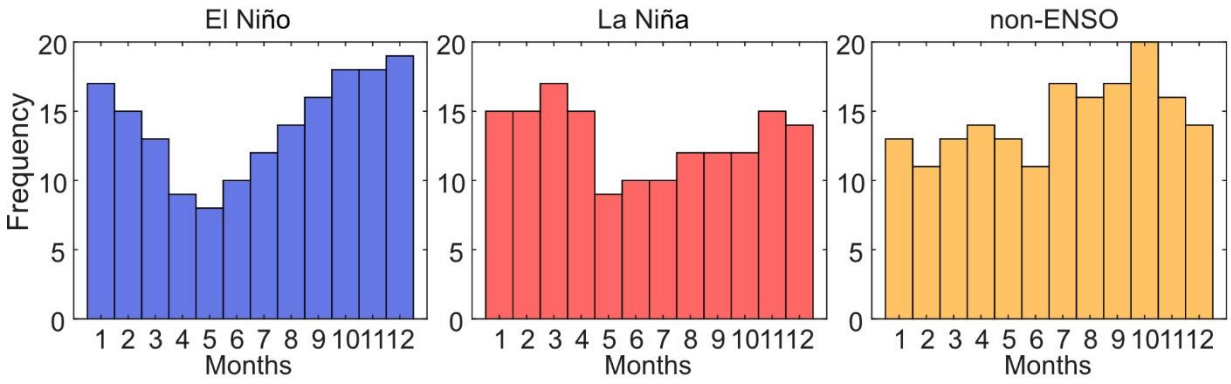

Figure S 4.5: Frequency of months classified as El Niño, La Niña and non-ENSO phases in the time period 1950-2009.

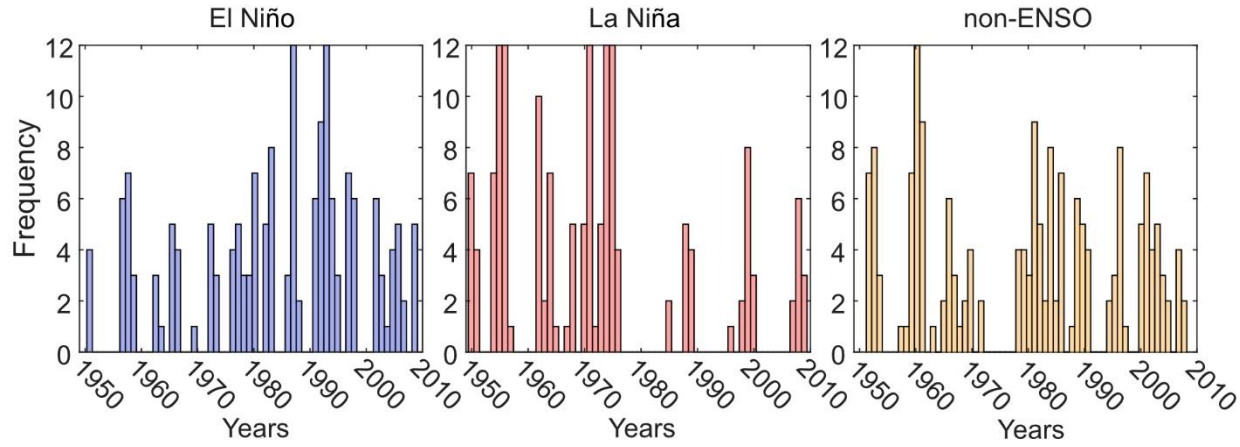

Figure S 4.6: Frequency of months during each year that are classified as El Niño, La Niña and non-ENSO phases in the time period 1950-2009.

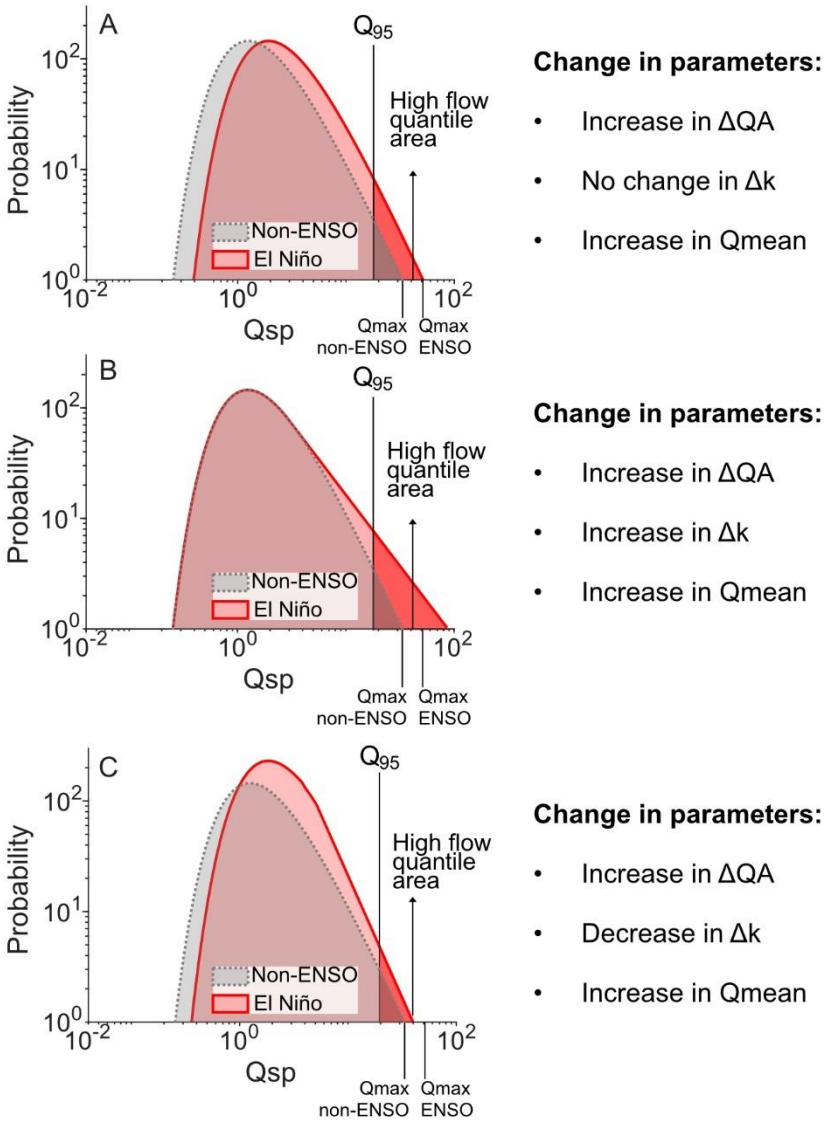

Figure S 4.7: Examples of changes in the empirical distributions of the daily specific discharge (Qsp). All of the distributions show and increase in the quantile area for high flows (ΔQA_{95}), however, the reasons for this increase are different, which can be revealed by the values of ΔQA, Δk and $\Delta Qmean$. A) An increase in ΔQA_{95} induced by a shift of the entire empirical frequency distribution towards higher specific discharge magnitudes, the shape of the distribution remains the same. This results in an increased Qmean, but a simar k-value. B) An increase in ΔQA_{95} induced by an increase in higher magnitude events only, the distribution for lower discharge magnitudes remains the same, and the increase in ΔQA_{95} is only result of a heavier right tail. In this case, the increase in ΔQA_{95} coincides with an increase in both Qmean and Δk. C) An increase in ΔQA_{95} induced by an increase in the magnitude of small and intermediate events mostly. For this case the increase in ΔQA_{95} results from an increase in Qmean, but the value of the k-parameter is decreasing because the right tail is becoming lighter compared to the non-ENSO empirical distribution.

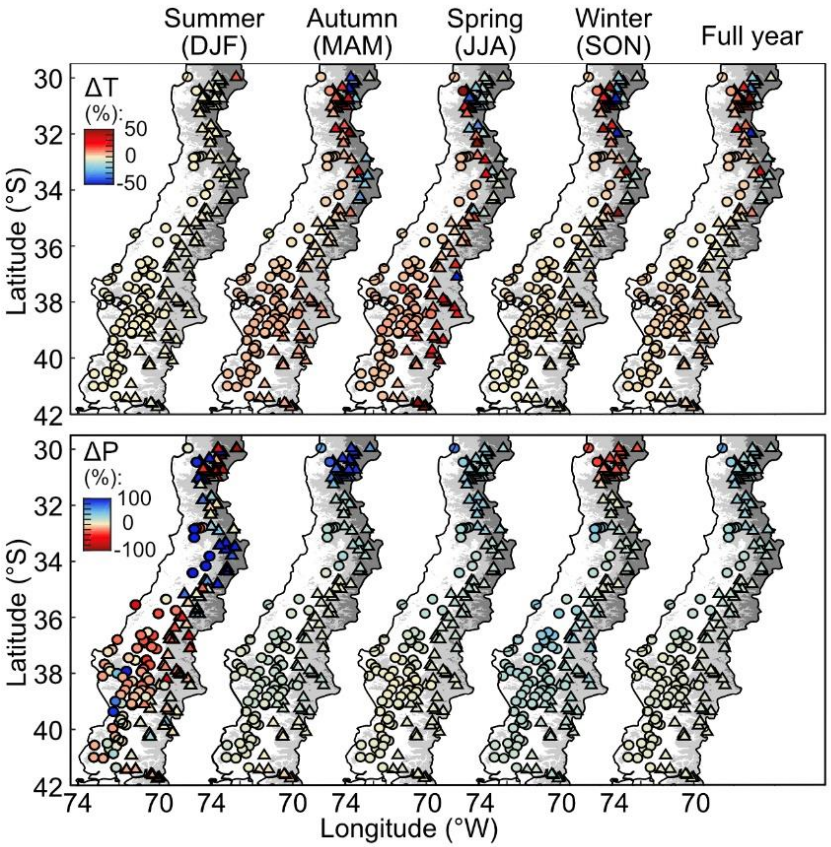

Figure S 4.8: Changes (in %) in precipitation (P) and temperature (T) during El Niño events, as compared to non-ENSO conditions. This figure presents the full data coverage between 1950-2009. The temporal and spatial patterns in ΔT and ΔP are generally similar to the patterns in Figure 4.4, which presents the P and T differences based only on the time period for which specific discharge data are available at each station.

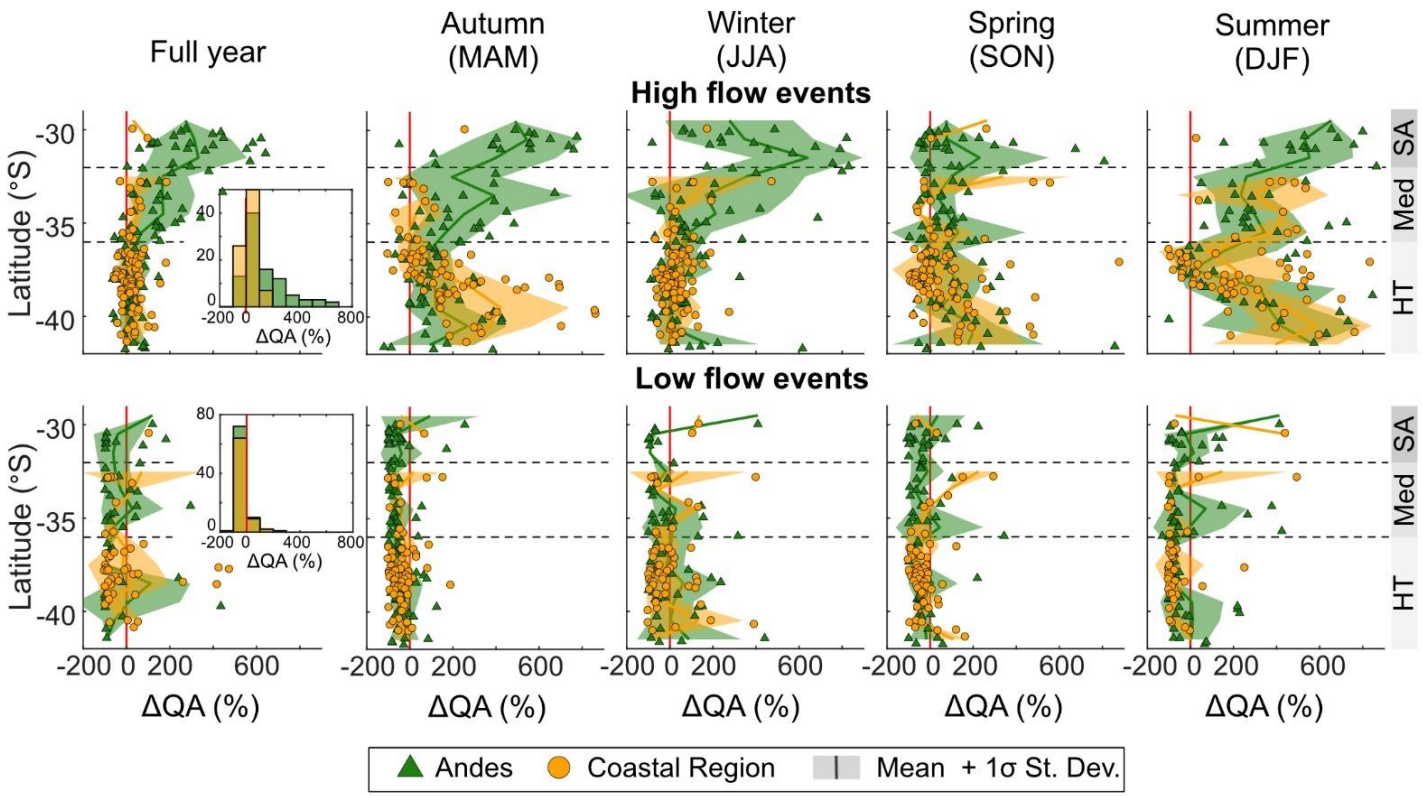

Figure S 4.9: Differences in the magnitude-frequency distribution of high flows (top row) and low flows (bottom row) between El Niño and non-ENSO phases. The method to create this figure is described in Figure 4.3. The markers represent the result of each individual station in the Andes (green triangles) and the coastal region (orange dots). On the background are shown the mean value (solid line) and the 1σ standard deviation (shaded background) for a 1° latitude moving window, for both the Andean region (green) and the coastal region (orange). The dotted lines indicate the boundaries between the climatic zones: semi-arid (SA), mediterranean (Med) and humid-temperate (HT). The histogram insets reveal the frequency of quantile area differences (%) during the full year for the Andes (green) and the coastal region (orange).

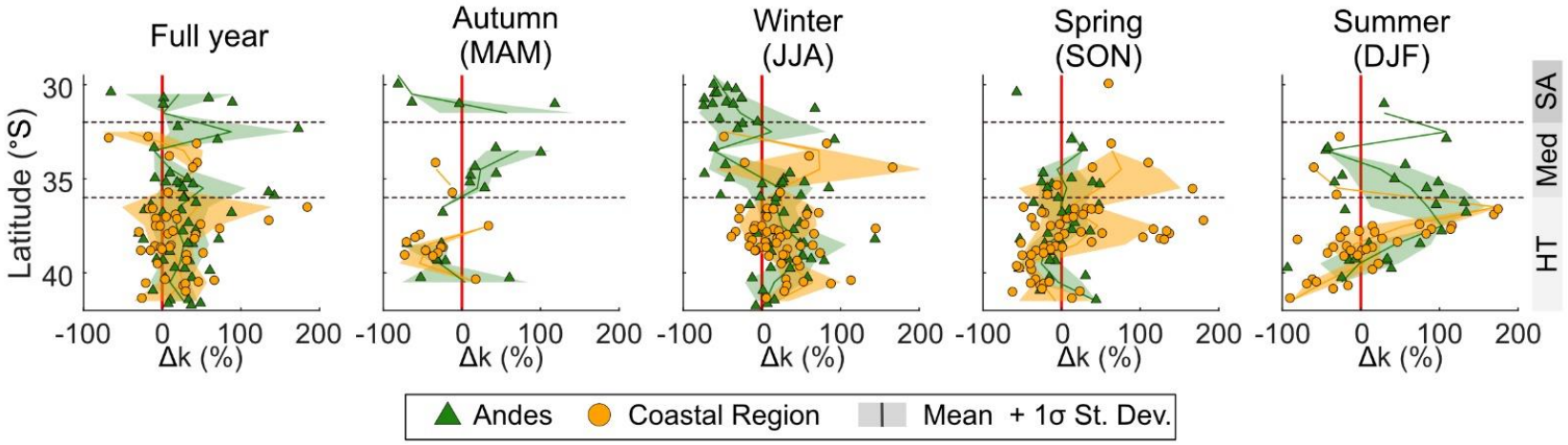

Figure S 4.10: Differences in the inverse gamma k-parameter between El Niño and non-ENSO conditions. The method to create this figure is described in Figure 4.3. The scatter represents the result of each individual station in the Andes (green triangles) and the coastal region (orange dots). On the background are shown the mean value (solid line) and the 1σ standard deviation for a 1° latitude moving window (shaded background), for both the Andean region (green) and the coastal region (orange). The dotted lines indicate the boundaries between the climatic zones: semi-arid (SA), mediterranean (Med) and humid-temperate (HT).

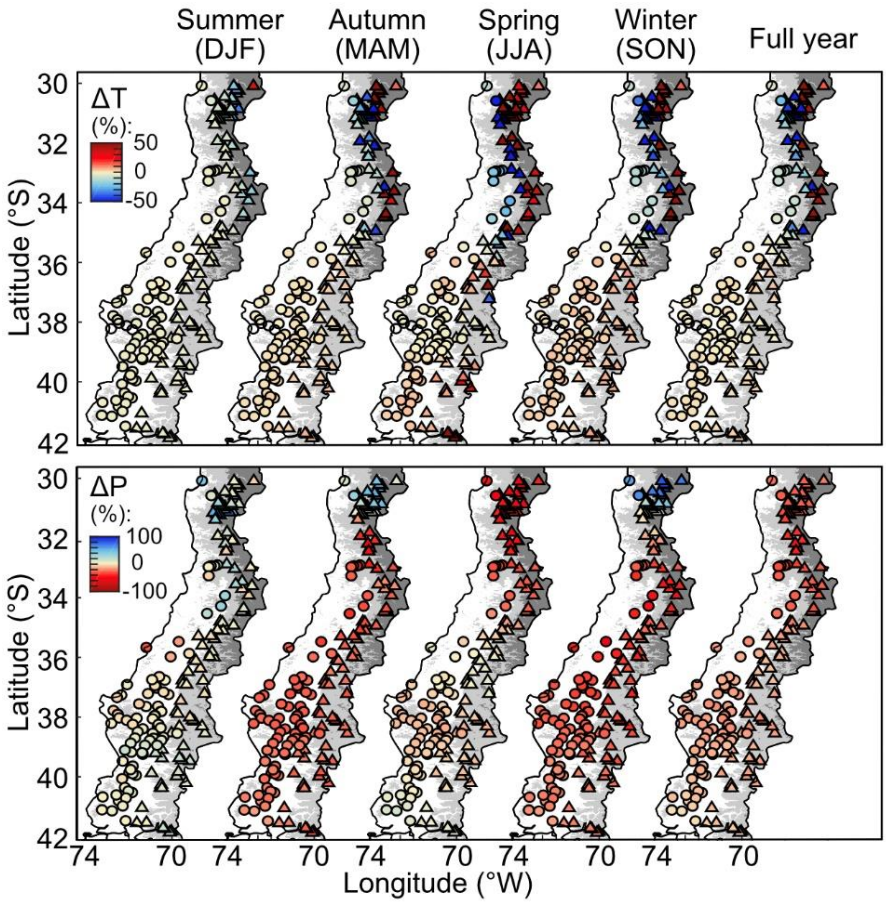

Figure S 4.11: Changes (in %) in precipitation (P) and temperature (T) during La Niña events, as compared to non-ENSO conditions. This figure presents the full data coverage between 1950-2009. The temporal and spatial patterns in ΔT and ΔP are generally similar to the patterns in Figure 4.6, which presents the P and T differences based only on the tie period for which specific discharge data are available at each station.

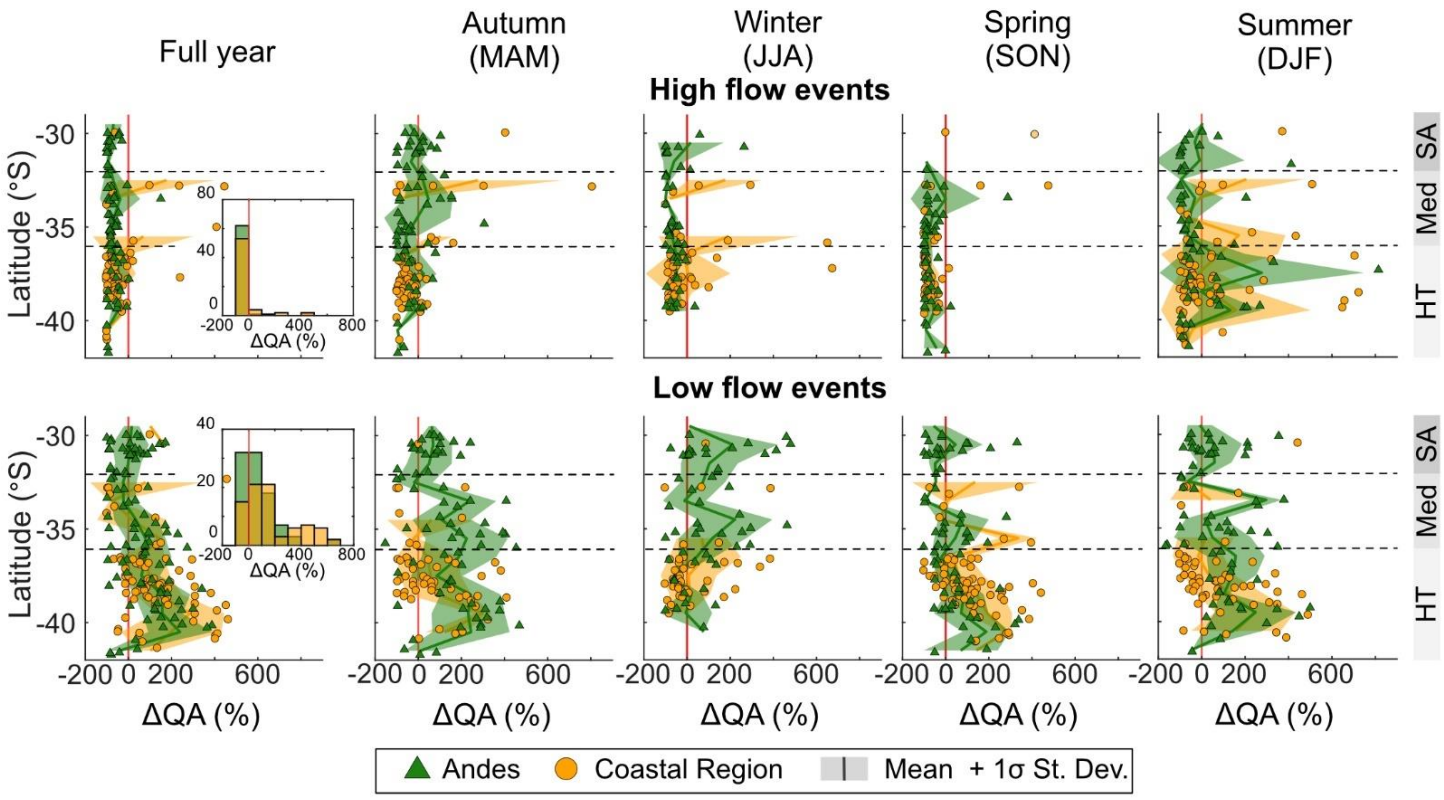

Figure S 4.12: Differences in the magnitude-frequency distribution of high flows (top row) and low flows (bottom row) between La Niña and non-ENSO phases. The method to create this figure is described in Figure 4.3. The markers represent the result of each individual station in the Andes (green triangles) and the coastal region (orange dots). On the background are shown the mean value (solid line) and the 1σ standard deviation (shaded background) for a 1° latitude moving window, for both the Andean region (green) and the coastal region (orange). The dotted lines indicate the boundaries between the climatic zones: semi-arid (SA), mediterranean (Med) and humid-temperate (HT). The histogram insets reveal the frequency of quantile area differences (%) during the full year for the Andes (green) and the coastal region (orange).

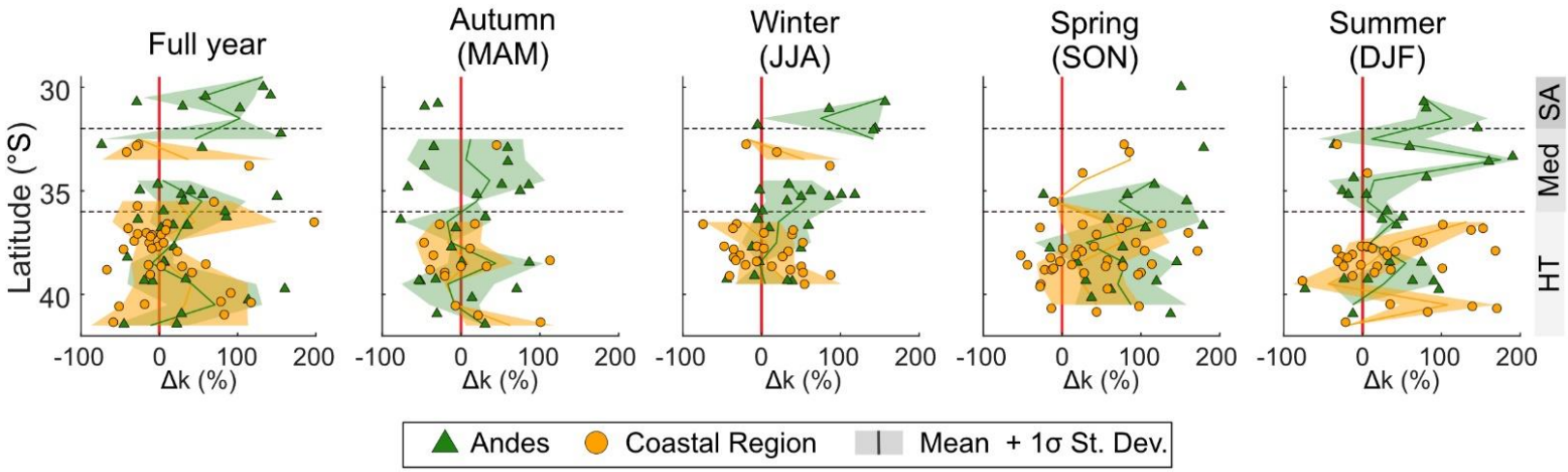

Figure S 4.13: Differences in the inverse gamma k-parameter between La Niña and non-ENSO conditions. The method to create this figure is described in Figure 4.3. The scatter represents the result of each individual station in the Andes (green triangles) and the coastal region (orange dots). On the background are shown the mean value (solid line) and the 1σ standard deviation for a 1° latitude moving window (shaded background), for both the Andean region (green) and the coastal region (orange). The dotted lines indicate the boundaries between the climatic zones: semi-arid (SA), mediterranean (Med), and humid-temperate (HT).

Chapter 5

Catchment average erosion rates along a climate gradient in Chile

Renee van Dongen[1,2], Dirk Scherler[1,3]

[1] GFZ German Research Centre for Geosciences, Earth Surface Geochemistry department, Telegrafenberg, 14473 Potsdam, Germany.
[2] International Centre for Water Resources and Global Change (UNESCO), German Federal Institute of Hydrology, Koblenz, Germany.
[3] Freie Universität Berlin, Institute for Geological Sciences, 12249 Berlin, Germany.

Abstract

Landscape evolution is controlled by several factors such as tectonic uplift, climate, lithology and biota. Even though the control of climate on landscape evolution seems obvious, it is difficult to quantify because other non-climatic factors (e.g., hillslope angles, lithology) may obscure the climatic signal. To investigate the control of climate on the erosion rates in the Coastal Cordillera of central Chile, we conducted a well-constrained study that focussed on three regions with similar granodioritic lithology, but contrasting climates (semi-arid, mediterranean, and humid-temperate). In each climate region, we measured ^{10}Be-derived catchment average erosion rates of 9 or 10 catchments with various normalized channel steepness indices. For all climate regions we found a positive linear relationship between the normalized channel steepness index and erosion rates. On top of that, a climatic signal could be observed; for a given normalized channel steepness index, the erosion rate was found to be the highest in the humid-temperate region, followed by the mediterranean region and semi-arid region. We compared the results of our study to previously published ^{10}Be-derived erosion rates of ~150 catchments in Chile and discussed the controlling factors on a larger scale. Despite the various lithologies underlying these catchments, we, also observe a combined tectonic and climatic control on the larger scale erosional patterns in Chile. The results of this study suggest that the fluvial erosion efficiency increases with increasing MAP in Chile. A modelling study is required to determine whether discharge variability and erosion thresholds play an important role in the gently sloping catchments of this study, and how this varies for different climate regions.

5.1 Introduction

Over the past decades, geoscientists have investigated numerous landscapes on earth to understand the complex interactions of tectonics, climate, lithology and biota on landscape evolution. The effect of climate on landscape evolution has gained much attention and seems obvious; nonetheless, studies found obscure relationships between climate and long-term erosion rates around the world (von Blanckenburg, 2005; Burbank et al., 2003; Godard et al., 2014; Perron, 2017; Riebe et al., 2001).

The extraordinary climatic-tectonic setting of Chile has motivated a large number of researchers to investigate erosion rates and landscape evolution processes along a latitudinal gradient. Chile features a climate gradient that ranges from the driest desert on Earth (Atacama Desert) with mean annual precipitation rates of close to zero, to the humid-most region in the Southern Hemisphere (Patagonia) with mean annual precipitation rates of >2500 mm (Miller, 1976; Montecinos and Aceituno, 2003). Furthermore, orographic precipitation induced by the high elevation Andes Mountain range promotes a second east-to-west precipitation gradient with, on average, 3 times higher precipitation rates in the east compared to the low elevation Coastal Cordillera in the west (Barrett and Hameed, 2017; Garreaud et al., 2009; Viale and Garreaud, 2014). As Chile is located eastward of a convergent plate boundary, where the Nazca plate has subducted under the South American plate since at least the Jurassic, Chile provides a spatially and temporally constant tectonic setting over a long latitudinal stretch (Jordan et al., 1983).

To date, ^{10}Be-derived catchment average erosion rates have been measured for ~150 catchments in Chile. The results of these studies are variable, and the analyses of the results are often contradictory. Most studies concluded that tectonic uplift rates, which are reflected in catchment steepness, are the dominant control on the measured erosion rates (e.g., Carretier et al., 2013, 2015b, 2018; Placzek et al., 2010). However, the relationship between mean annual precipitation (MAP) and erosion rate is less clear. A trend of increasing erosion rates with increasing mean annual precipitation has been observed in the northern part of Chile (<33°S) (Kober et al., 2009; Owen et al., 2011; Placzek et al., 2010), but erosion rates are found to decrease to the south of 35°S, despite increasing MAP (Aguilar et al., 2014; Carretier et al., 2013, 2015b, 2018; Tolorza et al., 2014). This might result from higher catchment steepness between 32°S and 35°S, whereas the Andes decrease in elevation and steepness south of 35°S (Aguilar et al., 2014; Carretier et al., 2013, 2015b, 2018; Tolorza et al., 2014). The observed rapid erosion between ~32°S-35°S is supported by studies that conclude that the erosive regime in the Andes at these latitudes is dominated by the frequency of landslides (Aguilar et al., 2014; Antinao and Gosse, 2009; Carretier et al., 2015b, 2018).

Several studies suggested that the dense vegetation cover might have controlled the decreasing erosion rates south of 35°S; however, as vegetation density covaries with precipitation rates, hillslope angles and the elevation of the Andes, it was impossible to

disentangle this control from the climatic and tectonic drivers (Carretier et al., 2013; Tolorza et al., 2014). Starke et al. (2020) investigated erosion patterns in the Peruvian and Chilean Andes (6°S-36°S) and found a positive correlation between vegetation cover and erosion rates between ~10-14°S and a negative correlation between ~18-32°S. The authors attributed this to the competing effect of climate and vegetation on erosion. Furthermore, Callaghan (2012) measured the erosion rates of 48 catchments along a climate gradient (26°S-41°S) in the Coastal Cordillera, and found that climate and vegetation affect sediment transport efficiency. The highest sediment transport efficiency was found in humid climates.

To further complicate things, the bedrock lithologies in Chile are highly variable, which results in different substrate erodibilities. Carretier et al., (2013) investigated a potential lithological control on erosion rates and suggested that higher fractions of granitoid rocks in catchments are correlated with lower the erosion rates. However, this observation has its limitations as the catchments with the lowest percentage of granitoid rocks and highest erosion rates, are also the steepest catchments.

Inferring climatic control on erosion rates based on the data of the above-described studies is challenging, because the catchments do not only vary in climate and vegetation cover along the latitudinal gradient, but also feature contrasts in catchment steepness and lithologies. Furthermore, some of the above-described studies focus on Andean catchments, of which some are currently affected by glacial erosion (especially around ~33°S-36°S) (Raup et al., 2007), or have been affected by the Patagonian ice sheet during the Last Glacial Maximum (>35°S) (Hulton et al., 2002) which adds additional complexity. Therefore, a well-constrained study is required to investigate the climatic control on landscape evolution.

Hence, we conducted a well-constrained study, by selecting three regions underlain by similar granodioritic lithologies, but that are affected by contrasting climate (semi-arid, mediterranean, humid-temperate). In each climate region, we sampled 9 to 10 catchments with different normalized channel steepness indices, a topographic metric that scales with tectonic uplift rates in a steady state landscape (e.g., Whipple, 2004). This allows us to constrain a relationship between the normalized channel steepness and ^{10}Be-erosion rates for each individual climate region. We present the erosion rates of the three climate regions, correlate the catchment average erosion rates to catchment attributes, and compare the results of this study to previously published ^{10}Be-derived catchment average erosion rates from Chile.

5.2 Study Area

We selected three study regions of roughly 0.5 to 1° latitudinal extent with a semi-arid climate (28.7-29.8°S), a mediterranean climate (32.0-33.1°S) and a humid-temperate climate (37.6-37.9°S) (Figure 5.1a). The three climatic regions feature a strong contrast in mean annual precipitation (MAP) with ~30 times higher MAP in the humid-temperate region compared to the semi-arid region (Table 5.1).

All of the climatic regions feature granodioritic lithologies that range from Carboniferous-Permian to Cretaceous age (Hervé et al., 1988, 2007; SERNAGEOMIN, 2003). Bedrock samples from each region revealed that minor differences in mineralogy exist (Oeser et al., 2018). The focus regions have not been glaciated during the Last Glacial Maximum (Hulton et al., 2002).

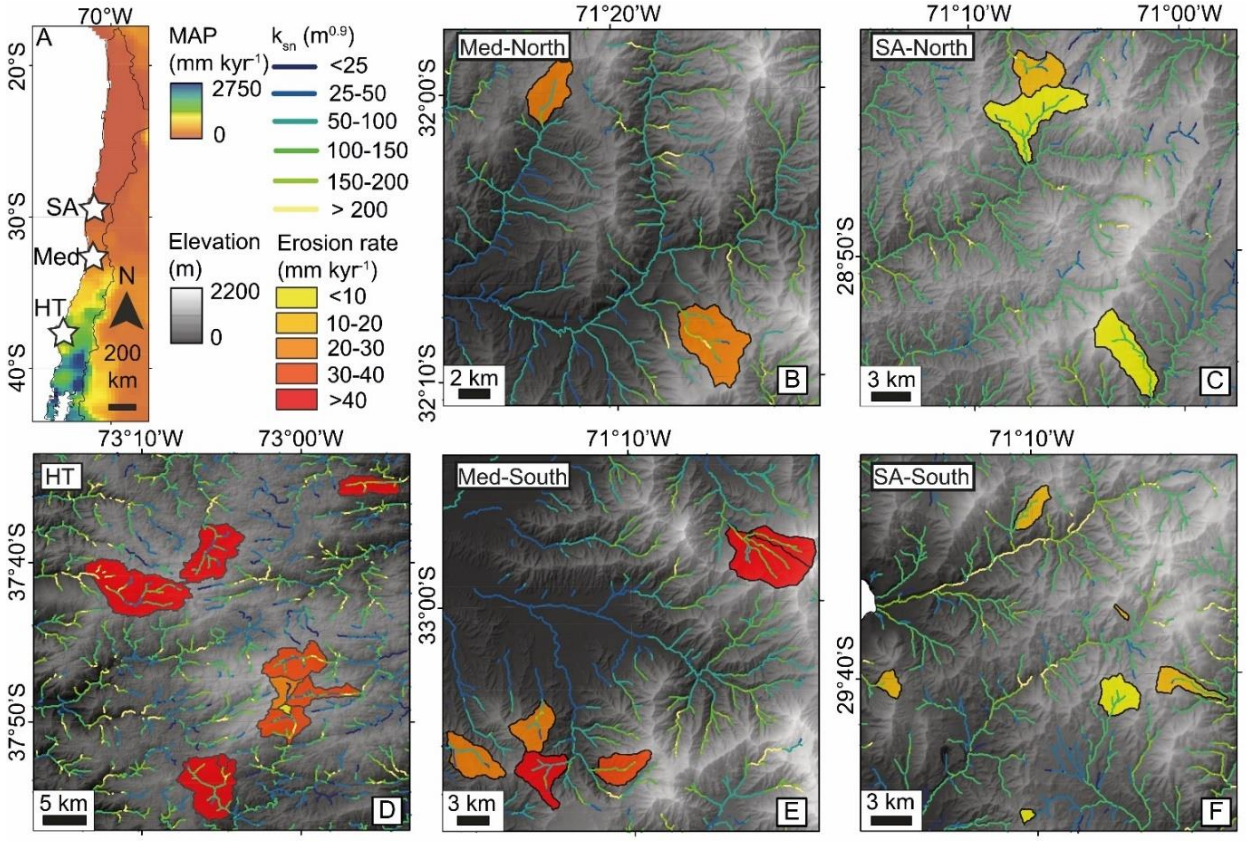

Figure 5.1: The study areas in central Chile. A) Mean annual precipitation (MAP) with the locations (stars) of the three climatic focus areas in this study: semi-arid (SA), mediterranean (Med) and humid-temperate (HT). B-F): 30m resolution Digital Elevation Models (DEM), provided by the Shuttle Radar Topography Mission (SRTM) (Jarvis et al., 2008), with channel networks color-coded by normalized channel steepness indices (k_{sn}) and the catchment outlines color-coded with ^{10}Be-derived catchment average erosion rates (yellow-to-red scale).

Table 5.1: Selected catchments in each climate zone. Catchment ID, International Geo-Sample Number (IGSN), climate zone, latitude, longitude, catchment area, mean channel steepness and mean annual precipitation (MAP).

ID	IGSN[a]	Climate zone	Latitude (°S)	Longitude (°W)	Area (km^2)	Mean channel steepness[b] $m^{0.9}$	MAP[c] (mm)
SG10	GFRD1001Q	Semi-arid	28.770	71.122	18.93	50.73	59
SG35	GFRD1001R	Semi-arid	29.568	71.181	4.27	79.03	82
SG39	GFRD1000M	Semi-arid	29.760	71.168	0.83	38.95	88
SG71	GFRD1001S	Semi-arid	29.695	71.110	7.43	56.20	86
SG74	GFRD1001T	Semi-arid	29.686	71.022	5.40	66.58	82
SG79	GFRD1001U	Semi-arid	29.671	71.294	6.72	65.72	86
SG91	GFRD1001V	Semi-arid	28.935	71.026	14.44	78.30	63
SG95	GFRD1001W	Semi-arid	28.696	71.131	9.39	51.06	56
SG102	GFRD1001X	Semi-arid	29.629	71.095	0.36	68.55	91
LC4	GFRD1001G	Mediterranean	32.510	71.368	1.76	69.26	290
LC21	GFRD1001J	Mediterranean	32.127	71.289	14.94	87.69	282
LC25	GFRD1001H	Mediterranean	32.019	71.381	7.19	80.83	269
LC33a	GFRD1001K	Mediterranean	33.110	71.221	9.79	66.51	463
LC34	GFRD1001L	Mediterranean	33.116	71.203	7.92	94.34	487
LC35	GFRD1001M	Mediterranean	33.067	71.243	7.98	70.90	445
LC37a	GFRD1001N	Mediterranean	32.945	71.083	24.19	91.83	432
LC37b	GFRD1002T	Mediterranean	32.953	71.068	6.72	101.02	445
LC48	GFRD1001P	Mediterranean	33.099	71.321	8.55	53.28	434
NB2	GFRD10017	Humid-temperate	37.882	73.082	1.35	41.85	1260
NB3	GFRD10018	Humid-temperate	37.859	73.013	13.69	69.92	1368
NB4	GFRD10019	Humid-temperate	37.804	72.938	16.47	42.25	1603
NB4c	GFRD10001	Humid-temperate	37.808	73.014	5.91	22.44	1664
NB5	GFRD1001A	Humid-temperate	37.771	72.974	16.61	51.75	1789
NB10	GFRD1001B	Humid-temperate	37.582	72.899	10.69	72.32	1325
NB14	GFRD1001C	Humid-temperate	37.678	73.227	38.82	71.05	1558
NB18	GFRD1001D	Humid-temperate	37.628	73.103	23.37	45.51	1714
NB23	GFRD1001E	Humid-temperate	37.928	73.074	29.45	62.92	1254
NB100	GFRD1001F	Humid-temperate	37.828	73.011	3.86	41.85	1400

[a] Open access metadata: http://igsn.org//[insert IGSN number here]

[b] Normalized channel steepness index, with θ_{ref}=0.45

[c] Boisier et al. (2018)

In each climatic zone, we selected 9 or 10 catchments that vary in mean basin normalized channel steepness indices (Figure 5.1b and Table 5.1). We targeted relatively small catchments (<40 km^2), to ensure a near-uniform precipitation distribution over the catchment (Leonard and Whipple, in review) and avoid grain size-dependent ^{10}Be as result of fluvial abrasion (Van Dongen et al., 2019). Furthermore, we aimed to sample catchments with natural vegetation cover and limited anthropogenic influence (e.g., dams, water extraction).

5.3 Methodology

5.1.1 ^{10}Be-derived erosion rates

We constrained the catchment average erosion rate of each catchment, by measuring cosmogenic-^{10}Be in river sediment. We collected ~4 to 5 kg of river sediment from each river channel during fieldwork. In the laboratory, we dried and sieved the samples and selected the grain size fraction 0.125-0.5 mm for further processing. We used established chemical and physical separation and purification methods, to isolate pure quartz from the river sediment sample (Kohl and Nishiizumi, 1992). Next, we weighted ~20 to 30 g pure quartz, spiked the samples with ~0.15 mg ^{9}Be carrier, dissolved the samples, and extracted beryllium in the ultra-clean laboratory (e.g., von Blanckenburg et al., 2004). The $^{10}Be/^{9}Be$ ratios were measured at the accelerator mass spectrometer at the University of Cologne in Germany and normalized to the KN01-6-2 (nominal $^{10}Be/^{9}Be$ ratio: 5.35×10^{-13}) and KN01-5-3 (nominal $^{10}Be/^{9}Be$ ratio: 6.32×10^{-12}) standards. Furthermore, we compiled the ^{10}Be concentrations of 150 different river basins in Chile, that have been published in previous studies (Table S 5.1). We calculated catchment average erosion rates for the measured and compiled ^{10}Be concentrations using the time-independent 'St'-scaling scheme (Lal, 1991; Stone, 2000) and the Sea Level High Latitude production rate of 4.01 at g^{-1} yr^{-1} (Borchers et al., 2016; Phillips et al., 2016).

5.1.2 Calculating catchment attributes

To investigate which climatic and non-climatic factors affect the measured erosion rates, we determined several climatic and topographic catchment attributes for the sampled and compiled catchments in this study.

With the use of a 30m Digital Elevation Model (DEM) from the Shuttle Radar Topography Mission (SRTM; Jarvis et al., 2008) and TopoToolbox V2 , we delineated the upstream river catchment at each sample location. Next, we calculated hillslope angles as the steepest downward gradient of an 8-grid cell-connected neighbourhood and the normalized channel steepness index for channel reaches of 200 m with a reference concavity (θ_{ref}) of 0.45 (Wobus et al., 2006). We determined mean basin slope and mean basin channels steepness values as the arithmetic mean of all values within the catchment.

Moreover, we calculated the mean annual precipitation rate for each catchment using the 0.05°-resolution CR2MET monthly gridded precipitation dataset (Boisier et al., 2018a), which is the best performing gridded precipitation dataset for Chile (Alvarez-Garreton et al., 2018; Chapter 4). We interpolated monthly precipitation values to each grid cell of the catchment's DEM by applying a nearest-neighbour linear interpolation method and calculated the mean basin monthly precipitation value as the arithmetic mean of all grid cells in a catchment. Finally, we calculated a 37-year average mean annual precipitation rate for each basin based on the obtained mean monthly precipitation values for the time period 1979-2016.

To investigate how the grain size of river sediment relates to erosion rates, we conducted a Wolman pebble count of 100 individual clasts, with a distance of 1 m between the measurements (Wolman, 1954) at each sample location of the sampled catchments in this study. We obtained a median (D_{50}) and 84th-percentile (D_{84}) grain size value for each catchment, using a bootstrapping method of 100 grab samples.

5.4 Results

The ^{10}Be concentrations and corresponding catchment average erosion rates for all catchments in the three climate zones are presented in Table 5.2. The catchment average erosion rates in the semi-arid region range between 5.3-18.7 mm kyr^{-1}. The catchment average erosion rates in the mediterranean region are higher and range between 8.2-258 mm kyr^{-1}. Finally, the catchments located in the humid-temperate region show catchment average erosion rates, which range between 21.6-56.6 mm kyr^{-1}.

The erosion rates of two of the catchments in the mediterranean region are a factor 10 higher (193 and 258 mm kyr^{-1}) compared to the other erosion rates within that region (~27 mm kyr^{-1} on average). Both catchments are located in near proximity from each other and are both tributaries from the same main river. One of these subcatchments (LC37b) was the subject of an earlier study, which reported a similar order of magnitude erosion rates for 7 different grain size classes (ranging between 0.5-64 mm) (Van Dongen et al., 2019). In agreement with another study, which was carried out in the same region, the high erosion rates were attributed to deep-seated erosion processes, because landslide scars and debris flow deposits were observed in the catchment (Van Dongen et al., 2019; Terweh et al., 2021). As these catchments are relatively small, the ^{10}Be concentrations are likely dominated by the deep-seated processes (Niemi et al., 2005; Yanites et al., 2009). We excluded these two catchments from the figures in this chapter.

A comparison between the measured catchment average erosion rates and MAP reveals that lowest erosion rates in the semi-arid region (Figure 5.2a). The erosion rates in the humid-temperate region are slightly higher than the mediterranean region, but there is a lot of overlap in erosion rates.

In spite of the large amount of scatter, we observe the steepest mean basin slope angles in the semi-arid (~16-22°) and mediterranean (~19-23°) regions, compared to the humid-temperate region (~8-15°) (Figure 5.2b). This reveals that the humid-temperate region comprises some of the highest erosion rates, despite gentle sloping basins. The humid-temperate and semi-arid regions show an increasing trend between hillslope angles and erosion rates. Interestingly, a steep negative trend can be observed between hillslope angles and erosion rates in the mediterranean region.

An increasing trend between the normalized channel steepness index and catchment average erosion rates is found for all climate regions (Figure 5.2c). For a given normalized channel steepness value, the erosion rates are the highest in the humid-temperate region, followed by the mediterranean region and the semi-arid region. Overall, the range of channel steepness values is low compared to other studies in active mountain belts (e.g., DiBiase and Whipple, 2011; Lague et al., 2005; Scherler et al., 2017).

No trends can be observed between catchment average erosion rates and the grain size of channel sediment (Figure 5.2d and e). The measured average grain sizes of river sediment are the finest in the semi-arid region (D_{50}= 0.2-7 cm, D_{84}=9.5-26.8 cm), followed by the mediterranean region (D_{50}=0.2-13 cm, D_{84}=20.5-44.6 cm) (Table S 5.2). The range of river sediment grain sizes is the largest for the humid-temperate region (D_{50}=0.2-32cm, D_{84}=19.8-80 cm), which contains 4 catchments with extremely coarse channel sediment (D_{50} >20 cm, D_{84} >40 cm). We further investigated a potential trend between channel sediment grain sizes and channel steepness; however, no trends could be observed (Figure S 5.1).

Table 5.2: Cosmogenic nuclide samples from the climate zones. ID, analyzed quartz mass, ^{9}Be carrier mass, $^{10}Be/^{9}Be$ ratio (±1σ), ^{10}Be concentrations (±2σ analytical error), spallation (P_{sp}) and muogenic (P_{mu}) production rates and calculated denudation rates (±2σ).

ID	IGSN[a]	Quartz mass	^{9}Be Carrier mass	$^{10}Be/^{9}Be$ ratio ± 1σ	$[^{10}Be]$ ± 2σ	P_{sp}	P_{mu}	Erosion rate ± 2σ
		(g)	*(mg)*	*x 10^{-14}*	*(x 10^{5} atoms g^{-1})*	*(atoms g_{qtz}^{-1} yr^{-1})*	*(atoms g_{qtz}^{-1} yr^{-1})*	*(mm kyr^{-1})*
SG10	GFRD1001Q	26.1	0.155	134.0 ± 4.9	5.31 ± 0.20	7.47	0.11	9.0 ± 1.2
SG35	GFRD1001R	23.2	0.155	52.4 ± 2.0	2.334 ± 0.094	6.85	0.10	19.7 ± 2.6
SG39	GFRD1000M	18.7	0.154	85.4 ± 2.8	4.71 ± 0.16	6.03	0.097	8.3 ± 1.0
SG71	GFRD1001S	24.6	0.155	124.4 ± 4.7	5.21 ± 0.20	7.31	0.11	9.0 ± 1.2
SG74	GFRD1001T	23.5	0.155	105.8 ± 3.9	4.65 ± 0.18	7.64	0.11	10.6 ± 1.4
SG79	GFRD1001U	24.4	0.155	60.9 ± 2.0	2.578 ± 0.090	5.65	0.095	14.8 ± 1.8
SG91	GFRD1001V	24.0	0.155	208.2 ± 7.4	8.95 ± 0.33	7.76	0.11	5.32 ± 0.71
SG95	GFRD1001W	24.6	0.154	103.2 ± 3.8	4.31 ± 0.16	7.55	0.11	11.3 ± 1.5
SG102	GFRD1001X	24.4	0.154	73.5 ± 2.8	3.10 ± 0.12	8.84	0.12	18.7 ± 2.4
LC4	GFRD1001G	31.1	0.155	123.9 ± 4.1	4.13 ± 0.14	5.15	0.089	8.2 ± 1.0
LC21	GFRD1001J	34.7	0.154	73.4 ± 2.5	2.182 ± 0.077	7.35	0.10	22.6 ± 2.7
LC25	GFRD1001H	31.2	0.155	43.3 ± 1.5	1.436 ± 0.053	6.17	0.096	29.7 ± 3.6
LC33a	GFRD1001K	31.6	0.155	27.0 ± 1.0	0.882 ± 0.034	5.70	0.092	45.9 ± 5.6
LC34	GFRD1001L	33.9	0.155	45.6 ± 1.6	1.391 ± 0.050	7.09	0.10	34.8 ± 4.2
LC35	GFRD1001M	30.5	0.155	43.8 ± 1.6	1.485 ± 0.055	5.62	0.092	26.3 ± 3.2
LC37a	GFRD1001N	31.0	0.155	9.59 ± 0.46	0.320 ± 0.016	8.95	0.11	193 ± 27
LC37b	GFRD1002T	19.4	0.154	4.98 ± 0.28	0.264 ± 0.015	9.97	0.12	258 ± 39
LC48	GFRD1001P	31.0	0.155	54.7 ± 1.9	1.828 ± 0.065	5.71	0.092	21.5 ± 2.6
NB2	GFRD10017	20.8	0.155	25.4 ± 1.0	1.264 ± 0.053	8.25	0.10	44.1 ± 5.7
NB3	GFRD10018	20.5	0.154	33.5 ±1.3	1.688 ± 0.066	9.66	0.11	37.9 ± 4.8
NB4	GFRD10019	20.6	0.155	35.7 ± 1.3	1.799 ± 0.069	10.07	0.11	36.9 ± 4.6
NB4c	GFRD10001	19.8	0.154	51.4 ± 1.8	2.67 ± 0.10	10.71	0.12	26.1 ± 3.2
NB5	GFRD1001A	20.9	0.155	37.4 ± 1.4	1.853 ± 0.071	9.91	0.11	35.3 ± 4.4
NB10	GFRD1001B	20.8	0.155	15.06 ± 0.65	0.748 ± 0.033	5.98	0.091	56.6 ± 7.4
NB14	GFRD1001C	20.5	0.155	27.5 ± 1.1	1.382 ± 0.057	8.45	0.11	41.1 ± 5.3
NB18	GFRD1001D	22.0	0.155	31.9 ± 1.3	1.499 ± 0.063	9.01	0.11	40.2 ± 5.3
NB23	GFRD1001E	21.3	0.155	21.92 ± 0.86	1.066 ± 0.043	6.69	0.095	43.4 ± 5.5
NB100	GFRD1001F	20.5	0.155	61.9 ± 2.2	3.12 ± 0.12	10.44	0.12	21.6 ± 2.7

[a] Open access metadata: http://igsn.org//[insert IGSN number here]

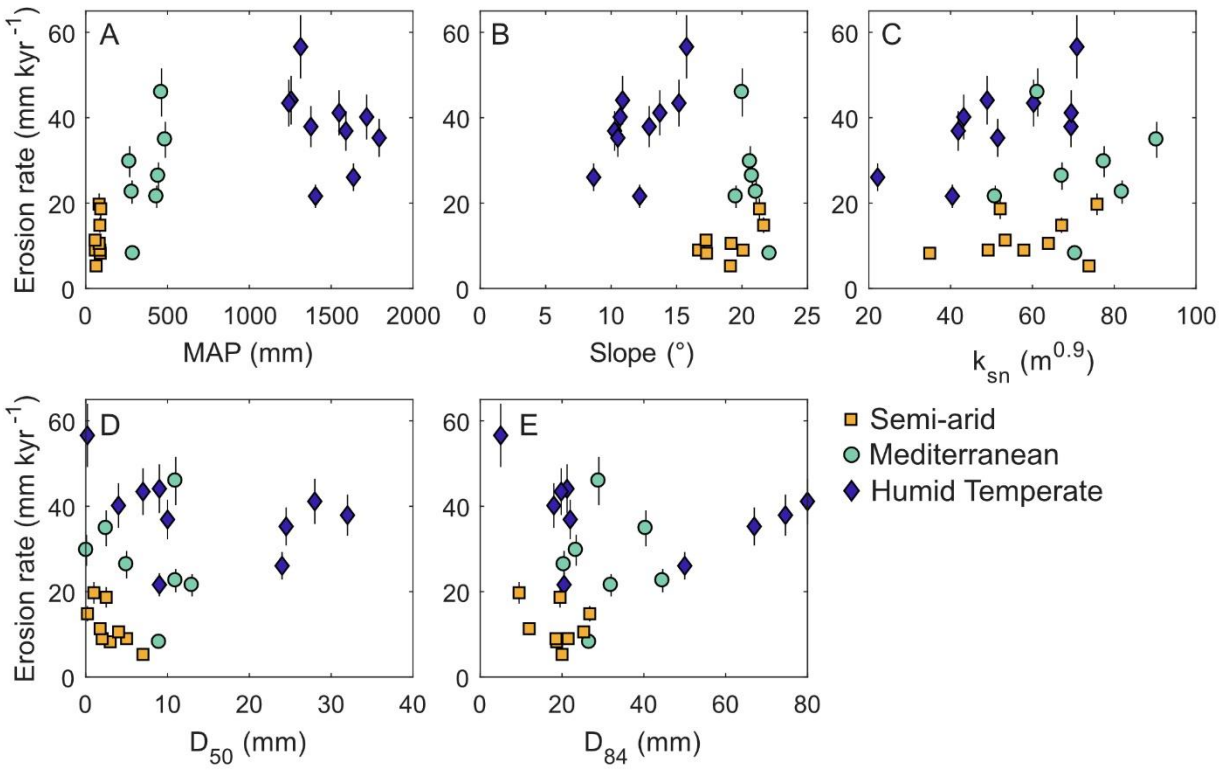

Figure 5.2: ^{10}Be-derived catchment average erosion rates in comparison to various catchment attributes. A) Mean Annual Precipitation (MAP), B) mean slope angles, C) normalized channel steepness, D) median grain size (D_{50}), E) 84th-percentile grain size (D_{84}).

5.5 Discussion

5.5.1 Results of this study

The results of this study suggest a combined climatic and topographic control on the measured erosion rates in the different climate regions. By comparing the erosion rates per climatic region alone, the erosion rates of the mediterranean and humid-temperate regions seem to largely overlap, despite a difference of ~1000 mm in MAP (Figure 5.2a). However, when also considering the mean basin slope angles, the data reveals that the sampled catchment are steeper in the semi-arid and mediterranean regions, whereas the catchments in the humid-temperate region are generally gently sloping (Figure 5.2b). This reveals that hillslope angels have, likely, resulted in higher erosion rates in the semi-arid and mediterranean regions. A positive trend between mean basin slope and erosion rates is observed for the humid-temperate and semi-arid regions, which reveals that erosion rates increase with increasing hillslope angles (e.g., Carretier et al., 2013; Ouimet et al., 2009).

Nonetheless, comparing mean basin slope angles to erosion rates to infer for tectonic processes is not recommended, because hillslopes reach a critical hillslope threshold (~30-35°) at which hillslopes cannot get any steeper and the erosion rate is dominated

by the frequency of landslides (Larsen and Montgomery, 2012; Montgomery and Brandon, 2002; Ouimet et al., 2009). Instead, it is recommended to use the normalized channel steepness index, which scales with long-term tectonic uplift rates in catchments that are in topographic steady state (e.g., Dibiase et al., 2010; Kirby and Whipple, 2012; Whipple et al., 2013; Wobus et al., 2006). This relationship has been used to study the tectonic control on erosion rates in various landscapes on earth (Cyr et al., 2010; Dibiase et al., 2010; Harkins et al., 2007; Kirby and Whipple, 2012; Mandal et al., 2015; Ouimet et al., 2009; Safran et al., 2005; Scherler et al., 2014, 2017; Starke et al., 2017). Similar to these previous studies, we observe a positive relationship between the normalized channel steepness indices and the catchment average erosion rates (Figure 5.2c). Additionally, we observe a climatic signal. For a given channel steepness index, the erosion rates are the highest in the humid-temperate region, followed by the mediterranean region and the semi-arid region. As the catchments have deliberately been selected based on similar lithology, the increase in fluvial erosion efficiency is most likely result of the contrasting mean annual precipitation rates (Callaghan, 2012). The observed increase in erosion rates with increasing precipitation do not fully comply with the study of Schaller et al. (2018), who measured erosion rates in soil profiles on granitic hillslopes located in the same focus regions in the Coastal Cordillera. They observed an increase in erosion rates with increasing precipitation (from arid to mediterranean), but a decrease in erosion rates in the humid-temperate region compared to the mediterranean region. The authors suggested that this could be attributed this to a reducing effect of dense vegetation cover on erosion in the humid region (Schaller et al., 2018). However, the conclusions of this study relied on one or two soil profiles per climate region only, and the local hillslope angles of the soil profile locations varied, which might additionally have affected the erosion rates.

We observed an overall increase in channel grain sizes from the semi-arid to the humid-temperate region. A similar pattern was reported by another study that comprehensively investigated the hillslope and channel grain size distributions in single catchments located in each of the climate regions (Terweh et al., 2021). The authors of this study found evidence for non-selective and transport limited transport in the semi-arid region, and size-selective and supply limited transport in the humid-temperate region. This implies, that the fine faction is still remaining in the channel of the semi-arid region, but has been transported in the humid-temperate region by selective transport, leaving a coarse grain size distribution behind (Terweh et al., 2021). The 4 catchments with very coarse grain size distributions in the humid-temperate region, are likely affected by core stones that have been observed on the hillslopes in these catchments (e.g., Oeser et al., 2018). However, we lack an explanation for the obscure relationships between erosion rate and grain size of channel sediment (Figure 5.2d and e), and between grain size and channel steepness indices (Figure S 5.1). We anticipated a positive relationship between channel grain sizes and the channel steepness index and channel grain sizes and erosion rate, such as observed for other catchments, resulting from deep-seated erosion processes in steep catchments that excavate coarse hillslope material (e.g., Attal et al., 2015; Attal and Lavé, 2006; Riebe et al., 2015;

Roda-Boluda et al., 2018). This trend can presumably not be observed because the catchments have relatively low channel steepness and deep-seated erosion processes are rather unlikely. Moreover, in spite of the similar lithology between climate regions, other bedrock characteristics such as bedrock fracture density could additionally affect the grain size distribution of channel sediment (Lebedeva and Brantley, 2017; Sklar et al., 2017). We do acknowledge that although we aimed to sample natural basins, anthropogenic processes such as tree logging and agricultural practices were realized in some of the catchments, especially in the humid-temperate and mediterranean regions. These practices could have obscured the grain size trends in these channels. Finally, we would like to stress that the measured channel sediment grain sizes only provide a snapshot in time, whereas the erosion rates and normalized channel steepness indices are the product of landscape evolution over several thousands of years.

5.5.2 Comparison to published data

The catchment average erosion rates of the three climate regions agree well with the catchment average erosion rates of other catchments that were sampled in the Coastal Cordillera, published by Callaghan (2012) (Figure 5.3b). Other previously published erosion rates, that mainly stem from Andean catchments are ~1 to 2 orders of magnitude higher than the erosion rates of this study. The two extreme erosion rates that we measured in the mediterranean region seem to equal the erosion rates measured in the landslide-dominated region in the Andes (~32°S-35°S) (Aguilar et al., 2014; Antinao and Gosse, 2009; Carretier et al., 2015b, 2018), which is an additional confirmation that the erosion rates of these two catchments are likely affected by deep-seated erosion processes.

We observe increasing erosion rates with increasing MAP for catchments located in the Coastal Cordillera (circles, Figure 5.3b). Unfortunately, we could not investigate the potential tectonic control on the erosion rates of many of the previously published catchments in the Coastal Cordillera, as it was impossible to locate the basins and calculate channel steepness indices of study of Callaghan (2012) due to poorly reported coordinates (Figure S 5.2). However, as no latitudinal increase in relief is observed in the Coastal Cordillera (Figure 5.3a) and the modern uplift rates of the Coastal Cordillera between 16°S-33°S are found to be relatively steady at 0.13 ± 0.4 mm yr^{-1} (Figure 5.3c; Melnick, 2016). Hence, it is unlikely that the observed latitudinal increase in erosion rates is solely induced by tectonic uplift. Therefore, we conclude that the observed latitudinal increase in erosion rates in the Chilean Coastal Cordillera is likely induced by increasing precipitation rates.

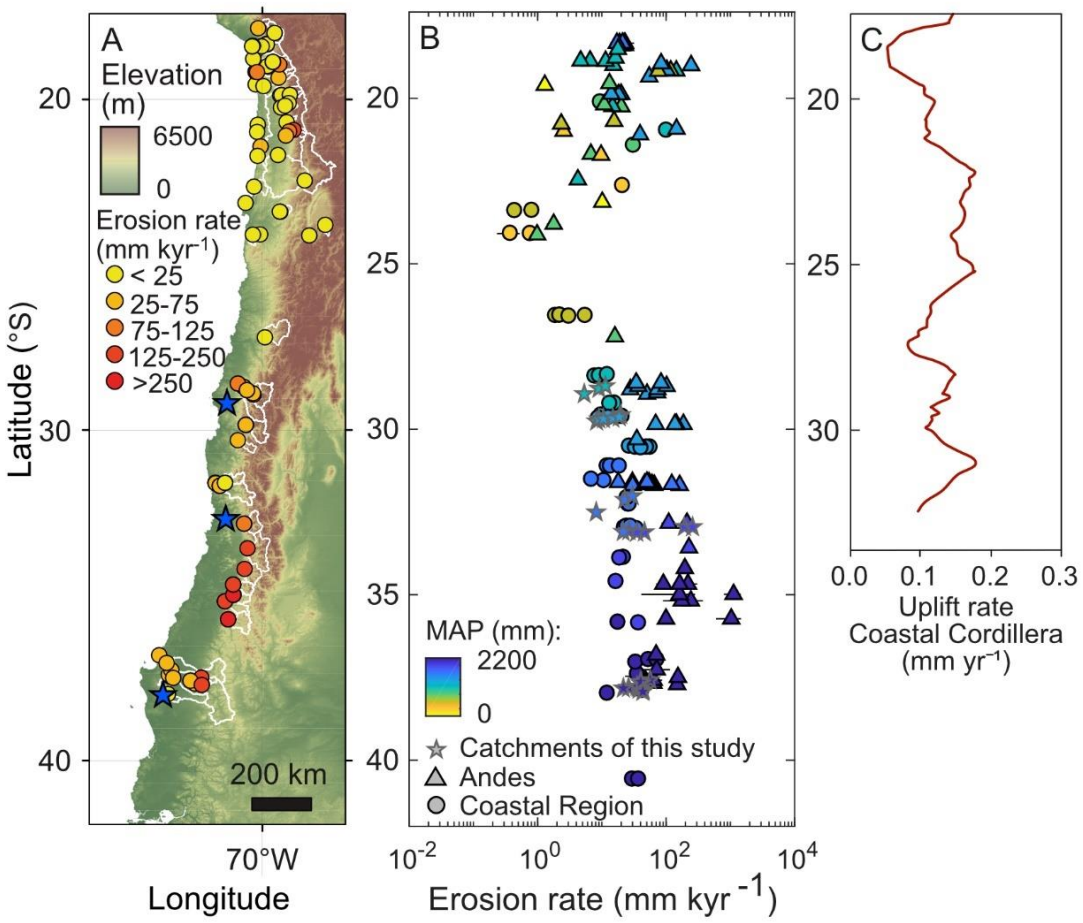

Figure 5.3: Previously published ^{10}Be-derived erosion rates in Chile. A) Map of Chile with ^{10}Be-derived catchment average erosion rates from previous studies (listed in Table S 5.1), blue stars represent the sample locations in this study. Note: the sampled catchments of Callaghan et al. (2012) are not shown on the map, because the basins could not be delineated due to poor coordinate resolution. B) Plot of the latitudinal variation in ^{10}Be-derived erosion rates, based on data from previous studies and the results from this study (stars with red outlines). The data of previous studies has been divided in catchments that are located in the Andes (triangles) and the Coastal region (circles). Data from: Aguilar et al. (2014), Callaghan (2012), Carretier et al. (2013, 2014, 2015a, 2015b), Cortés et al. (2012), Kober et al. (2009), Placzek et al. (2010), Starke et al. (2017), Tolorza (2015). C) Modern uplift rates of the Coastal Cordillera, modified from Melnick, (2016). A comparison in the latitudinal variations in erosion rates, channel steepness, and MAP are shown in Figure S 5.2.

A similar increase in erosion rates with increasing MAP is observed for the Andes (triangles, Figure 5.3b). However, as frequently reported, the erosion rates in the Andes slightly decrease south of ~35°S, despite increasing MAP (Figure 5.3b and Figure S 5.2). We attribute this to the decreasing hillslope angles and normalized channel steepness indices to the south of ~35°S (Figure S 5.2) (Carretier et al., 2013, 2018). Several studies suggested that, furthermore, dense vegetation cover could induce a potential control on the decreasing erosion rates south of ~35°S (Aguilar et al., 2014; Carretier et al., 2013, 2015b, 2018; Tolorza et al., 2014). The study of Starke et al. (2020) specifically

focussed on the role of vegetation on the erosional dynamics in the Andes between 6°S-36°S. The authors suggested a bidirectional effect of vegetation on erosion rates in the Andes (i.e., either a positive or a negative relationship, for different regions), which was explained by the competing effect of climate and vegetation on erosion rates. However, the region where the authors observed a reducing effect of dense vegetation (50 to 60% vegetation cover) on erosion rates, was observed in Peruvian Andes (10°S-14°S), which is outside of the latitudinal extent of this study. The authors could not determine a significant effect of vegetation in Chile, south of ~35°S, because the study area extend ended at ~36°S. For the Chilean segment of the study area, Starke et al. (2020) report an increase in erosion rates with increasing precipitation between 18°S-32°S and a strong control of catchment steepness on erosion rates between 32°S-36°S, which is in line with our conclusions. We conclude that, although vegetation cover might have an effect on erosion rates south of ~35°S, this cannot not be resolved due the co-variation between vegetation cover, MAP and the elevation and steepness of the Andes (Aguilar et al., 2014; Carretier et al., 2013, 2015b, 2018; Tolorza et al., 2014).

A final assessment of all currently available catchment average erosion rates for Chile plotted against their MAP and normalized channel steepness values reveals, despite the large scatter, an increasing trend in erosion rates with increasing MAP and normalized channel steepness (Figure 5.4a and b). Similar to the results of this study, Figure 5.4c reveals a positive trend between normalized channel steepness and erosion rates, but for a given channel steepness index, often the highest erosion rates are observed for catchments with the highest MAP (colour coding). We conclude that despite the large variation in lithologies, the erosion rates in Chile reveal a combined tectonic and climatic control, which means that the fluvial erosion efficiency increases with increasing MAP. This implies that, for a given lithology, steady state catchments in an arid climate must be steeper than catchments in a humid climate, to reach erosion rates that comply with tectonic uplift rates (Callaghan, 2012; Tucker and Bras, 2000; Whipple and Tucker, 1999).

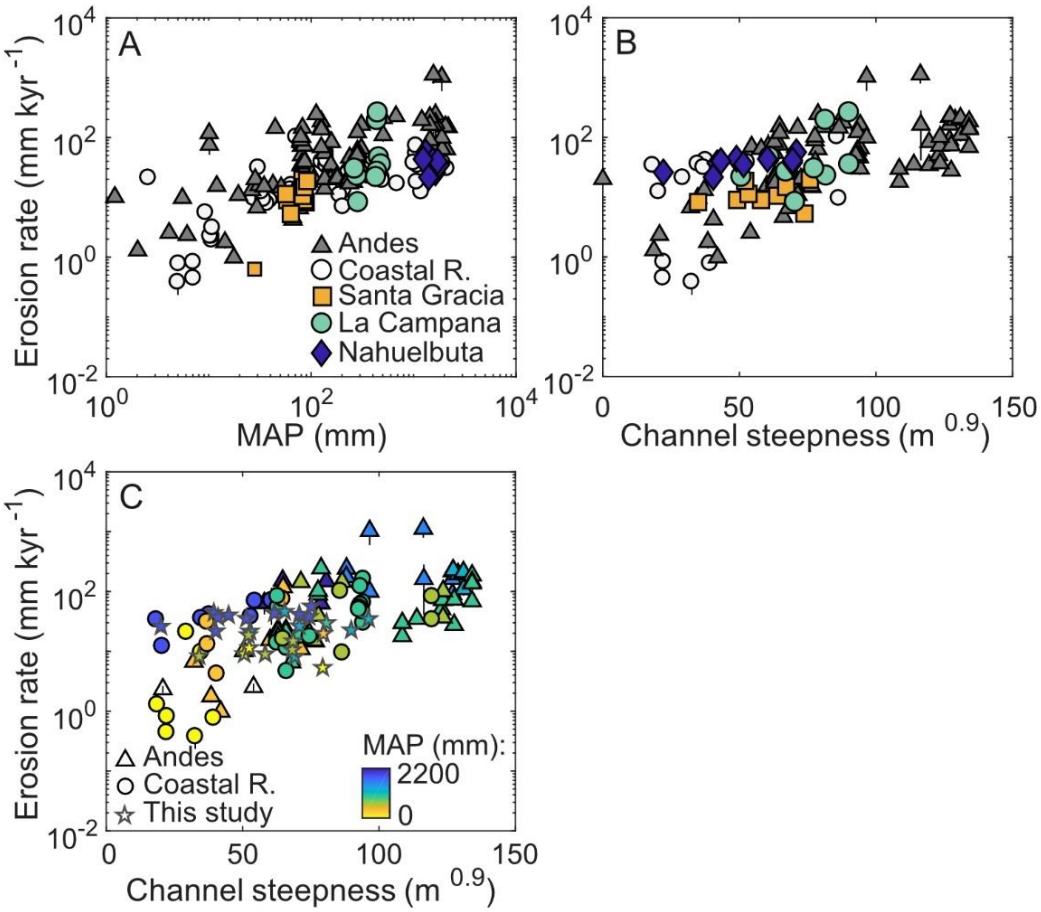

Figure 5.4: The combined tectonic control and climatic control on catchment average erosion rates in Chile. A) Relationship between mean annual precipitation (MAP) and erosion rates, B) relationship between normalized channel steepness (channel steepness) and erosion rates, C) relationship between normalized channel steepness and erosion rates, colour coded by mean annual precipitation (MAP). This figure includes the data from previously studies (except those of Callaghan (2012)) that are presented in Table S 5.1 and the data from the climatic regions that are part of this study.

Landscape evolution is strongly driven by the incision of rivers that set the boundary conditions for hillslope erosion (e.g., Whipple, 2004). Based on the results of this study we can conclude that, besides tectonic processes, MAP exerts a positive effect on erosion rates and, thus, the fluvial erosion efficiency in Chile (Callaghan, 2012; Tucker and Bras, 2000; Whipple and Tucker, 1999). However, MAP can affect the fluvial erosion efficiency in various ways, which cannot be disentangled based on ^{10}Be-derived erosion rates alone. For instance, MAP can affect the erodibility of the bedrock, as studies have suggested that chemical weathering rates depend on the flux of water through the bedrock (e.g., Maher, 2010; Sklar et al., 2017). Moreover, as precipitation is the main source for river discharge, climate has a direct control on the erosion efficiency parameter (K) that feeds into the stream power river incision model (e.g., Deal et al., 2018; Ferrier et al., 2013; Perron, 2017).

Furthermore, river incision is known to be a stochastic process, because bedload sediment sets a certain erosion threshold that river discharge needs to exceed to initiate the motion of bedload sediment and expose the riverbed to erosion (Lague, 2013; Sklar and Dietrich, 2004; Turowski et al., 2007). Based on the relatively coarse grain sizes that were measured in the catchments of this study and because the basins in this study have relatively low channel steepness indices, it is reasonable to assume that erosion thresholds do play a role in these catchments. Climate can also exert multiple effects on the threshold-behaviour of river incision. For instance the climatic control on physical and chemical weathering processes may affect the grain size of river sediment (e.g., Sklar et al., 2017). Moreover, the variability of river discharge (i.e., how often and by how much discharge deviates from the mean) is known to differ between arid and humid climates (e.g., Lague, 2013). Discharge variability is expected to be high in arid regions, where typically infrequent but extreme precipitation events occur. In contrast, humid regions typically display lower discharge variability, because rivers in these regions typically have constant baseflow, and vegetation and soils have a buffering effect that reduce the response of river discharge on a precipitation event.

A modelling study is required, to test whether erosion thresholds indeed play an important role in the catchments in the Chilean Coastal Cordillera and how this differs for different climate regions. This study is reported in Chapter 6.

5.6 Conclusion

In this study, we investigated the erosion rates of 9-10 catchments with similar lithology but contrasting normalized channel steepness indices, located in three different climate zones (semi-arid, mediterranean, and humid-temperate) in the Coastal Cordillera of central Chile. The results revealed a positive linear relationship between normalized channel steepness indices and erosion rates in each climate region. Moreover, a climatic signal could be observed. For a given channel steepness, erosion rates were the highest for the humid-temperate region, followed by the mediterranean region and the semi-arid region. This indicates that fluvial erosion efficiency increases with increasing mean annual precipitation. We could not observe any functional relationship between channel grain sizes and erosion rates or normalized channel steepness.

Furthermore, we compared our results to previously published erosion rates and conclude that a combined tectonic and climatic control can be observed in the erosion rates of Chile. To test whether erosion thresholds and discharge variability play an important role in the gently sloping catchments of this study, a modelling study is required.

5.7 Sample availability

The metadata of all samples in Table 5.1 can be accessed via http://igsn.org/[insert IGSN number here].

5.8 Acknowledgements

We acknowledge support from the German Science Foundation (DFG) priority research program SPP-1803 "EarthShape: Earth Surface Shaping by Biota" (grant SCHE 1676/4-1 to D.S.). We are grateful to the Chilean National Park Service (CONAF) for providing access to the sample locations and on-site support of our research. We thank H. Wittmann for the cosmogenic-^{10}Be laboratory training and laboratory supervision. We also thank L. Mao, R. Carrillo and M. Koelewijn for their support during fieldwork, and S. Binnie and S. Heinze from Cologne University for conducting AMS measurements.

5.9 Supplementary tables

Table S 5.1: Overview of previously published ^{10}Be-concentrations and ^{10}Be-derived catchment average erosion rates in Chile. Please note that the reported coordinates of Callaghan (2012) were too inaccurate to constrain the exact river basin, recalculate the erosion rates and calculate catchment attributes. Instead, we used the values that were reported in the study. The erosion rates of all other published samples are recalculated following the method that is described in the Methodology section (Section 0).

ID	Publication	Latitude	Longitude	^{10}Be-conc.	2σ ^{10}Be int. error.	Erosion rate	1σ uncertainty Erosion rate
		(°N)	*(°E)*	*(atoms g^{-1})*	*(atoms g^{-1})*	*(mm kyr^{-1})*	*(mm kyr^{-1})*
HUA3	Aguilar et al., (2014)	-28.892	-70.278	3.32	0.18	72.34	11.02
HUA9	Aguilar et al., (2014)	-28.797	-70.458	3.19	0.27	73.24	14.79
HUA11	Aguilar et al., (2014)	-28.702	-70.551	2.16	0.19	101.69	21.11
HUA14	Aguilar et al., (2014)	-28.598	-70.729	2.49	0.12	83.21	12.14
LC07_01	Callaghan (2012)	-32.990	-71.420	1.75	0.08	26.50	0.60
LC07_04	Callaghan (2012)	-32.980	-71.420	1.93	0.22	22.60	1.30
LC07_06	Callaghan (2012)	-32.980	-71.420	1.76	0.17	25.50	1.30
LC07_08	Callaghan (2012)	-32.940	-71.430	1.71	0.10	24.60	0.70
LC07_10	Callaghan (2012)	-33.010	-71.440	1.37	0.11	34.70	1.40
LC07_11	Callaghan (2012)	-31.120	-71.580	3.95	0.24	12.20	0.40
LC07_15	Callaghan (2012)	-31.120	-71.560	3.64	0.26	13.70	0.50
LC07_17	Callaghan (2012)	-31.120	-71.550	2.96	0.17	18.90	0.50

ID	Publication	Latitude	Longitude	^{10}Be-conc.	2σ ^{10}Be int. error.	Erosion rate	1σ uncertainty Erosion rate
		(°N)	*(°E)*	*(atoms g^{-1})*	*(atoms g^{-1})*	*(mm kyr^{-1})*	*(mm kyr^{-1})*
LC07_19	Callaghan (2012)	-30.550	-71.630	0.96	0.10	56.90	2.90
LC07_20	Callaghan (2012)	-30.550	-71.630	1.07	0.11	50.20	2.50
LC07_21	Callaghan (2012)	-29.620	-71.200	2.99	0.17	20.30	0.60
LC07_22	Callaghan (2012)	-29.620	-71.200	2.96	0.16	20.90	0.60
LC07_24	Callaghan (2012)	-29.620	-71.200	3.30	0.22	17.10	0.60
LC07_27	Callaghan (2012)	-29.580	-71.140	6.56	0.36	9.86	0.27
LC07_29	Callaghan (2012)	-29.570	-71.160	3.76	0.26	15.30	0.50
LC07_31	Callaghan (2012)	-29.220	-71.180	4.24	0.24	15.90	0.50
LC07_37	Callaghan (2012)	-29.230	-71.180	3.99	0.20	13.40	0.30
LC07_39	Callaghan (2012)	-28.410	-71.050	6.06	0.38	8.87	0.27
LC07_41	Callaghan (2012)	-28.400	-71.060	6.11	0.36	7.85	0.23
LC07_43	Callaghan (2012)	-28.390	-71.070	5.03	0.30	9.21	0.27
LC07_45	Callaghan (2012)	-28.360	-71.050	3.70	0.36	12.30	0.60
LC07_47	Callaghan (2012)	-26.570	-70.440	25.50	0.68	1.920	0.030
LC07_49	Callaghan (2012)	-26.560	-70.480	18.00	0.50	2.240	0.030
LC07_51	Callaghan (2012)	-26.560	-70.510	18.30	0.90	2.230	0.060
LC07_53	Callaghan (2012)	-26.590	-70.490	16.70	0.72	3.100	0.070
LC07_55	Callaghan (2012)	-26.570	-70.560	7.77	0.42	5.56	0.15
LC08_01	Callaghan (2012)	-40.580	-73.690	1.520	0.054	30.20	0.50

ID	Publication	Latitude	Longitude	^{10}Be-conc.	2σ ^{10}Be int. error.	Erosion rate	1σ uncertainty Erosion rate
		(°N)	*(°E)*	*(atoms g^{-1})*	*(atoms g^{-1})*	*(mm kyr^{-1})*	*(mm kyr^{-1})*
LC08_04	Callaghan (2012)	-40.580	-73.600	1.39	0.11	37.70	1.50
LC08_05	Callaghan (2012)	-37.900	-73.280	1.17	0.10	42.60	1.90
LC08_08	Callaghan (2012)	-36.970	-73.120	0.86	0.10	53.80	3.00
LC08_09	Callaghan (2012)	-36.970	-73.120	0.652	0.052	72.80	2.90
LC08_12	Callaghan (2012)	-35.840	-72.510	3.02	0.15	18.00	0.50
LC08_13	Callaghan (2012)	-35.860	-72.480	1.52	0.12	37.60	1.40
LC08_20	Callaghan (2012)	-34.610	-71.580	3.11	0.30	16.80	0.80
LC08_22	Callaghan (2012)	-33.880	-71.500	2.02	0.11	21.90	0.60
LC08_23	Callaghan (2012)	-33.900	-71.490	2.33	0.12	19.10	0.50
LC08_27	Callaghan (2012)	-32.940	-71.420	1.590	0.082	28.20	0.70
LC08_28	Callaghan (2012)	-32.270	-71.410	1.81	0.11	26.00	0.80
LC08_29	Callaghan (2012)	-32.270	-71.400	1.73	0.30	26.90	2.30
LC08_31	Callaghan (2012)	-32.080	-71.420	1.83	0.26	24.90	1.80
LC08_33	Callaghan (2012)	-31.560	-71.420	3.79	0.24	10.90	0.40
LC08_34	Callaghan (2012)	-31.520	-71.420	7.52	0.34	6.96	0.16
LC08_35	Callaghan (2012)	-30.520	-71.660	1.83	0.10	27.00	0.70
LC08_36	Callaghan (2012)	-30.530	-71.660	1.36	0.09	39.20	1.40
LC08_37	Callaghan (2012)	-30.550	-71.620	1.64	0.16	33.50	1.60
LC08_38	Callaghan (2012)	-30.570	-71.630	1.30	0.12	41.10	1.90

ID	Publication	Latitude	Longitude	^{10}Be-conc.	2σ ^{10}Be int. error.	Erosion rate	1σ uncertainty Erosion rate
		(°N)	*(°E)*	*(atoms g^{-1})*	*(atoms g^{-1})*	*(mm kyr^{-1})*	*(mm kyr^{-1})*
LC08_39	Callaghan (2012)	-29.650	-71.110	5.85	0.38	12.90	0.40
LC08_40	Callaghan (2012)	-29.670	-71.160	7.21	0.34	8.91	0.21
CAC1	Carretier et al. (2013)	-34.205	-70.529	0.914	0.054	195.63	31.07
MAI1	Carretier et al. (2013)	-33.579	-70.440	0.870	0.025	226.61	26.00
CHO0820	Carretier et al. (2013)	-31.657	-71.222	2.349	0.054	46.27	4.92
HUR1	Carretier et al. (2013)	-30.310	-70.731	5.93	0.19	35.02	4.26
ELK2	Carretier et al. (2013)	-29.847	-70.492	1.869	0.084	137.06	18.95
SAN1	Carretier et al. (2013)	-27.200	-69.920	10.28	0.77	15.96	3.04
MAU1	Carretier et al. (2013, 2014, 2015b)	-35.730	-71.019	1.294	0.074	99.51	15.55
LON1	Carretier et al. (2013, 2014, 2015b)	-35.184	-71.118	0.64	0.15	175.36	86.14
TEN1	Carretier et al. (2013, 2014, 2015b)	-34.991	-70.860	0.73	0.24	161.87	120.71
TIN1	Carretier et al. (2013, 2014, 2015b)	-34.676	-70.870	0.994	0.026	162.40	18.06
ACO1	Carretier et al. (2013, 2014, 2015b)	-32.835	-70.539	1.012	0.015	211.28	20.47
CHO1	Carretier et al. (2013, 2014, 2015b)	-31.690	-71.268	1.956	0.034	65.49	6.49
ELK1	Carretier et al. (2013, 2014, 2015b)	-29.847	-70.492	1.77	0.12	144.76	24.85
HUA1	Carretier et al. (2013, 2014, 2015b), Aguilar et al. (2014)	-28.937	-70.262	4.800	0.068	50.47	4.94
HUA7	Carretier et al. (2013, 2014, 2015b), Aguilar et al. (2014)	-28.799	-70.458	8.33	0.27	27.73	3.38

ID	Publication	Latitude (°N)	Longitude (°E)	^{10}Be-conc. (atoms g^{-1})	2σ ^{10}Be int. error. (atoms g^{-1})	Erosion rate (mm kyr^{-1})	1σ uncertainty Erosion rate (mm kyr^{-1})
HUA10	Carretier et al. (2013, 2014, 2015b), Aguilar et al. (2014)	-28.702	-70.552	5.890	0.083	36.82	3.60
HUA12	Carretier et al. (2013, 2014, 2015b), Aguilar et al. (2014)	-28.599	-70.728	5.99	0.12	34.22	3.63
CHO0822S	Carretier et al. (2013, 2014, 2015a,b)	-31.669	-71.294	1.982	0.029	60.34	5.78
CHO0823S	Carretier et al. (2013, 2014, 2015a,b)	-31.611	-71.395	2.181	0.047	54.10	5.66
ILL1	Carretier et al. (2013, 2015b)	-31.599	-71.111	4.690	0.068	29.85	2.91
ILL3	Carretier et al. (2013, 2015a)	-31.600	-71.113	7.68	0.64	18.00	3.68
CHO0822G	Carretier et al. (2013, 2015a)	-31.663	-71.300	0.985	0.058	122.39	19.41
CHO0823G	Carretier et al. (2013, 2015a)	-31.597	-71.405	2.338	0.078	50.30	6.06
Bbm1-2	Carretier et al. (2015a), Tolorza (2015)	-37.674	-72.010	1.170	0.095	63.37	12.36
CHIZ1	Carretier et al., (2015b)	-19.179	-70.153	1.17	0.17	75.33	23.96
MAU3	Carretier et al., (2015a)	-35.727	-71.021	0.126	0.025	1031.73	436.87
LON2	Carretier et al., (2015a)	-35.184	-71.116	0.47	0.12	242.50	132.90
TEN3	Carretier et al., (2015a)	-34.986	-70.865	0.106	0.014	1123.55	330.09
TIN2	Carretier et al., (2015a)	-34.677	-70.871	1.77	0.17	90.55	20.33
TIN3	Carretier et al., (2015a)	-34.677	-70.871	0.74	0.13	218.73	86.29
ACO3	Carretier et al., (2015a)	-32.835	-70.545	1.94	0.19	109.64	24.72
CHO2	Carretier et al., (2015a)	-31.692	-71.268	0.795	0.031	162.49	20.84
CHO3	Carretier et al., (2015a)	-31.692	-71.268	4.21	0.38	30.04	6.47

ID	Publication	Latitude	Longitude	^{10}Be-conc.	2σ ^{10}Be int. error.	Erosion rate	1σ uncertainty Erosion rate
		(°N)	*(°E)*	*(atoms g^{-1})*	*(atoms g^{-1})*	*(mm kyr^{-1})*	*(mm kyr^{-1})*
ELK3	Carretier et al., (2015a)	-29.848	-70.494	1.38	0.12	185.95	39.23
ELK5	Carretier et al., (2015a)	-29.848	-70.494	3.71	0.30	68.71	13.54
MF-D-4	Cortes et al. (2012)	-23.136	-70.501	2.800	0.070	10.14	1.10
LL2	Kober et al. (2009)	-18.400	-70.016	8.90	0.36	19.96	2.69
LL3	Kober et al. (2009)	-18.400	-70.302	7.90	0.49	20.30	3.41
LL3b	Kober et al. (2009)	-18.400	-70.302	7.92	0.41	22.88	3.45
LL3<0.335	Kober et al. (2009)	-18.380	-70.280	8.68	0.45	20.83	3.15
LL1b	Kober et al. (2009)	-18.337	-69.863	9.43	1.64	23.01	8.82
LL1	Kober et al. (2009)	-18.337	-69.863	9.75	0.51	22.22	3.38
LL1c	Kober et al. (2009)	-18.337	-69.863	11.48	0.97	18.81	3.89
LL1<0.335	Kober et al. (2009)	-18.330	-69.870	10.33	0.54	20.95	3.19
LL1_1-2	Kober et al. (2009)	-18.330	-69.870	12.58	1.06	17.12	3.55
ADSO-6SD	Placzek et al. (2010)	-24.120	-68.593	153.80	5.40	0.98	0.16
ASOI-SD	Placzek et al. (2010)	-24.096	-70.281	64.70	2.60	0.78	0.14
ADSO-3SD	Placzek et al. (2010)	-24.089	-70.063	67.70	6.10	0.38	0.15
ADSA-1SD	Placzek et al. (2010)	-23.799	-68.116	80.40	5.80	1.78	0.38
ADBA-12SDsm	Placzek et al. (2010)	-23.403	-69.461	104.00	1.90	0.444	0.078
ADBA-5SD	Placzek et al. (2010)	-23.395	-69.474	69.20	2.10	0.82	0.14
25	Starke et al. (2017)	-22.644	-70.245	2.51	0.11	21.15	2.85

ID	Publication	Latitude	Longitude	^{10}Be-conc.	2σ ^{10}Be int. error.	Erosion rate	1σ uncertainty Erosion rate
		(°N)	*(°E)*	*(atoms g^{-1})*	*(atoms g^{-1})*	*(mm kyr^{-1})*	*(mm kyr^{-1})*
34	Starke et al. (2017)	-22.457	-68.731	44.19	1.35	4.23	0.54
24	Starke et al. (2017)	-21.714	-70.140	5.61	0.19	9.72	1.21
23	Starke et al. (2017)	-21.685	-69.528	18.24	0.57	6.74	0.84
14	Starke et al. (2017)	-21.427	-70.051	3.76	0.13	31.30	3.85
33	Starke et al. (2017)	-21.098	-69.290	5.03	0.18	39.27	4.94
13	Starke et al. (2017)	-20.988	-70.153	11.21	0.38	2.54	0.35
32	Starke et al. (2017)	-20.973	-69.197	1.970	0.090	102.14	14.21
31	Starke et al. (2017)	-20.928	-69.062	1.510	0.090	145.14	23.36
12	Starke et al. (2017)	-20.771	-70.133	11.68	0.37	2.33	0.32
30	Starke et al. (2017)	-20.690	-69.270	7.78	0.25	15.48	1.88
28	Starke et al. (2017)	-20.250	-69.439	6.17	0.23	20.08	2.58
27	Starke et al. (2017)	-20.242	-69.390	11.22	0.38	14.66	1.83
29	Starke et al. (2017)	-20.193	-69.315	11.04	0.35	10.90	1.34
26	Starke et al. (2017)	-20.119	-69.210	14.25	0.47	9.55	1.20
19	Starke et al. (2017)	-19.884	-69.464	10.37	0.34	18.22	2.24
20	Starke et al. (2017)	-19.874	-69.423	10.13	0.34	19.95	2.48
21	Starke et al. (2017)	-19.867	-69.173	15.92	0.52	13.96	1.73
2	Starke et al. (2017)	-19.603	-69.963	31.70	0.97	1.29	0.19
1	Starke et al. (2017)	-19.551	-70.194	6.40	0.22	13.11	1.63

ID	Publication	Latitude	Longitude	^{10}Be-conc.	2σ ^{10}Be int. error.	Erosion rate	1σ uncertainty Erosion rate
		(°N)	*(°E)*	*(atoms g^{-1})*	*(atoms g^{-1})*	*(mm kyr^{-1})*	*(mm kyr^{-1})*
3	Starke et al. (2017)	-19.348	-69.512	3.84	0.14	54.63	6.90
4	Starke et al. (2017)	-19.169	-70.200	0.810	0.050	144.07	23.37
5	Starke et al. (2017)	-19.165	-70.168	0.750	0.070	117.83	25.52
7	Starke et al. (2017)	-19.159	-70.190	1.620	0.080	89.35	12.85
6	Starke et al. (2017)	-19.155	-70.185	1.410	0.060	102.81	13.70
10	Starke et al. (2017)	-19.007	-69.821	0.730	0.040	244.88	37.30
11	Starke et al. (2017)	-18.996	-69.848	7.82	0.25	15.19	1.85
15	Starke et al. (2017)	-18.951	-69.491	2.55	0.10	83.57	10.86
16	Starke et al. (2017)	-18.878	-69.683	13.81	0.44	11.42	1.41
17	Starke et al. (2017)	-18.868	-69.678	24.36	0.75	6.56	0.82
18	Starke et al. (2017)	-18.867	-69.681	32.21	1.00	4.67	0.60
9	Starke et al. (2017)	-18.777	-70.268	6.54	0.22	16.27	2.01
8	Starke et al. (2017)	-18.519	-70.189	7.60	0.26	17.74	2.21
R1	Tolorza (2015)	-37.987	-72.822	2.528	0.082	12.28	1.47
H1	Tolorza (2015)	-37.711	-71.809	0.412	0.032	148.52	27.57
D1-1	Tolorza (2015)	-37.584	-72.149	0.86	0.14	64.07	22.63
VC1-2	Tolorza (2015)	-37.497	-72.665	0.96	0.11	41.30	10.28
Ca1	Tolorza (2015)	-37.493	-71.824	0.360	0.025	152.81	26.35
C1-1b	Tolorza (2015)	-37.465	-72.749	1.14	0.21	38.28	15.29

ID	Publication	Latitude	Longitude	^{10}Be-conc.	2σ ^{10}Be int. error.	Erosion rate	1σ uncertainty Erosion rate
		(°N)	*(°E)*	*(atoms g^{-1})*	*(atoms g^{-1})*	*(mm kyr^{-1})*	*(mm kyr^{-1})*
C3-2	Tolorza (2015)	-37.405	-72.798	0.979	0.083	35.97	7.24
LC1	Tolorza (2015)	-37.266	-72.720	0.90	0.25	71.24	43.55
Mi2	Tolorza (2015)	-37.049	-72.861	0.938	0.043	34.08	4.54
Bbd2-2	Tolorza (2015)	-36.816	-73.085	0.76	0.10	69.87	19.61

Table S 5.2: Calculated D_{50} and D_{84} values, based Wolman pebble count data at each sample location.

ID	D_{50} (cm)	D_{84} (cm)
SG10	5	21.5
SG35	1	9.5
SG39	3	18.69
SG71	2	18.5
SG74	4	25.28
SG79	0.2	26.78
SG91	7	20
SG95	1.75	11.97
SG102	2.5	19.5
LC4	9	26.7
LC21	11	44.62
LC25	0.1	23.46
LC33	11	29
LC34	2.5	40.5
LC35	5	20.5
LC37	0.1	0.1
LC37b	0.3	28.28
LC48	13	32
NB2	9	21.22
NB3	32	74.62
NB4	10	22
NB4c	24	50
NB5	24.5	67
NB10	0.2	5
NB14	28	80
NB18	4	18
NB23	7	19.8
NB100	9	20.5

5.10 Supplementary figures

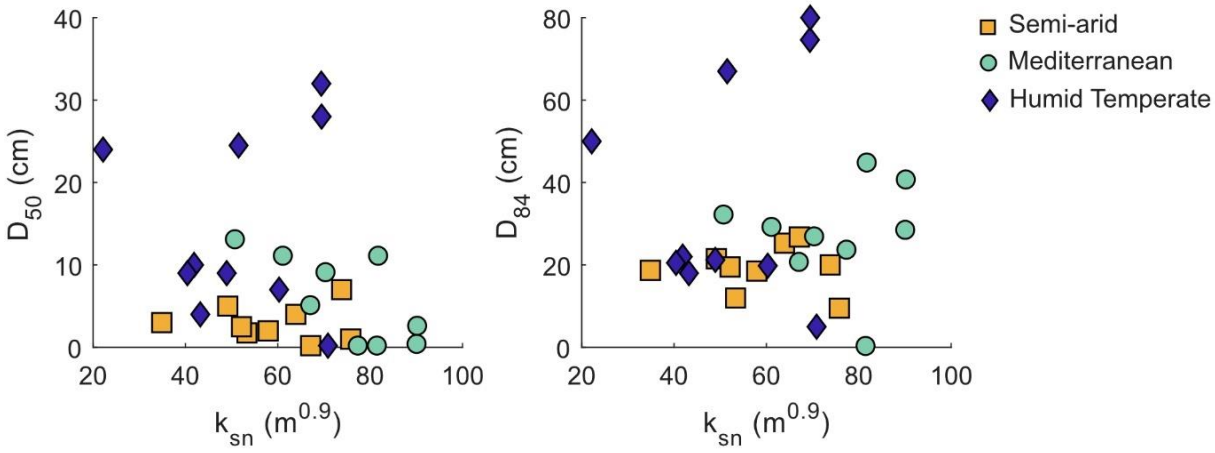

Figure S 5.1: Comparison of the median (D_{50}) and 84th-percentile (D_{84}) grain sizes of river sediment and the normalized channel steepness of the upstream basin.

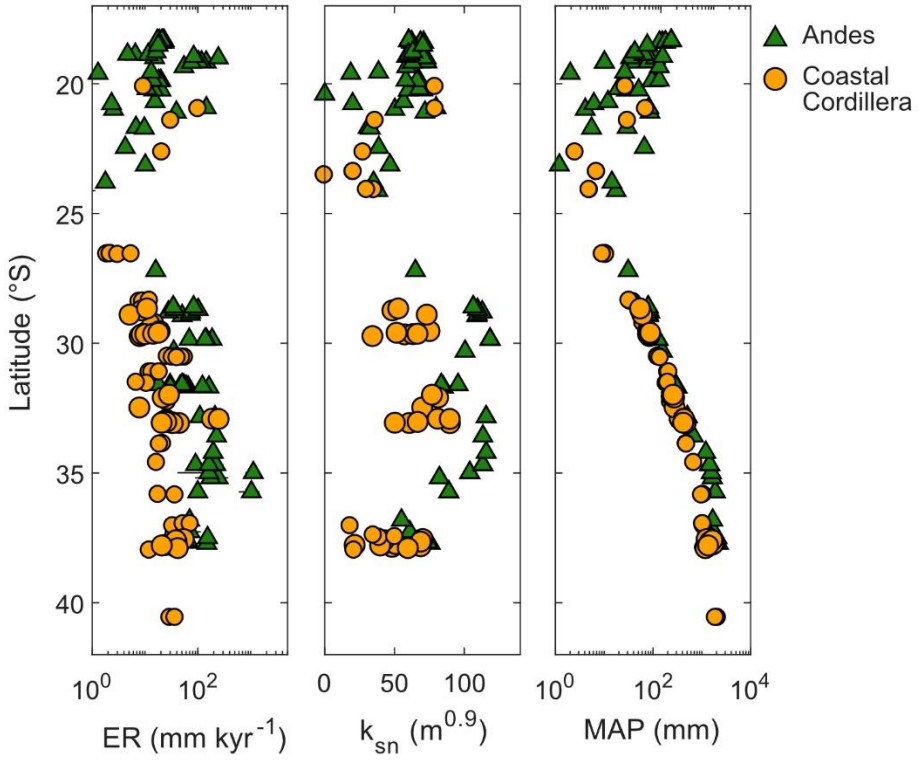

Figure S 5.2: Latitudinal variations in ^{10}Be-derived erosion rates (ER), normalized channel steepness (k_{sn}) and mean annual precipitation (MAP) in the Chilean Coastal Cordillera (orange circles) and Andes (green triangles). Data from this study and previous studies that are reported in Table S 5.1.

Chapter 6

Testing the role of erosion thresholds on river incision along a climate gradient in central Chile

Renee van Dongen[1,2], Dirk Scherler[1,3]

[1] GFZ German Research Centre for Geosciences, Earth Surface Geochemistry department, Telegrafenberg, 14473 Potsdam, Germany.
[2] International Centre for Water Resources and Global Change (UNESCO), German Federal Institute of Hydrology, Koblenz, Germany.
[3] Freie Universität Berlin, Institute for Geological Sciences, 12249 Berlin, Germany.

Abstract

River incision in bedrock is a crucial process in the context of landscape evolution. River incision is a stochastic process that occurs when river discharge exceeds an erosion threshold to mobilize bedload sediment and expose the riverbed to erosion. In this study we test the role of erosion thresholds in gently sloping catchments that are underlain by similar lithologies but feature large differences in climate (semi-arid, mediterranean, and humid-temperate). We used the stochastic-threshold stream power model, calibrated with field data, to model river incision rates, and compared the model performance to measured ^{10}Be-derived erosion rates. The results reveal that the stochastic-threshold stream power model with erosion thresholds performs better than the simple stream power model without thresholds. It was challenging to adequately combine all climate regions in one model with a constant substrate erodibility value, as the catchments are underlain by similar lithologies. We attribute this to the long ^{10}Be-integration times in the slowly eroding setting and the fact that climate was wetter during the Last Glacial Maximum. This poses a general challenge for studies that aim to investigate the role of climate on landscape evolution in slowly eroding settings. Nevertheless, we were able to test the sensitivity of modelled erosion rates to erosion thresholds for each climate region and found that in gently sloping basins the sensitivity of modelled erosion rates strongly depends on river discharge, because channel steepness is too low to additionally support the transport of river sediment. Generally, we found that erosion thresholds do play a role in the Coastal Cordillera of central Chile. River incision seems to occur frequently but with low magnitude in the humid-temperate region and infrequently but with large magnitude in the semi-arid region; however, this needs to be further tested. Hence, further investigation and testing of model input parameters is required, to better understand the role of erosion thresholds in the Coastal Cordillera of central Chile. The results of this study are relevant for the understanding of the link between climate and river incision rates in gently sloping landscapes, where erosion thresholds likely play a crucial role.

6.1 Introduction

The process of bedrock river incision is considered as an important driver of landscape evolution in mountainous landscapes. The river channel network defines the structure of mountain ranges, rivers form the base of hillslopes and define the rate and mode of hillslope transport, and finally, climatic and tectonic changes are propagated through the river network before the adjacent hillslopes respond (Whipple, 2004; Whipple and Tucker, 1999). River incision is induced by shear stresses exerted by flow at the riverbed. As precipitation is a major source for river discharge, the process of river incision is considered as an important link between climate and landscape evolution (Ferrier et al., 2013; Perron, 2017).

River incision rates depend on the erodibility of the riverbed, the slope of the channel, the variability of river discharge and an erosion threshold, which is defined by the grain size of channel sediment. When this erosion threshold is considerably high, river incision is non-linearly dependent on river discharge, because river discharge needs to exceed this erosion threshold to be able to transport the bedload sediment and expose the riverbed to erosion (Lague, 2013; Sklar and Dietrich, 2004; Turowski et al., 2007). The fluvial erosion efficiency of a river can, therefore, be strongly controlled by the variability of river discharge (i.e., how often and by how much discharge deviates from the mean) and the grain size of bedload sediment.

Even though the role of climate in long-term landscape evolution seems evident, it is difficult to quantify because other non-climatic factors can easily overprint the climatic signal (Ferrier et al., 2013; Perron, 2017). Ferrier et al. (2013) provided empirical evidence for a climatic control on river incision and erosion rates in a field setting with limited variations in non-climatic factors (e.g., lithology) but a strong orographic precipitation gradient the Hawai'ian Island of Kaua'i. They found that erosion thresholds did not play a significant role, as the river incision rates correlated linearly with stream power. However, a recent modelling study revealed that orographic precipitation gradients may obscure river channel profiles and thereby complicate the steady state relationship between climate and conventional topographic and erosional metrics (Leonard and Whipple, in review). Other studies have argued that erosion thresholds play an important role in other landscapes on earth (DiBiase and Whipple, 2011; Lague et al., 2005; Molnar, 2001; Snyder et al., 2003; Tucker, 2004; Tucker and Bras, 2000; Whipple and Tucker, 1999).

In an earlier study, in which we measured long-term erosion rates in catchments located in three different climate zones, we found that the fluvial erosion efficiency increases with increasing mean annual precipitation (Chapter 5). However, the way in which climate affects the fluvial erosion efficiency is manyfold and could not be disentangled based on the long-term erosion rates alone. The first and most straightforward control of climate on river incision is mean annual precipitation, as it is the direct source of the mean annual discharge of a river, and feeds into the erosional

efficiency parameter (Ferrier et al., 2013; Perron, 2017). Secondly, the discharge variability of a river varies considerably in different climate regimes (Lague, 2013; Molnar et al., 2006; Rossi et al., 2016). Finally, although weathering processes, that transfer rock into sediment, are primarily set by bedrock properties such as the lithology and fracture density (Lebedeva and Brantley, 2017; Sklar et al., 2017), mineral dissolution rates also depend on climate, which may lead to an additional effect of climate on the bedrock erodibility and the grain size of river sediment that sets the erosion threshold (Dixon et al., 2016; Riebe et al., 2004).

To disentangle these various climatic controls on river incision and to test whether erosion thresholds and discharge variability indeed play a role in the catchments located in the Chilean Costal Cordillera, a modelling study is required. DiBiase and Whipple (2011) and Scherler et al. (2017) calibrated the stochastic-threshold stream power model (stochastic-threshold SPM) to catchments in the San Gabriel Mountains, the Himalaya, and Eastern Tibet, to test the role of discharge variability and erosion thresholds. Both studies found that channel steepness induced an important control on the initial motion of channel sediment and that erosion thresholds mainly played a role in gently sloping catchments. Such modelling approaches provide a useful framework to study the effect of climate on the threshold-behaviour of river incision. However, the studies by DiBiase and Whipple (2011) and Scherler et al. (2017) only cover a small fraction of the various climatic zones on Earth (Köppen, 1900; Kottek et al., 2006). Moreover, these studies were performed in relatively steep and fast eroding landscapes, whereas erosion thresholds may play a significant role in gently sloping catchments. To date, the river incision dynamics, and the importance of erosion thresholds in gently sloping and slowly eroding landscapes, have not yet received much attention.

Hence, in this study, we investigate the river incision dynamics for gently sloping basins with contrasting climate in the Coastal Cordillera of central Chile. In particular, we test the threshold-behaviour of river incision processes and how this differs in the different climate regions.

6.2 Background

6.2.1 Theoretical framework

In this study we use the stochastic-threshold stream power model (stochastic-threshold SPM) calibrated with field and river discharge data to investigate the process of river incision in the Coastal Cordillera of central Chile (DiBiase and Whipple., 2011; Scherler et al., 2017).

The stochastic-threshold SPM calculates the river incision rate (I) as:

$$I = KQ^{*\gamma}k_s^n - \psi \quad (1)$$

The river incision rate, I, is a function of the erosional efficiency factor (K, Equation 2), normalized river discharge (Q*=Q/Qmean) raised to an exponent that determines the importance of discharge variability (γ), the channel steepness index of the river (k_s, Equation 3) and the erosion threshold of the river (ψ, Equation 4), which is set by the grain size of river sediment.

The erosional efficiency factor (K) is a lumped factor that includes many parameters and is calculated as:

$$K = k_e k_t^a k_w^{-\alpha a} \bar{R}^m \quad (2)$$

The erosional efficiency factor (K) is determined by a lithology-dependent erodibility constant (k_e), a constant which depends on the flow resistance (k_t), an empirical channel width index (k_w), the mean annual catchment-integrated runoff ($\bar{R}$) and a few exponents, including a function of the incision process (a), the flow resistance relationship (α) and the channel geometry (m), where m=aα(1-ω_b) (Whipple, 2004). Here, ω_b is an empirical channel-width scaling parameter.

The channel steepness index (k_s) represents the steepness of the river channel for a given upstream area and concavity (Hack 1957, Flint 1974). The channel steepness of a steady state landscape typically scales with tectonic uplift rates (Wobus et al., 2006). To be able to compare catchments with different concavities, the normalized channel steepness index (k_{sn}) based on a reference concavity is suggested, for which often a reference concavity of m/n=0.45 is used (DiBiase and Whipple, 2011; Wobus et al., 2006).

The normalized channel steepness index can be calculated as following:

$$k_{sn} = SA^{\theta ref} \quad (3)$$

In this equation, *S* is the channel slope, *A* is the upstream area and θ_{ref} is a reference concavity (Wobus et al., 2006).

Finally, the erosion threshold (ψ) can be calculated by:

$$\Psi = k_e \tau_c^a \quad (4)$$

The erosion threshold (ψ) depends on the critical shear stress (τ_c), the bedrock-dependent erodibility constant (k_e), and a constant (a) which can be related to the incision process. Under the assumption that flow occurs as a steady, uniform flow in wide and open channels, the bed shear stress can be derived by:

$$\tau_b = k_t \left(\frac{Q}{W}\right)^a S^\beta \tag{5}$$

Equation 5 shows that the bed shear stress is a function of a constant that depends on the flow resistance (k_t), water discharge (Q), channel width (W), gradient of the water surface, which is assumed to be equal to the channel bed slope (S), and two exponents (α and β) that depend on the flow resistance relationship (α=3/5, β=7/10 in the Gauckler-Mannin-Strickler relationship, and α=β=2/3 in the Darcy-Weissbach relationship) (Howard, 1994).

In the stochastic-threshold SPM, the erosion threshold determines what magnitude of river discharge events are erosive. When the erosion threshold is negligible (ψ=0), all river discharge events have erosive power, and the river incision equation can be simplified to: $I = K * k_{sn}$. When bedload sediment of a river sets a considerable erosion threshold (ψ>0), a non-linear relationship emerges between I and k_{sn} that depends on the erosion threshold and the exceedance frequency of daily discharge (DiBiase and Whipple, 2011; Forte et al., in review; Lague et al., 2005; Snyder et al., 2003; Tucker, 2004). In such cases, discharge events that do not exceed the erosion threshold are non-erosive, whereas the extreme discharge events that exceed the erosion threshold do the erosive work.

In topographic steady state, the long-term river incision rate ($\bar{I}$) can be estimated based on the frequency-magnitude distribution of daily river discharge, which describes how often and by how much river discharge exceeds the erosion threshold. Previous studies have parameterized the probability density function (pdf) of daily discharge with various methods and combined it with the stochastic-threshold SPM of Equation 1 (Lague et al., 2005; Tucker, 2004; Tucker and Bras, 2000):

$$\bar{I} = \int_{Q_c^*}^{Q_m^*} I(Q^*, k_s) pdf(Q^*) dQ^* \tag{6}$$

In this equation, Q_m^* is the normalized maximum discharge and Q_c^* is the normalized critical discharge that is required to exceed the erosion threshold. The critical discharge can be estimated by assuming I=0, which forms:

$$Q_c^* = \left(\frac{\Psi}{K k_s^n}\right)^{\frac{1}{\gamma}} = \left(\frac{\tau_c k_w^a}{k_t \bar{R}^{\alpha(1-\omega_b)} k_s^\beta}\right)^{\frac{a}{\gamma}} \quad (7)$$

This equation shows that the critical discharge that is required to exceed the erosion threshold depends on the threshold shear stress (τ_c), the river's channel steepness (k_s), the channel width index (k_w) that represents the river width for a given river discharge, and the mean annual runoff ($\bar{R}$). These are all parameters that describe the fluvial erosion efficiency of a river.

6.2.2 Study design

As described in the introduction, this study builds on a previous study in which we measured ^{10}Be-derived erosion rates for gently sloping catchments in the Coastal Cordillera of central Chile (Chapter 5). That study specifically targeted catchments with various channel steepness indices that were located in three different climate regions (semi-arid, mediterranean, humid-temperate) (Figure 6.1).

In the previous section (Section 6.2.1) we described that the river incision rate can be modelled based on the following model inputs: the erosional efficiency factor (K), the daily discharge distribution (pdf(Q*)), the normalized channel steepness index (k_{sn}) and the erosion threshold (ψ) of a river. In this study, we calibrate the stochastic-threshold SPM with field and river discharge data that we obtained for the different climate regions and run the model to obtain the best fit compared to the measured ^{10}Be-derived catchment average erosion rates, which in topographic steady state are equal to the river incision rate (e.g., Whipple, 2004).

In the following sections, we focus on each input parameter of the stochastic-threshold SPM. In each section, we first provide the theory and methodology to constrain the data for each model input component, then we provide the results and conclude with the input values that are used in the modelling approach. In the chapter thereafter, we perform model runs with different model configurations and discuss the results in the discussion and implication chapters.

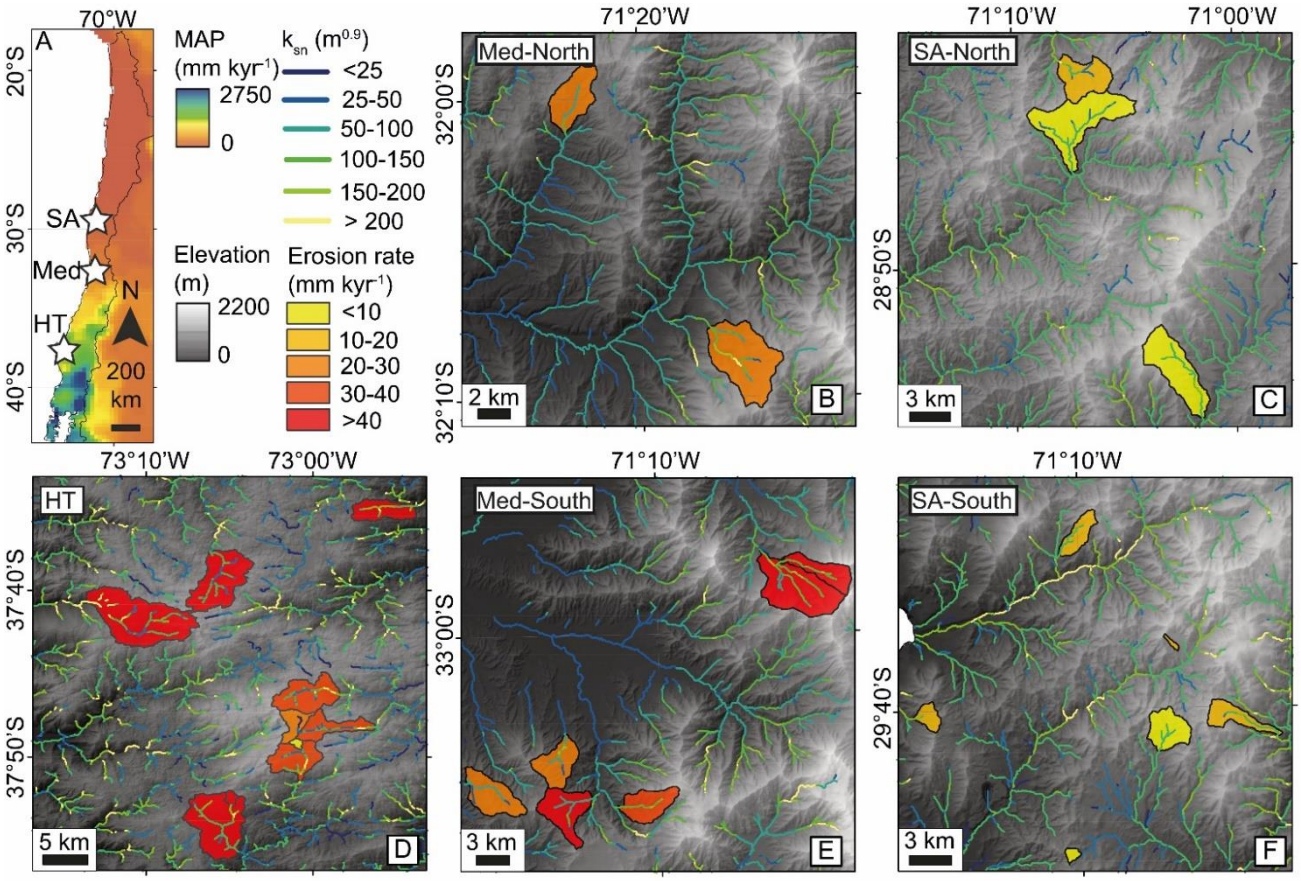

Figure 6.1: The study areas in central Chile.Mean annual precipitation (MAP) with the locations (stars) of the three climatic focus areas in this study: semi-arid (SA), mediterranean (Med) and humid-temperate (HT). B-F): 30m resolution Digital Elevation Models (DEM), provided by the Shuttle Radar Topography Mission (SRTM) (Jarvis et al., 2008), with channel network color-coded by normalized channel steepness indices (k_{sn}) and the catchment outlines color-coded with ^{10}Be-derived catchment average erosion rates (yellow-to-red scale).

6.3 Model input parameters

6.3.1 Channel steepness index

In Chapter 5, we used Equation 3 to calculate the normalized channel steepness indices for a range of catchments in each climate region and selected 9 or 10 catchments with contrasting channel steepness indices to constrain ^{10}Be-derived erosion rates (Table S 6.1). This allowed us to demonstrate a normalized channel steepness versus erosion rate relationship for each climate region.

The results revealed a positive linear relationship between k_{sn} and erosion rates (Figure 6.2, Table 6.1). The goodness of fit is the highest for the humid-temperate region (R^2=0.26) and lowest for the semi-arid region (R^2=-0.02). The relationship of the mediterranean region has a R^2 of 0.13; however, this relationship is strongly controlled by two catchments that have factor 10 higher erosion rates (Figure 6.2a). After excluding the two anomalously high erosion rates, the relationship fits the remaining catchments better (R^2=0.41) (Figure 6.2b).

As already concluded in Chapter 5, the k_{sn}-erosion rate relationships reveal that the fluvial erosion efficiency is the highest for the humid-temperate region and the lowest for the semi-arid region. The channel steepness indices that were calculated for each basin will be used as an input parameter for each catchment in the stochastic-threshold SPM.

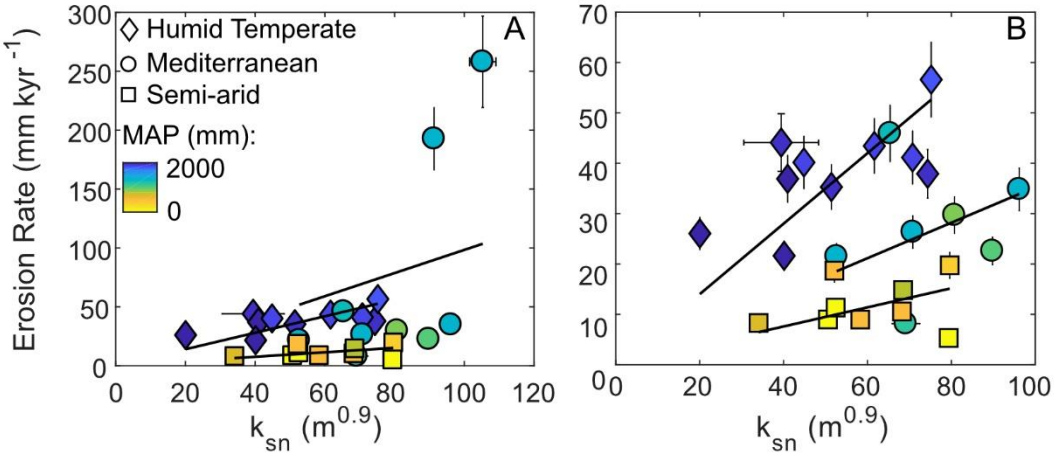

Figure 6.2: Relationship between the normalized channel steepness index (k_{sn}) and catchment average erosion rates for catchments which are located in three different climatic regions: Humid-temperate (diamonds), mediterranean (circles) and semi-arid (squares). A) The normalized channel steepness – erosion rate relationship for all data points, B) the normalized channel steepness – erosion rate relationship excluding the two extreme erosion rates for the mediterranean region. Scatter is color-coded by Mean Annual Precipitation (MAP) values, with a logarithmic colour-scale. The data is fitted with a linear regression model ($E=I=K*k_{sn}$); the linear fit results are listed in Table 6.1.

Table 6.1: Linear fit results for k_{sn}-erosion rate relationship ($E=I= K*k_{sn}$). The table includes the linear fit results for all data points (Figure 6.2a) and the results excluding the two extreme data points erosion rate for the mediterranean region (Figure 6.2b). The table includes the goodness of fit (R^2) and amount of fitted data points (n) for each linear fit.

Climate zone	K	R^2	n	K	R^2	n
Semi-arid	0.20	-0.02	10	0.20	-0.02	10
Mediterranean	1.02	0.13	9	0.36	0.41	7
Humid-temperate	0.72	0.26	9	0.72	0.26	9

6.3.2 Erosional efficiency factor

In Equation 2, we described that the erosional efficiency factor (K) is a lumped factor that includes various parameters (Whipple, 2004). Several of these parameters (k_t, a, α, m) are constants that are fixed (Table 6.2). The lithology-dependent erodibility constant (k_e), mean annual runoff ($\bar{R}$) and the empirical channel with index (k_w) need to be constrained for each study region. As the latter two parameters are climate-dependent, we constrain k_w and ($\bar{R}$) for each climate region individually.

The lithology-dependent erodibility constant (k_e) is the least-constrained parameter, for which the value is typically unknown. In this study, we use k_e as a free parameter, which will be obtained by the best-fit model result compared to ^{10}Be-derived catchment average erosion rates in a Monte Carlo simulation (Table 6.2). This approach is similar as the study of Scherler et al. (2017).

Due to the lack of river gauging stations in the sampled catchments, mean annual runoff (MAR) data was not available for the catchments in this study. Instead, we established an empirical MAP-MAR relationship for other river catchments in Chile, for which river gauging data was available and precipitation data that was derived from a gridded precipitation dataset. Next, we estimated MAR values for the catchments in this study by calculating MAP values derived from the same gridded precipitation product and transferring this into MAR estimations using the empirical MAP-MAR relationship.

River discharge data was obtained from the Catchment Attributes and Meteorology for Large Sample studies – Chile dataset (CAMELS-CL), which is a large, quality-checked hydrological-meteorological dataset that includes 516 river basins from Chile (Alvarez-Garreton et al., 2018). Besides river discharge and meteorological parameters, the CAMELS-CL dataset provides catchment metrics such as human intervention degree and the presence of big dams in a river catchment. The human intervention degree represents the percent volume of mean annual river discharge that is granted to be extracted (Alvarez-Garreton et al., 2018). To establish a reliable MAP-MAR relationship,

we excluded all river basins with a human intervention degree of >10% and river basins that have dams located in their upstream catchment, which resulted in 336 remaining river basins (Table S 6.2).

We recalculated river discharge data to runoff per unit area and calculated MAR for each station as the arithmetic mean of all years with <5% missing data. To calculate MAP, we used the 0.05° gridded precipitation dataset CR2MET, which is provided by the Center for Climate and Resilience Research (CR^2) (Boisier et al., 2018a). This dataset is developed specifically for Chile and was found to be perform better than globally gridded precipitation datasets (Alvarez-Garreton et al., 2018; Chapter 4), which perform especially poorly in Andean catchments with steep topography (Hobouchian et al., 2017). The CR2MET dataset provides monthly and daily precipitation data for the time period 1979-2016. We calculated MAP for the 336 selected river basins from the CAMELS-CL dataset by interpolating precipitation values to each grid cell of the catchments' DEM, using a nearest-neighbour linear interpolation method, and then calculated the arithmetic mean MAP for each basin.

Next, we fitted the MAP-MAR relationship with a second order polynomial model (Figure 6.3). We established the MAP-MAR relationship for all of the 336 river basis (Figure 6.3a), as well as for basins that solely drain the low elevation Coastal region (Figure 6.3b). The empirical MAP-MAR relationship follows the expected pattern, with lower MAR than MAP at the low- and intermediate precipitation range, due to water losses by evapotranspiration. Since the sampled catchments of this study are located in the Coastal region only, we used the empirical MAP-MAR relationship that was derived for the Coastal region, to estimate MAR values based on gridded CR2MET MAP-data for each catchment.

The last parameter that needs to be constrained for the erosional efficiency factor is the empirical channel with index (k_w). In a steady scale landscape, channel width scales with mean annual river discharge following a simple power law relationship (Leopold and Maddock, 1953; Montgomery and Gran, 2001; Wohl and David, 2008).

$$W_b = k_w * \bar{Q}^{\omega_b} \quad (6)$$

In this equation, k_w is a constant that represents the hydrometeorological conditions of a certain region, ω_b is an empirical scaling parameter and $\bar{Q}$ is the mean annual discharge. In bedrock rivers, ω_b is found to range between ~0.3-0.6 (Craddock et al., 2007; Godard et al., 2010; Kirby and Ouimet, 2011; Scherler et al., 2017; Whipple, 2004; Wohl and David, 2008; Yanites and Tucker, 2010). We constrained k_w and ωb by conducting ~150-200 river width measurements within each climate region using Google Earth. We solely focussed on rivers that drain the Coastal Cordillera and were unaffected by anthropogenic water extractions for e.g., agriculture. The upstream area of each river width measurement location was calculated using a 30 m STRM DEM. We interpolated MAP values from the CR2MET dataset to each grid cell of the DEM,

following the above-described method, to estimate upstream averaged mean annual precipitation. Next, the MAP values were transferred into mean annual runoff using the empirical MAP-MAR relationship (Figure 6.3) and, finally, Q was calculated by assuming $MAQ=MAR*A^c$, with c=1. We plotted the resulting MAQ and width measurements and fitted the data with a power law function (Figure 6.4a).

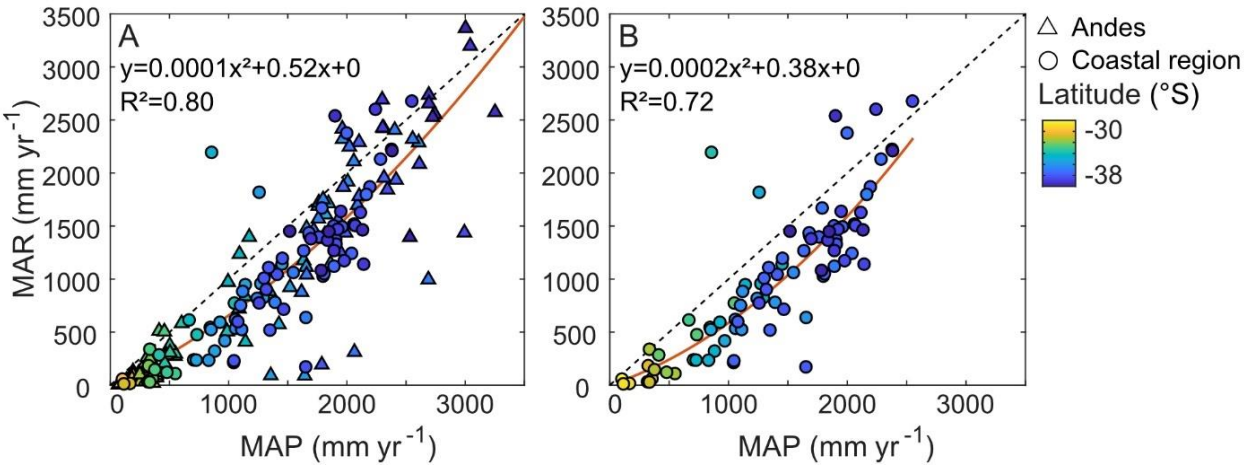

Figure 6.3: Mean annual precipitaion (MAP) - mean annual runoff (MAR) relationship based on river discharge data from the CAMELS-CL dataset (Alvarez-Garreton et al., 2018) and precipitation data obtained from the gridded CR2MET montly precipitation dataset (Boisier et al., 2018b). A) Relationship for all reamaining catchments in the CAMELS-CL dataset (n=336), B) Relationship for catchments that are solely located in the Coastal region (n=106). The relationships are parameterized with a second order polynomial model (red curve).

The fits resulted in reasonably good R^2-values of 0.71, 0.54 and 0.74 for the semi-arid, mediterranean and humid-temperate regions, respectively. The ω_b values of the three climatic zones range between 0.30-0.51 and fall within the range of previously reported values (Craddock et al., 2007; Godard et al., 2010; Kirby and Ouimet, 2011; Scherler et al., 2017; Whipple, 2004; Wohl and David, 2008; Yanites and Tucker, 2010). However, for the SPM model to be dimensionally correct with the resistance relation and the θ_{ref} value, we fixed ω_b to 0.55 (Figure 6.4b). The power law fit with a fixed exponent resulted in lower R^2-values of 0.56, 0.33, 0.74 for the semi-arid, mediterranean, and humid-temperate regions, respectively. The resulting k_w value is the highest for the semi-arid region (~ 53 $m^{-0.65}$ $s^{0.55}$), followed by the mediterranean region (~ 14 $m^{-0.65}$ $s^{0.55}$) and the humid-temperate region (~ 4 $m^{-0.65}$ $s^{0.55}$). This reveals that, for a given erosion threshold, the erosion efficiency is the highest in the humid-temperate, followed by the mediterranean region and the semi-arid region.

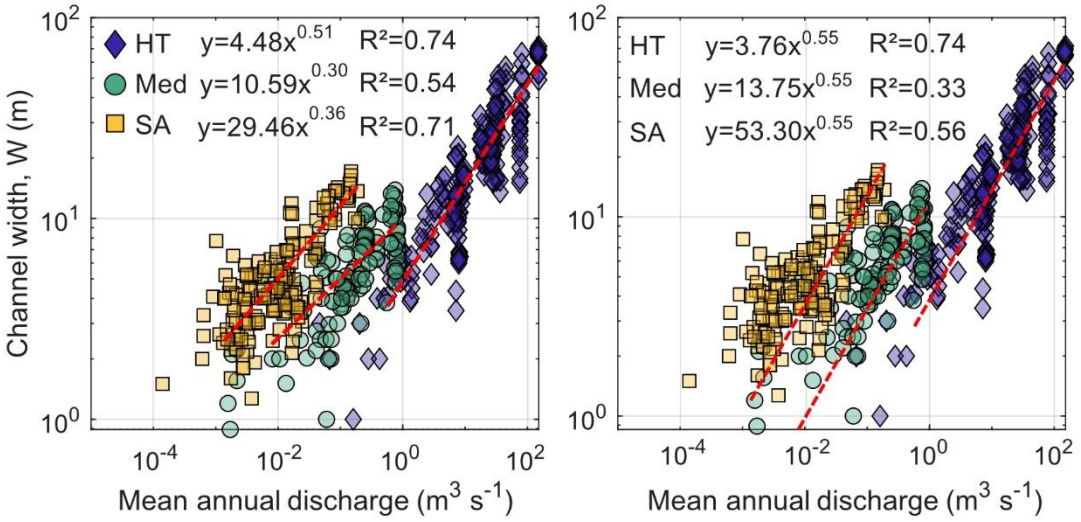

Figure 6.4: Mean annual discharge – channel with regationship for the three climatic zones: humid-temperate (HT; blue diamonds), Mediterranean (Med; tuqiose circles), semi-arid (SA; yellow squares). A) Power law fits to the data, with free exponent. B) Power law fits to the data with a forced exponent of 0.55.

6.3.3 Discharge variability

When erosion thresholds are considerably high, discharge variability is an important input parameter because it constrains how often, and by how much, river discharge exceeds the erosion threshold. A probability density function (PDF) of a river with low mean discharge and infrequent large magnitude events has high discharge variability and is characterized by a heavy right tail (Crave and Davy, 2001; Malamud and Turcotte, 2006; Molnar et al., 2006). The PDF of daily discharge can be parameterized with various methods (Lague et al., 2005; Tucker, 2004; Tucker and Bras, 2000) and included in the stochastic-threshold SPM (DiBiase and Whipple, 2011; Scherler et al., 2017).

One of the applied parameterization methods is the Pareto fit which performs especially well for heavy-tailed distributions (Malamud and Turcotte, 2006; Molnar et al., 2006; Turcotte and Greene, 1993). However, this approach insufficiently describes the rollover towards infrequent low magnitude events (Lague et al., 2005). More recent studies have, therefore, used the inverse gamma distribution, which combines an exponential fit for the low flow regime and a Pareto fit for the high flow regime (Crave and Davy, 2001; DiBiase and Whipple, 2011; Lague, 2013; Lague et al., 2005). Scherler et al. (2017) applied the weighted sum of two inverse gamma fits to properly describe daily discharge distributions with distinct low and high flow regimes. The inverse gamma distribution provides the parameter 'k' which is inversely proportional to the discharge variability, which means that 'k' is high for catchments with low discharge variability and vice versa.

We tested whether a single or the weighted sum of two inverse gamma distributions performs best for daily river discharge distributions from central Chile (Figure S 6.1). As revealed by the R^2-value, the weighted sum of two inverse gamma fits performs slightly better for almost all stations (98.8 %) in central Chile. However, it is also important to evaluate whether the second inverse gamma fit is useful in terms of the fraction of the discharge distribution that it describes; otherwise the high flow fit might be dominated by anomalously high outliers only (e.g., Scherler et al., 2017). Hence, we used a second criteria, which prescribes that the represented fraction of the high flow fit should be larger than 0.07 (i.e., more than 7% of the daily discharge data should be fitted by the high flow fit), which is the same threshold as used by Scherler et al. (2017). We found that the second inverse gamma fit describes more than 7% of the data for about half of the stations (52.3%) in central Chile, which are mostly located in the Andes (Figure S 6.1). In the Coastal region there is no clear spatial pattern for which regions two inverse gamma fits perform better than a single fit. As the increase in R^2 for the weighted sum of two inverse gamma fits relative to a single inverse gamma fit is for most stations only minor (up to 0.025) and we aim for the same method for all climatic regions, we decided to use a single inverse gamma fit to determine the discharge variability for all discharge stations in central Chile.

To constrain the discharge variability as an input component for the stochastic-threshold SPM, we had to again overcome the issue of non-existent river discharge data for the sampled catchments. Hence, for this input component we also established an empirical relationship between the k-parameter and MAR, which is used to estimate an k-value for the catchments in this study. To establish this relationship, we plotted MAR and k for stations with >5 years of data and an inverse gamma fit R^2 of >0.90, and fitted the data with a power law fit (Figure 6.5).

Overall, the obtained MAR-k relationships fall within the range and follow a similar pattern compared to previously published data from studies in the western Andes, the U.S., Taiwan, the Himalaya, and Eastern Tibet (Carretier et al., 2013; Lague et al., 2005; Molnar et al., 2006; Scherler et al., 2017) (Figure S 6.2). The obtained MAR-k relationship resulted in a R^2-value of 0.18 for all stations in the Andes and Coastal region and 0.17 for catchments that solely drain the Coastal region. We have tested whether a relationship between the k-parameter and other catchment indices (MAP, Aridity Index, latitude, catchment steepness and catchment area) would obtain a better relationship, however, this was not the case.

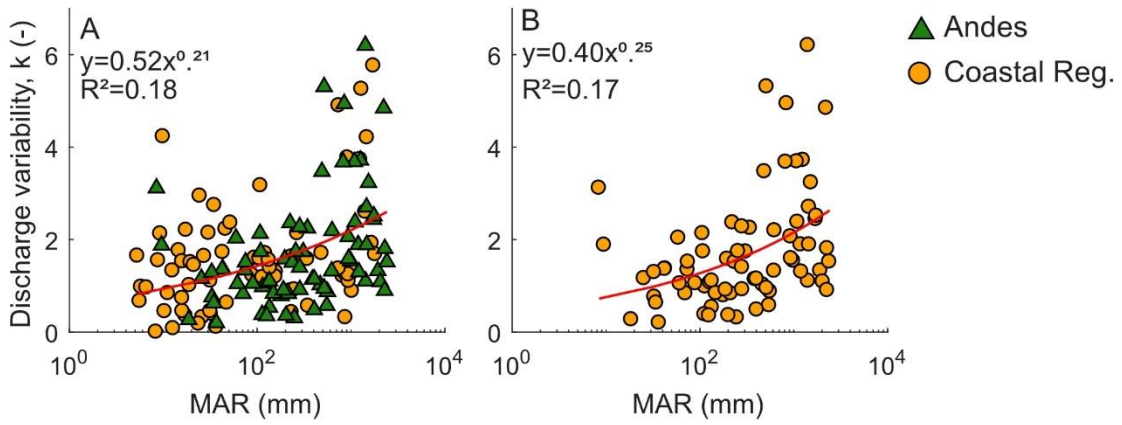

Figure 6.5: Relationship between mean annual discharge and the k-parameter for a single inverse gamma fit. A) All discharge stations located in both the Andes and Coastal region (n=169), B) Discharge stations that solely drain the Coastal region (n=86). Only stations with >5 years of data and inverse gamma fits with an R^2-value of >0.90 are used.

We decided to use the MAP-k relationship for catchments in the Coastal region to estimate a k-value for each climatic region. First, we estimated the k-parameter for each sampled catchment, based on the estimated MAR value. Then, we calculated a mean k-value for each climatic zone, based on the arithmetic mean of all catchments per climate zone (Table S 6.3). This resulted in the lowest k-value for the semi-arid region (k= 0.94), followed by the mediterranean region (k= 1.46) and the humid-temperate region (k= 2.25). As discharge variability is inversely proportional to the k-parameter, this reveals that discharge variability is the highest in the semi-arid region and lowest in the humid-temperate region, which follows the expected pattern (e.g., Lague, 2013).

6.3.4 Erosion threshold

The erosion threshold (ψ) depends on the critical shear stress (τ_c) and the substrate-dependent erodibility constant (k_e). The critical shear stress (τ_c^*) can be estimated using the Shields criterion for initial motion of sediment:

$$\tau_c^* = \frac{\tau_c}{D_{50} g (\rho_s - \rho_w)} \quad (8)$$

Here τ_c^* is the Shields number, D_{50} is the median grain size diameter, g is the gravitational acceleration constant and ρ_s and ρ_w are the densities of sediment and water, respectively (Table 6.2).

As written in Chapter 5, we conducted a Wolman pebble count at the sample location of each catchment to constrain the grain size distribution of channel sediment

(Wolman, 1954). For each pebble count, we counted 100 individual clasts with a distance of 1 m between the measurements, and calculated the median grain size (D_{50}) and 84th-percentile grain size (D_{84}) using a bootstrapping method.

The results revealed relatively coarse channel grain sizes that lacked any functional relationship to erosion rates or normalized channel steepness index (Chapter 5). Therefore, we decided to conduct various model runs with different D_{50} settings, to test the control of channel grain sizes on river incision rates in the Chilean Coastal Cordillera. Later, we discuss the feasibility of the D_{50} settings and compare them to the measured field data.

The first model run uses the simple stream power model, without erosion thresholds. The second model configuration obtains a single best fit D_{50} value for all catchments based on a Monte Carlo simulation. For this approach we predefined a parameter space of D_{50}=0 cm to D_{50}=40 cm, which equals the range of grain sizes that have been measured in the field. For the third model configuration we followed the approach of Scherler et al. (2017), who tested the use of k_{sn}-dependent D_{50} values, under the assumption that steeper catchments transport coarser material to the river channels (e.g., Attal et al., 2015; Attal and Lavé, 2006; Riebe et al., 2015; Roda-Boluda et al., 2018; Terweh et al., 2021). The k_{sn}-dependent D_{50} values were calculated following a power law relationship ($D_{50=}$ factor $*$ $k_{sn}^{0.4}$) that was found for the Feather river basin (Attal et al., 2015). The best fit grain size factors (F) were calculated for each climatic region individually. We tested grain size factors that ranged from 0 to $7*10^{-3}$, which provided a grain size range of 0 to ~40 cm.

6.4 Modelling approach

After constraining all required model parameters for each climate region (Table 6.2), we conducted three different model runs with various D_{50} settings (described in Section 6.3.4). As the erodibility constant (k_e) is the least constrained parameter, we ran Monte Carlo simulations to obtain the best fit k_e that provided the lowest misfit between the modelled and ^{10}Be-derived erosion rates. We allowed a large k_e parameter space for the Monte Carlo simulation, which ranged from $1*10^{-11}$ to $1*10^{-17}$.

We report the best fit results of each model configuration and discuss the plausibility of the obtained k_e and D_{50} values. We conducted the above-described model configurations for each individual climatic region (Section 6.4.1), but also with all climatic regions in one model (Section 6.4.2). For the latter approach, we assumed that the k_e parameter is constant for all climatic regions, as we specifically selected catchments based on granodioritic lithology.

6.4.1 Individual climate regions

For all of the three model configurations (simple SPM, single D_{50}, k_{sn}-dependent D_{50}), the individual climatic regions require a different order of magnitude substrate erodibility parameter (k_e), to obtain the best fit of modelled erosion rates compared to ^{10}Be-derived erosion rates (Table 6.3 and Figure 6.6). The magnitude of k_e is the highest for the semi-arid region (10^{-12} to 10^{-13}), followed by the mediterranean region (10^{-14}) and humid-temperate region (10^{-15}).

The simple stream power model performed reasonably well for all climate regions (Table 6.3 and Figure 6.6a-c). The second model configuration that used a single D_{50}, obtained from a Monte Carlo simulation using the best fit between measured and modelled erosion rates, showed a larger misfit than the simple SPM for the semi-arid and mediterranean regions, but a smaller misfit for the humid-temperate region (Table 6.3 and Figure 6.6d-f). The D_{50} value for each climatic region that were found as best fit by the Monte Carlo simulation were relatively fine, >1 cm. The third model configuration, which used k_{sn}-dependent D_{50} values, revealed the lowest misfit for all climate regions (Table 6.3 and Figure 6.6g-i). The D_{50} grain sizes that result from the best fit grain size factor (D_{50}= factor * $k_{sn}^{0.4}$) range from 3.3-4.6 cm for the semi-arid region, 3.2-4.2 cm for the mediterranean region, and 2.3-3.9 cm for the humid-temperate region.

Table 6.2: Stochastic-threshold SPM model input parameters that are constrained for this study.

Parameter	Type of parameter	Value	Unit	Description
a	Fixed	3/2	-	Stream power law exponent
α	Fixed	2/3	-	Exponent in flow resistance equation
β	Fixed	2/3	-	Exponent in flow resistance equation
m	Fixed	m=aα(1-ωb)	-	Channel geometry constant
k_{sn}	Catchment dependent	See Table S 6.1	$m^{0.9}$	Normalized channel steepness index
k_t	Fixed	1000	kg $m^{-7/3}$ $s^{-4/3}$	Flow resistance factor
k_e	Free parameter	Obtained by Monte Carlo simulation	-	Substrate erodibility
k_w	Region dependent	Semi-arid: 4 Mediterranean: 13 Humid-temperate: 51	$m^{-0.65}$ $s^{0.55}$	Normalized channel width index
$\bar{R}$	Region dependent	Semi-arid: ~30 Mediterranean: ~180 Humid-temperate: ~1000	mm	Mean annual runoff, calculated for each individual catchment using MAP data and the empirical MAP-MAR relationship (Figure 6.3)
ω_b	Fixed	0.55	-	Downstream mean annual discharge-channel width scaling exponent
τ_c*	Fixed	0.045	-	Shield's number
D_{50}	Catchment dependent	Different scenarios	mm	Median bedload grain size
g	Fixed	9.81	m s^{-2}	Gravitational acceleration constant
ρ_w	Fixed	1	g cm^{-3}	Density of water
ρ_s	Fixed	2.7	g cm^{-3}	Density of granitic bedload sediment

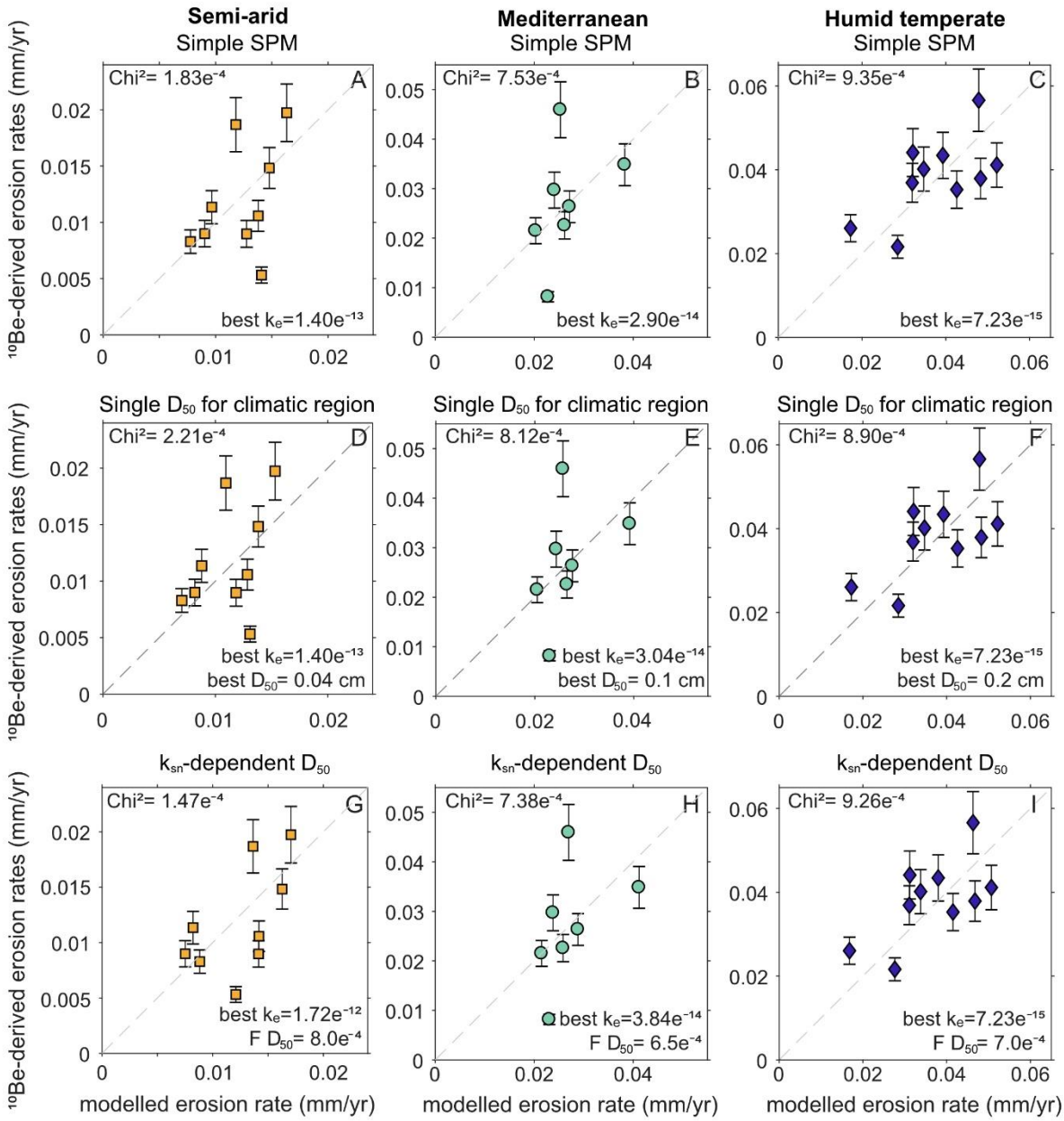

Figure 6.6: Best fit model results for each climatic region, based on the three different model configurations. A-C: Simple stream power model (simple SPM). D-F: Single D_{50} for each climatic region, obtained from best fit Monte Carlo simulation. G-I: k_{sn}-dependent D_{50} values (D_{50}= factor * $k_{sn}^{0.4}$) based on the best fit grain size factor (F D_{50}). The misfit (Chi^2), the best fit erodibility parameter (best k_e), best fit D_{50} (best D_{50}) and best fit grain size factor (F D_{50}) parameters are reported in the corner of each figure.

6.4.2 All climate regions

Under the assumption that all catchments have the same substrate erodibility (k_e) value, as they are all based on similar granodioritic lithology, we further conducted model runs with all climate regions in one model. The first (simple SPM) and second (single D_{50}) show identical results, because the second model that uses a single D_{50} for all catchments in the model returned a D_{50} of 0 cm (i.e., no erosion threshold). The best fit of modelled versus ^{10}Be-derived erosion rates is, for both approached, obtained with a k_e of $7.93 \cdot 10^{-15}$ (Table 6.3 and Figure 6.7a-b). However, for these model configurations only the erosion rates of the humid-temperate region are properly estimated, whereas the erosion rates for the mediterranean and semi-arid regions are strongly underestimated.

The model performance is better for the third modelling approach that uses k_{sn}-dependent D_{50} values, with a different multiplication factor for each climate region (Table 6.3 and Figure 6.7c). This model found a best fit k_e value of $2.90 \cdot 10^{-14}$. The erosion rates of the humid-temperate and mediterranean regions are relatively well estimated, but the erosion rates of the semi-arid region are underestimated. The grain size multiplication factors for the k_{sn}-dependent D_{50} values result in grain sizes of 0 cm for the semi-arid region, 2.4-3.2 cm for the mediterranean region and 23.2-39.4 cm for the humid-temperate region.

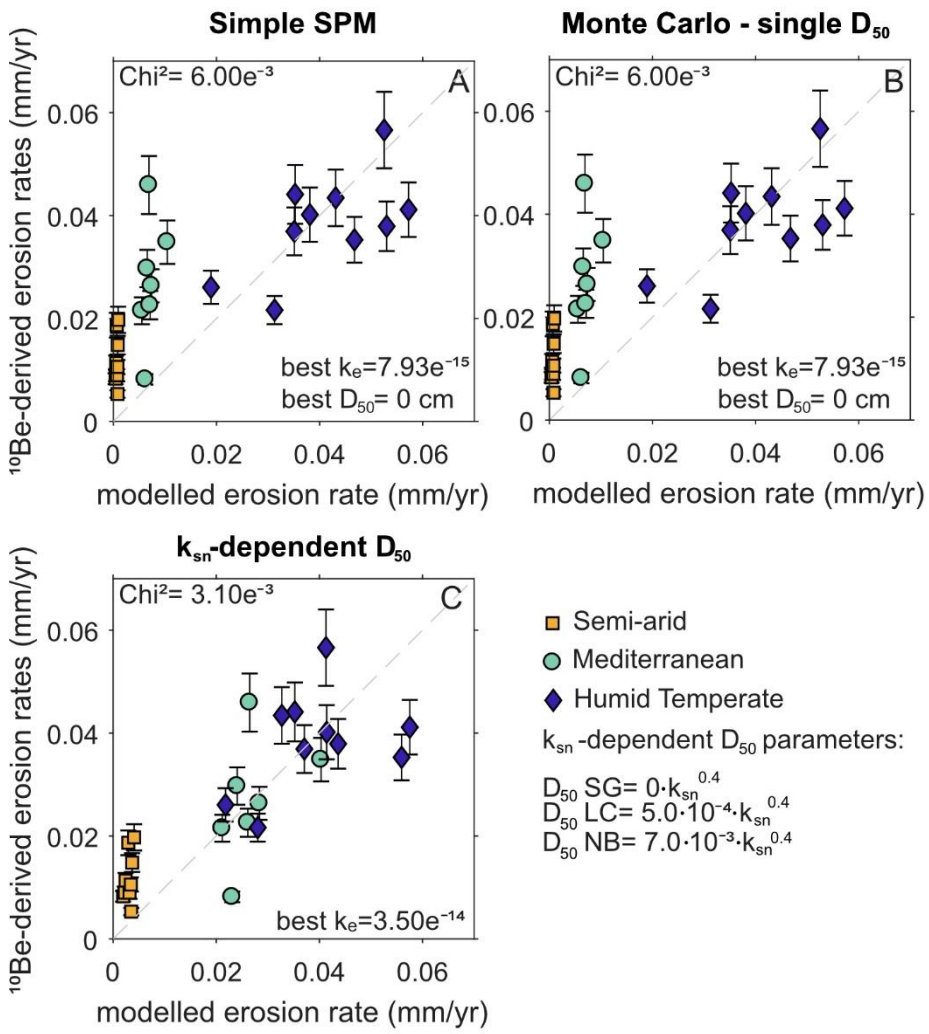

Figure 6.7: Best fit model results for all climatic region combined in one model. Modelling approach based on the three different model configurations. A: Simple stream power model (simple SPM), B: Single D_{50} for all climatic regions, obtained from best fit Monte Carlo simulation. C: k_{sn}-dependent D_{50} values (D_{50}= factor * k_{sn}) based on the best fit grain size factor (F D_{50}). The misfit (Chi^2), the best fit erodibility parameter (best k_e) and best fit D_{50} (best D_{50}) parameters are shown in the corners. The grain size factor of each climatic region is shown in the legend.

Table 6.3: Best fit model result of each model configuration. Model run 1 and 4 are performed using the simple stream power model (simple SPM), model run 2, 3, 4 and 6 are performed with the stochastic-threshold stream power model (ST-SPM). The model runs have been performed for the climate regions individually (SA=semi-arid, Med=mediterranean, HT= humid-temperate). The corresponding D_{50} values of each model configuration in this table are compared to the measured D_{50} values in the channel in Figure 6.8.

Model	Model type	Region	Figure	k_e ($m^{2.5}\ s^2\ kg^{-1}$)	D_{50} (cm)	Factor D_{50}	Misfit $((m\ s^{-1})^2)$
Climate regions in individual models							
1	Simple SPM	SA	Figure 6.6a	$1.40 \cdot 10^{-13}$			$1.83 \cdot 10^{-4}$
1	Simple SPM	Med	Figure 6.6b	$2.90 \cdot 10^{-14}$			$7.53 \cdot 10^{-4}$
1	Simple SPM	HT	Figure 6.6c	$7.23 \cdot 10^{-15}$			$9.35 \cdot 10^{-4}$
2	ST-SPM Fixed D_{50}	SA	Figure 6.6d	$1.40 \cdot 10^{-13}$	0.04		$2.21 \cdot 10^{-4}$
2	ST-SPM Fixed D_{50}	Med	Figure 6.6e	$3.04 \cdot 10^{-14}$	0.1		$8.12 \cdot 10^{-4}$
2	ST-SPM Fixed D_{50}	HT	Figure 6.6f	$7.23 \cdot 10^{-15}$	0.2		$8.90 \cdot 10^{-4}$
3	ST-SPM k_{sn}-dependent D_{50}	SA	Figure 6.6g	$1.72 \cdot 10^{-12}$		$8.00 \cdot 10^{-4}$	$1.47 \cdot 10^{-4}$
3	ST-SPM k_{sn}-dependent D_{50}	Med	Figure 6.6h	$3.84 \cdot 10^{-14}$		$6.50 \cdot 10^{-4}$	$7.38 \cdot 10^{-4}$
3	ST-SPM k_{sn}-dependent D_{50}	HT	Figure 6.6i	$7.23 \cdot 10^{-15}$		$7.00 \cdot 10^{-4}$	$9.26 \cdot 10^{-4}$
All climate regions in one model							
4	Simple SPM	All	Figure 6.7a	$7.93 \cdot 10^{-15}$			$6.00 \cdot 10^{-3}$
5	ST-SPM Fixed D_{50}	All	Figure 6.7b	$7.93 \cdot 10^{-15}$	0		$6.00 \cdot 10^{-3}$
6	ST-SPM k_{sn}-dependent D_{50}	All	Figure 6.7c	$3.50 \cdot 10^{-14}$		SA: 0.00 Med: $5.00 \cdot 10^{-4}$ HT: $7.00 \cdot 10^{-3}$	$3.10 \cdot 10^{-3}$

6.4.3 Comparison measured and modelled D_{50} values

The above-described model runs were performed with different D_{50} settings. In Figure 6.8 the measured D_{50} values in each climate region are compared to the best fit modelled D_{50} values of each model configuration.

As expected, the model runs with the simple SPM (model run 1 and 4) have a D_{50} value of zero, because the simple SPM does not include erosion thresholds. The model runs with a fixed D_{50} value for all catchments (model run 2 and 5) returned very fine (>0.2 cm) channel grain sizes, which are considerably finer than the grain sizes measured in the field (Figure 6.8). The model runs with k_{sn}-dependent D_{50} values revealed relatively good D_{50} estimations for the model runs for individual climate regions (model run 3).

However, when combining all climate regions in one model with a single k_e value and k_{sn}-dependent D_{50} values that differed per climate region (model run 6) the best fit D_{50} values underestimated the D_{50} values for the semi-arid region and overestimated the D_{50} values for the humid-temperate region.

It was impossible to model the erosion rates with the measured D_{50} values from field data as an input, because the large range of measured D_{50} values (ranging from 0.2 cm to several centimetres/decimetres), made it impossible to obtain a reliable model result for all catchments with a single substrate erodibility (k_e) (Figure S 6.3). Moreover, we lacked a functional understanding of these measured D_{50} values (Section 6.3.4 and Chapter 5).

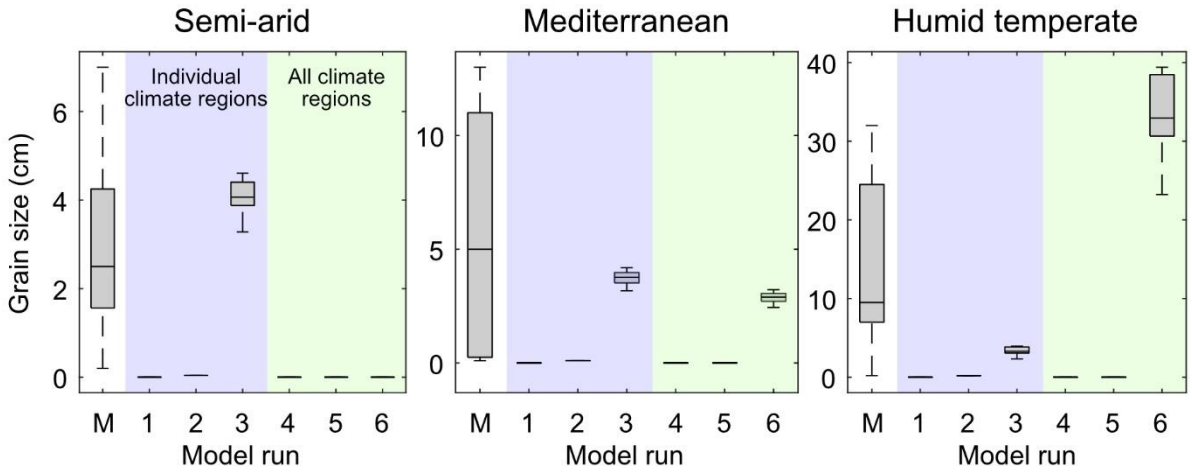

Figure 6.8: A comparison of measured D_{50} values in the field (M) and the modelled values of the different model configurations. The model run numbers correspond to the model run details that are listed in Table 6.3. The model runs are performed for each climate region individually (run 1 to 3, boxplots in blue range) and with all climate regions in one plot (model run 4 to 6, boxplots in green range).

6.5 Discussion

In this discussion, we focus on whether erosion thresholds play a role in Chile, and how this differs for the various climate regions. As the performance of the stochastic-threshold SPM with fixed D_{50} values (model runs 2 and 5) was not significantly better than the simple SPM, and we expect the channel grain sizes to vary with catchment steepness (e.g., Attal et al., 2015; Attal and Lavé, 2006; Sklar et al., 2017), we focus our discussion on the comparison between the simple SPM, without thresholds (model runs 1 and 4), and stochastic-threshold SPM with k_{sn}-dependent D_{50} values (model runs 3 and 6).

The results of individual models for each climate region revealed that the stochastic-threshold stream power model with k_{sn}-dependent D_{50} values (model run 3) has a slightly lower misfit than the simple SPM (model run 1). The k_{sn}-dependent D_{50} values that were obtained for these individual models range from ~2-4 cm (Figure 6.8), which suggests that erosion thresholds that are set by medium-sized grain sizes are required to model erosion rates that match the measured ^{10}Be-derived erosion rates of each climate zone. However, the best fit substrate erodibility factors (k_e) differed between the climate regions by orders of magnitude: the best fit k_e-value was highest (i.e., highest substrate erodibility) for the semi-arid region and lowest for the humid-temperate region (i.e., lowest substrate erodibility).

By selecting catchments that are underlain by similar lithologies, we expected the substrate erodibilities to be relatively similar between the climate regions. Hence, we conducted a similar modelling approach that combined all climate regions in one model, with a constant k_e-value for all climate regions (model runs 4 to 6). This model set up revealed a considerably better performance of the stochastic-threshold SPM with k_{sn}-dependent D_{50} values (model run 6), compared to the simple SPM (model run 4). The obtained best fit grain sizes of the various climate regions differed considerably in size. The best fit D_{50} values were zero (i.e., no erosion threshold) in the semi-arid region, medium-sized (2.4-3.2 cm) for the mediterranean region and very coarse (23.2-39.4 cm) for the humid-temperate region (Figure 6.8). A trend of increasing grain sizes from semi-arid to humid-temperate climate was also measured in the field by the authors of this study and Terweh et al. (2021). But overall, the model-derived D_{50} values underestimate the grain sizes of the semi-arid region and overestimate the grain sizes of the humid-temperate region (Figure 6.8, Terweh et al., 2021).

It is challenging to combine all three climate regions in one model, under the assumption of a constant substrate erodibility (single k_e-value) and find a well-performing model (Figure 6.7c). A high k_e-value overestimated the erosion rates of the humid-temperate region, whereas a low k_e-value underestimated the erosion rates of the semi-arid and mediterranean regions. The best model fit was found for an average k_e-value; however, extremely coarse grain sizes were needed to suppress the erosion rates of the humid-temperate region, whereas the erosion rates of the semi-arid region remained slightly underestimated, even without erosion thresholds. As described above, these best fit D_{50} grain sizes for the humid-temperate and semi-arid regions show an offset compared to the grain sizes that were measured in the field (Figure 6.8, Terweh et al., 2021). This suggests that our assumption that all climate regions can be combined in one model with a single k_e-value, could be wrong. This may have two reasons: 1) either the climate regions have, despite relatively similar lithologies, different substrate erodibilities, or 2) one or more of the constrained model input parameters for the different climate regions are incorrect. One of the major limitations of the SPM is the fact that the model requires runoff and discharge variability estimations as an input, for which typically only modern observations (e.g., gauging data) are available, whereas the SPM estimates erosion rates over millennial-year

timescales (Deal et al., 2018; Perron, 2017; Scherler et al., 2017; Tucker and Bras, 2000). In the following sections we discuss whether the above called reasons may, indeed, play a role.

6.5.1 Different substrate erodibilities (k_e)

In the previous section, we discussed whether the assumption that all climate regions have a similar substrate erodibility (k_e) is correct. Although we deliberately located catchments based on granodioritic lithology, variations in substrate erodibilities may nevertheless exist (Sklar and Dietrich, 2001).

A study that measured the mineralogy of the granodioritic bedrock in each of the climate regions found that some differences in the mineralogy exist (Oeser et al., 2018). The authors reported relatively similar bedrock SiO_2-contents in the humid-temperate and mediterranean regions, but a lower bedrock SiO_2-content in the semi-arid region. Oeser et al. (2018) classified the rock types based on their mineralogy and revealed that the rocks in the semi-arid region are more mafic compared to the other climate regions (Table 6.4). Besides contrasts in mineralogy, the degree of weathering additionally affects the substrate erodibility (Shobe et al., 2017; Sklar and Dietrich, 2001). Differences in the chemical depletion factor (CDF), a measure of the degree of weathering (Riebe et al., 2003), appear to be minor between the semi-arid region and mediterranean region, whereas, no CDF value could be determined for the humid-temperate region (Table 6.4, Oeser et al., 2018). Finally, Schmidt Hammer rebound values have been measured at bedrock outcrops and boulders in catchments of each climate region. The results revealed the highest rebound values for the semi-arid region, followed by the mediterranean region and humid-temperate region (Table 6.4, E. Lodes, personal communication, 2021). Although a direct relation between Schmidt Hammer values and the weathering degree have not been proven (Aydin and Basu, 2005; McCarroll, 1991), a study on tributaries of the Potomac river concluded that Schmidt Hammer rebound values correlated to the weathering-related bedrock erodibility of the channel profile (Shobe et al., 2017). Besides these bedrock properties, the bedrock fracture density might additionally control the substrate erodibility (Lebedeva and Brantley, 2017). However, detailed data on fracture density is lacking. It is worth noting that the bedrock samples that were sampled and measured by Oeser et al. (2018) and E. Lodes (pers. comm., 2021) stem from a single catchment of ~10-20 km^2 located in each climate region, and may not fully cover the variability in bedrock properties that exist in the catchments of this study, that extend over a larger area in each climate region.

The above-described contrasts in bedrock properties between the climate regions do not provide a coherent picture about differences in bedrock erodibility. We cannot derive well-founded conclusions based on the mineralogy and CDF-values alone. In addition, the Schmidt hammer results seem to suggest that the substrate erodibility of the semi-arid region is the lowest (less weathered) and highest in the humid-temperate

region (most weathered) (Shobe et al., 2017; Sklar and Dietrich, 2001), which contradicts the best fit substrate erodibilities obtained from the model runs for the individual climate regions. To date, we have not yet fully resolved whether assuming a similar substrate erodibility parameter for all climate regions is legitimate. However, we think that the 2-3 orders of magnitude differences in bedrock erodibility between the climate regions, that resulted from the climate regions in individual model runs, are unlikely.

Table 6.4: Bedrock properties for each climate zone obtained from various sources.

Climate region	SiO_2-content[a]	Rock classification[a,b]	Rock classification[a,c]	CDF[a,d]	Schmidt Hammer rebound value[e]
Semi-arid	50-64%	Gabbro, Gabbroic Diorite, Diorite, Granodiorite	Quartz Diorite, Quartz Gabbro, Gabbro	~0.4-0.5	63.1 ± 17.5
Mediterranean	70-75%	Granite	Granodiorite, Tonalite	~0.3-0.6	40.7 ± 13.3
Humid-temperate	65-70%	Granodiorite	Tonalite	n.d.	36.4 ± 9.4

[a] Data obtained from Oeser et al. (2018)
[b] Classification based on Le Bas et al. (1986)
[c] Classification based on Streckeisen and Le Maitre (1979)
[d] Chemical Depletion Factor based on Riebe et al. (2003)
[e] Lodes, personal communication (2021)

6.5.2 Different river discharge estimates

As described above, a major limitation of the stochastic-threshold stream power model is the fact that the model requires runoff and discharge variability estimates to simulate the river incision process that develops over millennial timescales, whereas typically only modern-day runoff and discharge variability estimates are available (Deal et al., 2018; Perron, 2017; Scherler et al., 2017; Tucker and Bras, 2000).

The mean annual runoff and discharge variability estimates of this study are based on river discharge records that have a record length of 30 years, on average (Table S 6.2). Since large flood events in arid regions have a low reoccurrence time (e.g., Deal et al., 2018; Rossi et al., 2016), we might underestimate the discharge variability factor for the semi-arid region, if such infrequent, but large magnitude events have not yet occurred during the discharge record time.

Moreover, as in situ cosmogenic ^{10}Be is produced over a large depth-interval, the ^{10}Be-erosion rates integrate over timescales that equal the residence time of minerals in the upper ~60 cm for granitic lithologies (e.g., Granger and Schaller, 2014). A simple calculation reveals that the ^{10}Be-derived erosion rates of this study record an erosional

history that integrates over the past ~30-120 kyr for the semi-arid region, ~13-75 kyr for the mediterranean region and ~11-30 kyr for the humid-temperate region.

Modelling studies on the paleoclimate of Chile revealed that the Chilean climate was wetter during the Last Glacial Maximum (~21 kyr BP) (e.g., Mutz et al., 2018; Werner et al., 2018). As the ^{10}Be integration times of the climate regions in this study go far beyond the Last Glacial Maximum (LGM), this wetter phase is incorporated in the measured erosion rates of the catchments that are located in the semi-arid region, and (partially) in the measured erosion rates of some of the catchments that are located the mediterranean and humid-temperate regions. Based on the estimates of Werner et al. (2018), the mean annual precipitation during the LGM was ~two times higher in the semi-arid region, ~100 mm higher in the mediterranean region and ~200 mm higher in the humid-temperate region.

To test whether the model performance improves and to test whether all climate regions better fit in one model with a single k_e-value when using LGM precipitation, we conducted another model run, but with LGM mean annual precipitation estimates instead of modern mean annual precipitation rates (Table 6.5; Werner et al., 2018).

The results of this test revealed that all different model configurations (i.e., simple SPM, ST-SPM with a single D_{50} and ST-SPM with a k_{sn}-dependent D_{50}) showed a lower misfit with LGM mean annual precipitation rates compared to modern day precipitation rates (Figure 6.9). Like the model runs with modern-day precipitation, the ST-SPM model run with k_{sn}-dependent D_{50} values performed best of the three models. This model properly estimated the erosion rates for the humid-temperate and mediterranean regions and showed a reduced underestimation of the modelled erosion rates of the semi-arid region, as compared to the model with modern precipitation rates (Figure 6.9c).

Table 6.5: ^{10}Be-integration times for each climate region and comparison of current day mean annual precipitation (MAP) and the mean annual precipitation rate during the Last Glacial Maximum (LGM).

Climate region	Erosion rate *(mm kyr^{-1})*	^{10}Be-integration time *(years)*	Current day MAP[a] *(mm)*	LGM MAP[b] *(mm)*
Semi-arid	~5-20	120.000-30.000	~80	~150
Mediterranean	~8-45	75.000-13.000	~350	~450
Humid-temperate	~20-55	30.000-11.000	~1300	~1500

[a] 30-year average (1979-2009) based on CR2MET data (Boisier et al., 2018b).

[b] Last Glacial Maximum (LGM) precipitation based on Werner et al., 2018.

The best fit k_{sn}-dependent D_{50} grain sizes range from 0 cm (i.e., no erosion thresholds) for the semi-arid region, 4.4-5.8 cm for the mediterranean region and 19.9-33.8 cm for the humid-temperate region. This reveals that the best fit k_{sn}-dependent grain sizes of the humid-temperate region compare better to the measured grain sizes in the field, when using LGM precipitation (Figure 6.8). The lower misfit and the fact that the predicted grain sizes show a better comparison to measured grain sizes in the field, suggests that the catchments in the semi-arid and some of the catchments in the mediterranean and humid-temperate regions were likely affected by different climatic conditions during the LGM.

It is worth noticing that for this test, we have only changed the mean annual precipitation input value. We acknowledge that the discharge variability parameter and the MAP-MAR relationship were likely also different during the LGM, but due to the lack of reliable estimations, we kept the discharge variability parameter and the MAP-MAR relationship at modern estimates. Discharge variability is, besides climate variability, strongly affected by catchment properties such as regolith thickness and vegetation cover (Rossi et al., 2016); however, these properties are unlikely to rapidly change over the considered timescales (e.g., Werner et al., 2018). Moreover, for slowly eroding catchments (i.e., in the semi-arid region) the measured ^{10}Be-derived erosion rates integrate over timescales that go far beyond the LGM, for which the climatic conditions are unknown. It would be worth testing whether a model run based on a climate estimation that integrates over each catchments' ^{10}Be-integration timescale performs better.

Despite some of the limitations, this test shows that the measured erosion rates are better estimated based on wetter conditions than current day conditions. This poses a general challenge for studying long-term river incision processes in slowly eroding environments, because the topography and river incision rates integrate over time-scales at which the climate might not have been stable (Mutz et al., 2018; Mutz and Ehlers, 2019).

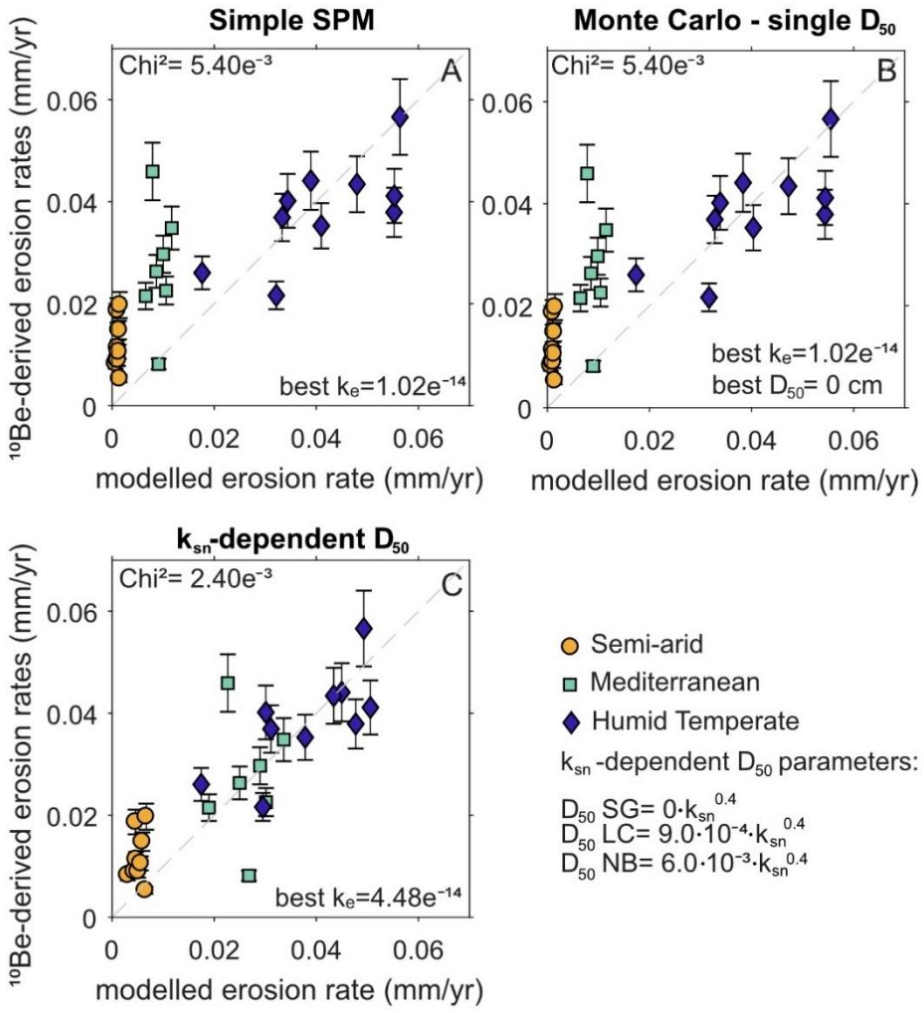

Figure 6.9: Best fit model results for all climatic region combined in one model using mean annual precipitation rates from the Last Glacial Maximum (Werner et al., 2018). Modelling approach based on the two different model configurations. A: Simple stream power model (simple SPM), B: Single D_{50} for each climatic region, obtained from best fit Monte Carlo simulation. C: k_{sn}-dependent D_{50} values (D_{50}= factor * $k_{sn}^{0.4}$) based on the best fit grain size factor (F D_{50}). The misfit (Chi^2), the best fit erodibility parameter (best k_e) and best fit D_{50} (best D_{50}) parameters are shown in the corners. The grain size factor of each climatic region is shown in the legend.

6.5.3 Threshold-behaviour per climatic region

For both model runs with modern-day mean annual precipitation and LGM precipitation, we observe an increase in the modelled D_{50} grain sizes, with increasing precipitation (i.e., grain sizes are the finest in the semi-arid region and coarsest in the humid-temperate region). Even though the measured D_{50} grain sizes slightly deviate from the modelled values, the grain sizes measured in this study and by Terweh et al. (2021) reveal the same trend of increasing D_{50} from the semi-arid region to the humid-temperate region. Terweh et al. (2021) attributed this to non-selective and transport limited conditions in the semi-arid region and selective and supply limited conditions in

the humid-temperate region. Therefore, we conducted another analysis, to test these different transport regimes and to test how sensitive the modelled erosion rates of each climate region are to erosion thresholds, that are set by different channel grain sizes (Figure 6.10). In this sensitivity test, we used the model input parameters that were constrained for each climate region (Table 6.2) and the best fit k_e-value that was obtained for the best performing model that combined all climate regions in one model, with k_{sn}-dependent D_{50} values (model run 6). We applied a k_{sn} range from 0 to 200 $m^{0.9}$ and varied the D_{50} values from 0 to 20 cm.

The results reveal that in the semi-arid region hardly any erosion occurs for erosion thresholds that are set by a grain size of >1 cm (Figure 6.10a). For the mediterranean region, erosion thresholds set by a grain size of > 2.5 cm also considerably reduce the erosion rates (Figure 6.10b). Finally, the humid-temperate region is least sensitive to erosion thresholds. In this region the modelled erosion rates only decrease considerably for high erosion thresholds that are set by a grain size of >10 cm (Figure 6.10c). It is worth noticing that each climate region would have been less sensitive to erosion thresholds if higher mean annual precipitation values were used, for instance the LGM precipitation estimates. Nevertheless, this test reveals that with increasing aridity, the transport capacity of coarse grain sizes is generally low (Terweh et al., 2021), resulting in a rapid decrease of river incision rates for increasing erosion thresholds (i.e., increasing grain sizes).

We would like to highlight the strong contrast in river incision rates for low (<100 $m^{0.9}$) and high channel steepness indices (>100 $m^{0.9}$). Previous studies reported that channel steepness, mean river discharge and discharge variability play a crucial role in the initial motion of sediment and, thus, the onset of river incision (DiBiase and Whipple, 2011; Scherler et al., 2017). They found that erosion thresholds only played a significant role in gently sloping basins, which confirms the rapid decrease of river incision rates or low channel steepness indices (<100 $m^{0.9}$) in the Chilean Coastal Cordillera. Hence, the importance of mean runoff and runoff variability to initiate the transport of bedload sediment strongly increases in gently sloping basins, because channel steepness does not additionally promote the mobilisation of bedload sediment (e.g., Lague, 2013; Scherler et al., 2017). The results of the erosion threshold sensitivity test confirm the importance of river discharge in gently sloping basins; despite the relatively low channel steepness indices, the transport capacity of river discharge level under a humid-temperate climate is high enough to transport grain sizes of considerable size (Figure 6.10). This is in line with the study of Terweh et al. (2021), who concluded that hardly any channel grains are transported in the semi-arid region, whereas the smallest grains are easily transported in the humid-temperate region, leaving the coarsest grains behind.

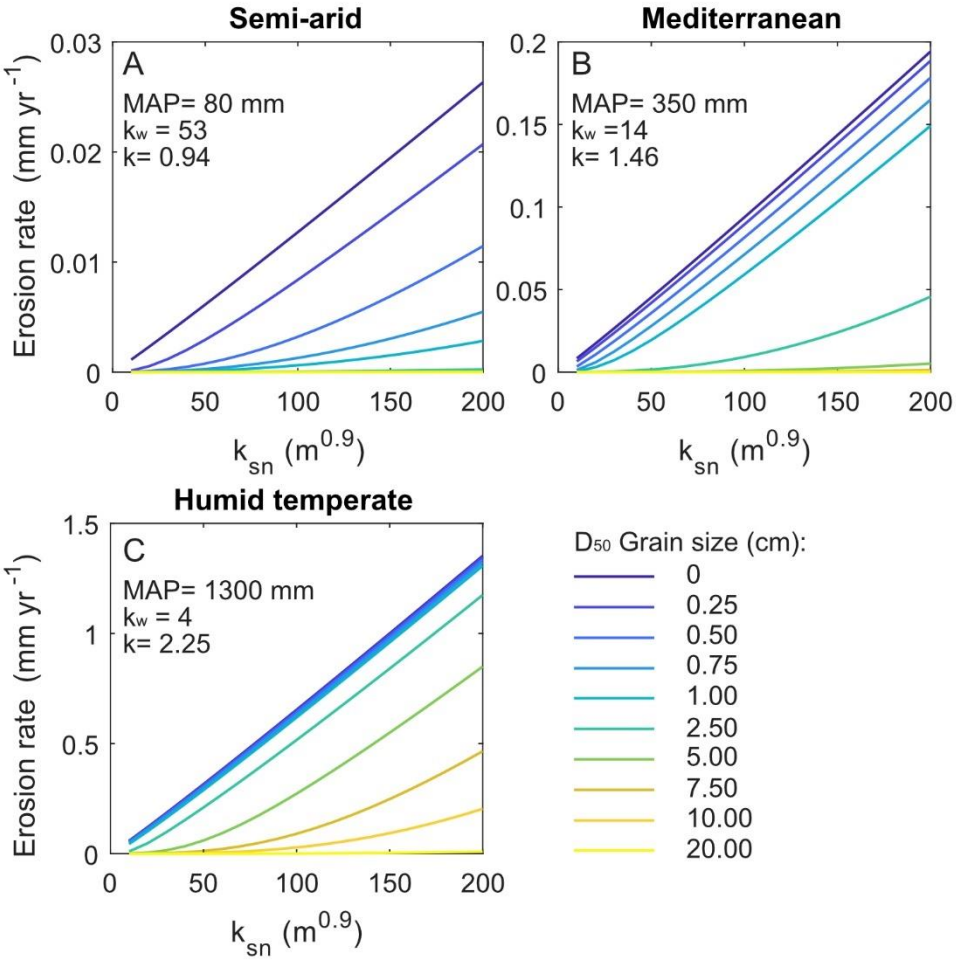

Figure 6.10: Testing the sensitivity of the modelled erosion rates for each climate region to different erosion thresholds that are set by the median grain size (D_{50}) or river sediment. We used the model parameters that were obtained for each climate region and listed in Table 6.2 and a k_e-value of $3.50 \cdot 10^{-14}$ $m^{2.5}$ s^2 kg^{-1}, which was the best fit k_e-value obtained for model run 6.

6.6 Implications

In this study, we modelled the river incision rates of gently sloping river catchments in three climatic regions (semi-arid, mediterranean, humid-temperate) located in the Coastal Cordillera of central Chile and compared them to the measured ^{10}Be-derived erosion rates. The results revealed an improved performance of the stochastic-threshold stream power model as compared to the simple stream power model without thresholds, which suggests that erosion thresholds do play a role in the gently sloping catchments of the Chilean Coastal Cordillera.

Despite similar lithologies, it appeared to be challenging to fit all climate regions in one model with a single substrate erodibility value. In this model we found good model estimations for the humid-temperate and mediterranean regions, but slight underestimations for the semi-arid region. Based on data on the bedrock properties,

we think it is unlikely that large differences in the substrate erodibility is the reason for this. Since the measured ^{10}Be-derived erosion rates integrate over long timescales, we discussed whether the erosion rates reflect climatic conditions that were different in the past. Interestingly, the model performance improves with precipitation estimates for the Last Glacial Maximum as model input. The long ^{10}Be-integration time in slowly eroding settings presents a general challenge for studies that aim to investigate the influence of climate on landscape evolution in slowly eroding landscapes (Mutz et al., 2018; Mutz and Ehlers, 2019). Nevertheless, the north-to-south increasing trend in precipitation remained during the LGM, with ~10 times higher MAP in the southern region (~38°S) as compared to the northern region (~29°S) (Mutz et al., 2018; Werner et al., 2018), which suggest that we can nonetheless use the results of this study to discuss the differences in river incision rates and the sensitivity of the different climate regions to erosion thresholds.

The best fit stochastic-threshold SPM suggested non-existing erosion thresholds for the semi-arid region, which is in contradiction to the grain sizes measured in the field. We attribute the contrasting model output to the fact that based on the current model input parameters, the erosion rates of the semi-arid region are systematically underestimated. The model possibly suggests non-existing erosion thresholds because that slightly increases the modelled erosion rates. Combining the measured grain sizes in the semi-arid region (~2.9 cm, on average), with the results of the erosion threshold sensitivity test (Figure 6.10), suggests that the measured channel grain sizes set a considerable erosion threshold for semi-arid conditions, suggesting that the river incision process is highly stochastic in the semi-arid region. Another reason for the mismatch between the modelled and measured D_{50} grain sizes might be the fact that river incision probably only occurs during rare flood events (Aguilar et al., 2014, 2015; Vargas et al., 2000, 2006). Possibly the magnitudes of these flood events are so high, that it no longer matters whether erosion thresholds are non-existing or set by grain sizes of ~3 cm. The observation that the modelled erosion rates of the humid-temperate region show a low sensitivity to erosion thresholds may suggest that active river incision occurs frequently in this region (Figure 6.10). However, due to the relatively low discharge variability, the long-term river incision rate is likely composed of many small magnitude events (Perron, 2017; Tucker and Bras, 2000).

That landscape forming processes occur infrequently in arid regions, and more frequently in humid regions, has been observed by previous studies that investigated other regions on earth (e.g., Lague, 2013; Scherler et al., 2017; Tucker and Bras, 2000). The contrast in stochasticity of erosion and river incision processes between the arid and humid regions of Chile agree with previously published observations for Chile. For instance, event-based erosion processes, induced by El Niño, have been reported by previous studies in the arid region of Chile (e.g., Aguilar et al., 2011, 2014; Vargas et al., 2000, 2006). A large precipitation event in the arid region of Chile in March 2015 resulted in a high estimated catchment average erosion rate of 6 ± 1 mm (Aguilar et al., 2015). To meet the long-term erosion rate of the region (~0.04-0.07 mm yr^{-1}) it is likely that

erosion and river incision processes are generally slow to non-existing for a long time span and only occur during extreme events with the recurrence time of ~100 years (Carretier et al., 2018). That erosion and, thus, river incision is occurring more continuously in the humid-temperate region and is rather event-based in the arid region, is furthermore suggested by a study that compared long-term catchment average erosion rates to modern catchment average erosion estimates obtained from river gauging data with record lengths of ~5-50 years (Carretier et al., 2013, 2018). Because the long-term and modern erosion rates agreed well for the humid region but showed a mismatch for the arid region, the authors suggested that erosion for the humid region must be rather continuous, whereas large events with a long recurrence time make up the long-term erosion rates for the arid region (Carretier et al., 2013, 2018).

Nevertheless, further investigation is required to draw reliable conclusions on the reoccurrence time and magnitude of river incision in the different climate regions. This is the first study that tested the threshold-behaviour of river incision in gently sloping catchments located in different climate regions. We conclude that in gently sloping catchments, the modelled erosion rates strongly depend on the river discharge that mobilizes river sediment, because the channel steepness is not high enough to support bedload mobilization. This has strong implications for many bedrock rivers in low relief mountain ranges around the world, where the processes of sediment-mobilization and river incision seems to show a stronger climate-dependence than in steep and high relief mountain ranges.

6.7 Author contributions

R. van Dongen carried out the data analysis and interpretation with help from D. Scherler. D. Scherler acquired the project funding and was the main supervisor.

6.8 Competing interests

The authors declare that they have no conflict of interest.

6.9 Acknowledgements

We acknowledge support from the German Science Foundation (DFG) priority research program SPP-1803 "EarthShape: Earth Surface Shaping by Biota" (grant SCHE 1676/4-1 to D.S.). We are grateful to the Chilean National Park Service (CONAF) for providing access to the sample locations and on-site support of our research. We thank H. Wittmann for the cosmogenic-^{10}Be laboratory training and laboratory supervision. We also thank L. Mao, R. Carrillo and M. Koelewijn for their support during fieldwork, and S. Binnie and S. Heinze from Cologne University for conducting AMS measurements.

6.10 Supplementary Tables

Table S 6.1: ^{10}Be-derived erosion rates and channel steepness indices for the catchments in the three climate zones, that were measured in Chapter 5, and are used to calibrate the stochastic-threshold model in this chapter.

ID	IGSN[a]	Erosion rate ± 2σ *(mm kyr^{-1})*	Mean channel steepness[b] *$m^{0.9}$*
SG10	GFRD1001Q	9.0 ± 1.2	50.73
SG35	GFRD1001R	19.7 ± 2.6	79.03
SG39	GFRD1000M	8.3 ± 1.0	38.95
SG71	GFRD1001S	9.0 ± 1.2	56.20
SG74	GFRD1001T	10.6 ± 1.4	66.58
SG79	GFRD1001U	14.8 ± 1.8	65.72
SG91	GFRD1001V	5.32 ± 0.71	78.30
SG95	GFRD1001W	11.3 ± 1.5	51.06
SG102	GFRD1001X	18.7 ± 2.4	68.55
LC4	GFRD1001G	8.2 ± 1.0	69.26
LC21	GFRD1001J	22.6 ± 2.7	87.69
LC25	GFRD1001H	29.7 ± 3.6	80.83
LC33a	GFRD1001K	45.9 ± 5.6	66.51
LC34	GFRD1001L	34.8 ± 4.2	94.34
LC35	GFRD1001M	26.3 ± 3.2	70.90
LC37a	GFRD1001N	193 ± 27	91.83
LC37b	GFRD1002T	258 ± 39	101.02
LC48	GFRD1001P	21.5 ± 2.6	53.28
NB2	GFRD10017	44.1 ± 5.7	41.85
NB3	GFRD10018	37.9 ± 4.8	69.92
NB4	GFRD10019	36.9 ± 4.6	42.25
NB4c	GFRD10001	26.1 ± 3.2	22.44
NB5	GFRD1001A	35.3 ± 4.4	51.75
NB10	GFRD1001B	56.6 ± 7.4	72.32
NB14	GFRD1001C	41.1 ± 5.3	71.05
NB18	GFRD1001D	40.2 ± 5.3	45.51
NB23	GFRD1001E	43.4 ± 5.5	62.92
NB100	GFRD1001F	21.6 ± 2.7	41.85

[a] Open access metadata: http://igsn.org//[insert IGSN number here]

[b] Normalized channel steepness index, with θ_{ref}=0.45

Table S 6.2: All stations (n=336) from the CAMELS-CL dataset that are used in this study. Stations with large dams and human water extraction levels of >10% have been excluded. The station information includes, station ID, station name, latitude, longitude, geographical class (class), start of the monitoring period, end of the monitoring period, amount of discharge observations (n), catchment area (area), mean catchment elevation (mean elevation).

ID	Station Name	Latitude (°N)	Longitude (°E)	Class	Start monitoring period	End monitoring period	n	Area (km^2)	Mean elevation (m)
1001002	Río Caquena En Vertedero	-17.994	-69.255	Andes	27/11/1969	31/07/2017	13419	467.6	4652.6
1021002	Río Guallatire En Guallatire	-18.493	-69.149	Andes	26/05/1971	09/03/2018	15075	49.7	4613.1
1041002	Río Isluga En Bocatoma	-19.271	-68.680	Andes	25/05/1995	31/07/2017	6281	654.5	4322.2
1044001	Río Cancosa En El Tambo	-19.859	-68.586	Andes	10/08/1994	31/07/2017	7596	992.0	4339.1
1050002	Río Piga En Collacagua	-20.034	-68.831	Andes	15/11/1959	31/07/2017	17745	444.8	4331.8
1050004	Río Collacagua En Peablanca	-20.112	-68.841	Andes	11/02/1981	30/09/2017	10943	739.3	4309.6
1201001	Río Colpitas En Alcerreca	-17.992	-69.626	Andes	13/12/1961	23/08/2017	14091	448.6	4393.1
1201003	Río Lluta En Alcerreca	-18.004	-69.633	Andes	03/11/1961	09/03/2018	15861	1331.9	4339.4
1210001	Río Lluta En Tocontasi	-18.367	-69.900	Andes	01/07/1946	15/02/2017	11038	2589.7	4017.3
1211001	Río Lluta En Panamericana	-18.400	-70.300	Andes	01/01/1985	09/03/2018	8780	3340.2	3475.9
1310002	Río San Jose En Ausipar	-18.584	-69.811	Andes	15/05/1967	09/03/2018	10260	1281.5	3466.0
1410004	Río Codpa En Cala-Cala	-18.827	-69.667	Andes	11/10/1982	09/03/2018	10389	370.7	3901.9
1610002	Quebrada Camiña En Altusa	-19.296	-69.389	Andes	30/10/1978	02/03/2001	6136	514.8	4084.6
1730001	Río Coscaya En Pampa Lirima	-19.876	-68.959	Andes	08/12/1977	10/02/1989	4003	144.8	4263.3

ID	Station Name	Latitude	Longitude	Class	Start monitoring period	End monitoring period	n	Area	Mean elevation
		(°N)	*(°E)*					*(km^2)*	*(m)*
1730002	Río Tarapaca En Mina San Juan	-19.830	-69.287	Andes	10/12/1984	20/12/2003	5752	1325.5	3892.5
1730003	Río Coscaya En Saitoco	-19.864	-68.930	Andes	15/05/1985	14/07/2017	9937	113.8	4270.3
1730007	Q. Tarapaca En Sibaya	-19.783	-69.143	Andes	25/08/1928	09/03/2018	8063	619.4	4174.5
2101001	Río Loa Antes Represa Lequena	-21.656	-68.662	Andes	11/07/1967	09/03/2018	15480	2053.3	4094.0
2103014	Río Siloli Antes B.T. Fcab	-22.010	-68.027	Andes	22/02/2001	09/03/2018	5628	233.6	4699.3
2105005	Río Salado A. J. Loa	-22.365	-68.642	Andes	03/10/1916	27/08/2013	8347	2389.8	3580.9
2105007	Río Toconce Antes Represa Sendos	-22.273	-68.144	Andes	25/11/1982	27/04/2016	9540	156.3	4434.6
2113001	Río Huatacondo En Copaquire	-20.933	-68.883	Andes	20/12/1977	19/06/2017	12298	186.9	4326.3
2510001	Río San Pedro En Cuchabrachi	-22.823	-68.198	Andes	23/06/1947	07/07/2015	18345	1416.2	4030.4
3041001	Río Barros Negros Antes Junta Valle Ancho	-27.264	-68.998	Andes	24/04/1979	31/07/2017	7556	86.0	4757.1
3050001	Río Astaburuaga En Cono	-27.460	-69.045	Andes	16/12/1979	12/04/2017	5984	900.2	4538.5
3404001	Río Jorquera En Vertedero	-28.043	-69.957	Andes	08/02/1949	31/07/2017	18660	4198.0	3793.0
3414001	Río Pulido En Vertedero	-28.086	-69.941	Andes	04/02/1964	09/03/2018	18973	2021.8	3566.1
3421001	Río Manflas En Vertedero	-28.148	-69.994	Andes	04/02/1964	31/07/2017	17307	981.6	3564.5
3430003	Río Copiapo En Pastillo	-28.000	-69.975	Andes	15/10/1927	09/03/2018	19724	7463.9	3650.2
3814001	Río Carmen En San Felix	-28.940	-70.457	Andes	28/11/1929	03/02/1988	8405	2796.0	3614.4
3814003	Río Carmen En El Corral	-29.109	-70.414	Andes	11/10/1991	09/03/2018	9354	2434.3	3772.9
3815001	Río Carmen En Ramadillas	-28.750	-70.487	Andes	01/11/1918	30/06/2017	21918	3038.9	3470.8
3815002	Río Carmen En Pte. La Majada	-28.932	-70.458	Andes	26/09/1988	31/07/2017	8056	2756.5	3631.8

ID	Station Name	Latitude	Longitude	Class	Start monitoring period	End monitoring period	n	Area	Mean elevation
		(°N)	*(°E)*					*(km^2)*	*(m)*
4302001	Río Toro Antes Junta Río La Laguna	-29.971	-70.093	Andes	05/06/1985	09/03/2018	11185	467.4	3904.6
4311001	Estero Derecho En Alcohuaz	-30.221	-70.493	Andes	03/11/1983	31/07/2017	12249	338.2	3544.4
4313001	Río Cochiguaz En El Peñón	-30.122	-70.434	Andes	11/08/1983	08/06/2017	12252	675.3	3510.8
4314001	Río Claro En Montegrande	-30.090	-70.493	Andes	24/01/1947	31/03/1983	12673	1249.1	3328.8
4314002	Río Claro En Rivadavia	-29.978	-70.553	Andes	16/03/1914	09/03/2018	34943	1512.8	3198.9
4400001	Estero Culebrón En El Sifón	-29.979	-71.286	Coastal	01/03/1986	08/07/2017	11020	190.4	286.6
4501001	Río Hurtado En San Agustín	-30.462	-70.536	Andes	17/12/1962	18/02/2018	18321	672.4	3723.7
4501002	Río Hurtado En Las Breas	-30.383	-70.600	Andes	10/06/1928	30/11/1977	10721	840.2	3564.7
4502001	Río Hurtado En La Cortadera	-30.333	-70.767	Andes	16/02/1968	28/02/1983	4388	1258.0	3061.0
4503001	Río Hurtado En Angostura De Pangue	-30.439	-71.002	Andes	01/09/1918	09/03/2018	32616	1837.3	2554.2
4506002	Río Hurtado En Entrada Embalse Recoleta	-30.477	-71.069	Andes	26/05/1928	31/01/1984	7585	2259.2	2265.4
4511002	Río Grande En Las Ramadas	-31.012	-70.581	Andes	18/05/1961	08/02/2018	18920	568.5	3097.6
4512001	Río Tascadero En Desembocadura	-31.012	-70.664	Andes	23/10/1962	31/07/2017	18576	241.0	2888.4
4513001	Río Grande En Cuyano	-30.924	-70.773	Andes	05/05/1959	09/03/2018	20719	1286.6	2726.1
4514001	Río Mostazal En Cuestecita	-30.813	-70.613	Andes	03/10/1969	31/07/2017	16358	393.7	3066.7
4515002	Río Mostazal En Carén	-30.842	-70.769	Andes	24/07/1972	31/07/2017	13538	640.2	2588.9
4516001	Río Grande En Coipo	-30.783	-70.822	Andes	01/12/1942	26/04/1978	9143	2134.2	2548.1
4520001	Río Los Molles En Ojos De Agua	-30.744	-70.439	Andes	22/05/1970	31/07/2017	16041	155.3	3677.9
4522001	Río Rapel En Paloma	-30.733	-70.617	Andes	02/10/1941	23/03/1983	4702	510.5	3221.4

ID	Station Name	Latitude (°N)	Longitude (°E)	Class	Start monitoring period	End monitoring period	n	Area (km^2)	Mean elevation (m)
4522002	Río Rapel En Junta	-30.708	-70.873	Andes	01/04/1959	31/07/2017	18595	820.6	2661.3
4523001	Río Grande En Agua Chica	-30.702	-70.900	Andes	15/09/1946	28/02/1983	12390	3015.8	2544.0
4523002	Río Grande En Puntilla San Juan	-30.705	-70.924	Andes	01/03/1942	09/03/2018	25038	3529.4	2483.6
4530001	Río Cogotí En Fraguita	-31.112	-70.885	Andes	14/09/1971	09/03/2018	14957	490.5	2601.4
4531001	Río Cogotí En Cogotí 18	-31.083	-70.956	Andes	01/01/1942	31/03/1983	9880	530.9	2500.9
4531002	Río Cogotí Entrada Embalse Cogotí	-31.033	-71.040	Andes	10/01/1953	25/02/2018	18232	753.1	2123.7
4532001	Río Combarbala En Ramadillas	-31.228	-70.913	Andes	27/12/1975	31/07/2017	13551	189.0	2787.7
4533002	Río Pama En Valle Hermoso	-31.266	-70.991	Andes	27/10/1987	31/07/2017	10022	155.7	2289.8
4534001	Río Pama Entrada Embalse Cogoti	-31.083	-71.067	Coastal	13/01/1953	30/04/1983	7452	798.2	1769.5
4556001	Estero Punitaqui En Chalinga	-30.750	-71.417	Coastal	01/08/1968	31/03/1983	4724	839.0	573.2
4557002	Estero Punitaqui Antes Junta Río Limari	-30.672	-71.527	Coastal	16/10/1962	28/02/2017	11733	1286.2	484.1
4703001	Río Choapa Sobre El Río Valle	-31.983	-70.567	Andes	07/12/1965	03/12/1982	4366	1091.6	3188.7
4703002	Río Choapa En Cuncumén	-31.967	-70.594	Andes	14/10/1965	09/03/2018	17941	1131.6	3142.3
4704001	Río Cuncumen Antes Junta Choapa (Chacay)	-31.817	-70.600	Andes	01/01/2000	09/03/2018	5994	368.9	2799.6
4704002	Río Cuncumen Antes Bocatoma De Canales	-31.829	-70.597	Andes	15/10/1965	01/12/2005	10120	274.6	2881.7
4711001	Río Choapa En Salamanca	-31.812	-70.930	Andes	01/06/1931	09/03/2018	20875	2211.9	2634.9
4712001	Río Chalinga En La Palmilla	-31.696	-70.716	Andes	29/10/1991	24/01/2018	9330	243.9	3037.6
4721001	Río Illapel En Las Burras	-31.507	-70.813	Andes	04/03/1962	23/02/2018	19057	557.1	3131.6
5100001	Río Sobrante En Piadero	-32.225	-70.712	Andes	06/08/1928	09/03/2018	19263	241.1	2609.6

ID	Station Name	Latitude	Longitude	Class	Start monitoring period	End monitoring period	n	Area	Mean elevation
		(°N)	*(°E)*					*(km^2)*	*(m)*
5101001	Río Pedernal En Tejada	-32.071	-70.756	Coastal	22/12/1962	31/07/2017	14260	56.1	1624.6
5110002	Río Petorca En Peon O Hierro Viejo	-32.279	-70.989	Coastal	05/05/1979	31/07/2017	11299	947.2	1782.3
5120001	Río Petorca En Longotoma O Puente Ff	-32.378	-71.372	Coastal	07/05/1979	31/07/2017	10236	1969.5	1295.6
5200001	Río Alicahue En Colliguay	-32.330	-70.738	Andes	30/11/1963	09/03/2018	17991	348.0	2402.6
5221002	Río Ligua En Quinquimo	-32.441	-71.314	Coastal	05/05/1979	31/07/2016	11106	1951.9	1142.5
5401002	Río Juncal Ante Junta Rio Blanco	-32.904	-70.294	Andes	16/01/1914	31/12/1930	5787	504.0	3470.7
5401003	Rio Juncal En Juncal	-32.863	-70.168	Andes	15/02/1913	09/03/2018	20985	343.1	3661.9
5405001	Río Los Riecillos Antes Junta Río Colorado	-32.750	-70.317	Andes	01/07/1929	30/04/1942	4676	233.4	3486.8
5406002	Río Colorado Antes Junta Río Aconcagua	-32.856	-70.409	Andes	21/05/1914	30/04/1944	8244	831.6	3260.1
5410001	Río Aconcagua En Vizcachas	-32.850	-70.500	Andes	01/10/1913	07/06/1936	3667	2099.2	3189.8
5410002	Río Aconcagua En Chacabuquito	-32.850	-70.509	Andes	02/09/1936	09/03/2018	26570	2113.4	3177.6
5411001	Estero Pocuro En El Sifón	-32.916	-70.540	Andes	19/12/1930	31/07/2017	26261	181.0	2006.1
5411002	Estero Pocuro Antes Junta Río Aconcagua	-32.764	-70.725	Andes	01/11/1929	01/08/1983	7779	488.8	1393.2
5420002	Estero De Los Campos En Antes Junta Río Aconcagua	-32.802	-70.929	Coastal	12/07/1962	08/07/1983	7348	105.7	713.8
5421002	Estero Catemu En Puente Santa Rosa	-32.777	-70.977	Coastal	01/11/1985	31/07/2017	11010	279.9	1059.2
5422001	Estero Las Vegas En Desembocadura	-32.835	-70.998	Coastal	01/07/1962	04/06/2002	12562	328.4	840.5
5423004	Estero Romeral Antes Junta Río Aconcagua	-32.833	-71.083	Coastal	20/07/1962	30/06/1984	5333	37.0	804.8
5423006	Estero Rabuco En Fundo Rabuco	-32.867	-71.133	Coastal	01/01/1969	07/09/1983	5012	124.4	801.2

ID	Station Name	Latitude (°N)	Longitude (°E)	Class	Start monitoring period	End monitoring period	n	Area (km^2)	Mean elevation (m)
5701001	Río Maipo En Las Hualtatas	-33.978	-70.146	Andes	27/02/1979	08/01/2013	11272	1035.5	3318.9
5701002	Río Maipo En Las Melosas	-33.848	-70.196	Andes	25/01/1962	31/10/2015	9000	1462.7	3190.5
5702001	Río Volcón En Queltehues	-33.806	-70.209	Andes	26/10/1914	09/03/2018	29614	523.4	3366.8
5705001	Río Colorado Antes Junta Río Olivares	-33.490	-70.134	Andes	30/03/1977	09/03/2018	11834	783.4	3737.2
5706001	Río Olivares Antes Junta Río Colorado	-33.488	-70.137	Andes	09/02/1977	09/03/2018	13787	541.6	3690.0
5707002	Río Colorado Antes Junta Río Maipo	-33.588	-70.367	Andes	25/07/1940	09/03/2018	25235	1662.8	3418.7
5715001	Río Paine En Longitudinal	-33.833	-70.750	Coastal	04/12/1962	07/12/1983	6602	317.6	773.3
5716001	Río Angostura En Valdivia De Paine	-33.811	-70.884	Coastal	16/06/1981	31/07/2017	13115	1480.8	1100.4
5721001	Estero Yerba Loca Antes Junta San Francisco	-33.341	-70.364	Andes	03/11/1986	09/03/2018	11372	110.0	3424.3
5722002	Río Mapocho En Los Almendros	-33.370	-70.451	Andes	03/08/1948	31/08/2017	22276	638.0	2779.0
5730008	Quebrada Ramón En Recinto EMOS	-33.433	-70.514	Andes	13/02/1991	31/01/2016	8456	35.6	1982.6
5741001	Estero Puangue En Boquerón	-33.167	-71.131	Coastal	26/06/1929	31/07/2017	22212	144.2	1136.5
5746001	Estero Puangue En Ruta 78	-33.661	-71.337	Coastal	26/10/1986	09/03/2018	11196	1713.4	506.7
6000003	Río Las Leas Ante Junta Río Cachapoal	-34.363	-70.306	Andes	26/11/2006	09/03/2018	3699	172.8	2949.8
6002001	Río Cortaderal Ante Junta Río Cachapoal	-34.367	-70.326	Andes	06/09/1985	09/03/2018	5575	425.7	2961.1
6003001	Río Cachapoal 5 Km. Aguas Abajo Junta Cortaderal	-34.346	-70.376	Andes	27/06/1989	09/03/2018	8421	964.7	2930.0
6006001	Río Pangal En Pangal	-34.247	-70.328	Andes	08/11/1985	09/03/2018	10515	519.9	3071.2
6008005	Río Cachapoal En Pte Termas De Cauquenes	-34.250	-70.567	Andes	01/01/2000	09/03/2018	5320	2461.6	2639.8

ID	Station Name	Latitude (°N)	Longitude (°E)	Class	Start monitoring period	End monitoring period	n	Area (km^2)	Mean elevation (m)
6011001	Estero De La Cadena Antes Junta Río Cachapoal	-34.184	-70.844	Coastal	10/05/1983	09/03/2018	11355	598.9	706.0
6018001	Estero Zamorano En Puente El Niche	-34.431	-71.168	Coastal	16/10/1985	30/06/2017	9833	1022.6	672.3
6025001	Río Tinguiririca Aguas Abajo Junta Río Azufre	-34.816	-70.564	Andes	08/05/1970	22/04/1993	5519	970.4	2841.5
6027001	Río Claro En El Valle	-34.687	-70.874	Andes	01/05/1970	09/03/2018	16057	349.4	1604.5
6028001	Río Tinguiririca Bajo Los Bríones	-34.719	-70.827	Andes	01/11/1921	09/03/2018	26634	1438.3	2549.8
6033001	Estero Chimbarongo En Convento Viejo	-34.769	-71.118	Coastal	31/10/1968	10/12/1993	8362	682.7	505.4
6043001	Estero Alhue En Quilamuta	-34.062	-71.242	Coastal	11/05/1970	12/02/2017	14683	801.8	797.6
7103001	Río Claro En Los Queñes	-34.998	-70.809	Andes	01/05/1929	30/06/2017	31614	354.4	1856.6
7104001	Estero El Manzano Antes Junta Río Teno	-34.965	-70.942	Andes	01/08/1959	30/10/1984	8408	133.7	1276.1
7112001	Río Colorado En Junta Con Palos	-35.278	-71.003	Andes	11/11/1917	30/06/2017	21702	877.9	2288.2
7115001	Río Palos En Junta Con Colorado	-35.274	-71.016	Andes	01/05/1947	09/03/2018	18048	490.0	1973.4
7116001	Estero Upeo En Upeo	-35.173	-71.091	Andes	15/02/1963	30/06/2017	17984	367.2	1197.1
7306001	Río Cipreses En Dasague Laguna La Invernada	-35.738	-70.778	Andes	31/10/2002	09/03/2018	4673	867.5	2458.3
7308001	Estero Las Garzas	-35.753	-71.003	Andes	13/09/2002	09/03/2018	5603	107.2	1459.1
7317003	Río Melado En Zona De Presa	-35.754	-71.086	Andes	20/12/2002	09/03/2018	5559	2269.4	1921.4
7317005	Río Melado En El Salto	-35.884	-71.019	Andes	01/01/2003	09/03/2018	5375	2127.6	1964.3
7320003	Río Claro En San Carlos	-35.699	-71.068	Andes	01/01/2000	09/03/2018	5574	401.2	1932.8
7330001	Río Perquilauquén En San Manuel	-36.376	-71.623	Andes	02/09/1930	09/03/2018	27100	502.4	1100.3

ID	Station Name	Latitude (°N)	Longitude (°E)	Class	Start monitoring period	End monitoring period	n	Area (km^2)	Mean elevation (m)
7335002	Estero Curipeumo En Lo Hernandez	-35.967	-72.017	Coastal	12/01/1968	30/06/2017	16570	216.9	137.2
7336001	Río Cauquenes En El Arrayan	-36.017	-72.383	Coastal	14/03/1945	30/06/2017	22605	622.8	308.4
7340001	Estero Cardo Verde En Lo Ubaldo	-35.883	-72.017	Coastal	19/08/1968	31/12/1984	3776	158.6	122.8
7341001	Río Purapel En Nirivilo	-35.550	-72.100	Coastal	31/03/1957	30/04/2016	18049	262.9	324.9
7343001	Río Purapel En Sauzal	-35.750	-72.067	Coastal	02/06/1981	27/07/2016	11509	673.9	257.2
7350003	Río Longavé en El Castillo	-36.256	-71.338	Andes	21/05/1964	15/06/2017	16410	466.9	1563.6
7354001	Río Achibueno En Los Pegnascos	-35.964	-71.488	Andes	22/03/1947	30/09/1986	12580	974.2	1263.9
7354002	Río Achibueno En La Recova	-36.003	-71.442	Andes	01/11/1986	09/03/2018	11069	894.3	1328.9
7355003	Río Ancoa Antes Tunel Canal Melado	-35.867	-71.117	Andes	30/11/1961	16/04/1995	6672	84.5	1682.7
7358001	Río Putagán En Yerbas Buenas	-35.772	-71.585	Coastal	14/04/1946	31/01/2016	22857	390.5	471.5
7372001	Río Claro En Camarico	-35.178	-71.385	Coastal	01/03/1936	30/03/2017	23490	703.0	969.3
7374001	Río Lircay En Puente Las Rastras	-35.486	-71.293	Coastal	18/12/1961	30/06/2017	17973	382.3	1052.0
7379001	Río Claro En Talca	-35.417	-71.681	Coastal	26/11/1958	09/11/1996	13668	2695.9	565.0
7379002	Río Claro En Rauquen	-35.453	-71.733	Coastal	16/02/1999	09/03/2018	6811	2807.8	547.8
7381001	Estero Los Puercos En Puente Los Puercos	-35.374	-71.829	Coastal	20/02/1986	30/06/2017	10936	558.8	205.5
7400001	Río Loanco En Desembocadura	-35.569	-72.583	Coastal	03/07/1987	30/09/2010	7535	222.7	350.9
8104001	Río Sauces Antes Junta Con Ñuble	-36.665	-71.274	Andes	31/10/1966	30/06/2017	16326	606.7	1682.9
8105001	Río Ñuble En La Punilla	-36.658	-71.321	Andes	06/04/1957	30/06/2017	19852	1254.3	1695.8
8106001	Río Ñuble En San Fabian	-36.570	-71.555	Andes	01/05/1946	30/11/1998	17940	1657.9	1593.5

ID	Station Name	Latitude (°N)	Longitude (°E)	Class	Start monitoring period	End monitoring period	n	Area (km^2)	Mean elevation (m)
8106002	Río Ñuble En San Fabian N 2	-36.586	-71.526	Andes	03/03/1999	09/03/2018	6811	1645.6	1601.1
8112001	Río Niblinto Antes Canal Alimentador Emb. Coihueco	-36.655	-71.756	Andes	02/02/1971	30/06/2017	10374	162.0	1157.1
8117001	Río Chillán En Longitudinal	-36.633	-72.217	Coastal	14/02/1958	12/05/1983	6036	730.8	542.4
8117004	Río Chillán En Esperanza	-36.787	-71.749	Andes	03/03/1939	03/09/1994	19878	206.0	1295.3
8117005	Río Chillán En Camino A Confluencia	-36.617	-72.317	Andes	29/09/1956	30/06/2017	15908	798.3	502.2
8117006	Río Chillán En Esperanza N 2	-36.800	-71.661	Andes	27/11/2003	09/03/2018	4702	167.4	1411.6
8117008	Río Quilmo En Camino A Yungay (Ca)	-36.667	-72.150	Coastal	19/07/1957	17/04/1995	9591	129.0	281.7
8118001	Río Changaral Camino A Portezuelo	-36.550	-72.283	Coastal	01/10/1956	31/07/2004	13309	1131.9	165.8
8123001	Río Itata En Cholguán	-37.150	-72.067	Andes	22/01/1924	30/06/2017	30629	859.6	833.7
8124001	Río Itata En General Cruz	-36.933	-72.350	Coastal	05/01/1956	30/06/2017	18576	1661.5	612.8
8124002	Río Itata En Trilaleo	-37.067	-72.183	Andes	11/11/1957	30/06/2017	17585	1147.7	752.0
8130001	Río Renegado En Invernada	-36.861	-71.625	Andes	01/03/1940	30/06/2017	24526	128.6	1614.0
8130002	Río Diguillin En San Lorenzo (Atacalco)	-36.924	-71.576	Andes	23/05/1946	09/03/2018	25113	204.4	1510.9
8132001	Río Diguillin En Longitudinal	-36.867	-72.333	Coastal	21/09/1956	30/06/2017	17388	1299.8	785.0
8133001	Río Itata En Cerro Negro	-36.850	-72.383	Coastal	14/09/1956	31/08/1984	9816	3187.4	649.4
8134002	Río Larqui En Camino Yungay	-36.733	-72.133	Coastal	01/10/1985	10/01/2003	5946	60.7	238.2
8134003	Río Larqui En Santa Cruz De Cuca	-36.700	-72.383	Coastal	16/01/1985	30/06/2017	10823	636.3	150.0
8135002	Río Itata En Balsa Nueva Aldea	-36.650	-72.450	Coastal	12/09/1956	09/03/2018	20611	4510.1	503.6

ID	Station Name	Latitude (°N)	Longitude (°E)	Class	Start monitoring period	End monitoring period	n	Area (km^2)	Mean elevation (m)
8144001	Río Lonquén En Trehuaco	-36.425	-72.667	Coastal	08/10/1985	12/11/2014	6105	1161.1	173.7
8220001	Río Andalién Camino A Penco	-36.817	-73.033	Coastal	01/11/1960	09/03/2018	18247	751.7	210.0
8304001	Río Lonquimay Antes Junta Río Bio Bio	-38.433	-71.233	Andes	28/03/1985	31/05/2016	10989	466.7	1359.2
8307002	Río Biobío En Llanquén	-38.201	-71.299	Andes	01/01/2000	09/03/2018	5471	3355.6	1459.7
8312000	Río Biobío En Angostura Ralco 1	-38.037	-71.478	Andes	01/01/2000	09/03/2018	5106	5127.5	1453.3
8312001	Río Biobío Ante Junta Huiri Huiri	-37.990	-71.520	Andes	07/12/2002	30/06/2017	5045	5233.1	1451.8
8313000	Río Pangue En Captación	-37.899	-71.581	Andes	19/11/2002	09/03/2018	5254	135.6	1515.2
8313001	Río Biobío Ante Junta Pangue	-37.900	-71.624	Andes	01/01/2000	09/03/2018	5539	5437.8	1440.8
8317001	Río Biobío En Rucalhue	-37.711	-71.902	Andes	01/06/1937	09/03/2018	27455	7252.5	1383.1
8317002	Río Lirquén En Cerro El Padre	-37.776	-71.863	Andes	10/12/1942	30/06/2017	26750	103.4	668.1
8319001	Río Biobío En Longitudinal	-37.602	-72.278	Andes	05/04/1965	03/04/2017	4685	7860.0	1307.2
8323001	Río Duqueco En Cerrillos	-37.542	-72.312	Andes	01/07/1962	09/03/2018	17547	1338.9	741.0
8323002	Río Duqueco En Villucura	-37.550	-72.033	Andes	01/01/1941	30/06/2017	26218	817.0	1022.8
8330001	Río Mulchén En Mulchén	-37.717	-72.250	Coastal	23/03/1937	09/03/2018	24450	428.2	462.2
8332001	Río Bureo En Mulchén	-37.717	-72.233	Coastal	12/05/1929	31/03/2009	25167	540.8	663.2
8334001	Río Biobio En Coihue	-37.550	-72.590	Andes	23/11/1928	09/03/2018	11910	11136.9	1078.6
8342001	Río Renaico En Longitudinal	-37.850	-72.383	Andes	18/06/1982	30/06/2017	11795	688.1	833.3
8343001	Río Mininco En Longitudinal	-37.864	-72.394	Coastal	01/06/1963	30/06/2017	18805	440.4	449.6
8350001	Río Malleco En La Laguna	-38.214	-71.828	Andes	01/06/1960	10/03/1984	5646	46.1	1254.9

ID	Station Name	Latitude	Longitude	Class	Start monitoring period	End monitoring period	n	Area	Mean elevation
		(°N)	*(°E)*					*(km^2)*	*(m)*
8351001	Río Malleco En Collipulli	-37.965	-72.436	Coastal	19/02/1920	09/03/2018	23205	415.1	800.9
8356001	Río Rahue En Quebrada Culén	-37.943	-72.809	Coastal	01/07/1997	30/06/2017	6938	671.6	214.1
8362001	Río Nicodahue En Pichún	-37.462	-72.753	Coastal	01/04/1988	28/05/2015	8681	741.1	584.7
8372002	Río Polcura En Cuatro Junta	-37.107	-71.242	Andes	19/11/2002	09/03/2018	5169	235.4	1995.7
8376001	Río Rucúe En Camino a Antuco	-37.340	-71.794	Andes	18/11/1983	16/10/2016	9615	210.9	1213.8
8385001	Río Claro En Camino Yumbel-Estación	-37.118	-72.545	Coastal	09/01/1985	31/08/2000	5342	531.1	137.3
8430001	Río Laraquete En El Cajón	-37.167	-73.167	Coastal	01/03/1985	31/12/1996	3972	35.4	395.5
8530001	Río Carampangue En Carampangue	-37.250	-73.267	Coastal	15/12/1970	31/12/1983	3806	912.8	394.0
8720001	Río Lebu En Las Corrientes (En Los Alamos)	-37.683	-73.350	Coastal	17/05/1963	11/05/2015	5974	667.7	372.2
8820001	Río Caramavida En Caramavida	-37.600	-73.483	Coastal	17/02/1953	30/06/2017	13387	92.9	703.5
8821001	Río Cayucupil En Cayucupil	-37.817	-73.250	Coastal	10/08/1950	31/12/1983	11325	170.3	779.3
8821002	Río Butamalal En Butamalal	-37.817	-73.250	Coastal	10/08/1950	10/05/2017	19164	123.4	778.9
8821003	Río Reputo En Reputo	-37.817	-73.367	Coastal	29/09/1950	31/12/1983	11849	27.2	254.4
8822001	Río Tucapel En Cagnete	-37.800	-73.400	Coastal	06/12/1953	31/07/1997	10706	260.3	429.0
8822002	Río Elicura En Puente Elicura	-37.933	-73.217	Coastal	01/08/1987	31/01/2003	5206	68.6	564.2
8910001	Río Lleu-Lleu En Desagüe Lago Lleu-Lleu	-38.117	-73.400	Coastal	01/04/1972	30/06/2017	15617	581.9	295.4
9101001	Río Purén En Tranaman	-38.033	-73.017	Coastal	07/02/1948	09/03/2018	20490	295.0	555.9
9101002	Río Purén En Purén	-38.013	-73.043	Coastal	01/09/1994	30/04/2009	5148	289.7	564.3
9102001	Río Lumaco En Lumaco	-38.150	-72.900	Coastal	18/10/1947	09/03/2018	24170	855.0	340.8

ID	Station Name	Latitude (°N)	Longitude (°E)	Class	Start monitoring period	End monitoring period	n	Area (km^2)	Mean elevation (m)
9104001	Río Traiguén En Victoria	-38.217	-72.317	Coastal	24/10/1950	30/06/2017	22983	93.8	513.0
9104002	Río Dumo En Santa Ana	-38.150	-72.300	Coastal	01/01/1987	28/02/2017	10741	393.3	484.8
9106001	Río Quino En Longitudinal	-38.300	-72.383	Coastal	22/08/1959	28/02/2017	19153	276.8	581.2
9107001	Estero Chufquen En Chufquen	-38.300	-72.667	Coastal	25/08/1987	28/02/2017	9751	854.2	428.9
9107002	Estero Chanco Camino Curacautin	-38.267	-72.250	Coastal	01/09/1969	30/04/1983	3897	38.6	476.7
9111001	Río Quillén En Longitudinal	-38.450	-72.433	Coastal	18/08/1959	30/04/1983	8093	148.2	456.9
9113001	Río Quillén En Galvarino	-38.400	-72.783	Coastal	29/09/1959	06/09/2016	20037	710.7	284.5
9116001	Río Cholchol En Cholchol	-38.608	-72.848	Coastal	01/03/1929	09/03/2018	22722	5055.8	342.1
9122002	Río Blanco En Curacautín	-38.451	-71.866	Andes	22/10/1986	28/10/2015	10048	170.9	1296.6
9123001	Río Cautín En Rari-Ruca	-38.430	-72.011	Andes	01/03/1929	09/03/2018	31264	1305.3	1124.6
9126001	Río Collin En Codahue	-38.578	-72.186	Coastal	27/07/1996	29/09/2015	5930	254.6	688.3
9127001	Río Muco En Puente Muco	-38.617	-72.417	Coastal	07/03/1950	30/06/2017	22372	650.4	536.7
9129002	Río Cautin En Cajon	-38.687	-72.503	Coastal	03/03/1949	09/03/2018	23763	2755.4	762.7
9131001	Río Quepe En Vilcun	-38.683	-72.233	Coastal	23/03/1946	30/04/2015	21841	378.9	931.2
9134001	Río Huichahue En Faja 24000	-38.850	-72.333	Coastal	17/01/1985	31/01/2017	11050	348.1	605.2
9135001	Río Quepe En Quepe	-38.850	-72.617	Coastal	13/12/1929	29/02/2016	19166	1666.1	506.0
9140001	Río Cautin En Almagro	-38.780	-72.947	Coastal	16/05/1965	30/06/2017	17778	5549.4	552.7
9402001	Río Allipén En Melipeuco	-38.865	-71.734	Andes	17/01/1985	26/10/2016	11104	829.6	1292.6
9404001	Río Allipén En Los Laureles	-38.983	-72.233	Andes	18/03/1946	09/03/2018	24896	1674.1	1020.6

ID	Station Name	Latitude	Longitude	Class	Start monitoring period	End monitoring period	n	Area	Mean elevation
		(°N)	*(°E)*					*(km^2)*	*(m)*
9405001	Río Curaco En Colico	-39.033	-72.083	Andes	31/10/1986	30/06/2017	8890	414.1	768.0
9412001	Río Trancura En Curarrehue	-39.360	-71.581	Andes	01/09/1968	09/03/2018	17286	356.9	1195.3
9414001	Río Trancura Antes Río Llafenco	-39.333	-71.767	Andes	01/10/1970	30/06/2017	16287	1379.4	1146.7
9416001	Río Liucura En Liucura	-39.256	-71.824	Andes	01/10/1971	30/06/2017	14372	349.0	1038.1
9420001	Río Toltén En Villarica	-39.267	-72.233	Andes	05/03/1929	09/03/2018	30759	2931.8	964.4
9423001	Río Toltén En Coipué	-39.100	-72.383	Andes	16/12/1929	09/03/2018	11064	3488.0	879.5
9433001	Río Puyehue En Quitratué	-39.150	-72.667	Coastal	07/10/1947	10/04/2017	23672	153.7	200.3
9434001	Río Donguil En Gorbea	-39.100	-72.683	Coastal	06/10/1947	10/04/2017	18343	770.6	206.2
9436001	Río Mahuidanche En Santa Ana	-39.083	-72.933	Coastal	17/03/1987	30/06/2017	10508	384.6	189.0
9437002	Río Toltén En Teodoro Schmidt	-39.014	-73.083	Coastal	12/02/1991	09/03/2018	9735	6622.6	611.8
10100002	Río Fui En Desagüe Lago Pirihueico	-39.875	-71.890	Andes	01/03/1926	20/03/2017	11231	1498.5	1171.1
10100006	Río Huahum En La Frontera	-40.097	-71.676	Andes	16/04/2002	31/03/2017	5107	1029.1	1194.8
10102001	Río Liquiñe En Liquiñe	-39.727	-71.850	Andes	22/07/1986	24/04/2016	9780	367.9	1122.3
10111001	Río San Pedro En Desagüe Lago Riñihue	-39.767	-72.475	Andes	01/01/1929	30/06/2017	13047	4384.5	873.6
10121001	Río Collileufu En Los Lagos	-39.858	-72.825	Coastal	01/02/1987	30/04/2017	10405	627.5	196.7
10122001	Río Calle Calle En Balsa San Javier	-39.775	-72.983	Coastal	01/02/1987	30/05/2008	7663	6621.2	684.2
10122002	Río Calle Calle En Antilhue	-39.800	-72.967	Coastal	07/12/1928	30/06/1939	3821	6609.4	685.3
10122003	Río Calle Calle En Pupunahue	-39.804	-72.903	Coastal	08/03/2007	09/03/2018	4005	6497.1	693.9
10134001	Río Cruces En Rucaco	-39.550	-72.900	Coastal	01/05/1969	09/03/2018	17553	1804.8	281.9

ID	Station Name	Latitude (°N)	Longitude (°E)	Class	Start monitoring period	End monitoring period	n	Area (km^2)	Mean elevation (m)
10137001	Río Inaque En Mafil	-39.668	-72.950	Coastal	20/02/1928	30/04/2017	12615	539.8	203.8
10140001	Río Santo Domingo En Rinconada De Piedra	-39.383	-73.133	Coastal	01/03/1992	31/10/2016	8790	107.8	335.1
10142003	Río Futa En Tres Chiflones	-39.972	-73.147	Coastal	23/05/2002	30/06/2017	5054	518.4	316.9
10304001	Río Calcurrupe En Desembocadura	-40.250	-72.267	Andes	01/07/1986	30/04/2017	10749	1725.6	935.8
10305001	Río Caunahue Camino A Llifén	-40.152	-72.251	Andes	01/01/1997	31/03/2017	6902	355.7	951.5
10306001	Río Nilahue En Mayay	-40.267	-72.233	Andes	01/08/1987	09/03/2018	11123	376.0	815.9
10311001	Río Bueno En Bueno	-40.317	-72.967	Coastal	11/07/1926	31/05/2017	12278	4160.2	670.5
10313001	Río Llollelhue En La Union	-40.267	-73.083	Coastal	06/03/1928	09/03/2018	6315	691.0	182.4
10327001	Río Chirre Antes Junta Río Pilmaiquén	-40.433	-72.917	Coastal	30/07/2001	31/05/2017	4949	777.2	388.0
10328001	Río Pilmaiquén En San Pablo	-40.384	-73.002	Coastal	23/03/1929	30/06/2017	20410	2475.4	561.6
10340001	Río Rahue En Desague Lago Rupanco	-40.789	-72.689	Andes	01/02/1986	09/03/2018	11359	1002.1	529.1
10343001	Río Coihueco Antes Junta Pichicope	-40.933	-72.700	Andes	01/08/1987	31/03/2017	10318	313.7	607.6
10351001	Río Toro En Tegualda	-41.050	-73.383	Coastal	30/05/2000	30/04/2017	5796	340.4	162.0
10356001	Río Negro En Chahuilco	-40.714	-73.228	Coastal	01/03/1986	09/03/2018	10835	2285.7	151.9
10362001	Río Damas En Tacamo	-40.618	-73.059	Coastal	01/02/1986	31/03/2017	10916	467.6	132.1
10363002	Río Forrahue En Aromos	-40.886	-73.133	Coastal	04/12/1991	30/04/2017	8455	169.4	134.6
10364001	Río Rahue En Forrahue	-40.517	-73.283	Coastal	27/02/1986	31/07/2017	10587	5614.2	234.4
10401001	Río Tranallaguín En Carrico	-40.583	-73.600	Coastal	09/06/2000	30/04/2017	4198	413.5	279.0
10405002	Río Hueyusca En Camarones	-41.017	-73.617	Coastal	30/08/2001	30/04/2017	5468	218.5	360.9

ID	Station Name	Latitude	Longitude	Class	Start monitoring period	End monitoring period	n	Area	Mean elevation
		(°N)	*(°E)*					*(km^2)*	*(m)*
10411002	Río Negro En Las Lomas	-41.383	-73.067	Coastal	25/04/1989	30/04/2017	8899	253.7	118.1
10411003	Río Maullin En Llanquihue	-41.267	-73.017	Coastal	12/03/1929	29/11/1946	6461	1627.1	159.6
10414001	Río Maullin En Las Quemas	-41.400	-73.217	Coastal	24/08/1995	31/07/2016	6554	2282.2	143.3
10431000	Río Blanco Ante Junta Río Chamiza	-41.428	-72.593	Andes	17/10/2002	23/04/2015	3871	30.5	528.7
10431001	Río Lenca Bajo Bocatoma	-41.508	-72.645	Andes	17/10/2002	13/07/2014	3876	66.2	765.4
10432002	Río Chamiza Ante Junta Río Chico	-41.442	-72.809	Andes	15/10/2002	11/02/2018	5223	589.6	608.6
10432003	Río Chico Ante Río Chamiza	-41.439	-72.818	Coastal	14/03/2003	09/03/2018	4552	136.9	298.5
10503001	Río Manso Antes Junta Río Puelo	-41.722	-72.014	Andes	27/05/2001	30/04/2017	5225	3589.5	1184.1
10514001	Río Puelo Antes Junta Con Manso	-41.757	-72.053	Andes	24/07/2001	23/08/2016	5041	4784.3	1012.7
10520001	Río Puelo En Desague Lago Tagua Tagua	-41.639	-72.169	Andes	30/05/2002	22/11/2016	4616	8640.9	1073.7
10523002	Río Puelo En Carrera Basilio	-41.604	-72.206	Andes	01/01/2003	09/03/2018	5361	8851.6	1071.7
10701002	Río Espolon En Desagüe Lago Espolon	-43.209	-71.937	Andes	13/07/2001	30/06/2017	5191	486.8	1059.9
10702002	Río Futaleufu En La Frontera	-43.174	-71.754	Andes	01/01/2000	09/03/2018	5847	7329.9	1032.3
10704002	Río Futaleufu Ante Junta Río Malito	-43.449	-72.108	Andes	10/04/2002	21/10/2016	4665	8682.4	1027.3
11020004	Río Tigre En La Frontera	-43.717	-71.711	Andes	12/07/2001	28/02/2017	5115	325.8	1242.4
11040001	Río Palena Bajo Junta Rosselot	-43.819	-72.383	Andes	13/06/1999	09/03/2018	6244	12429.1	934.9
11130001	Río Ventisquero En Carretera Austral	-44.463	-72.558	Andes	21/09/1991	12/10/2016	6855	163.6	1160.1
11141001	Río Cisnes En Estancia Río Cisnes	-44.594	-71.548	Andes	12/12/1984	31/05/2017	10412	1105.6	1063.3
11143001	Río Cisnes Antes Junta Río Moro	-44.659	-71.808	Andes	25/08/1988	09/03/2018	10255	2258.4	1048.7

ID	Station Name	Latitude (°N)	Longitude (°E)	Class	Start monitoring period	End monitoring period	n	Area (km^2)	Mean elevation (m)
11143002	Río Moro Antes Junta Río Cisnes	-44.750	-72.717	Andes	28/06/1988	30/06/2017	9072	133.8	1186.6
11147001	Río Cisnes En Puerto Cisnes	-44.750	-72.717	Andes	23/04/2001	25/03/2016	4854	5152.3	924.7
11147002	Río Grande En Carretera Austral	-44.644	-72.275	Andes	21/09/1991	20/12/2016	8245	127.8	1010.3
11302001	Río Ñireguao En Villa Mañiguales	-45.150	-72.117	Andes	18/06/1980	12/04/2017	11924	1789.8	906.2
11307001	Río Emperador Guillermo Antes Junta Mañiguales	-45.233	-72.233	Andes	18/06/1980	31/03/2017	11122	604.8	956.1
11308001	Río Mañiguales Antes Junta Río Simpson	-45.383	-72.467	Andes	06/05/1970	01/01/2018	10415	4348.5	917.5
11310001	Río Huemules Frente Cerro Galera	-45.837	-71.777	Andes	25/05/1979	30/04/2017	12192	1117.6	821.3
11310002	Río Oscuro En Camino Cerro Portezuelo	-45.907	-71.708	Andes	23/05/1979	28/02/2017	11164	105.1	1232.0
11310003	Río Blanco Chico Antes Junta Oscuro	-45.885	-71.721	Andes	23/05/1979	14/11/2016	9654	205.3	820.9
11312001	Río Blanco Antes Junta Huemules	-45.812	-71.915	Andes	06/11/1979	07/03/2001	6346	376.4	1230.2
11315001	Río Claro En Pisicultura	-45.567	-72.083	Andes	01/05/1984	31/01/2017	5524	104.9	845.8
11316001	Río Coyhaique En Tejas Verdes	-45.567	-72.033	Andes	11/10/1979	30/04/2017	9488	596.1	893.1
11317001	Río Simpson Bajo Junta Coyhaique	-45.552	-72.068	Andes	16/04/1969	09/03/2018	11611	1375.8	785.9
11335002	Río Blanco En Desague Lago Caro	-45.783	-72.617	Andes	22/02/1985	30/06/2017	9047	3213.4	902.7
11337001	Río Blanco Antes Junta Río Aysen	-45.400	-72.600	Andes	01/11/1998	09/03/2018	6327	4783.5	848.5
11342001	Río Aysen En Puerto Aysen	-45.406	-72.623	Andes	30/12/1995	09/03/2018	7640	11343.4	858.0
11405001	Río Lagunillas En Desague Lago Condor	-45.467	-72.933	Andes	30/07/1985	10/07/2013	7567	172.4	667.3
11505001	Río Ibaez En Desembocadura	-46.269	-71.991	Andes	01/08/1970	09/03/2018	11985	2404.7	1054.9

ID	Station Name	Latitude	Longitude	Class	Start monitoring period	End monitoring period	n	Area	Mean elevation
		(°N)	*(°E)*					*(km^2)*	*(m)*
11514001	Río Murta En Desembocadura	-46.433	-72.700	Andes	27/02/1985	31/03/2017	10313	898.5	920.6
11521001	Río El Bagno En Chile Chico	-46.552	-71.892	Andes	18/12/1995	04/05/2016	6652	90.1	1400.5
11530000	Río Baker En Desague Lago Bertrand	-47.067	-72.800	Andes	01/01/2000	09/03/2018	5384	16002.7	904.1
11536001	Río Cochrane En Cochrane	-47.252	-72.564	Andes	01/06/1985	09/03/2018	8566	5083.1	780.1
11536004	Río Baker En Angostura Chacabuco	-47.141	-72.726	Andes	01/01/2003	09/03/2018	5361	16799.8	905.0
11542001	Río Baker En Colonia	-47.350	-72.850	Andes	14/02/2001	09/03/2018	6047	25927.6	894.9
11545000	Río Baker Bajo Ñadis	-47.500	-72.975	Andes	01/01/2003	09/03/2018	4736	27115.7	895.8
11701001	Río Mayer En Desembocadura	-48.483	-72.600	Andes	03/05/1985	09/03/2018	9196	5327.0	1041.7
11710000	Río Pascua En Desague Lago OHiggins	-48.378	-72.959	Andes	29/03/2003	30/06/2017	4231	13778.8	981.5
11711000	Río Pascua Ante Junta Río Quetru	-48.159	-73.089	Andes	01/01/2003	09/03/2018	5287	14134.1	975.3
12280002	Río Paine En Parque Nacional 2	-50.960	-72.793	Andes	26/02/1985	09/03/2018	11632	582.5	827.2
12284002	Río Baguales En Cerro Guido	-51.017	-72.483	Andes	29/07/1980	31/08/2016	12765	564.6	822.1
12284003	Río Vizcachas En Cerro Guido	-51.017	-72.483	Andes	27/08/1980	30/06/2017	12613	1730.1	579.5
12284005	Río Don Guillermo En Cerro Castillo	-51.267	-72.483	Andes	07/06/1980	17/04/2013	8780	500.1	439.0
12284006	Río Las Chinas En Cerro Guido	-51.051	-72.517	Andes	08/06/1980	09/03/2018	13215	902.4	740.8
12284007	Río Las Chinas antes Desague Del Toro	-51.250	-72.517	Andes	16/03/1990	09/03/2018	10123	3938.7	611.4
12285001	Río Chorrillos Tres Pasos Ruta N 9	-51.450	-72.467	Andes	25/11/1981	31/03/2017	12156	101.2	425.3
12285003	Río Tres Pasos en Desague Lago Toro	-51.310	-72.621	Andes	13/01/2005	31/03/2017	4375	569.1	420.2
12287001	Río Grey antes Junta Serrano	-51.183	-73.017	Andes	25/10/1981	09/03/2018	12997	867.0	837.7

ID	Station Name	Latitude (°N)	Longitude (°E)	Class	Start monitoring period	End monitoring period	n	Area (km^2)	Mean elevation (m)
12289001	Río Serrano en Desembocadura	-51.333	-73.109	Andes	15/12/1994	09/03/2018	7975	8583.3	590.7
12289002	Río Serrano en Desagüe Lago Del Toro	-51.200	-72.933	Andes	22/05/1986	09/03/2018	11301	5287.8	544.4
12291001	Río Prat en Desembocadura	-51.558	-72.735	Andes	18/01/2005	30/04/2017	4345	220.2	351.6
12400003	Río Tranquilo en Ruta N 9	-51.823	-72.159	Andes	27/12/2005	30/04/2017	3804	380.4	213.9
12448001	Río Grande en Isla Riesco	-52.996	-71.871	Andes	11/12/1981	30/04/2017	9671	604.1	362.3
12452001	Río Perez en Desembocadura	-52.549	-71.975	Andes	19/05/1991	09/03/2018	9173	308.2	467.2
12563001	Río Calete en Seno Otway	-53.207	-71.616	Andes	27/01/2005	31/05/2017	4019	214.1	408.2
12582001	Río San Juan en Desembocadura	-53.650	-70.967	Andes	03/05/1970	09/03/2018	14112	864.0	342.3
12585001	Río Tres Brazos antes Bt. Sendos	-53.279	-70.979	Andes	08/06/1982	09/03/2018	11798	100.0	369.0
12586001	Río Las Minas en Bt. Sendos	-53.138	-70.988	Andes	07/06/1982	09/03/2018	10826	35.6	452.0
12600001	Río Rubens en Ruta N 9	-52.030	-71.941	Andes	24/11/1981	09/03/2018	12837	504.4	414.6
12622001	Río Penitente en Morro Chico	-52.051	-71.425	Andes	10/06/1980	06/01/2018	12944	1479.5	439.2
12660001	Río Ci-Aike antes Frontera	-52.043	-70.058	Andes	15/01/2005	31/08/2016	3877	1460.4	198.5
12802001	Río Side en Cerro Sombrero	-52.768	-69.277	Andes	12/06/1980	09/03/2018	13274	808.5	225.4
12805001	Río Oscar en Bahia San Felipe	-52.850	-69.754	Andes	12/06/1980	30/04/2017	12870	559.6	262.8
12820001	Río Caleta en Tierra Del Fuego	-53.859	-69.999	Andes	01/01/2006	09/03/2018	4079	87.9	339.4
12825002	Río Azopardo en Desembocadura	-54.503	-68.824	Andes	14/02/2006	01/01/2017	3823	3524.5	321.9
12861001	Río Cullen en Frontera	-52.845	-68.632	Andes	14/01/2005	31/05/2017	4270	708.6	147.7
12865001	Río Chico en Ruta Y-895	-53.544	-68.691	Andes	11/01/2005	30/04/2017	4013	590.8	308.9

ID	Station Name	Latitude	Longitude	Class	Start monitoring period	End monitoring period	n	Area	Mean elevation
		(°N)	*(°E)*					*(km^2)*	*(m)*
12872001	Río Herminita en Ruta Y-895	-53.806	-68.673	Andes	12/01/2005	16/02/2016	3654	590.8	230.8
12876001	Río Grande en Tierra Del Fuego	-53.893	-68.884	Andes	12/05/1981	09/03/2018	12874	2841.0	259.1
12878001	Río Rasmussen en Frontera (Estancia Vicuña)	-54.018	-68.653	Andes	21/01/2004	31/05/2017	4799	468.9	307.7
12930001	Río Robalo en Puerto Williams	-54.947	-67.639	Andes	01/01/2003	09/03/2018	4846	20.6	520.8

Table S 6.3: Estimated mean annual precipitation (MAP), mean annual runoff (MAR) and discharge variability (k) values for the sampled catchments in each climate zone. The estimated mean annual precipitation (MAP) during the Last Glacial Maximum (LGM) is obtained from (Werner et al., 2018).

ID	MAP[a]	MAR[b]	mean MAR	k[c]	mean k	MAP LGM[d]
SG10	59	23.1		0.88		150
SG35	82	32.5		0.96		150
SG39	88	35.0		0.97		150
SG71	86	34.2		0.97		150
SG74	82	32.5	30.5	0.96	0.94	150
SG79	86	34.2		0.97		150
SG91	63	24.7		0.89		150
SG95	56	21.9		0.87		150
SG102	91	36.2		0.98		150
LC4	290	127.0		1.34		450
LC21	282	123.1		1.33		450
LC25	269	116.7		1.31		450
LC33a	463	218.8		1.54		450
LC34	487	232.5	182.2	1.56	1.46	450
LC35	445	208.7		1.52		450
LC37a	432	201.5		1.51		450
LC37b	445	208.7		1.52		450
LC48	434	202.6		1.51		450
NB2	1260	796.3		2.12		1500
NB3	1368	894.1		2.19		1500
NB4	1603	1123.1		2.32		1500
NB4c	1664	1186.1		2.35		1500
NB5	1789	1319.9	1020.6	2.41	2.25	1500
NB10	1325	854.6		2.16		1500
NB14	1558	1077.5		2.29		1500
NB18	1714	1238.9		2.37		1500
NB23	1254	791.0		2.12		1500
NB100	1400	924.0		2.21		1500

[a] Nearest neighbour linear interpolation from CR2MET precipitation dataset (Boisier et al., 2018b).

[b] Based on empirical relationship: R=0.0002P+0.38 (Figure 6.3).

[c] Based on empirical relationship: $k=0.40R^{0.25}$ (Figure 6.5).

[d] Based on (Werner et al., 2018).

6.11 Supplementary Figures

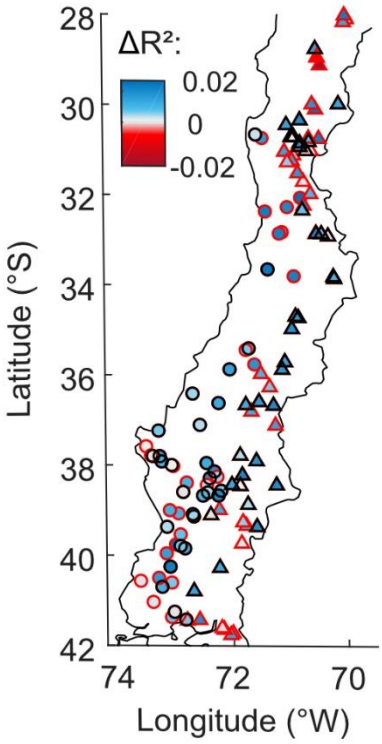

Figure S 6.1: Discharge stations in the Coastal region (circles) and Andes (triangles) color-coded with the difference in R^2 between a single inverse gamma fit and the weighted sum of two inverse gamma fits (ΔR^2= R^2 weighted sum of two inverse gamma fits – R^2 single inverse gamma fit). Blue colours indicate a better performance of the weighted sum of two inverse gamma fits. Stations with red outlines represent stations for which the high flow fraction is <0.07, stations with black outlines represent stations with a high flow fraction of >0.07.

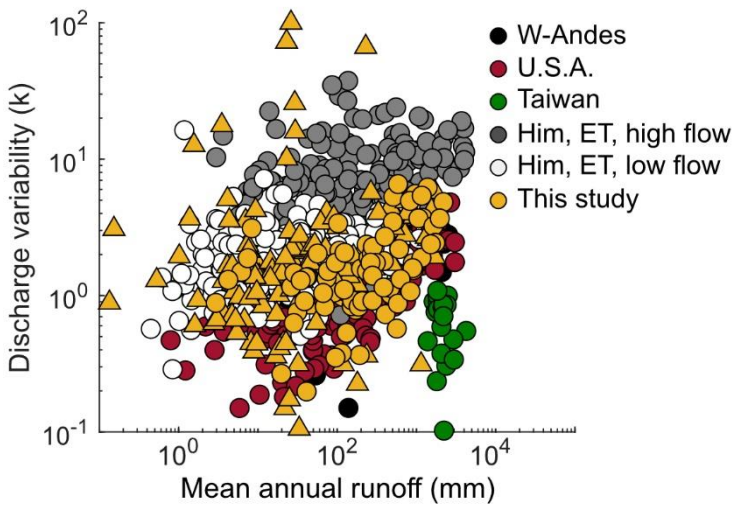

Figure S 6.2: Relationship between mean annual runoff and discharge variability for various study regions. Data of this study (yellow) compared to catchments in the western-Andes (Carretier et al., 2013), United States of America (Molnar et al., 2006), Taiwan (Lague et al., 2005), Himalayas (Him) and Eastern Tibet (ET) low flow and high flow regimes (Scherler et al., 2017). Figure modified from Scherler et al., (2017).

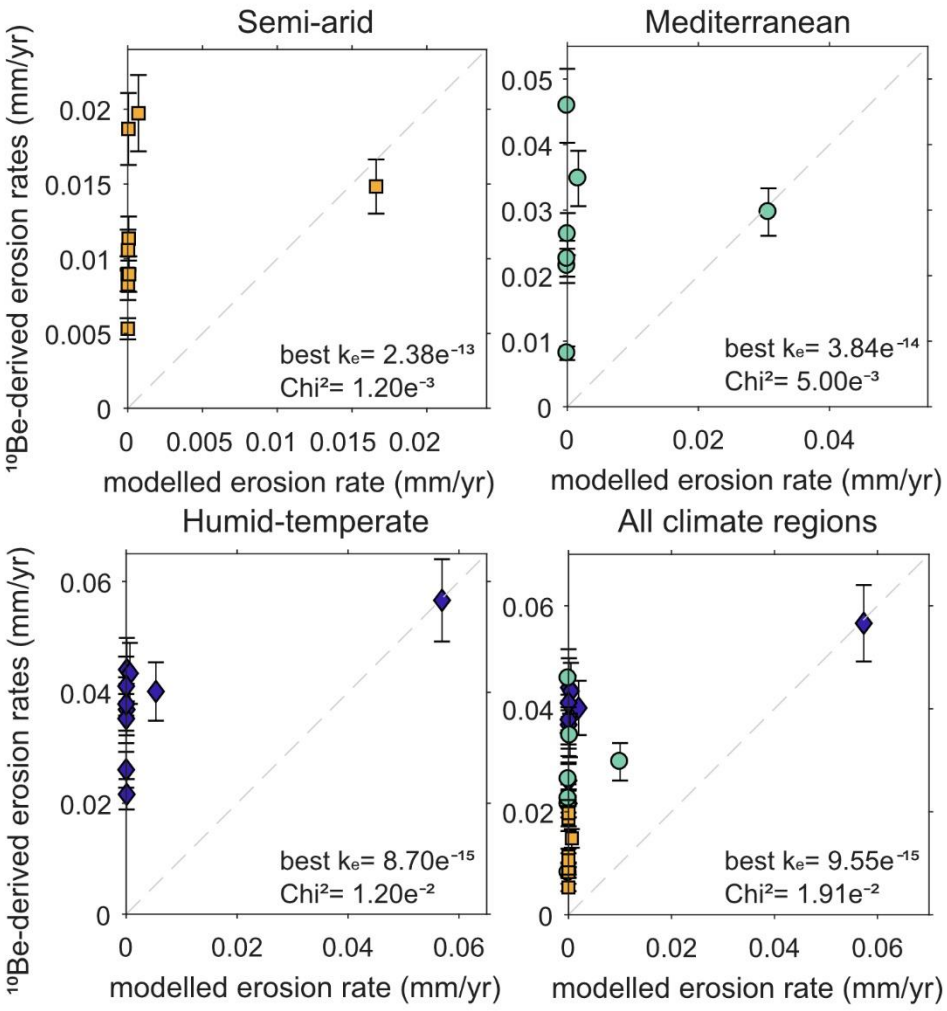

Figure S 6.3: Stochastic-threshold stream power model results based on the D_{50} values that we measured in the river channel.

Chapter 7

Discussion

7.1 Final synthesis

In this PhD research, I have investigated several components that play a role in the process of landscape evolution along a climate gradient in Chile. Some of the studies in this PhD thesis, were not specifically presented with a strong focus on river incision but do play an important role. In this final discussion chapter, I integrate all studies with the focus on the process of bedrock river incision.

The study on grain size-dependent ^{10}Be concentrations (Chapter 3) strongly focussed on the consequences of grain size-dependent ^{10}Be concentrations for potentially biased catchment average erosion rates (Van Dongen et al., 2019). Nevertheless, this study is relevant to the overall topic of this PhD research, because most of the analysis and conclusions of this work relied on river incision rates that were inferred from ^{10}Be-derived catchment average erosion rates. Based on the results of this first study, we may conclude that the ^{10}Be-derived erosion rates in this study are unlikely biased, because we sampled relatively small and gently sloping catchments that are underlain by strong granodioritic lithologies and vary in climate, but do not exceed mean annual precipitation rates of 2000 mm yr^{-1}.

Moreover, the processes we have identified that cause grain size-dependent ^{10}Be concentrations are also processes that affect the erosion threshold of river incision. We concluded that deep-seated erosion processes in steep (>25°) and humid catchments (>2000 mm yr^{-1}) can induce grain size-dependent ^{10}Be concentrations. Such processes transport coarse material to the channel, resulting in high erosion thresholds (Attal et al., 2015; Attal and Lavé, 2006; Sklar et al., 2017). The process of fluvial abrasion additionally affects grain size-dependent ^{10}Be concentrations, but as this process induces the progressive fining of grains, this process contributes to a lowering of the erosion threshold (Attal and Lavé, 2009; Kodoma, 1994; Sklar et al., 2006). Grain size-dependent ^{10}Be concentrations may, therefore, provide an opportunity to investigate

which processes have contributed to the grain size distribution of channel sediment. Some studies have used ^{10}Be concentrations in different grain sizes to investigate deep-seated erosion processes (e.g., Aguilar et al., 2014; Tofelde et al., 2018) and fluvial abrasion (Carretier and Regard, 2011), but since many processes can induce grain size-dependent ^{10}Be concentrations, it is complex infer single processes based on grain size-dependent ^{10}Be concentrations. Lukens et al. (2016) suggested to measure both ^{10}Be concentrations and thermochronometric ages in different grain sizes to gain a better understanding of the sources if the material, and, furthermore, discussed the use of fluvial abrasion models. However, also these authors concluded that with our current understanding, it is complex to apply grain size-dependent ^{10}Be concentrations as a useful method to infer for processes. Further investigation and modelling studies are required to better understand the processes that induce grain size-dependent ^{10}Be concentrations and affect the grain size distribution of channel sediment, to find out whether grain size-dependent ^{10}Be can be used in a useful manner to detect processes.

Even though the study on the hydrological response to El Niño Southern Oscillation (ENSO) (Chapter 4) did not specifically discuss the river discharge behaviour in the context of river incision, much can be learned from hydrological response to ENSO along the climate gradient and the contrasts between coastal and Andean catchments. We found that snow dynamics strongly modulate the climatic forcing in basins with the nival discharge regime. This included: 1) inducing a delayed river discharge peak during the snowmelt season, 2) providing a minimum low flow during La Niña-induced precipitation deficit. Both modulations contribute to a third control, namely, that snow dynamics in snowmelt-dominated basins induce a low discharge variability, as snowmelt generates non-flashy river discharge with a longer hydrological response time (Deal et al., 2018a; Forte et al., in review.; Rossi et al., 2016). This implies that for basins with a similar mean annual runoff value, the nival type of basins which has lower discharge variability is less likely to exceed erosion thresholds (DiBiase and Whipple, 2011; Forte et al., in review). A recent study in the Caucasus has shown that low discharge variability in snow covered basins has resulted in steeper topography, because erosion thresholds were infrequently exceeded (Forte et al., in review).

Based on the study that focussed on ENSO-induced hydrological extremes (Chapter 4), we can, furthermore, conclude that El Niño-induced floods in the semi-arid region contribute to the high discharge variability that is observed for the semi-arid region (Carretier et al., 2013; Houston, 2006; Ortlieb, 1994; Waylen and Poveda, 2002). Combining this with the conclusion that river incision processes only occur during large magnitude events and linking this to studies on extreme erosional events during El Niño phases (Aguilar et al., 2015; Carretier et al., 2013; Vargas et al., 2000, 2006), we can argue that El Niño likely has a large contribution to river incision and landscape evolution processes in the semi-arid region (Carretier et al., 2013, 2018). This would indicate that the river incision rates strongly depend on the intensity and frequency of ENSO, which might increase in the future due to climate change (Cai et al., 2014).

The results of Chapter 5 revealed a combined tectonic and climatic control on the erosion rates in Chile. This contrasts with many previous studies that found obscure relationships between mean annual precipitation and erosion rates (von Blanckenburg, 2005; Burbank et al., 2003; Godard et al., 2014; Perron, 2017; Riebe et al., 2001) and demonstrates that by planning a well-constrained study, that reduces the influence of other non-climatic controls on erosion rates, a climatic signal can be detected. The climatic signal could be observed as different slopes of the channel steepness versus erosion rate relationship for the three climate regions (Figure 6.2). The relationship became markedly steeper with increasing mean annual precipitation, which demonstrates that in the Chilean Coastal Cordillera, the fluvial erosion efficiency increases with increasing mean annual precipitation. We applied this specific approach because, in steady state landscapes, erosion rates are dictated by tectonic uplift rates (e.g., Whipple, 2004). In these landscapes, factors such as climate, vegetation cover and lithology determine the erosional efficiency and, thus, how steep the topography has to become to reach erosion rates that equal tectonic uplift rates (Tucker and Bras, 2000; Whipple and Tucker, 1999). The results of this study suggest that arid landscapes have to reach steeper topography than humid landscapes to reach erosion rates that equal a similar magnitude tectonic uplift rate (Tucker and Bras, 2000; Whipple, 2004; Whipple and Tucker, 1999). This principle has often been discussed and demonstrated by modelling studies, but the results of this study show conclusive empirical evidence.

The results of Chapter 6, furthermore, reveal that the river incision rates in the gently sloping landscapes in the Chilean Coastal Cordillera are controlled by erosion thresholds and show a strong climate sensitivity in exceeding these thresholds. This indicates that such landscapes are easily affected by changes in climate. Even though the timescales of climate change are short in comparison to the timescales that are relevant in the context of landscape evolution, river discharge in Chilean rivers is predicted to rapidly decrease as result of climate change-induced precipitation reductions (Boisier et al., 2018a; Cai et al., 2020) and rapid declines in permanent snow and glacier volumes (Barcaza et al., 2017; Braun et al., 2019; Dussaillant et al., 2019; Mardones and Garreaud, 2020). On the short term, this result in a reduced transport capacity of rivers, followed by the deposition of bedload sediment and, on the long term, aggradation of channels (e.g., Dey et al., 2016; Juyal et al., 2010). However, how the future climate will develop over longer timescales is unknown, typically, short-term oscillations in aggradation and incision cycles are found to not significantly affect the river longitudinal profile (Snyder et al., 2002; Whipple, 2001). Furthermore, discharge variability may also increase in Chilean rivers as the climate is also predicted to become more variable (IPCC, 2012) and Andean basins are expected to shift from the nival towards the pluvial discharge regime, which is typically more variable (Deal et al., 2018; Mardones and Garreaud, 2020; Rossi et al., 2016). In such cases, despite the decrease in river mean discharge, the predicted increase in discharge variability might still account for bedload transport and the exceedance of the erosion threshold (DiBiase and Whipple, 2011). It is worth noticing that climate change could, on the short-term, additionally affect the sediment flux and grain size distribution that is entering the

channel and sets the erosion threshold. For instance, by enhanced hillslope erosion or the triggering rainfall-induced landslides during extreme precipitation events (e.g., Chen and Lee, 2003; Tsou et al., 2011). Different climatic conditions could, on long time scales, also affect the grain size distribution of river sediment and the bedrock erodibility, through its effect on chemical weathering (Dixon et al., 2016; Riebe et al., 2004). However, a recent study revealed that chemical weathering in the Chilean Coastal Cordillera predominantly affects the fine sediment fraction, whereas the coarse mode is mainly set by bedrock properties such as e.g., fracture density (Terweh et al., 2021). This highlights the need for further investigation on (1) processes that affect river discharge and discharge variability and, (2) processes that control the grain size distribution of river sediment, because both topics are crucial to understand the threshold-behaviour of river incision, which does play an important role in gently sloping basins.

The conclusion that erosion thresholds do play an important role in gently sloping basins and that the exceedance of thresholds in gently sloping basins shows a strong climate-dependence, has implications for other low relief and gently sloping mountain ranges, which cover roughly 15% of the Earth's surface (estimated for 5-15°; Larsen et al., 2014).

7.2 Implications for EarthShape

This PhD project was part of the DFG-funded priority program "EarthShape". The aim of the EarthShape project is to investigate the role of biota on earth surface processes along a climate and vegetation gradient in the Coastal Cordillera of central Chile. Investigating the role of biota on earth surface shaping in the context of large-scale and long-term processes is challenging, because climate and vegetation cover are strongly correlated (e.g., Jeffery et al., 2014; Starke et al., 2020). As vegetation cover covaries with multiple catchment attributes (e.g., climate, lithology, hillslope angles), that on themself also control erosion rates, it is complex to disentangle the biotic effect from the other factors on a catchment-scale. For instance, earlier studies that also measured long-term catchment average erosion rates along a latitudinal gradient in the Chilean Andes hypothesized that dense vegetation might have an reducing effect on erosion, however, the biotic control could not be disentangled because of the strong correlation between the vegetation cover, climate and the topography of the Andes (Carretier et al., 2013; Tolorza et al., 2014).

The results of this PhD thesis revealed a positive relationship between mean annual precipitation (MAP) and the fluvial erosion efficiency. This is in contrast to some other studies that suggested that the positive relationship between precipitation and erosion rates can be obscured by vegetation that has a reducing effect on erosion rates (Schaller et al., 2018; Starke et al., 2020). Starke et al. (2020) concluded that vegetation exerted a reducing effect on erosion rates in a region in the Peruvian Andes, which featured a vegetation cover of 50-60% and mean annual precipitation rates of ~200-

300 mm. The vegetation cover in my study reaches up to ~70% for the humid-temperate region (Didan, 2015), however, the mean annual precipitation rate is much higher (~1300 mm). Perhaps, a reducing effect of vegetation on erosion rates that overrules the effect of MAP could be observed for other regions in the Coastal Cordillera with a different combination of MAP and vegetation density, however, such a location might be difficult to find because of the strong correlation between MAP and vegetation cover.

It is worth noticing, that the erosion rates in this study are likely affected by the reducing effect of vegetation on erosion rages, however, the enhancing effect of climate on erosion rates is stronger, with the consequence that the climatic signal overrules the vegetation signal. Without vegetation cover, the positive relationships between erosion rates and normalized channel steepness (Figure 6.2) would likely have been markedly steeper for the wetter regions. This is confirmed by a study that also measured ^{10}Be-derived erosion rates along the climate gradient in the Chilean Coastal Cordillera (~26-41°S) (Callaghan, 2012). This study concluded that in the arid region (0-100 mm), the erosional efficiency rapidly increases with MAP, but shows a much slower increase in erosional efficiency with increasing MAP for regions with >100 mm MAP and denser vegetation. But overall, also in this study, MAP was identified as having the most dominant control on erosion in the Chilean Coastal Cordillera.

The finding that the erosional efficiency increases with increasing MAP from semi-arid to humid-temperate climate does not fully agree with the findings of Schaller et al. (2018), who measured ^{10}Be concentrations in soil profiles in the four EarthShape sites. The authors of this paper found an increase in erosion rates from the arid to the mediterranean site, but lower erosion rates for the humid-temperate site compared to the mediterranean site. This disagreement can potentially be explained by a disagreement between local erosion rates and catchment average erosion rates (Lukens et al., 2016). Vegetation cover may exert a reducing effect on erosion on a local hillslope scale, but not show up in catchment averaged erosion rates, which include higher elevation hillslopes with e.g., less dense vegetation. However, the catchment average erosion rates of the EarthShape catchments (presented in Chapter 3) do follow the same pattern as observed by Schaller et al. (2018). But, interestingly, the catchment average erosion rates of the mediterranean EarthShape site (La Campana, LC37a and b, Table 5.2) show 10 times higher erosion rates as compared to the catchment average erosion rates of surrounding catchments in the mediterranean region. We attributed this to steep topography and deep-seated erosion processes that dominate the ^{10}Be-concentrations (Chapter 3 and 5). Even though these deep-seated erosion processes may not have directly affected the soil pits on the hillslopes that were investigated by Schaller et al. (2018), it is likely that the overall steeper topography of the La Campana catchment has also contributed to the higher erosion rates that were measured by Schaller et al. (2018).

As described in Section 7.1, when studying the process of river incision, we assume a topographic steady state landscape in which the erosion rate equals the tectonic uplift

rate (e.g., Whipple, 2004). In such case, climatic and biotic controls on landscape evolution only affect the erosional efficiency of a landscape, which determines how much a landscape has to steepen to equal the tectonic uplift rate (Tucker and Bras, 2000; Whipple and Tucker, 1999). It is commonly thought that vegetation has a reducing effect on erosion (e.g., Schaller et al., 2018; Starke et al., 2020), which implies that landscapes under dense vegetation will become steeper to reach a topographic steady state with the tectonic uplift rates (Jeffery et al., 2014; Tucker and Bras, 2000; Whipple and Tucker, 1999). In detachment-limited landscape evolution models, the effect of vegetation is included as a factor that enhances surface roughness, infiltration rates and the channelization of overland flow (Istanbulluoglu et al., 2004; Istanbulluoglu and Bras, 2005; Schmid et al., 2018), which results in a lower drainage density and higher topography.

In this PhD-thesis, we mainly discussed how climate affects river incision rates. Biota can additionally affect river incision rates by influencing the grain size distribution of river sediment and the discharge variability of a river. For instance, biota can enhance chemical and physical weathering because growing roots can fracture bedrock, uproot coarse sediment by tree throw and microbes contribute to chemical weathering processes (Brantley et al., 2017; Drever, 1994; Ehrlich, 1998; Gabet and Mudd, 2010; Roering et al., 2010). However, a recent study found that a dense vegetation cover can also result in reduced chemical weathering rates, because nutrients are obtained from recycling of plant litter material (Oeser and von Blanckenburg, 2020). Another study concluded that bio-climatic weathering only affects the fine fraction of river sediment (Terweh et al., 2021). Furthermore, as vegetation contributes to hydrological processes such as: infiltration, interception and evapotranspiration, vegetation can also affect the discharge variability of a river and, thereby, affect the exceedance of the erosion threshold (Rossi et al., 2016). In this PhD-thesis I could not disentangle the biotic controls from the climatic controls. To achieve this, further investigation on the effect of biota on the grain size distribution of river sediment and the discharge variability of a river is required.

References

Aceituno, P., Prieto, M. D. R., Solari, M. E., Martínez, A., Poveda, G. and Falvey, M.: The 1877-1878 El Niño episode: Associated impacts in South America, Clim. Change, 92(3–4), 389–416, doi:10.1007/s10584-008-9470-5, 2009.

Adams, R. M., Chen, C., MccCarl, B. A. and Weiher, R. F.: The economic consequences of ENSO events for agriculture, Clim. Res., 13, 165–172, doi:10.3354/cr013165, 1999.

Aguilar, G., Riquelme, R., Martinod, J., Darrozes, J. and Maire, E.: Variability in erosion rates related to the state of landscape transience in the semi-arid Chilean Andes, Earth Surf. Process. Landforms, 36(13), 1736–1748, doi:10.1002/esp.2194, 2011.

Aguilar, G., Carretier, S., Regard, V., Vassallo, R., Riquelme, R. and Martinod, J.: Grain size-dependent 10Be concentrations in alluvial stream sediment of the Huasco Valley, a semi-arid Andes region, Quat. Geochronol., 19, 163–172, doi:10.1016/j.quageo.2013.01.011, 2014.

Aguilar, G., Cabré, A., Guaita, C., González, F., Ortega, F., Carretier, S., Riquelme, R. and Comte, D.: Denudación por flujos de detritos durante las lluvias torrenciales de marzo de 2015 en Atacama, in XIV Congreso Geológico Chileno, pp. 816–818, SERNAGEOMIN, La Serena., 2015.

Aitken, D., Rivera, D., Godoy-Faúndez, A. and Holzapfel, E.: Water scarcity and the impact of the mining and agricultural sectors in Chile, Sustain., 8(2), doi:10.3390/su8020128, 2016.

Allen, P. A., Armitage, J. J., Whittaker, A. C., Michael, N. A., Roda-boluda, D. and Arcy, M. D.: Fragmentation Model of the Grain Size Mix of Sediment Supplied to Basins, J. Geol., 123, 405–427, doi:10.1086/683113, 2015.

Alvarez-Garreton, C., Mendoza, P. A., Boisier, J. P., Addor, N., Galleguillos, M., Zambrano-Bigiarini, M., Lara, A., Puelma, C., Cortes, G., Garreaud, R., McPhee, J. and Ayala, A.: The CAMELS-CL dataset: Catchment attributes and meteorology for large sample studies-Chile dataset, Hydrol. Earth Syst. Sci., 22(11), 5817–5846, doi:10.5194/hess-22-5817-2018, 2018.

Alvarez-Garreton, C., Boisier, J. P., Garreaud, R., Seibert, J. and Vis, M.: Progressive water deficits during multi-year droughts in central-south Chile, Hydrol. Earth Syst. Sci. Discuss., 25, 429–446, doi:10.5194/hess-2020-249, 2021.

Ancapichún, S. and Garcés-Vargas, J.: Variabilidad del anticiclón subtropical del pacífico sudeste y su impacto sobre la temperatura superficial del mar frente a la costa Centro-Norte de Chile, Ciencias Mar., 41(1), 1–20, doi:10.7773/cm.v41i1.2338, 2015.

Anderson, S. P.: Breaking it Down: Mechanical Processes in the Weathering Engine, Elements, 15(4), 247–252, doi:10.2138/gselements.15.4.247, 2019.

Anderson, S. P., von Blanckenburg, F. and White, A.: Physical and Chemical Controls on the Chritical Zone, Elements, 3(5), 315–319, doi:10.2113/gselements.3.5.315, 2007.

Andrews, E. D., Antweiler, R. C., Neiman, P. J. and Ralph, F. M.: Influence of ENSO on flood frequency along the California coast, J. Clim., 17(2), 337–348, doi:10.1175/1520-0442(2004)017<0337:IOEOFF>2.0.CO;2, 2004.

Antinao, J. L. and Gosse, J.: Large rockslides in the Southern Central Andes of Chile (32-34.5°S): Tectonic control and significance for Quaternary landscape evolution, Geomorphology, 104(3–4), 117–133, doi:10.1016/j.geomorph.2008.08.008, 2009.

Armijo, R., Lacassin, R., Coudurier-Curveur, A. and Carrizo, D.: Coupled tectonic evolution of Andean orogeny and global climate, Earth-Science Rev., 143, 1–35, doi:10.1016/j.earscirev.2015.01.005, 2015.

Attal, M. and Lavé, J.: Changes ofbedload characteristics along the Marsyandi River (central Nepal): Implications for understanding hillslope sediment supply, sediment load evolution along, Tectonics, Clim. Landsc. Evol., 2398(09), 143–171, doi:10.1130/2006.2398(09)., 2006.

Attal, M. and Lavé, J.: Pebble abrasion during fluvial transport: Experimental results and implications for the evolution of the sediment load along rivers, J. Geophys. Res. Earth Surf., 114(4), 1–22, doi:10.1029/2009JF001328, 2009.

Attal, M., Mudd, S. M., Hurst, M. D., Weinman, B., Yoo, K. and Naylor, M.: Impact of change in erosion rate and landscape steepness on hillslope and fluvial sediments grain size in the Feather River Basin (Sierra Nevada, California), Earth Surf. Dyn., 3(201), 1047–1092, doi:10.5194/esurfd-2-1047-2014, 2015.

Ayala, Á., Farías-Barahona, D., Huss, M., Pellicciotti, F., McPhee, J. and Farinotti, D.: Glacier runoff variations since 1955 in the Maipo River basin, in the semiarid Andes of central Chile, Cryosphere, 14(6), 2005–2027, doi:10.5194/tc-14-2005-2020, 2020.

Aydin, A. and Basu, A.: The Schmidt hammer in rock material characterization, Eng. Geol., 81(1), 1–14, doi:10.1016/j.enggeo.2005.06.006, 2005.

Balco, G., Stone, J. O., Lifton, N. A. and Dunai, T. J.: A complete and easily accessible means of calculating surface exposure ages or erosion rates from 10Be and 26Al measurements, Quat. Geochronol., 3(3), 174–195, doi:10.1016/j.quageo.2007.12.001, 2008.

Barazangi, M. and Isacks, B. L.: Spatial distribution of earthquakes and subduction of the Nazca plate beneath South America: Comment, Geology, 5(9), 576–578, doi:10.1130/0091-7613(1977)5<576:SDOEAS>2.0.CO;2, 1977.

Barcaza, G., Nussbaumer, S. U., Tapia, G., Valdés, J., García, J. L., Videla, Y., Albornoz, A. and Arias, V.: Glacier inventory and recent glacier variations in the Andes of Chile, South America, Ann. Glaciol., 58(75), 166–180, doi:10.1017/aog.2017.28, 2017.

Barnes, J. B. and Ehlers, T. A.: End member models for Andean Plateau uplift, Earth-Science Rev., 97(1–4), 105–132, doi:10.1016/j.earscirev.2009.08.003, 2009.

Barrett, B. S. and Hameed, S.: Seasonal variability in precipitation in central and southern Chile: Modulation by the South Pacific high, J. Clim., 30(1), 55–69, doi:10.1175/JCLI-D-16-0019.1, 2017.

Le Bas, M. J., Maitre, R. W. L., Streckeisen, A. and Zanettin, B.: A chemical classification of volcanic rocks based on the total alkali-silica diagram, J. Petrol., 27(3), 745–750, doi:10.1093/petrology/27.3.745, 1986.

Beckage, B., Platt, W. J., Slocum, M. G. and Panko, B.: Influence of the El Niño Southern Oscillation on fire regimes in the Florida Everglades, Ecology, 84(12), 3124–3130, doi:10.1890/02-0183, 2003.

Belmont, P., Pazzaglia, F. J. and Gosse, J. C.: Cosmogenic 10Be as a tracer for hillslope and channel sediment dynamics in the Clearwater River, western Washington State, Earth Planet. Sci. Lett., 264(1–2), 123–135, doi:10.1016/j.epsl.2007.09.013, 2007.

Bierman, P. and Steig, E. J.: ESTIMATING RATES OF DENUDATION USING COSMOGENIC ISOTOPE ABUNDANCES IN SEDIMENT, Earth Surf. Process. Landforms, 21, 125–139, 1996.

Binnie, S. A., Phillips, W. M., Summerfield, M. A. and Keith Fifield, L.: Sediment mixing and basin-wide cosmogenic nuclide analysis in rapidly eroding mountainous environments, Quat. Geochronol., 1(1), 4–14, doi:10.1016/j.quageo.2006.06.013, 2006.

Binnie, S. A., Phillips, W. M., Summerfield, M. A. and Fifield, L. K.: Tectonic uplift, threshold hillslopes, and denudation rates in a developing mountain range, Geology, 35(8), 743–746, doi:10.1130/G23641A.1, 2007.

von Blanckenburg, F.: The control mechanisms of erosion and weathering at basin scale from cosmogenic nuclides in river sediment, Earth Planet. Sci. Lett., 237(3–4), 462–479, doi:10.1016/j.epsl.2005.06.030, 2005.

von Blanckenburg, F., Hewawasam, T. and Kubik, P. W.: Cosmogenic nuclide evidence for low weathering and denudation in the wet , tropical highlands of Sri Lanka, J. Geophys. Res., 109, doi:10.1029/2003JF000049, 2004.

Blöschl, G., Hall, J., Viglione, A., Perdigão, R. A. P., Parajka, J., Merz, B., Lun, D., Arheimer, B., Aronica, G. T., Bilibashi, A., Boháč, M., Bonacci, O., Borga, M., Čanjevac, I., Castellarin, A., Chirico, G. B., Claps, P., Frolova, N., Ganora, D., Gorbachova, L., Gül, A., Hannaford, J., Harrigan, S., Kireeva, M., Kiss, A., Kjeldsen, T. R., Kohnová, S., Koskela, J. J., Ledvinka, O., Macdonald, N., Mavrova-Guirguinova, M., Mediero, L., Merz, R., Molnar, P., Montanari, A., Murphy, C., Osuch, M., Ovcharuk, V., Radevski, I., Salinas, J. L., Sauquet, E., Šraj, M., Szolgay, J., Volpi, E., Wilson, D., Zaimi, K. and Živković, N.: Changing climate both increases and decreases European river floods, Nature, 573(7772), 108–111, doi:10.1038/s41586-019-1495-6, 2019.

Boisier, J. P., Rondanelli, R., Garreaud, R. D. and Muñoz, F.: Anthropogenic and natural contributions to the Southeast Pacific precipitation decline and recent megadrought in central Chile, Geophys. Res. Lett., 43(1), 413–421, doi:10.1002/2015GL067265, 2016.

Boisier, J. P., Alvarez-Garreton, C., Cordero, R. R., Damiani, A., Gallardo, L., Garreaud, R. D., Lambert, F., Ramallo, C., Rojas, M. and Rondanelli, R.: Anthropogenic drying in central-southern Chile evidenced by long-term observations and climate model simulations, Elementa, 6(74), 1–20, doi:10.1525/elementa.328, 2018a.

Boisier, J. P., Alvarez-Garretón, C., Cepeda, J., Osses, A., Vásquez, N. and Rondanelli, R.: CR2MET: A high-resolution precipitation and temperature dataset for hydroclimatic research in Chile, Geophys. Res. Abstr., 20(Vic), 2018–19739, 2018b.

Borchers, B., Marrero, S., Balco, G., Caffee, M., Goehring, B., Lifton, N., Nishiizumi, K., Phillips, F., Schaefer, J. and Stone, J.: Geological calibration of spallation production rates in the CRONUS- Earth project, Quat. Geochronol., 31, 188–198, doi:10.1016/j.quageo.2015.01.009, 2016.

Botter, G., Porporato, A., Rodriguez-Iturbe, I. and Rinaldo, A.: Basin-scale soil moisture dynamics and the probabilistic characterization of carrier hydrologic flows: Slow, leaching-prone components of the hydrologic response, Water Resour. Res., 43(2), 1–14, doi:10.1029/2006WR005043, 2007.

Brady, P. V. and Carroll, S. A.: Direct effects of CO2 and temperature on silicate weathering: Possible implications for climate control, Geochim. Cosmochim. Acta, 58(7), 1853–1856, doi:10.1016/0016-7037(94)90543-6, 1994.

Brantley, S. L., Eissenstat, D. M., Marshall, J. A., Godsey, S. E., Balogh-Brunstad, Z., Karwan, D. L., Papuga, S. A., Roering, J., Dawson, T. E., Evaristo, J., Chadwick, O., McDonnell, J. J. and Weathers, K. C.: Reviews and syntheses: On the roles trees play in building and plumbing the critical zone, Biogeosciences, 14(22), 5115–5142, doi:10.5194/bg-14-5115-2017, 2017.

Braun, M. H., Malz, P., Sommer, C., Farías-Barahona, D., Sauter, T., Casassa, G., Soruco, A., Skvarca, P. and Seehaus, T. C.: Constraining glacier elevation and mass changes in South America, Nat. Clim. Chang., 9(2), 130–136, doi:10.1038/s41558-018-0375-7, 2019.

Brown, E. T., Stallard, R. F., Larsen, M. C., Raisbeck, G. M. and Yiou, F.: Denudation rates determined from the accumulation of in situ-produced 10Be in the luquillo experimental forest, Puerto Rico, Earth Planet. Sci. Lett., 129(1–4), 193–202, doi:10.1016/0012-821X(94)00249-X, 1995.

Burbank, D. W., Leland, J., Fielding, E., Anderson, R. S., Brozovic, N., Reid, M. R. and Duncan, C.: Bedrock incision, rock uplift and threshold hillslopes in the northwestern Himalayas, Nature, 379, 505–510, doi:https://doi.org/10.1038/379505a0, 1996.

Burbank, D. W., Blythe, A. E., Putkonen, J., Pratt-Sitaula, B., Gabet, E., Oskin, M., Barros, A. and Ojha, T. P.: Decoupling of erosion and precipitation in the Himalayas, Nature, 426(6967), 652–655, doi:10.1038/nature02187, 2003.

Cai, W., Borlace, S., Lengaigne, M., Van Rensch, P., Collins, M., Vecchi, G., Timmermann, A., Santoso, A., McPhaden, M. J., Wu, L., England, M. H., Wang, G., Guilyardi, E. and Jin, F. F.: Increasing frequency of extreme El Niño events due to greenhouse warming, Nat. Clim. Chang., 4(2), 111–116, doi:10.1038/nclimate2100, 2014.

Cai, W., McPhaden, M. J., Grimm, A. M., Rodrigues, R. R., Taschetto, A. S., Garreaud, R. D., Dewitte, B., Poveda, G., Ham, Y.-G., Santoso, A., Ng, B., Anderson, W., Wang, G., Geng, T., Jo, H.-S., Marengo, J. A., Alves, L. M., Osman, M., Li, S., Wu, L., Karamperidou, C., Takahashi, K. and Vera, C.: Climate impacts of the El Niño–Southern Oscillation on South America, Nat. Rev. Earth Environ., 1(4), 215–231, doi:10.1038/s43017-020-0040-3, 2020.

Callaghan, L. E.: Climate and vegetation effects on sediment transport and catchment properties along an arid to humid climatic gradient, The University of Edinburgh. [online] Available from: http://hdl.handle.net/1842/6213, 2012.

Carretier, S. and Regard, V.: Is it possible to quantify pebble abrasion and velocity in rivers using terrestrial cosmogenic nuclides?, J. Geophys. Res. Earth Surf., 116(4), 1–17, doi:10.1029/2011JF001968, 2011.

Carretier, S., Regard, V. and Soual, C.: Theoretical cosmogenic nuclide concentration in river bed load clasts: Does it depend on clast size?, Quat. Geochronol., 4(2), 108–123, doi:10.1016/j.quageo.2008.11.004, 2009.

Carretier, S., Regard, V., Vassallo, R., Aguilar, G., Martinod, J., Riquelme, R., Pepin, E., Charrier, R., Hérail, G., Farías, M., Guyot, J. L., Vargas, G. and Lagane, C.: Slope and climate variability control of erosion in the Andes of central Chile, Geology, 41(2), 195–198, doi:10.1130/G33735.1, 2013.

Carretier, S., Tolorza, V., Rodriguez, M. P., Pepin, E., Aguilar, G., Regard, V., Martinod, J., Riquelme, R., Bonnet, S., Brichau, S., Herail, G., Pinto, L., Farías, M., Charrier, R. and Guyot, J. L.: Erosion in the Chilean Andes between 27 S and 39 S: tectonic, climatic and geomorphic control, Geol. Soc. London, Spec. Publ., 401–418, doi:10.1144/SP399.16, 2014.

Carretier, S., Regard, V., Vassallo, R., Aguilar, G., Martinod, J., Riquelme, R., Christophoul, F., Charrier, R., Gayer, E., Farías, M., Audin, L. and Lagane, C.: Differences in 10Be concentrations between river sand, gravel and pebbles along the western side of the central Andes, Quat. Geochronol., 27(April), 33–51, doi:10.1016/j.quageo.2014.12.002, 2015a.

Carretier, S., Tolorza, V., Rodríguez, M. P., Pepin, E., Aguilar, G., Regard, V., Martinod, J., Riquelme, R., Bonnet, S., Brichau, S., Hérail, G., Pinto, L., Farías, M., Charrier, R. and Guyot, J. L.: Erosion in the Chilean Andes between 27°S and 39°S: tectonic, climatic and geomorphic control, Geol. Soc. London, Spec. Publ., 399(October 2015), 401–418, doi:10.1144/SP399.16, 2015b.

Carretier, S., Tolorza, V., Regard, V., Aguilar, G., Bermúdez, M. A. and Martinod, J.: Review of erosion dynamics along the major N-S climatic gradient in Chile and perspectives, Geomorphology, 300, 45–68, doi:10.1016/j.geomorph.2017.10.016, 2018.

Casagli, N., Ermini, L. and Rosati, G.: Determining grain size distribution of the material composing landslide dams in the Northern Apennines: Sampling and processing methods, Eng. Geol., 69(1–2), 83–97, doi:10.1016/S0013-7952(02)00249-1, 2003.

Chang, K. T., Chiang, S. H. and Hsu, M. L.: Modeling typhoon- and earthquake-induced landslides in a mountainous watershed using logistic regression, Geomorphology, 89(3–4), 335–347, doi:10.1016/j.geomorph.2006.12.011, 2007.

Charrier, R., Pinto, L. and Rodrígues, M. P.: Tectonostratigraphic evolution of the Andean Orogen in Chile, in The Geology of Chile, edited by T. Moreno and W. Gibbons, pp. 21–114, The Geological Society, Barcelona., 2007.

Chen, H. and Lee, C. F.: A dynamic model for rainfall-induced landslides on natural slopes, Geomorphology, 51(4), 269–288, doi:10.1016/S0169-555X(02)00224-6, 2003.

Chen, H., Dadson, S. and Chi, Y. G.: Recent rainfall-induced landslides and debris flow in northern Taiwan, Geomorphology, 77(1–2), 112–125, doi:10.1016/j.geomorph.2006.01.002, 2006.

Clapp, E. M., Bierman, P. R. and Caffee, M.: Using 10Be and 26Al to determine sediment generation rates and identify sediment source areas in an arid region drainage basin, Geomorphology, 45(1–2), 89–104, doi:10.1016/S0169-555X(01)00191-X, 2002.

Clarke, B. A. and Burbank, D. W.: Quantifying bedrock - fracture patterns within the shallow subsurface : Implications for rock mass strength , bedrock landslides, and erodibility, J. Geophys. Res., 116(F04009), doi:10.1029/2011JF001987, 2011.

Codilean, A. T., Munack, H., Cohen, T. J., Saktura, W. M., Gray, A. and Mudd, S. M.: OCTOPUS: An Open Cosmogenic Isotope and Luminescence Database, Earth Syst. Sci. Data Discuss., (March), 1–23, doi:10.5194/essd-2018-32, 2018.

Cordero, R. R., Asencio, V., Feron, S., Damiani, A., Llanillo, P. J., Sepulveda, E., Jorquera, J., Carrasco, J. and Casassa, G.: Dry-Season Snow Cover Losses in the Andes (18°–40°S) driven by Changes in Large-Scale Climate Modes, Sci. Rep., 9(1), 1–10, doi:10.1038/s41598-019-53486-7, 2019.

Cortés, G. and Margulis, S.: Impacts of El Niño and La Niña on interannual snow accumulation in the Andes: Results from a high-resolution 31 year reanalysis, Geophys. Res. Lett., 44(13), 6859–6867, doi:10.1002/2017GL073826, 2017.

Cortés, J. A., González L., G., Binnie, S. A., Robinson, R., Freeman, S. P. H. T. and Vargas, G. E.: Paleoseismology of the mejillones fault, northern Chile: Insights from cosmogenic 10Be and optically stimulated luminescence determinations, Tectonics, 31(2), 1–21, doi:10.1029/2011TC002877, 2012.

Craddock, W. H., Burbank, D. W., Bookhagen, B. and Gabet, E. J.: Bedrock channel geometry along an orographic rainfall gradient in the upper Marsyandi River valley in central Nepal, J. Geophys. Res. Earth Surf., 112(3), 1–17, doi:10.1029/2006JF000589, 2007.

Crave, A. and Davy, P.: A stochastic " precipiton " model for simulating erosion / sedimentation dynamics, Comput. Geosci., 27(August), 815–827, doi:10.1016/S0098-3004(00)00167-9, 2001.

Crosby, B. T. and Whipple, K. X.: Knickpoint initiation and distribution within fluvial networks: 236 waterfalls in the Waipaoa River, North Island, New Zealand, Geomorphology, 82(1–2), 16–38, doi:10.1016/j.geomorph.2005.08.023, 2006.

Cyr, A. J., Granger, D. E., Olivetti, V. and Molin, P.: Quantifying rock uplift rates using channel steepness and cosmogenic nuclide-determined erosion rates: Examples from northern and southern Italy, Lithosphere, 2(3), 188–198, doi:10.1130/L96.1, 2010.

Deal, E., Botter, G. and Braun, J.: Understanding the role of rainfall and hydrology in determining fluvial erosion efficiency, J. Geophys. Res. Earth Surf., doi:10.1002/2017JF004393, 2018.

Derrieux, F., Siame, L. L., Bourlès, D. L., Chen, R. F., Braucher, R., Léanni, L., Lee, J. C., Chu, H. T. and Byrne, T. B.: How fast is the denudation of the Taiwan mountain belt? Perspectives from in situ cosmogenic 10Be, J. Asian Earth Sci., 88, 230–245, doi:10.1016/j.jseaes.2014.03.012, 2014.

Dettinger, M. D., Cayan, D. R., McCabe, G. J. and Marengo, J. A.: Multiscale streamflow variability associated with El Niño/Southern Oscillation, in El Niño and the Southern Oscillation-Multiscale Variability and Global and Regional Impacts, edited by H. F. Diaz and V. Markgraf, pp. 113–148, Cambridge University Press., 2000.

Dey, S., Thiede, R. C., Schildgen, T. F., Wittmann, H., Bookhagen, B., Scherler, D., Jain, V. and Strecker, M. R.: Climate-driven sediment aggradation and incision since the late Pleistocene in the NW Himalaya, India, Earth Planet. Sci. Lett., 449, 321–331, doi:10.1016/j.epsl.2016.05.050, 2016.

DGA: Chapter 4: Water Management, in Atlas del Agua Chile, p. 60., 2016.

Diaz, H. F. and Kiladis, G. N.: Climatic variability on decadal to century time-scales, Elsevier Science B.V., 1995.

Dibiase, R. A., Whipple, K. X., Heimsath, A. M. and Ouimet, W. B.: Landscape form and millennial erosion rates in the San Gabriel Mountains , CA, Earth Planet. Sci. Lett., 289(1–2), 134–144, doi:10.1016/j.epsl.2009.10.036, 2010.

DiBiase, R. A. and Whipple, K. X.: The influence of erosion thresholds and runoff variability on the relationships among topography, climate, and erosion rate, J. Geophys. Res., 116(F4), F04036, doi:10.1029/2011JF002095, 2011.

Didan, K.: MOD13Q1 MODIS/Terra Vegetation Indices 16-Day L3 Global 250m SIN Grid V006., NASA EOSDIS L. Process. DAAC., 2015.

Dietrich, W. E. and Perron, J. T.: The search for a topographic signature of life, Nature, 439(7075), 411–418, doi:10.1038/nature04452, 2006.

Dima, I. M. and Wallace, J. M.: On the seasonality of the Hadley Cell, J. Atmos. Sci., 60(12), 1522–1527, doi:10.1175/1520-0469(2003)060<1522:OTSOTH>2.0.CO;2, 2003.

Dixon, J. L. and von Blanckenburg, F.: Soils as pacemakers and limiters of global silicate weathering, Comptes Rendus - Geosci., 344(11–12), 597–609, doi:10.1016/j.crte.2012.10.012, 2012.

Dixon, J. L., Chadwick, O. A. and Vitousek, P. M.: Climate-driven threshold for chemical weathering in postglacial soils of New Zealand, J. Geophys. Res. Earth Surf., 121, 1619–1634, doi:10.1002/2016JF003864.Received, 2016.

Van Dongen, R., Scherler, D., Wittmann, H. and Von Blanckenburg, F.: Cosmogenic 10 Be in river sediment: Where grain size matters and why, Earth Surf. Dyn., 7(2), 393–410, doi:10.5194/esurf-7-393-2019, 2019.

Draebing, D. and Krautblatter, M.: The Efficacy of Frost Weathering Processes in Alpine Rockwalls, Geophys. Res. Lett., 46(12), 6516–6524, doi:10.1029/2019GL081981, 2019.

Drever, J. I.: The effect of land plants on weathering rates of silicate minerals, Geochim. Cosmochim. Acta, 58(10), 2325–2332, doi:10.1016/0016-7037(94)90013-2, 1994.

Dunne, T., Malmon, D. V. and Mudd, S. M.: A rain splash transport equation assimilating field and laboratory measurements, J. Geophys. Res. Earth Surf., 115(1), 1–16, doi:10.1029/2009JF001302, 2010.

Dussaillant, I., Berthier, E., Brun, F., Masiokas, M., Hugonnet, R., Favier, V., Rabatel, A., Pitte, P. and Ruiz, L.: Two decades of glacier mass loss along the Andes, Nat. Geosci., 12(10), 802–808, doi:10.1038/s41561-019-0432-5, 2019.

Ehrlich, H. L.: Geomicrobiology: Its significance for geology, Earth Sci. Rev., 45(1–2), 45–60, doi:10.1016/S0012-8252(98)00034-8, 1998.

Elliott, W. P. and Angell, J. K.: Evidence for Changes in Southern Oscillation Relationships during the Last 100 Years, J. Clim., 1(7), 729–737, 1988.

Emerton, R., Cloke, H. L., Stephens, E. M., Zsoter, E., Woolnough, S. J. and Pappenberger, F.: Complex picture for likelihood of ENSO-driven flood hazard, Nat. Commun., 8, 1–9, doi:10.1038/ncomms14796, 2017.

Emerton, R. E., Stephens, E. M. and Cloke, H. L.: What is the most useful approach for forecasting hydrological extremes during El Niño?, Environ. Res. Commun., 1(3), 031002, doi:10.1088/2515-7620/ab114e, 2019.

Eppes, M. C. and Keanini, R.: Mechanical weathering and rock erosion by climate-dependent subcritical cracking, Rev. Geophys., 55(2), 470–508, doi:10.1002/2017RG000557, 2017.

Eppes, M. C., Magi, B., Hallet, B., Delmelle, E., Mackenzie-Helnwein, P., Warren, K. and Swami, S.: Deciphering the role of solar-induced thermal stresses in rock weathering, Bull. Geol. Soc. Am., 128(9–10), 1315–1338, doi:10.1130/B31422.1, 2016.

Eppes, M. C., Magi, B., Scheff, J., Warren, K., Ching, S. and Feng, T.: Warmer, Wetter Climates Accelerate Mechanical Weathering in Field Data, Independent of Stress-Loading, Geophys. Res. Lett., 47(24), 1–11, doi:10.1029/2020GL089062, 2020.

Fan, Y. and van den Dool, H.: A global monthly land surface air temperature analysis for 1948-present, J. Geophys. Res. Atmos., 113(1), 1–18, doi:10.1029/2007JD008470, 2008.

Fasullo, J. T., Otto-Bliesner, B. L. and Stevenson, S.: ENSO's Changing Influence on Temperature, Precipitation, and Wildfire in a Warming Climate, Geophys. Res. Lett., 45(17), 9216–9225, doi:10.1029/2018GL079022, 2018.

Ferguson, R., Hoey, T., Wathen, S. and Werritty, A.: Field evidence for rapid downstream fining of river gravels through selective transport, Geology, 24(2), 179–182, doi:10.1130/0091-7613(1996)024<0179:FEFRDF>2.3.CO;2, 1996.

Ferrier, K. L., Huppert, K. L. and Perron, J. T.: Climatic control of bedrock river incision, Nature, 496(7444), 206–209, doi:10.1038/nature11982, 2013.

Fick, S. E. and Hijmans, R. J.: WorldClim 2: new 1-km spatial resolution climate surfaces for global land areas, Int. J. Climatol., 37(12), 4302–4315, doi:10.1002/joc.5086, 2017.

Forte, A. M., Leonard, J. S., Rossi, M. W., Whipple, K. X., Heimsath, A. M., Sukhishvili, L., Godoladze, T. and Kardirov, F.: Low variability, snowmelt runoff inhibits coupling of climate, tectonics and toporgraphy in the Greater Caucasus, Earth Planet. Sci. Lett., 68–70, doi:https://doi.org/10.31223/X5V02X, in Review.

Fuenzalida, H.: A country of extreme climate, in Chile: Essence and Evolution (in Spanish), edited by H. García, pp. 27–35, Instituto de Estudios Regionales de la Universidad de Chile., 1982.

Funk, C. C., Peterson, P. J., Landsfeld, M. F., Pedreros, D. H., Verdin, J. P., Rowland, J. D., Romero, B. E., Husak, G. J., Michaelsen, J. C. and Verdin, A. P.: A Quasi-Global Precipitation Time Series for Drought Monitoring, U.S. Geol. Surv. Data Ser., 832, 4, 2014.

Gabet, E. J. and Dunne, T.: Landslides on coastal sage-scrub and grassland hillslopes in a severe El Niño winter: The effects of vegetation conversion on sediment delivery, Bull. Geol. Soc. Am., 114(8), 983–990, doi:10.1130/0016-7606(2002)114<0983:LOCSSA>2.0.CO;2, 2002.

Gabet, E. J. and Dunne, T.: Sediment detachment by rain power, Water Resour. Res., 39(1), ESG 1-1-ESG 1-12, doi:10.1029/2001wr000656, 2003.

Gabet, E. J. and Mudd, S. M.: Bedrock erosion by root fracture and tree throw: A coupled biogeomorphic model to explore the humped soil production function and the persistence of hillslope soils, J. Geophys. Res. Earth Surf., 115(4), 1–14, doi:10.1029/2009JF001526, 2010.

Gabet, E. J., Reichman, O. J. and Seabloom, E. W.: The Effects of Bioturbation on Soil Processes and Sediment Transport, Annu. Rev. Earth Planet. Sci., 31(1), 249–273, doi:10.1146/annurev.earth.31.100901.141314, 2003.

Garreaud, R. D. and Battisti, D. S.: Interannual (ENSO) and interdecadal (ENSO-like) variability in the Southern Hemisphere tropospheric circulation, J. Clim., 12(7), 2113–2123, doi:10.1175/1520-0442(1999)012<2113:IEAIEL>2.0.CO;2, 1999.

Garreaud, R. D., Vuille, M., Compagnucci, R. and Marengo, J.: Present-day South American climate, Palaeogeogr. Palaeoclimatol. Palaeoecol., 281(3–4), 180–195, doi:10.1016/j.palaeo.2007.10.032, 2009.

Garreaud, R. D., Alvarez-Garreton, C., Barichivich, J., Boisier, J. P., Christie, D., Galleguillos, M., LeQuesne, C., McPhee, J. and Zambrano-Bigiarini, M.: The 2010-2015 megadrought in central Chile: Impacts on regional hydroclimate and vegetation, Hydrol. Earth Syst. Sci., 21(12), 6307–6327, doi:10.5194/hess-21-6307-2017, 2017.

Garreaud, R. D., Boisier, J. P., Rondanelli, R., Montecinos, A., Sepúlveda, H. H. and Veloso-Aguila, D.: The Central Chile Mega Drought (2010–2018): A climate dynamics perspective, Int. J. Climatol., 40(1), 421–439, doi:10.1002/joc.6219, 2020.

Glodny, J., Graaefe Kirsten and Rosenau, M.: Mesozoic to Quaternary continental margin dynamics in South-Central Chile (36 – 42 ° S): the apatite and zircon fission track perspective, Int. J. Earth Sci., 97, 1271–1291, doi:10.1007/s00531-007-0203-1, 2008.

Godard, V., Lavé, J., Carcaillet, J., Cattin, R., Bourlès, D. and Zhu, J.: Spatial distribution of denudation in Eastern Tibet and regressive erosion of plateau margins, Tectonophysics, 491(1–4), 253–274, doi:10.1016/j.tecto.2009.10.026, 2010.

Godard, V., Bourlès, D. L., Spinabella, F., Burbank, D. W., Bookhagen, B., Fisher, G. B., Moulin, A. and Léanni, L.: Dominance of tectonics over climate in himalayan denudation, Geology, 42(3), 243–246, doi:10.1130/G35342.1, 2014.

Gonzalez, V. S., Schmidt, A. H., Bierman, P. R. and Rood, D. H.: Spatial and temporal replicability of meteoric and in situ 10Be concentrations in fluvial sediment, Earth Surf. Process. Landforms, 42(15), 2570–2584, doi:10.1002/esp.4205, 2017.

Gosse, J. C. and Phillips, F. M.: Terrestrial in situ cosmogenic nuclides:theory and application, Quat. Sci. Rev., 20, 1475–1560, doi:10.1016/S0277-3791(00)00171-2, 2001.

Granger, D., Kirchner, J. and Finkel, R.: Spatially averaged long-term erosion rates measured from in situ-produced cosmogenic nuclides in alluvial sediment, J. Geol., 104(3), 249–257, doi:10.1086/629823, 1996.

Granger, D. E. and Schaller, M.: Cosmogenic nuclides and erosion at the watershed scale, Elements, 10(5), 369–373, doi:10.2113/gselements.10.5.369, 2014.

Grömping, U.: R package relaimpo: relative importance for linear regression, J. Stat. Softw., 17(1), 139–147, doi:10.1016/j.foreco.2006.08.245, 2006.

Hales, T. C. and Roering, J. J.: Climatic controls on frost cracking and implications for the evolution of bedrock landscapes, J. Geophys. Res. Earth Surf., 112(2), 1–14, doi:10.1029/2006JF000616, 2007.

Harkins, N., Kirby, E., Heimsath, A., Robinson, R. and Reiser, U.: Transient fluvial incision in the headwaters of the Yellow River, northeastern Tibet, China, J. Geophys. Res. Earth Surf., 112(3), 1–21, doi:10.1029/2006JF000570, 2007.

Harrison, M.: Understanding and Visualizing and ENSO-Based Fire Climatology in Florida , USA : A Case Method Using Cluster Analysis, Southeast. Geogr., 53(4), 381–402, 2013.

Hartley, A. J. and Evenstar, L.: Cenozoic stratigraphic development in the north Chilean forearc: Implications for basin development and uplift history of the Central Andean margin, Tectonophysics, 495(1–2), 67–77, doi:10.1016/j.tecto.2009.05.013, 2010.

Hartley, A. J., May, G., Chong, G., Turner, P., Kape, S. J. and Jolley, E. J.: Development of a continental forearc: A Cenozoic example from the Central Andes, northern Chile, Geology, 28(4), 331–334, doi:10.1130/0091-7613(2000)028<0331:DOACFA>2.3.CO;2, 2000.

Hartley, A. J., Chong, G., Houston, J. and Mather, A. E.: 150 million years of climatic stability: Evidence from the Atacama Desert, northern Chile, J. Geol. Soc. London., 162(3), 421–424, doi:10.1144/0016-764904-071, 2005.

Hartmann, J. and Moosdorf, N.: The new global lithological map database GLiM: A representation of rock properties at the Earth surface, Geochemistry, Geophys. Geosystems, 13(12), 1–37, doi:10.1029/2012GC004370, 2012.

Heimsath, A. M., Fink, D. and Hancock, G. R.: The ' humped ' soil production function : eroding Arnhem Land , Australia, Earth Surf. Process. Landforms, 1684, 1674–1684, doi:10.1002/esp.1859, 2009.

Hervé, F., Munizaga, F., Parada, M. A., Brook, M., Pankhurst, R. J., Snelling, N. J. and Drake, R.: Granitoids of the Coast Range of central Chile: Geochronology and geologic setting, J. South Am. Earth Sci., 1(2), 185–194, doi:10.1016/0895-9811(88)90036-3, 1988.

Hervé, F., Faundez, V., Calderón, M., Massonne, H. J. and Willner A P: Metamorphic and plutonic basement complexes, in The Geology of Chile, edited by T. Moreno and W. Gibbons, pp. 5–19, The Geological Society, Barcelona., 2007.

Hirabayashi, Y., Mahendran, R., Koirala, S., Konoshima, L., Yamazaki, D., Watanabe, S., Kim, H. and Kanae, S.: Global flood risk under climate change, Nat. Clim. Chang., 3(9), 816–821, doi:10.1038/nclimate1911, 2013.

Hobouchian, M. P., Salio, P., García Skabar, Y., Vila, D. and Garreaud, R.: Assessment of satellite precipitation estimates over the slopes of the subtropical Andes, Atmos. Res., 190, 43–54, doi:10.1016/j.atmosres.2017.02.006, 2017.

Hoey, T. B. and Ferguson, R.: Numerical simulation of downstream fining by selective transport in gravel bed rivers: Model development and illustration, Water Resour., 30(7), 2251–2260, doi:https://doi.org/10.1029/94WR00556, 1994.

Horton, B. K.: Tectonic Regimes of the Central and Southern Andes: Responses to Variations in Plate Coupling During Subduction, Tectonics, 37(2), 402–429, doi:10.1002/2017TC004624, 2018.

Houston, J.: Variability of precipitation in the Atacama Desert: Its causes and hydrological impact, Int. J. Climatol., 26, 2181–2198, doi:10.1002/joc, 2006.

Hovius, N., Stark, C. P. and Allen, P. A.: Sediment flux from a mountain belt derived by landslide mapping, Geology, March(3), 231–234, doi:https://doi.org/10.1130/0091-7613(1997)025<0231:SFFAMB>2.3.CO;2, 1997.

Howard, A. D.: A detachment-limited model of drainage basin evolution, Water Resour. Res., 30(7), 2261–2285, doi:10.1029/94WR00757, 1994.

Huang, C., Gascuel-Odoux, C. and Cros-Cayot, S.: Hillslope topographic and hydrologic effects on overland flow and erosion, Catena, 46(2–3), 177–188, doi:10.1016/S0341-8162(01)00165-5, 2002.

Hulton, N. R. J., Purves, R. S., McCulloch, R. D., Sugden, D. E. and Bentley, M. J.: The Last Glacial Maximum and deglaciation in southern South America, Quat. Sci. Rev., 21(1–3), 233–241, doi:10.1016/S0277-3791(01)00103-2, 2002.

Iizumi, T., Luo, J., Challinor, A. J., Sakurai, G., Yokozawa, M., Sakuma, H., Brown, M. E. and Yamagata, T.: Impacts of El Niño Southern Oscillation on the global yields of major crops, Nat. Commun., 5(May), 1–7, doi:10.1038/ncomms4712, 2014.

Inman, D. L. and Jenkins, S. A.: Climate change and the episodicity of sediment flux of small California Rivers, J. Geol., 107(3), 251–270, doi:10.1086/314346, 1999.

IPCC, Field, C. B., Barros, V., Stocker, T. F., Qin, D., Dokken, D. J., Ebi, K. L., Mastrandrea, M. D., Mach, K. J., Plattner, G.-K., Allen, S. K., Tignor, M. and Midgley, P. M. (Eds. .: Managing the Risks of Extreme Events and Disasters to Advance Climate Change Adaptation., 2012.

Istanbulluoglu, E.: An eco-hydro-geomorphic perspective to modeling the role of climate in catchment evolution, Geogr. Compass, 3(3), 1151–1175, doi:10.1111/j.1749-8198.2009.00229.x, 2009.

Istanbulluoglu, E. and Bras, R. L.: Vegetation-modulated landscape evolution: Effects of vegetation on landscape processes, drainage density, and topography, J. Geophys. Res. Earth Surf., 110(2), 1–19, doi:10.1029/2004JF000249, 2005.

Istanbulluoglu, E., Tarboton, D. G., Pack, R. T. and Luce, C. H.: Modeling of the interactions between forest vegetation, disturbances, and sediment yields, J. Geophys. Res. Earth Surf., 109(F1), 1–22, doi:10.1029/2003jf000041, 2004.

Jaksic, F. M.: the Multiple Facets of El Niño/Southern Oscillation in Chile, Rev. Chil. Hist. Nat., 71(April), 121–131, 1998.

Jarvis, A., Reuter, H. I., Nelson, A. and Guevara, E.: Hole-filled SRTM for the globe Version 4, available from the CGIAR-CSI SRTM 90m Database, [online] Available from: http://srtm.csi.cgiar.org, 2008.

Jeffery, M. L., Yanites, B. J., Poulsen, C. J. and Ehlers, T. A.: Vegetation-precipitation controls on Central Andean topography, J. Geophys. Res. Earth Surf., 119(6), 1354–1375, doi:10.1002/2013JF002919, 2014.

Jenny, B., Valero-Garcés, B. L., Villa-Martínez, R., Urrutia, R., Geyh, M. and Veit, H.: Early to mid-Holocene aridity in central Chile and the southern Westerlies: The Laguna Aculeo record (34°S), Quat. Res., 58(2), 160–170, doi:10.1006/qres.2002.2370, 2002.

Jordan, T. E., Isacks, B. L., Allmendinger, R. W., Brewer, J. A., Ramos, V. A. and Ando, C. J.: Andean tectonics related to geometry of subducted Nazca plate., Geol. Soc. Am. Bull., 94(3), 341–361, doi:10.1130/0016-7606(1983)94<341:ATRTGO>2.0.CO;2, 1983.

Juez-Larré, J., Kukowski, N., Dunai, T. J., Hartley, A. J. and Andriessen, P. A. M.: Thermal and exhumation history of the Coastal Cordillera arc of northern Chile revealed by thermochronological dating, Tectonophysics, 495(1–2), 48–66, doi:10.1016/j.tecto.2010.06.018, 2010.

Julien, P. Y. and Simons, D. B.: Sediment Transport Capacity of Overland Flow, Am. Soc. Agric. Eng., 28(3), 755–762, 1985.

Juyal, N., Sundriyal, Y., rana, N., chaudhary, S. and Singhvi, A. k.: Late Quaternary fluvial aggradation and incision in the monsoon-dominated Alaknanda valley, Central Himalaya, Uttrakhand, India, J. Quat. Sci., 25(8), 1293–1304, doi:10.1002/jqs.1413, 2010.

Kemter, M., Merz, B., Marwan, N., Vorogushyn, S. and Blöschl, G.: Joint Trends in Flood Magnitudes and Spatial Extents Across Europe, Geophys. Res. Lett., 47(7), 1–8, doi:10.1029/2020GL087464, 2020.

Kiladis, G. N. and Diaz, H. F.: American Meteorological Society Global Climatic Anomalies Associated with Extremes in the Southern Oscillation Author (s): George N . Kiladis and Henry F . Diaz Published by : American Meteorological Society Stable URL : https://www.jstor.org/stable/261, J. Clim., 2(9), 1069–1090, 1989.

Kirby, E. and Ouimet, W.: Tectonic geomorphology along the eastern margin of Tibet: Insights into the pattern and processes of active deformation adjacent to the Sichuan Basin, Geol. Soc. Spec. Publ., 353, 165–188, doi:10.1144/SP353.9, 2011.

Kirby, E. and Whipple, K. X.: Expression of active tectonics in erosional landscapes, J. Struct. Geol., 44, 54–75, doi:10.1016/j.jsg.2012.07.009, 2012.

Kober, F., Ivy-Ochs, S., Zeilinger, G., Schlunegger, F., Kubik, P. W., Baur, H. and Wieler, R.: Complex multiple cosmogenic nuclide concentration and histories in the arid Rio Lluta catchment, northern Chile, Earth Surf. Process. Landforms, 34(3), 398–412, doi:10.1002/esp.1748, 2009.

Kodama, Y.: Previous Studies of Abrasion on Downstream Fining Purpose of This Study, J. Sediment. Res., A64(1), 68–75, 1994.

Kodoma, Y.: Experimental Study of Abrasion and Its Role in Producing Downstream Fining in Gravel-Bed Rivers, J. Sediment. Res., 64A(1), 76–85, 1994.

Kohl, C. P. and Nishiizumi, K.: Chemical isolation of quartz for measurement of in-situ -produced cosmogenic nuclides, Geochim. Cosmochim. Acta, 56(9), 3583–3587, doi:10.1016/0016-7037(92)90401-4, 1992.

Kolmogorov, A. .: Sulla determinazione empirica di una legge di distribuzione, G. dell'Instituto Ital. degli Attuari, 4, 83–91, 1933.

Köppen: Versuch einer Klassifikation der Klimate, vorzugsweise nach ihren Beziehungen zur Pflanzenwelt, Geogr. Zeitschrift, 6, 593–611, 1900.

Kottek, M., Grieser, J., Beck, C., Rudolf, B. and Rubel, F.: World map of the Köppen-Geiger climate classification updated, Meteorol. Zeitschrift, 15(3), 259–263, doi:10.1127/0941-2948/2006/0130, 2006.

Krumbein, W. C.: Size frequency distributions of sediments, J. Sediment. Petrol., 4, 65–77, 1934.

Krumbein, W. C.: Size frequency distributions of sediments and the normal phi curve, J. Sediment. Petrol., 8(84–90), 1938.

Kukowski, N. and Oncken, O.: Subduction Erosion — the "Normal" Mode of Fore-Arc Material Transfer along the Chilean Margin?, The Andes, (January), 217–236, doi:10.1007/978-3-540-48684-8_10, 2006.

Lague, D.: The stream power river incision model: evidence, theory and beyond, Earth Surf. Process. Landforms, 39(1), 38–61, doi:10.1002/esp.3462, 2013.

Lague, D., Hovius, N. and Davy, P.: Discharge, discharge variability, and the bedrock channel profile, J. Geophys. Res. Earth Surf., 110(4), 1–17, doi:10.1029/2004JF000259, 2005.

Lal, D.: Cosmic ray labeling of erosion surfaces : in situ nuclide production rates and erosion models, Earth Planet. Sci. Lett., 104, 424–439, 1991.

Larsen, I. J. and Montgomery, D. R.: Landslide erosion coupled to tectonics and river incision, Nat. Geosci., 5(7), 468–473, doi:10.1038/ngeo1479, 2012.

Larsen, I. J., Montgomery, D. R. and Greenberg, H. M.: The contribution of mountains to global denudation, Geology, 42(6), 527–530, doi:10.1130/G35136.1, 2014.

Lasaga, A. C., Soler, J. M., Ganor, J., Burch, T. E. and Nagy, K. L.: Chemical weathering rate laws and global geochemical cycles, Geochim. Cosmochim. Acta, 58(10), 2361–2386, doi:10.1016/0016-7037(94)90016-7, 1994.

Lebedeva, M. I. and Brantley, S. L.: Weathering and erosion of fractured bedrock systems, Earth Surf. Process. Landforms, 42(13), 2090–2108, doi:10.1002/esp.4177, 2017.

Lee, D., Ward, P. J. and Block, P.: Identification of symmetric and asymmetric responses in seasonal streamflow globally to ENSO phase, Environ. Res. Lett., 13(4), doi:10.1088/1748-9326/aab4ca, 2018.

Leonard, J. S. and Whipple, K. X.: Influence of Spatial Rainfall Gradients on River Longitudinal Profiles and the Topographic Expression of Spatio-temporally Variable Climate in Mountain Landscapes, J. Geophys. Res. Earth Surf., 1–46, doi:https://doi.org/10.1002/essoar.10506651.1, in Review.

Leopold, L. B. and Maddock, T.: The Hydraulic Geometry of Stream Channels and Some Physiographic Implications, U.S. Government Printing Office, Washington., 1953.

Lewin, J. and Brewer, P. A.: Laboratory Simulation of Clast Abrasion, Earth Surf. Process. Landforms, 27, 145–164, doi:10.1177/0022034509333968, 2002.

Lin, G. W., Chen, H., Chen, Y. H. and Horng, M. J.: Influence of typhoons and earthquakes on rainfall-induced landslides and suspended sediments discharge, Eng. Geol., 97(1–2), 32–41, doi:10.1016/j.enggeo.2007.12.001, 2008.

Lindeman, R. H., Merenda, P. F. and Gold, R. Z.: Introduction to Bivariate and Multivariate Analysis, Glenview, 1(144), 1980.

Lukens, C. E., Riebe, C. S., Sklar, L. S. and Shuster, D. L.: Grain size bias in cosmogenic nuclide studies of stream sediment in steep terrain, J. Geophys. Res. Earth Surf., 121, 978–999, doi:10.1002/2016JF003859.Received, 2016.

Lupker, M., Lavé, J., France-Lanord, C., Christl, M., Bourlès, D. L., Carcaillet, J., Maden, C., Wieler, R., Rahman, M., Bezbaruah, D. and Xiaohan, L.: 10Be systematics in the Tsangpo-Brahmaputra catchment: the cosmogenic nuclide legacy of the eastern Himalayan syntaxis, Earth Surf. Dyn., 9(2), 429–449, 2017.

Maher, K.: The dependence of chemical weathering rates on fluid residence time, Earth Planet. Sci. Lett., 294(1–2), 101–110, doi:10.1016/j.epsl.2010.03.010, 2010.

Malamud, B. D. and Turcotte, D. L.: The applicability of power-law frequency statistics to floods, J. Hydrol., 322(1–4), 168–180, doi:10.1016/j.jhydrol.2005.02.032, 2006.

Mandal, S. K., Lupker, M., Burg, J.-P., Valla, P. ., Haghipour, N. and Christl, M.: Spatial variability of 10Be-derived erosion rates across the southern Peninsular Indian escarpment: A key to landscape evolution across passive margins, Earth Planet. Sci. Lett., 425, 154–167, 2015.

Mardones, P. and Garreaud, R. D.: Future changes in the free tropospheric freezing level and rain–snow limit: The case of central Chile, Atmosphere (Basel)., 11(11), 1–16, doi:10.3390/atmos11111259, 2020.

Masiokas, M. H., Villalba, R., Luckman, B. H., Le Quesne, C. and Aravena, J. C.: Snowpack variations in the central Andes of Argentina and Chile, 1951-2005: Large-scale atmospheric influences and implications for water resources in the region, J. Clim., 19(24), 6334–6352, doi:10.1175/JCLI3969.1, 2006.

Mason, S. J. and Goddard, L.: Probabilistic precipitation anomalies associated with ENSO, Bull. Am. Meteorol. Soc., 82(4), 619–638, 1994.

Mather, A. E., Hartley, A. J. and Griffiths, J. S.: The giant coastal landslides of Northern Chile: Tectonic and climate interactions on a classic convergent plate margin, Earth Planet. Sci. Lett., 388, 249–256, doi:10.1016/j.epsl.2013.10.019, 2014.

Matmon, A., Bierman, P. R., Larsen, J., Southworth, S., Pavich, M., Finkel, R. and Caffee, M.: Erosion of an ancient mountain range, the Great Smoky Mountains, North Carolina and Tennessee, Am. J. Sci., 303(9), 817–855, doi:10.2475/ajs.303.9.817, 2003.

Matsuoka, N.: Frost weathering and rockwall erosion in the southeastern Swiss Alps : Long-term (1994 – 2006) observations, Geomorphology, 99, 353–368, doi:10.1016/j.geomorph.2007.11.013, 2008.

McCarroll, D.: The Schmidt hammer, weathering and rock surface roughness, Earth Surf. Process. Landforms, 16, 477–480, 1991.

McFadden, L. D., Eppes, M. C., Gillespie, A. R. and Hallet, B.: Physical weathering in arid landscapes due to diurnal variation in the direction of solar heating, Bull. Geol. Soc. Am., 117(1–2), 161–173, doi:10.1130/B25508.1, 2005.

McPhaden, M. J., Zebiak, S. E. and Glantz, M. H.: ENSO as an Integrating Concept in Earth Science, Science (80-.)., 314(5806), 1740–1745, doi:10.1126/science.1132588, 2006.

Melnick, D.: Rise of the central Andean coast by earthquakes straddling the Moho, Nat. Geosci., (March), 1–8, doi:10.1038/ngeo2683, 2016.

Melnick, D. and Echtler, H. P.: Morphotectonic and Geologic Digital Map Compilations of the South-Central Andes (36°–42°S), The Andes, 565–568, doi:10.1007/978-3-540-48684-8_30, 2006.

Melnick, D., Bookhagen, B., Strecker, M. R. and Echtler, H. P.: Segmentation of megathrust rupture zones from fore-arc deformation patterns over hundreds to millions of years, Arauco peninsula, Chile, J. Geophys. Res. Solid Earth, 114(1), 1–23, doi:10.1029/2008JB005788, 2009.

Meyer-Christoffer, A., Becker, A., Finger, P., Rudolf, B., Schneider, U. and Ziese, M.: GPCC Climatology Version 2015 at 0.25°: Monthly Land-Surface Precipitation Climatology for Every Month and the Total Year from Rain-Gauges built on GTS-based and Historic Data., 2015.

Meza, F. J.: Variability of reference evapotranspiration and water demands. Association to ENSO in the Maipo river basin, Chile, Glob. Planet. Change, 47(2-4 SPEC. ISS.), 212–220, doi:10.1016/j.gloplacha.2004.10.013, 2005.

Meza, F. J.: Recent trends and ENSO influence on droughts in Northern Chile: An application of the Standardized Precipitation Evapotranspiration Index, Weather Clim. Extrem., 1, 51–58, doi:10.1016/j.wace.2013.07.002, 2013.

Milana, J. P.: Predicción de caudales de ríos alimentados por deshielo mediante balances de energía: Aplicación en los Andes Centrales, Argentina., Rev. Asoc. Arg. Sedimentol., 5(2), 53–69, 1998.

Miller, A.: The climate of Chile, edited by W. Schwerdtgefer, Clim. Cent. South Am., 12, 113–145, 1976.

Miller, S. R., Sak, P. B., Kirby, E. and Bierman, P. R.: Bumps in the long road to flat, in American Geophysical Union, Fall Meeting, pp. EP41D-0653., 2011.

Miller, S. R., Miller, S. R., Sak, P. B., Kirby, E. and Bierman, P. R.: Neogene rejuvenation of Central Appalachian topography : Evidence for differential rock uplift from stream profiles and erosion rates Neogene rejuvenation of central Appalachian topography : Evidence for differential rock uplift from stream pro fi les and, Earth Planet. Sci. Lett., 369–370(October), 1–12, doi:10.1016/j.epsl.2013.04.007, 2016.

Molnar, P.: Climate change, flooding in arid environments, and erosion rates, Geology, 29(12), 1071–1074, doi:10.1130/0091-7613(2001)029<1071:CCFIAE>2.0.CO, 2001.

Molnar, P., Anderson, R. S., Kier, G. and Rose, J.: Relationships among probability distributions of stream discharges in floods, climate, bed load transport, and river incision, J. Geophys. Res., 111(F02001), 1–10, doi:10.1029/2005JF000310, 2006.

Montecinos, A. and Aceituno, P.: Seasonality of the ENSO-related rainfall variability in central Chile and associated circulation anomalies, J. Clim., 16(2), 281–296, doi:10.1175/1520-0442(2003)016<0281:SOTERR>2.0.CO;2, 2003.

Montecinos, A., Díaz, A. and Aceituno, P.: Seasonal diagnostic and predictability of rainfall in subtropical South America based on tropical Pacific SST, J. Clim., 13(4), 746–758, doi:10.1175/1520-0442(2000)013<0746:SDAPOR>2.0.CO;2, 2000.

Montgomery, D. R. and Brandon, M. T.: Topographic controls on erosion rates in tectonically active mountain ranges, Earth Planet. Sci. Lett., 201(3–4), 481–489, doi:10.1016/S0012-821X(02)00725-2, 2002.

Montgomery, D. R. and Gran, K. B.: Downstream variations in the width of bedrock channels, Water Resour., 37(6), 1841–1846, 2001.

Morera, S. B., Condom, T., Crave, A., Steer, P. and Guyot, J. L.: The impact of extreme El Niño events on modern sediment transport along the western Peruvian Andes (1968–2012), Sci. Rep., 7(September), 1–14, doi:10.1038/s41598-017-12220-x, 2017.

Mosley, M. P.: Regional differences in the effects of El Niño and La Niña on low flows and floods, Hydrol. Sci. J., 45(2), 249–267, doi:10.1080/02626660009492323, 2000.

Muñoz Sabater, J.: ERA5-Land monthly averaged data from 1981 to present, Copernicus Clim. Chang. Serv. Clim. Data Store, doi:10.24381/cds.68d2bb3, 2019.

Mutz, S. G. and Ehlers, T. A.: Detection and explanation of spatiotemporal patterns in Late Cenozoic palaeoclimate change relevant to Earth surface processes, Earth Surf. Dyn., 7(3), 663–679, doi:10.5194/esurf-7-663-2019, 2019.

Mutz, S. G., Ehlers, T. A., Werner, M., Lohmann, G., Stepanek, C. and Li, J.: Estimates of late Cenozoic climate change relevant to Earth surface processes in tectonically active orogens, Earth Surf. Dyn., 6(2), 271–301, doi:10.5194/esurf-6-271-2018, 2018.

Neilson, T. B., Schmidt, A. H., Bierman, P. R., Rood, D. H. and Sosa Gonzalez, V.: Efficacy of in situ and meteoric 10Be mixing in fluvial sediment collected from small catchments in China, Chem. Geol., 471(September), 119–130, doi:10.1016/j.chemgeo.2017.09.024, 2017.

Niemi, N. A., Oskin, M., Burbank, D. W., Heimsath, A. M. and Gabet, E. J.: Effects of bedrock landslides on cosmogenically determined erosion rates, Earth Planet. Sci. Lett., 237(3–4), 480–498, doi:10.1016/j.epsl.2005.07.009, 2005.

Oberlander, T. M.: Morphogenesis of Granitic Boulder Slopes in the Mojave Desert, California, J. Geol., 80(1), 1–20, 1972.

Oertel, M., Meza, F. J. and Gironás, J.: Observed trends and relationships between ENSO and standardized hydrometeorological drought indices in central Chile, Hydrol. Process., 34(2), 159–174, doi:10.1002/hyp.13596, 2020.

Oeser, R. and von Blanckenburg, F.: Decoupling silicate weathering from primary productivity – how ecosystems regulate nutrient uptake along a climate and vegetation gradient, Biogeosciences Discuss., (March), 1–43, doi:10.5194/bg-2020-69, 2020.

Oeser, R. A., Stroncik, N., Moskwa, L., Bernhard, N., Schaller, M., Canessa, R., Brink, L. Van Den, Köster, M., Brucker, E., Stock, S., Pablo, J., Godoy, R., Javier, F., Oses, R., Osses, P., Paulino, L., Seguel, O., Bader, M. Y., Boy, J., Dippold, M. A., Ehlers, T. A., Kühn, P., Kuzyakov, Y., Leinweber, P., Scholten, T., Spielvogel, S., Spohn, M., Übernickel, K., Tielbörger, K., Wagner, D. and Blanckenburg, F. Von: Chemistry and microbiology of the Critical Zone along a steep climate and vegetation gradient in the Chilean Coastal Cordillera, Catena, 170(April), 183–203, doi:10.1016/j.catena.2018.06.002, 2018.

Ortlieb, L.: Major historical rainfalls in central chile and the chronology of ENSO events during the 16th–19th-centuries, Revisita Chil. Hist. Nat., 67, 463–485, 1994.

Ouimet, W. B., Whipple, K. X. and Granger, D. E.: Beyond threshold hillslopes: Channel adjustment to base-level fall in tectonically active mountain ranges, Geology, 37(7), 579–582, doi:10.1130/G30013A.1, 2009.

Owen, J. J., Amundson, R., Dietrich, W. E., Nishiizumi, K., Sutter, B. and Chong, G.: The sensitivity of hillslope bedrock erosion to precipitation, Earth Surf. Process. Landforms, 36(1), 117–135, doi:10.1002/esp.2083, 2011.

Palumbo, L., Hetzel, R., Tao, M. and Li, X.: Catchment-wide denudation rates at the margin of NE Tibet from in situ-produced cosmogenic 10Be, Terra Nov., 23(1), 42–48, doi:10.1111/j.1365-3121.2010.00982.x, 2009.

Parada, M. A., Rivano, S., Sepulveda, P., Herve, M., Herve, F., Puig, A., Munizaga, F., Brook, M., Pankhurst, R. and Snelling, N.: Mesozoic and cenozoic plutonic development in the Andes of central Chile (30°30'-32°30'S), J. South Am. Earth Sci., 1(3), 249–260, doi:10.1016/0895-9811(88)90003-X, 1988.

De Perez, E. C., Stephens, E., Bischiniotis, K., Van Aalst, M., Van Den Hurk, B., Mason, S., Nissan, H. and Pappenberger, F.: Should seasonal rainfall forecasts be used for flood preparedness?, Hydrol. Earth Syst. Sci., 21(9), 4517–4524, doi:10.5194/hess-21-4517-2017, 2017.

Perras, M. A. and Diederichs, M. S.: A Review of the Tensile Strength of Rock: Concepts and Testing, Geotech. Geol. Eng., 32(2), 525–546, doi:10.1007/s10706-014-9732-0, 2014.

Perron, J. T.: Climate and the Pace of Erosional Landscape Evolution, Annu. Rev. Earth Planet. Sci., 45, 561–591, doi:https://doi.org/10.1146/annurev-earth-060614- 105405, 2017.

Phillips, F. M., Argento, D. C., Balco, G., Caffee, M. W., Clem, J., Dunai, T. J., Finkel, R., Goehring, B., Gosse, J. C., Hudson, A. M., Jull, A. J. T., Kelly, M. A., Kurz, M., Lal, D., Lifton, N., Marrero, S. M., Nishiizumi, K., Reedy, R. C., Schaefer, J., Stone, J. O. H., Swanson, T. and Zreda, M. G.: The CRONUS-Earth Project: A synthesis, Quat. Geochronol., 31, 119–154, doi:10.1016/j.quageo.2015.09.006, 2016.

Piechota, T. C., Dracup, J. A., Brown, E. F., McMahon, T. and Chiew, F.: South American Streamflow and the Extreme Phases of the Southern Oscillation, in Proceedings of the Eleventh Annual Pacific Climate (PACLIM) Worskhop, edited by C. M. Isaacs and V. L. Tharp, pp. 85–92, California Department of Water Resources., 1995.

Pinto, L., Hérail, G., Sepúlveda, S. A. and Krop, P.: A Neogene giant landslide in Tarapacá, northern Chile: A signal of instability of the westernmost Altiplano and palaeoseismicity effects, Geomorphology, 102(3–4), 532–541, doi:10.1016/j.geomorph.2008.05.044, 2008.

Pizarro, R., Valdés, R., García-Chevesich, P., Vallejos, C., Sangüesa, C., Morales, C., Balocchi, F., Abarza, A. and Fuentes, R.: Latitudinal analysis of rainfall intensity and mean annual precipitation in Chile, Chil. J. Agric. Res., 72(2), 252–261, doi:10.4067/s0718-58392012000200014, 2012.

Placzek, C. J., Matmon, A., Granger, D. E., Quade, J. and Niedermann, S.: Evidence for active landscape evolution in the hyperarid Atacama from multiple terrestrial cosmogenic nuclides, Earth Planet. Sci. Lett., 295(1–2), 12–20, doi:10.1016/j.epsl.2010.03.006, 2010.

Portenga, E. W. and Bierman, P. R.: Understanding earth's eroding surface with 10Be, GSA Today, 21(8), 4–10, doi:10.1130/G111A.1, 2011.

Post, D. A. and Jakeman, A. J.: Relationships between catchment attributes and hydrological response characteristics in small Australian mountain ash catchments, Hydrol. Process., 10(6), 877–892, doi:10.1002/(SICI)1099-1085(199606)10:6<877::AID-HYP377>3.0.CO;2-T, 1996.

Poveda, G., Álvarez, D. M. and Rueda, Ó. A.: Hydro-climatic variability over the Andes of Colombia associated with ENSO: A review of climatic processes and their impact on one of the Earth's most important biodiversity hotspots, Clim. Dyn., 36(11–12), 2233–2249, doi:10.1007/s00382-010-0931-y, 2011.

Poveda, G., Espinoza, J. C., Zuluaga, M. D., Solman, S. A., Garreaud, R. and van Oevelen, P. J.: High Impact Weather Events in the Andes, Front. Earth Sci., 8(May), 1–32, doi:10.3389/feart.2020.00162, 2020.

Puchol, N., Lavé, J., Lupker, M., Blard, P. H., Gallo, F. and France-Lanord, C.: Grain-size dependent concentration of cosmogenic 10Be and erosion dynamics in a landslide-dominated Himalayan watershed, Geomorphology, 224(November), 55–68, doi:10.1016/j.geomorph.2014.06.019, 2014.

Raup, B., Racoviteanu, A., Khalsa, S. J. S., Helm, C., Armstrong, R. and Arnaud, Y.: The GLIMS geospatial glacier database: A new tool for studying glacier change, Glob. Planet. Change, 56(1–2), 101–110, doi:10.1016/j.gloplacha.2006.07.018, 2007.

Reinhardt, L. J., Hoey, T. B., Barrows, T. T., Dempster, T. J., Bishop, P. and Fifield, L. K.: Interpreting erosion rates from cosmogenic radionuclide concentrations measured in rapidly eroding terrain, Earth Surf. Process. Landforms, 32, 390–406, doi:10.1002/esp.1415, 2007.

Riebe, C. S., Kirchner, J. W., Granger, D. E. and Finkel, R. C.: Minimal climatic control on erosion rates in the Sierra Nevada, California, Geology, 29(5), 447–450, doi:10.1130/0091-7613(2001)029<0447:mccoer>2.0.co;2, 2001.

Riebe, C. S., Kirchner, J. W. and Finkel, R. C.: Long-term rates of chemical weathering and physical erosion from cosmogenic nuclides and geochemical mass balance, Geochim. Cosmochim. Acta, 67(22), 4411–4427, doi:10.1016/S0016-7037(03)00382-X, 2003.

Riebe, C. S., Kirchner, J. W. and Finkel, R. C.: Erosional and climatic effects on long-term chemical weathering rates in granitic landscapes spanning diverse climate regimes, Earth Planet. Sci. Lett., 224(3–4), 547–562, doi:10.1016/j.epsl.2004.05.019, 2004.

Riebe, C. S., Sklar, L. S., Lukens, C. E. and Shuster, D. L.: Climate and topography control the size and flux of sediment produced on steep mountain slopes, Proc. Natl. Acad. Sci., (November), 201503567, doi:10.1073/pnas.1503567112, 2015.

Roda-Boluda, D. C., D'Arcy, M., McDonald, J. and Whittaker, A. C.: Lithological controls on hillslope sediment supply: insights from landslide activity and grain size distributions, Earth Surf. Process. Landforms, 43(5), 956–977, doi:10.1002/esp.4281, 2018.

Roering, J. J., Kirchner, J. W. and Dietrich, W. E.: Evidence for nonlinear, diffusive sediment transport on hillslopes and implications for landscape morphology, Water Resour. Res., 35(3), 853–870, doi:10.1029/1998WR900090, 1999.

Roering, J. J., Marshall, J., Booth, A. M., Mort, M. and Jin, Q.: Evidence for biotic controls on topography and soil production, Earth Planet. Sci. Lett., 298(1–2), 183–190, doi:10.1016/j.epsl.2010.07.040, 2010.

Rollins, H. B., Richardson, J. B. and Sandweiss, D. H.: The birth of El Niño: Geoarchaeological evidence and implications, Geoarchaeology, 1(1), 3–15, doi:10.1002/gea.3340010102, 1986.

Ropelewski, C. F. and Halpert, M. S.: Global and regional scale precipitation patterns associated with the El Niño/Southern Oscillation, Mon. Weather Rev., 115(8), 1606–1626, doi:10.1175/1520-0493(1987)115<1606:garspp>2.0.co;2, 1987.

Rossi, M., Whipple, K. X. and Vivoni, R.: Precipitation and evapotranspiration controls on daily runoff variability in the contiguous United States and Puerto Rico, J. Geophys. Res. Earth Surf., 121, 128–145, doi:10.1002/2014JF003270.Received, 2016.

Rubio-Álvarez, E. and McPhee, J.: Patterns of spatial and temporal variability in streamflow records in south central Chile in the period 1952-2003, Water Resour. Res., 46(5), 1–16, doi:10.1029/2009WR007982, 2010.

Rust, W., Cuthbert, M., Bloomfield, J., Corstanje, R., Howden, N. and Holman, I.: Exploring the role of hydrological pathways in modulating North Atlantic Oscillation (NAO) teleconnection periodicities from UK rainfall to streamflow, Hydrol. Earth Syst. Sci. Discuss., (July), 1–37, doi:10.5194/hess-2020-312, 2020.

Rutland, R. W. R.: Andean orogeny and ocean floor spreading, Nature, 233(5317), 252–255, doi:10.1038/233252a0, 1971.

Rutllant, J. and Fuenzalida, H.: Synoptic aspects of the central chile rainfall variability associated with the southern oscillation, Int. J. Climatol., 11(1), 63–76, doi:10.1002/joc.3370110105, 1991.

Rutllant, J. A., Fuenzalida, H. and Aceituno, P.: Climate dynamics along the arid northern coast of Chile: The 1997-1998 Dinámica del Clima de la Región de Antofagasta (DICLIMA) experiment, J. Geophys. Res. Atmos., 108(17), 1–13, doi:10.1029/2002jd003357, 2003.

Ruxton, B. P. and Berry, L.: Weathering of granite and associated erosional features in Hong Kong, Bull. Geol. Soc. Am., 68(10), 1263–1292, doi:10.1130/0016-7606(1957)68[1263:WOGAAE]2.0.CO;2, 1957.

Safran, E. B., Bierman, P. R., Aalto, R., Dunne, T., Whipple, K. X. and Caffee, M.: Erosion rates driven by channel network incision in the Bolivian Andes, Earth Surf. Process. Landforms, 30(8), 1007–1024, doi:10.1002/esp.1259, 2005.

Salas, H. D., Poveda, G., Mesa, Ó. J. and Marwan, N.: Generalized synchronization between ENSO and hydrological variables in Colombia: A recurrence quantification approach, Front. Appl. Math. Stat., 6(March), 1–20, doi:10.3389/fams.2020.00003, 2020.

Schaller, M., Ehlers, T. A., Lang, K. A. H., Schmid, M. and Fuentes-Espoz, J. P.: Addressing the contribution of climate and vegetation cover on hillslope denudation, Chilean Coastal Cordillera (26°–38°S), Earth Planet. Sci. Lett., 489, 111–122, doi:10.1016/j.epsl.2018.02.026, 2018.

Scherler, D., Bookhagen, B. and Strecker, M. R.: Tectonic control on 10 Be-derived erosion rates in the Garhwal Himalaya, India, J. Geophys. Res. Earth Surf., 119(February), 83–105, doi:10.1002/2013JF002955, 2014.

Scherler, D., Lamb, M. P., Rhodes, E. J. and Avouac, J. P.: Climate-change versus landslide origin of fill terraces in a rapidly eroding bedrock landscape: San Gabriel River, California, Bull. Geol. Soc. Am., 128(7), 1228–1248, doi:10.1130/B31356.1, 2016.

Scherler, D., DiBiase, R. A., Fisher, G. B. and Avouac, J. P.: Testing monsoonal controls on bedrock river incision in the Himalaya and Eastern Tibet with a stochastic-threshold stream power model, J. Geophys. Res. Earth Surf., 122(7), 1389–1429, doi:10.1002/2016JF004011, 2017.

Scheuber, E., Bogdanic, T., Jensen, A. and Reuttner, K. J.: Tectonic Development of the North Chilean Andes in Relation to Plate Convergence and Magmatism Since the Jurassic, in Tectonics of the Southern Central Andes. Structure and Evolution of an Active Continental Margin, edited by K. J. Reutter, E. Scheuber, and P. J. Wigger, pp. 121–139, Springer-Verlag, Berlin Heidelbarg., 1994.

Schlaepfer, D. R., Bradford, J. B., Lauenroth, W. K., Munson, S. M., Tietjen, B., Hall, S. A., Wilson, S. D., Duniway, M. C., Jia, G., Pyke, D. A., Lkhagva, A. and Jamiyansharav, K.: Climate change reduces extent of temperate drylands and intensifies drought in deep soils, Nat. Commun., 8, doi:10.1038/ncomms14196, 2017.

Schmid, M., Ehlers, T. A. and Hickler, T.: Effect of changing vegetation on denudation (part 2): Landscape response to transient climate and vegetation cover, , (February), 1–36, 2018.

Schneider, W., Donoso, D., Garcés-Vargas, J. and Escribano, R.: Water-column cooling and sea surface salinity increase in the upwelling region off central-south Chile driven by a poleward displacement of the South Pacific High, Prog. Oceanogr., 151, 38–48, doi:10.1016/j.pocean.2016.11.004, 2017.

Schwanghart, W. and Scherler, D.: Short Communication: TopoToolbox 2 – MATLAB-based software for topographic analysis and modeling in Earth surface sciences, Earth Surf. Dynam., 2(1), 1–7, doi:10.5194/esurf-2-1-2014, 2014.

SERNAGEOMIN: Mapa Geológico de Chile: versión digital, Serv. Nac. Geol. y Minería, Publicación Geológica Digit., 1–25, 2003.

Shobe, C. M., Hancock, G. S., Eppes, M. C. and Small, E. E.: Field evidence for the influence of weathering on rock erodibility and channel form in bedrock rivers, Earth Surf. Process. Landforms, 42(13), 1997–2012, doi:10.1002/esp.4163, 2017.

Sklar, L. S. and Dietrich, W. E.: River longitudinal profiles and bedrock incision models, Fluv. Process. Bedrock Channels, 107, 237–260, 1998.

Sklar, L. S. and Dietrich, W. E.: Sediment and rock strength controls on river incision into bedrock, Geology, 29(12), 1087–1090, doi:10.1130/0091-7613(2001)029<1087:SARSCO>2.0.CO, 2001.

Sklar, L. S. and Dietrich, W. E.: A mechanistic model for river incision into bedrock by saltating bed load, Water Resour. Res., 40, 1–22, doi:10.1029/2003WR002496, 2004.

Sklar, L. S. and Dietrich, W. E.: Implications of the Saltation-Abrasion Bedrock Incision Model for Steady-State River Longitudinal Profile Relief and Concavity, Earth Surf. Process. Landforms, 33(7), 1129–1151, doi:10.1002/esp, 2008.

Sklar, L. S., Dietrich, W. E., Foufoula-Georgiou, E., Lashermes, B. and Bellugi, D.: Do gravel bed river size distributions record channel network structure?, Water Resour. Res., 42(SUPPL.), 1–22, doi:10.1029/2006WR005035, 2006.

Sklar, L. S., Riebe, C. S., Marshall, J. A., Genetti, J., Leclere, S., Lukens, C. L. and Merces, V.: The problem of predicting the size distribution of sediment supplied by hillslopes to rivers, Geomorphology, 277, 31–49, doi:10.1016/j.geomorph.2016.05.005, 2017.

Smirnov, N. V.: On the estimation of the discrepancy between empirical curves of distribution for two independent samples, Bull. Math. Univ. Moscou, 2(2), 3–16, 1939.

Snyder, N. P., Whipple, K. X., Tucker, G. E. and Merritts, D. J.: Interactions between onshore bedrock-channel incision and nearshore wave-base erosion forced by eustasy and tectonics, Basin Res., 14(2), 105–127, doi:10.1046/j.1365-2117.2002.00169.x, 2002.

Snyder, N. P., Whipple, K. X., Tucker, G. E. and Merritts, D. J.: Importance of a stochastic distribution of floods and erosion thresholds in the bedrock river incision problem, J. Geophys. Res., 108(B2), 2117, doi:10.1029/2001JB001655, 2003.

Sosa Gonzalez, V., Bierman, P. R., Fernandes, N. F. and Rood, D. H.: Long-term background denudation rates of southern and southeastern Brazilian watersheds estimated with cosmogenic 10Be, Geomorphology, 268, 54–63, 2016a.

Sosa Gonzalez, V., Bierman, P. R., Nichols, K. K. and Rood, D. H.: Long-term erosion rates of Panamanian drainage basins determined using in situ 10Be, Geomorphol. Tech., 275, 1–15, 2016b.

Starke, J., Ehlers, T. A. and Schaller, M.: Tectonic and Climatic Controls on the Spatial Distribution of Denudation Rates in Northern Chile (18°S to 23°S) Determined From Cosmogenic Nuclides, J. Geophys. Res. Earth Surf., 122(10), 1949–1971, doi:10.1002/2016JF004153, 2017.

Starke, J., Ehlers, T. A. and Schaller, M.: Latitudinal effect of vegetation on erosion rates identified along western South America, Science (80-.)., 367(March), 1358–1361, 2020.

Stephens, E., Day, J. J., Pappenberger, F. and Cloke, H.: Precipitation and floodiness, Geophys. Res. Lett., 42(23), 10316–10323, doi:10.1002/2015GL066779, 2015.

Stevenson, S. L.: Significant changes to ENSO strength and impacts in the twenty-first century: Results from CMIP5, Geophys. Res. Lett., 39(17), 1–5, doi:10.1029/2012GL052759, 2012.

Stock, G. M., Frankel, K. L., Ehlers, T. a., Schaller, M., Briggs, S. M. and Finkel, R. C.: Spatial and temporal variations in denudation of the Wasatch Mountains, Utah, USA, Lithosphere, 1, 34–40, doi:10.1130/L15.1, 2009.

Stone, J. O.: Air pressure and cosmogenic isotope production, J. Geophys. Res., 105(1), 753–759, doi:10.1029/2000JB900181, 2000.

Streckeisen, A. and Le Maitre, R. W.: A chemical approximation to the modal QAPF classification of the igneous rocks, Neues Jahrb. für Mineral., 136(2), 169–206, 1979.

Sullivan, C. L.: 10Be Erosion Rates and Landscape Evolution of the Blue Ridge Escarpment, Southern Appalachian Mountains, 2007.

Terweh, S., Hassan, M. A., Mao, L., Schrott, L. and Hoffmann, T. O.: Bio-climate affects hillslope and fluvial sediment grain size along the Chilean Coastal Cordillera, Geomorphology, 384, 107700, doi:10.1016/j.geomorph.2021.107700, 2021.

Tofelde, S., Duesing, W., Schildgen, T. F., Wickert, A. D., Wittmann, H., Alonso, R. N. and Strecker, M.: Effects of deep-seated versus shallow hillslope processes on cosmogenic10Be concentrations in fluvial sand and gravel, Earth Surf. Process. Landforms, 43(15), 3086–3098, doi:10.1002/esp.4471, 2018.

Tolorza, V.: Magnitud y dinámica de la erosión integrade de cuenca en el Río Biobío, Universidad de Chile., 2015.

Tolorza, V., Carretier, S., Andermann, C., Ortega-Culaciati, F., Pinto, L. and Mardones, M.: Contrasting mountain and piedmont dynamics of sediment discharge associated with groundwater storage variation in the Biob??o River, J. Geophys. Res. F Earth Surf., 119(12), 2730–2753, doi:10.1002/2014JF003105, 2014.

Tsou, C. Y., Feng, Z. Y. and Chigira, M.: Catastrophic landslide induced by Typhoon Morakot, Shiaolin, Taiwan, Geomorphology, 127(3–4), 166–178, doi:10.1016/j.geomorph.2010.12.013, 2011.

Tucker, G. E.: Drainage basin sensitivity to tectonic and climatic forcing: implications of a stochastic model for the role of entrainment and erosion thresholds, Earth Surf. Process. Landforms, 29(2), 185–205, doi:10.1002/esp.1020, 2004.

Tucker, G. E. and Bras, R. L.: A stochastic approach to modeling the role of rainfall variability in drainage basin evolution, Water Resour. Res., 36(7), 1953–1964, doi:10.1029/2000wr900065, 2000.

Turcotte, D. L. and Greene, L.: A scale-invariant approach to flood-frequency analysis, Stoch. Hydrol. Hydraul., 7(1), 33–40, doi:10.1007/BF01581565, 1993.

Turowski, J. M.: Stochastic modeling of the cover effect and bedrock erosion, Water Resour. Res., 45(3), 1–13, doi:10.1029/2008WR007262, 2009.

Turowski, J. M., Lague, D. and Hovius, N.: Cover effect in bedrock abrasion: A new derivation and its implications for the modeling of bedrock channel morphology, J. Geophys. Res. Earth Surf., 112(4), 1–16, doi:10.1029/2006JF000697, 2007.

Valdés-Pineda, R., Pizarro, R., García-Chevesich, P., Valdés, J. B., Olivares, C., Vera, M., Balocchi, F., Pérez, F., Vallejos, C., Fuentes, R., Abarza, A. and Helwig, B.: Water governance in Chile: Availability, management and climate change, J. Hydrol., 519(PC), 2538–2567, doi:10.1016/j.jhydrol.2014.04.016, 2014.

Valdés-Pineda, R., Pizarro, R., Valdés, J. B., Carrasco, J. F., García-Chevesich, P. and Olivares, C.: Spatio-temporal trends of precipitation, its aggressiveness and concentration, along the Pacific coast of South America (36–49°S), Hydrol. Sci. J., 61(11), 2110–2132, doi:10.1080/02626667.2015.1085989, 2016.

Vargas, G., Ortlieb, L. and Rutllant, J.: Historic mudflows in Antofagasta, Chile, and their relationship to the El Niño/southern oscillation events, Rev. Geol. Chile, 27(2), 157–176, 2000.

Vargas, G., Rutllant, J. and Ortlieb, L.: ENSO tropical-extratropical climate teleconnections and mechanisms for Holocene debris flows along the hyperarid coast of western South America (17°-24°S), Earth Planet. Sci. Lett., 249(3–4), 467–483, doi:10.1016/j.epsl.2006.07.022, 2006.

Vázquez, M., Ramírez, S., Morata, D., Reich, M., Braun, J. J. and Carretier, S.: Regolith production and chemical weathering of granitic rocks in central Chile, Chem. Geol., 446, 87–98, doi:10.1016/j.chemgeo.2016.09.023, 2016.

Viale, M. and Garreaud, R.: Summer precipitation events over the western slope of the subtropical andes, Mon. Weather Rev., 142(3), 1074–1092, doi:10.1175/MWR-D-13-00259.1, 2014.

Walder, J. and Hallet, B.: Theoretical Model of the Fracture of Rock During Freezing., Bull. Geol. Soc. Am., 96(3), 336–346, doi:10.1130/0016-7606(1985)96<336:atmotf>2.0.co;2, 1985.

Ward, P. J., Eisner, S., Flörke, M., Dettinger, M. D. and Kummu, M.: Annual flood sensitivities to El Niño-Southern Oscillation at the global scale, Hydrol. Earth Syst. Sci., 18(1), 47–66, doi:10.5194/hess-18-47-2014, 2014.

Ward, P. J., Kummu, M. and Lall, U.: Flood frequencies and durations and their response to El Niño Southern Oscillation: Global analysis, J. Hydrol., 539, 358–378, doi:10.1016/j.jhydrol.2016.05.045, 2016.

Waylen, P. and Poveda, G.: El Niño-Southern Oscillation and aspects of western South American hydro-climatology, Hydrol. Process., 16(6), 1247–1260, doi:10.1002/hyp.1060, 2002.

Waylen, P. R. and Caviedes, C. N.: Annual and seasonal fluctuations of precipitation and streamflow in the aconcagua river basin, Chile, J. Hydrol., 120, 79–102, 1990.

Waylen, P. R., Caviedes, C. N. and Juricic, C.: El Niño-Southern Oscillation and the surface hydrology of chile: A window on the future?, Can. Water Resour. J., 18(4), 425–441, doi:10.4296/cwrj1804425, 1993.

Werner, C., Schmid, M., Ehlers, T. A., Pablo Fuentes-Espoz, J., Steinkamp, J. S., Forrest, M., Liakka, J., Maldonado, A. and Hickler, T.: Effect of changing vegetation and precipitation on denudation - Part 1: Predicted vegetation composition and cover over the last 21 thousand years along the Coastal Cordillera of Chile, Earth Surf. Dyn., 6(4), 829–858, doi:10.5194/esurf-6-829-2018, 2018.

West, A. J., Hetzel, R., Li, G., Jin, Z., Zhang, F., Hilton, R. G. and Densmore, A. L.: Dilution of 10 Be in detrital quartz by earthquake-induced landslides : Implications for determining denudation rates and potential to provide insights into landslide sediment dynamics, Earth Planet. Sci. Lett., 396, 143–153, doi:10.1016/j.epsl.2014.03.058, 2014.

Whipple, K. X.: Fluvial landscape response time: How plausible is steady-state denudation?, Am. J. Sci., 301(4–5), 313–325, doi:10.2475/ajs.301.4-5.313, 2001.

Whipple, K. X.: Bedrock Rivers and the Geomorphology of Active Orogens, Annu. Rev. Earth Planet. Sci., 32(1), 151–185, doi:10.1146/annurev.earth.32.101802.120356, 2004.

Whipple, K. X. and Tucker, G. E.: Dynamics of the stream-power river incision model: Implications for height limits of mountain ranges, landscape response timescales and research needs, J. Geophys. Res., 104(B8), 661–674, 1999.

Whipple, K. X., DiBiase, R. A. and Crosby, B. T.: Bedrock rivers, in Treatise on Geomorphology.on Geomorphology., vol. 22, edited by J. Shroder and E. Wohl, pp. 735–740, Academic Press, San Diego, CA, San Diego., 2013.

White, A. F. and Blum, A. E.: Effects of climate on chemical, weathering in watersheds :, Geochim. Cosmochim. Acta, 59(9), 1729–1747, 1995.

White, A. F., Blum, A. E., Bullen, T. D., Vivit, D. V., Schulz, M. and Fitzpatrick, J.: The effect of temperature on experimental and natural chemical weathering rates of granitoid rocks, Geochim. Cosmochim. Acta, 63(19–20), 3277–3291, 1999.

Willenbring, J. K., Gasparini, N. M., Crosby, B. T. and Brocard, G.: What does a mean mean? The temporal evolution of detrital cosmogenic denudation rates in a transient landscape, Geology, 41(12), 1215–1218, doi:10.1130/G34746.1, 2013.

Willett, S. D.: Orogeny and orography : The effects of erosion on the structure Processes, J. Geophys. Res., 104(B12), 28957–28981, 1999.

Williams, A. and de Vries, F. T.: Plant root exudation under drought: implications for ecosystem functioning, New Phytol., 225(5), 1899–1905, doi:10.1111/nph.16223, 2020.

Wobus, C., Whipple, K. X., Kirby, E., Snyder, N., Johnson, J., Spyropolou, K., Crosby, B. and Sheehan, D.: Tectonics from topography: procedurses, promise, and pitfalls, Geol. Soc. Am. Spec. Pap., 398(04), 55–74, doi:10.1130/2006.2398(04)., 2006.

Wohl, E. and David, G. C. L.: Consistency of scaling relations among bedrock and alluvial channels, J. Geophys. Res. Earth Surf., 113(4), 1–16, doi:10.1029/2008JF000989, 2008.

Wolman, M. G.: A method of sampling coarse river-bed material, Trans. Am. Geophys. Union, 35(6), 951–956, doi:https://doi.org/10.1029/TR035i006p00951, 1954.

Wolter, K.: Multivariate ENSO Index, Natl. Ocean. Atmos. Adm., 1 [online] Available from: https://psl.noaa.gov/enso/mei.old/table.html (Accessed 20 January 2005), 2018.

Wolter, K. and Timlin, M. S.: Monitoring ENSO in COADS with a Seasonally Adjusted Principle Component Index, in Proc. 17th Climate Diagnostics Workshop, Norman, OK, NOAA, pp. 52–57., 1993.

Wolter, K. and Timlin, M. S.: Measureing the stregth of ENSO events: How does 1997/98 rank?, Weather, 53(9), 315–324, 1998.

Yanites, B. J. and Tucker, G. E.: Controls and limits on bedrock channel geometry, J. Geophys. Res. Earth Surf., 115(4), doi:10.1029/2009JF001601, 2010.

Yanites, B. J., Tucker, G. E. and Anderson, R. S.: Numerical and analytical models of cosmogenic radionuclide dynamics in landslide-dominated drainage basins, J. Geophys. Res. Earth Surf., 114(1), doi:10.1029/2008JF001088, 2009.

Zhao, Y., Feng, D., Yu, L., Wang, X., Chen, Y., Bai, Y., Hernández, H. J., Galleguillos, M., Estades, C., Biging, G. S., Radke, J. D. and Gong, P.: Detailed dynamic land cover mapping of Chile: Accuracy improvement by integrating multi-temporal data, Remote Sens. Environ., 183(June), 170–185, doi:10.1016/j.rse.2016.05.016, 2016.